Technische Universität München

Fakultät für Physik

Understanding Structural Transformations in Metal-Organic Frameworks to Design Active Oxygen Evolution Electrocatalysts

Shujin Hou

Vollständiger Abdruck der von der Fakultät für Physik der Technischen Universität München zur Erlangung des akademischen Grades eines Doktors der Naturwissenschaften (Dr. rer. nat.) genehmigten Dissertation.

Vorsitzender: Prof. Dr. David Egger

Prüfer der Dissertation:

1. Prof. Dr. Aliaksandr S. Bandarenka
2. Prof. Dr. Roland A. Fischer

Die Dissertation wurde am 11.05.2022 bei der Technischen Universität München eingereicht und durch die Fakultät für Physik am 27.06.2022 angenommen.

Abstract

To reduce the carbon footprint and accelerate the transition to renewable energy systems, the optimization of a number of electrocatalytic reactions is critical. As a concept that has seen a recent surge in interest, the hydrogen economy paints a promising picture in which "green" hydrogen can be obtained by electrocatalytic water splitting and can be cleverly coupled with renewable energy sources. However, the shortfall in efficiency impedes the widespread application of this hydrogen production technology, owing largely to the intrinsically sluggish kinetics of the oxygen evolution reaction (OER) at the anode of the electrolyzer. Therefore, the development of high-performing, low-cost, and robust OER electrocatalysts is of paramount importance. In this work, a facile layer-by-layer synthesis strategy was exploited to produce heterostructured and strained surface-mounted metal-organic frameworks (SURMOFs). The catalytically active species, NiFe (oxy)hydroxides, in the SURMOF derivatives were identified, offering insights into the structural transformation mechanisms and structure-performance relationships. Upon the immersion of the as-prepared SURMOFs into the electrolyte and subsequent electrochemical cycling, a morphological transformation and the self-activation of SURMOFs were confirmed to lead to advanced OER electrocatalysts. The derived NiFe (oxy)hydroxides yielded record oxygen evolution mass activities. Furthermore, to deepen the understanding of the role of the electrified electrode/electrolyte interface in the aforementioned electrocatalytic systems, *in-situ* techniques, *i.e.*, Raman spectroscopy and a laser-induced current transient (LICT) method, elucidated the role of alkali metal cations in impacting the electrocatalytic OER activities of SURMOF derivatives. Moving down in the alkali metal group of the periodic table, the activity increase followed a trend opposite to the Raman shifts of the Ni-O bending vibration, suggesting strong interactions between the cations and the reaction intermediates. The potential of maximum entropy (PME), obtained by the LICT measurements, was used to characterize the electrical double layer (EDL) properties. Interestingly, the influence of the cations on the OER activity is found consistent with the trend of the PMEs, following the activity order $Cs^+ > K^+ > Na^+ > Li^+$. Finally, strain engineering was demonstrated in the SURMOFs, resulting in changes in the electronic structure and further improvement of the catalytic activity. With the herein-obtained results, deeper insights into the development of state-of-the-art OER electrocatalysts using the metamorphosis of SURMOFs are provided.

Zusammenfassung

Um die CO_2-Bilanz zu verringern und den Übergang zu grünen, erneuerbaren Energiesystemen zu beschleunigen, ist es entscheidend, eine Reihe von elektrokatalytischen Reaktionen zu optimieren. Die Wasserstoffwirtschaft, ein Konzept, das immer größeres Interesse anzieht, zeichnet ein vielversprechendes Bild, bei dem grüner Wasserstoff durch elektrokatalytische Wasserspaltung gewonnen und geschickt mit erneuerbaren Energiequellen gekoppelt werden kann. Die mangelnde Effizienz hindert jedoch die allgemeine Verbreitung dieser Wasserstoffproduktionstechnologie, was zu großen Teilen auf die träge Kinetik der Sauerstoffentwicklungsreaktion (OER) an der Anode des Elektrolyseurs zurückzuführen ist. Daher ist die Entwicklung hochaktiver, kostengünstiger und robuster OER-Elektrokatalysatoren von größter Bedeutung. In dieser Arbeit wurde eine einfache Schicht-für-Schicht-Synthese zur Herstellung von heterostrukturierten und gespannten oberflächenmontierten metallorganischen Gerüsten (SURMOFs) genutzt. Die katalytische Spezies - NiFe-(Oxy)hydroxid - in SURMOF-Derivaten wurde analysiert und ein detailliertes Verständnis der strukturellen Umwandlungsmechanismen und der Beziehungen zwischen Struktur und Leistung wurde geschaffen. Es wurde bestätigt, dass Morphologieumwandlung, Strukturmetamorphose und Selbstaktivierung bei SURMOFs zur Herstellung von verbesserten Elektrokatalysatoren führen. Die abgeleiteten NiFe-(oxy)hydroxide erbrachten Rekordwerte für die Aktivität bei der Sauerstoffentwicklung. Um das Verständnis des Mechanismus der elektrifizierten Elektrode/Elektrolyt-Grenzfläche in dem oben genannten elektrokatalytischen System zu vertiefen, wurde mit Hilfe von zwei *in-situ*-Lasermethoden, Raman-Spektroskopie und laserinduzierter Stromübergang (LICT), der Einfluss von Kationen auf die elektrokatalytische OER-Aktivität von SURMOF-Derivaten aufgeklärt. Je weiter man sich in der Alkalimetallgruppe nach unten bewegt, desto mehr nimmt die Aktivität zu. Die Raman-Verschiebung der Ni-O-Schwingungen folgt einem entgegengesetzten Trend, was auf eine starke Wechselwirkung zwischen den Kationen an der Grenzfläche und den Reaktionszwischenprodukten hindeutet. Das Potenzial der maximalen Entropie (PME) wurde mit der LICT Methode bestimmt und dazu verwendet, die Struktur der elektrischen Doppelschicht (EDL) zu charakterisieren. Interessanterweise stimmt die Kationenabhängigkeit der OER-Aktivität mit dem Trend der PMEs überein und folgt der Reihenfolge $Cs^+ > K^+ > Na^+ > Li^+$. Abschließend wurde gezeigt, dass Anspannungen in den SURMOFs die elektronische

Struktur verändern und die katalytische Aktivität weiter verbessern können. Mit den hier erzielten Ergebnissen wurde das Wissen um die Entwicklung von modernen OER-Elektrokatalysatoren durch die Metamorphose von SURMOFs vertieft.

List of Publications

1. S. Hou, W. Li, S. Watzele, R. M. Kluge, S. Xue, S. Yin, X. Jiang, M. Döblinger, A. Welle, B. Garlyyev, M. Koch, P. Müller-Buschbaum, C. Wöll, A. S. Bandarenka, R. A. Fischer, Metamorphosis of Heterostructured Surface-Mounted Metal-Organic Frameworks Yielding Record Oxygen Evolution Mass Activities. *Advanced Materials* 33 (2021) 2103218.

2. S. Hou, L. Xu, X. Ding, R. M. Kluge, T. K. Sarpey, R. W. Haid, B. Garlyyev, S. Mukherjee, J. Warnan, M. Koch, S. Zhang, W. Li, A. S. Bandarenka, R. A. Fischer, Dual *In-situ* Laser Techniques Underpin the Role of Cations in Impacting Electrocatalysts. *Angewandte Chemie International Edition* 2022, accepted, https://doi.org/10.1002/ange.202201610.

3. S. Hou,‡ R. M. Kluge,‡ R. W. Haid,‡ E. L. Gubanova, S. A. Watzele, A. S. Bandarenka, B. Garlyyev, A Review on Experimental Identification of Active Sites in Model Bifunctional Electrocatalytic Systems for Oxygen Reduction and Evolution Reactions. *ChemElectroChem* 8 (2021) 3433-3456.

4. J. Liu,‡ S. Hou,‡ W. Li, A. S. Bandarenka, R. A. Fischer, Recent Approaches to Design Electrocatalysts Based on Metal-Organic Frameworks and Their Derivatives. *Chemistry—An Asian Journal* 14 (2019) 3474-3501.

5. W. Li, S. Xue, S. Watzele, S. Hou, J. Fichtner, A. L. Semrau, L. Zhou, A. Welle, A. S. Bandarenka, R. A. Fischer, Advanced Bifunctional Oxygen Reduction and Evolution Electrocatalyst Derived from Surface-Mounted Metal-Organic Frameworks. *Angewandte Chemie International Edition* 59 (2020) 5837-5843.

6. M. H. Aufa,‡ S. A. Watzele,‡ S. Hou, R. W. Haid, R. M. Kluge, A. S. Bandarenka, B. Garlyyev, Fast and Accurate Determination of the Electroactive Surface Area of MnO_x. *Electrochimica Acta* 389 (2021) 138692.

7. S. Tu,‡ T. Tian,‡ A. Lena Oechsle, S. Yin, X. Jiang, W. Cao, N. Li, M. A. Scheel, L. K. Reb, S. Hou, A. S. Bandarenka, M. Schwartzkopf, S. V. Roth, P. Müller-Buschbaum, Improvement of the Thermoelectric Properties of PEDOT:PSS Films via DMSO Addition and DMSO/Salt Post-Treatment Resolved from a Fundamental View. *Chemical Engineering Journal* 429 (2022) 132295.

8. S. Xue, R. W. Haid, R. M. Kluge, X. Ding, B. Garlyyev, J. Fichtner, S. Watzele, S. Hou, A. S. Bandarenka, Enhancing the Hydrogen Evolution Reaction Activity of Platinum Electrodes in Alkaline Media Using Nickel–Iron Clusters. *Angewandte Chemie International Edition* 59 (2020) 10934.

9. X. Ding,‡ T. K. Sarpey,‡ S. Hou, B. Garlyyev, W. Li, R. A. Fischer, A. S. Bandarenka, Prospects of Using the Laser-Induced Temperature Jump Techniques for Characterisation of Electrochemical Systems. *ChemElectroChem* 9 (2022) e202101175.

10. S. Mukherjee, S. Hou, S. A. Watzele, B. Garlyyev, W. Li, A. S. Bandarenka, R. A. Fischer, Avoiding Pyrolysis and Calcination: Advances in the Benign Routes Leading to MOF-derived Electrocatalysts. *ChemElectroChem* 9 (2022) e202101476.

11. R. M. Kluge,‡ E. Psaltis,‡ R. W. Haid, S. Hou, T. O. Schmidt, O. Schneider, B. Garlyyev, F. Calle-Vallejo, A. S. Bandarenka, Revealing the Nature of Active Sites on Pt-Gd and Pt-Pr Alloys during the Oxygen Reduction Reaction. *ACS Applied Materials & Interfaces* 2022, accepted, https://doi.org/10.1021/acsami.2c03604.

‡ Authors contributed equally to the publication.

Conference Contributions

1. S. Hou, W. Li, R. A. Fischer, A. S. Bandarenka, Structural Conversion of Surface-Mounted Metal-Organic Framework Heteromultilayers Enables a Record Mass Activity towards Oxygen Evolution Reaction. 72nd Annual Meeting of the International Society of Electrochemistry, Hybrid Meeting - Jeju Island, Korea/Online, 29 August - 3 September 2021. (Oral presentation)

2. S. Hou, W. Li, R. A. Fischer, A. S. Bandarenka, Structural Conversion of Surface-Mounted Metal-Organic Framework Heteromultilayers Enables a Record Mass Activity towards Oxygen Evolution Reaction. 32. Deutsche Zeolith-Tagung, online, 10 - 11 March 2021. (Oral presentation)

3. S. Hou, R. A. Fischer, A. S. Bandarenka, Elucidating Electrolyte Effects in Oxygen Evolution Electrocatalytic Activities of some Metal-organic Framework Derivatives. 32nd Topical Meeting of the International Society of Electrochemistry, Stockholm, Sweden, 19 - 22 June 2022. (Poster presentation)

4. The COORNETS Summer School: Conductive Metal-Organic Frameworks – From Synthesis To Functions, online, 6 - 9 September 2021. (Attendance)

5. The SUNCAT Summer Institute: Catalysis for a Sustainable Future, virtual meeting, 16 - 19 August 2021. (Attendance)

6. 11th Energy Colloquium of the Munich School of Engineering, online, Garching, 28 July 2021. (Attendance)

7. 10th Energy Colloquium of the Munich School of Engineering, online, Garching, 30 July 2020. (Attendance)

8. ECS Student Chapter Munich, 3rd Symposium: Interdisciplinarity in Electrochemistry, Garching, 24 September 2019. (Attendance)

9. 9th Energy Colloquium of the Munich School of Engineering, Garching, 1 August 2019. (Attendance)

10. ECS Student Chapter Munich, Panel Discussion: Fueling Tomorrow - Energy Supply for Future Mobility, 23 October 2018. (Attendance)

Acknowledgments

I would like to express my heartfelt gratitude to the many people who have provided help and support for my doctoral study and this dissertation. There is no doubt that I could not have made it without their dedication.

Foremost, I would like to thank my supervisor **Prof. Dr. Aliaksandr S. Bandarenka** for giving me not only the opportunity to work in his ECS group but also the patient guidance and support throughout all the time of my doctoral research. The treasures that I gained from him, *e.g.*, rigorous research attitude, scientific ways of thinking, and adept problem-solving skills, will benefit me all my life. It was really my honor to work and study at the TUM under his supervision.

Sincere gratitude from the bottom of my heart also goes to my co-supervisor **Prof. Dr. Roland A. Fischer**, who has guided me throughout my thesis and offered an excellent research environment in the Catalysis Research Center. I am especially grateful for his invaluable advice and encouragement during my manuscripts' preparation and submission. It was my fortune to go through my doctoral study with his warm support and assistance.

I would also like to thank the **China Scholarship Council (CSC)** for supporting the cost of my study and life abroad.

My thanks also go to **Dr. Weijin Li** for his advice, discussions, and comments on my experiments, manuscripts, and thesis. Especially, his meticulous help during the experimental training in the beginning stages of my doctoral study was highly valuable for my subsequent research. I am also thankful to **Dr. Batyr Garlyyev**, who patiently gave guidance on my paper writing and encouraged me to speak English bravely. Whenever I asked for help, he always replied to me in detail.

Next, I would like to thank all the warm and friendly ECS members who created a great working atmosphere. It was a real pleasant time working with you over the last years. I am grateful to my colleagues, **Dr. Sebastian Watzele**, **Dr. Regina Kluge**, **Dr. Song Xue**, **Dr. Xing Ding**, **Richard Haid**, **Theophilus Kobina Sarpey**, and **Dr. Elena Gubanova** for the collaborations on the topic of my thesis. Many thanks for your constructive feedback and profound discussions.

I am equally thankful to the former and current members of the ECS: **Dr. Yunchang Liang**, **Dr. Daniel Scieszka**, **Dr. Jeongsik Yun**, **Dr. Johannes Fichtner**, **Dr. Rohit Ranganathan Gaddam**, **Philipp Marzak**, **Xiaohan Sun**, **Jongho Kim**, **Simon Helmer**, **Muhamad Hilmi Aufa**, **Nina Thomsen**, **Leon Katzenmeier**, **Xaver Lamprecht**, **Leif Carstensen**, **Thorsten Schmidt**, **Kun-Ting Song**, **Göktug Yesilbas**, **Peter Schneider**, **Felix Haimerl**, **Rainer Götz**, **Emre Keleş**, and **Yapeng Cheng**. Furthermore, I sincerely thank **Siegfried Schreier** and **Manuela Ritter** for their wholehearted dedication to our ECS group.

I would like to extend my thanks to all the e-conversion subgroup members in the AMC chair. Special thanks to **Dr. Julien Warnan**, **Dr. Soumya Mukherjee**, **Xiaoxin Ma**, **Zhenyu Zhou**, and **Ruirui Zhang** for the fruitful discussions and the precious advice on my research work. I learned a lot from our weekly group seminars and the frequent scientific discussions, providing me with new insights into the topic of my research.

I would like to express a big thanks to my collaborators: **Prof. Dr. Christof Wöll** (Karlsruhe Institute of Technology), **Dr. Alexander Welle** (Karlsruhe Institute of Technology), **Prof. Dr. Peter Müller-Buschbaum** (Physics, TUM), **Dr. Markus Döblinger** (Ludwig Maximilian University of Munich), **Shanshan Yin** (Physics, TUM), **Xinyu Jiang** (Physics, TUM), **Suo Tu** (Physics, TUM), **Prof. Shengli Zhang** (Nanjing University of Science and Technology), **Lili Xu** (Nanjing University of Science and Technology), **Dr. Rachit Khare** (Chemistry, TUM), and **Max Koch** (Chemistry, TUM). I really appreciate their technical support. Without their kind help and suggestions, the accomplishment of my research work would have been impossible.

Last but not least, I am deeply indebted to **my parents** for their unconditional understanding and encouragement, which motivated me to keep going forward. I would like to apologize for the lack of companionship in recent years. I know that no matter where I am and how "difficult" my life is, my family is always the strongest support for me.

Contents

1 Introduction

1.1 The Importance of Renewable Energy Sources

There is an urgent need to develop sustainable alternatives to fossil fuels to mitigate climate change and accelerate the transition to a low-carbon emitting society. In essence, this is primed to meet today's rapidly growing energy demand and create a "greener" tomorrow.[1,2,3,4] In recent years, the nations of the world have taken swift and effective action to develop renewable energy sources for a greener future. Renewable energy sources include wind, solar, geothermal, wave, tidal, hydroelectric, and biomass, each at a different stage of commercial maturity and development.[5,6,7] According to the "Renewables 2021 Global Status Report",[8] renewable energy targets and supporting policies are in place in nearly all countries. Renewable energy accounts for 26% of the world's electricity today, but according to the International Energy Agency (IEA), its share is expected to reach 30% by 2024. Despite the high promises of alternative energy technologies such as wind, solar, hydro, geothermal, and tidal, these are often handicapped by geographic and climatic factors.[9,10] The disadvantage of intermittency affects the reliability of the electricity grid.

Conversely, hydrogen allows renewable energy storage in a supply-based and flexible manner, helping to balance energy supply and demand (*cf.* **Figure 1.1**).[11,12] Unsurprisingly, hydrogen assumes critical importance in the modern energy landscape, thanks to its favorable features as a carrier. Reaping the benefits of its high theoretical energy conversion efficiency and energy density, hydrogen and its derivatives open new avenues to decarbonize areas where renewable electricity cannot be used directly. The German federal government, for example, has recognized the future of hydrogen technology in the long term.[13] To achieve the goal of being greenhouse gas neutral and striving towards meeting the goals of the Paris Agreement,[14] Germany has established hydrogen as one of the decarbonization options. It has supported funding volumes of up to € 1.4 billion between 2016 and 2026. Today the primary demand for hydrogen is for petroleum refining and ammonia production.[15] The United States Department of Energy (DOE) is dedicated to developing ways to reduce the cost of producing hydrogen at a price of \$ 2 kg^{-1} by 2025 and \$1 kg^{-1} by 2030 through a net-zero carbon pathway. Indeed, the development of clean hydrogen, also known as "green" hydrogen, requires overcoming some challenges.[16] Conventionally, producing hydrogen is not a clean process. Natural gas

reforming is currently the large-scale way of hydrogen production, consuming around 6% of the global natural gas use.[17,18] Producing hydrogen from fossil fuels also implies an increase in carbon dioxide emissions as the demand for hydrogen soars. To meet the emission reduction targets set by the Paris Agreement, fossil fuel companies will face increasingly stringent restrictions on all production sectors. Therefore, there is an urgent demand to develop technologies to produce carbon-free hydrogen from renewable and nuclear energy resources.

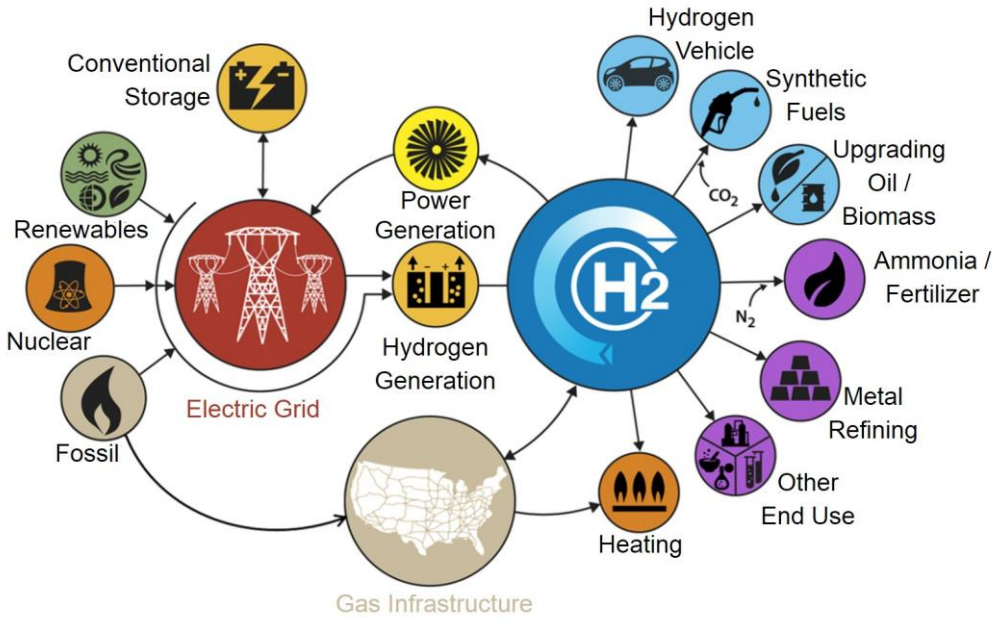

Figure 1.1. *Various schemes for the production routes and the uses of renewable hydrogen and electricity: concept at the crux of a sustainable hydrogen economy. Adapted from ref. [19].*

1.2 Electrochemical Strategies to Produce Fuels and Chemicals

Water electrolysis has been used for over a century to produce hydrogen in industrial applications. Still, in recent decades, its use has been rapidly increasing due to emerging technologies and the availability of low-cost electricity.[20,21] In addition, alternatives to "classical" electrochemical water spitting are arising, including thermochemical water splitting, photochemical water splitting, and biological pathways.[22] Widely regarded as a promising approach to producing carbon-free hydrogen, electrolysis is a process that uses electricity to split water into hydrogen and oxygen. The reaction takes place in a so-called electrolyzer. The "green" hydrogen production uses not fossil fuels but renewable energy sources to power the water electrolyzer and produce hydrogen.[23] Converting renewable energy into storable gas overcomes two limitations: 1) renewable energy is dynamic and intermittent (solar and wind

are dependent on solar irradiation and wind, respectively);[9,24] 2) electricity generation is not always in line with the demand.[25]

The electrolytic cell is simple in construction, consisting of an anode and a cathode separated by an electrolyte. Several types of electrolyzers have been extensively studied and differentiated according to the specific electrolyte used[26,27]: polymer electrolyte membrane electrolyzers, alkaline electrolyzers, and solid oxide electrolyzers.

In addition to the production of hydrogen, electricity from renewable energy sources can also be used to convert abundant small molecules (CO_2 and N_2) into valuable base chemicals (*e.g.*, methanol, light olefins, and ammonia) through electrochemical processes.[28] These chemical products are usually expressed in the form of liquids or gases that facilitate storage, transport, and use. Using sustainable electrochemical methods to produce synthetic chemicals and thereby replace fossil resources will allow us to close the carbon cycle and minimize net CO_2 emissions (*cf.* **Figure 1.2**), which will be a powerful tool in our fight against climate change.

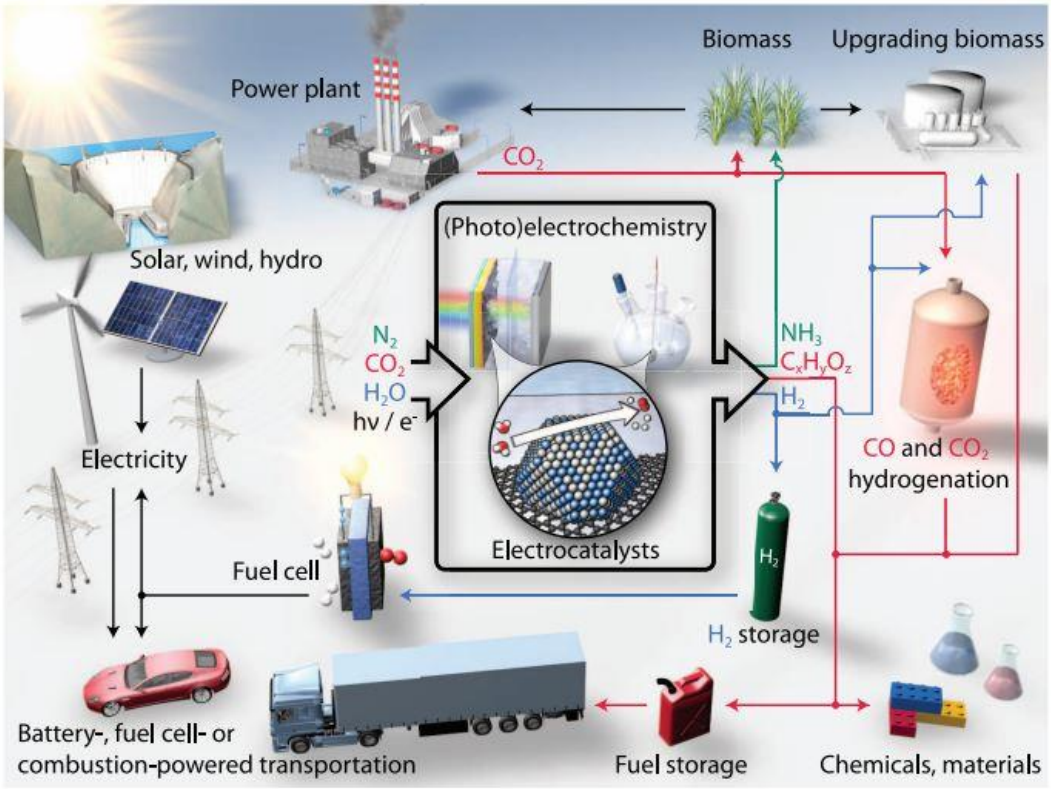

Figure 1.2. *Schematic of converting electricity into sustainable fuels and chemicals via an electrochemical catalytic process. Adapted with permission from ref. [1]. Copyright © 2017, Science.*

1.3 Metal-Organic Frameworks

1.3.1 A Short History of Metal-Organic Frameworks

Metal-organic frameworks (MOFs), also known as porous coordination polymers, are a class of ordered, porous, crystalline materials formed by the coordination of organic ligands with metal ions (clusters).[29,30,31] Due to their ultrahigh porosity (up to 90% free volume), high specific surface area (extending beyond 6000 m^2 g^{-1}), tunable pore structure, ligand designability, and easy modification, MOFs have been widely used in research fields such as separation, catalysis, sensing, and drug delivery in the past two decades.[32,33,34]

The study and application of porous coordination polymers have a long history. For instance, Prussian blue was already used as a pigment in the 18th century. Still, it was not until 1977 that researchers used X-ray single-crystal diffractometry to reveal its structure as interlaced octahedral sites Fe(II)/Fe(III) coordinated with cyano groups to form a 3D structure.[35] In 1893, Alfred Werner first described the octahedral configuration of transition metal complexes and proposed a coordination chemistry theory including coordination numbers and valence states.[36] For this, he was awarded the Nobel Prize in Chemistry in 1913.[37] In addition, the Hofmann clathrate is another early example of a coordination compound with an extended two-dimensional (2D) structure.[38] Its formula is $[Ni(CN)_2(L)](C_6H_6)$, where L is NH_3 and benzene (C_6H_6) represents guests. Notably, the Hofmann clathrate structure will collapse when the guest molecule is removed from the structure. It is widely accepted that in 1990, Hoskins and Robson reported the use of organic molecular building blocks (ligands) and metal ions to construct 3D MOFs, starting a new chapter in MOF research.[39] In the following decade, significant progress was made in the field of MOF design, thanks to the efforts of the groups of Yaghi,[40] Kitagawa,[41] and Férey.[42] In fact, the term "Metal-organic frameworks" was first introduced for $[Cu(4,4'\text{-bipyridine})_{1.5}](NO_3)$ by the Yaghi group in 1995.[40] During this period, the two most representative MOFs were developed,[43,44] namely MOF-5 ($Zn_4O(bdc)_3$, bdc = 1,4-benzenedicarboxylate) and HKUST-1 ($Cu_3(btc)_2$, btc = 1,3,5-benzenetricarboxylate; HKUST = The Hong Kong University of Science and Technology), as shown in **Figure 1.3**. These are composed of polynuclear metal clusters and charged ligands and exhibit a strong porosity and relatively high stability. In the MOFs mentioned above, polynuclear clusters, often called secondary building units (SBUs), can achieve a more robust structure by replacing individual metal ion nodes in the coordination networks.[45,46] The reason is that metal ion chelation forms

polynuclear clusters, which can provide rigidity and definitive directionality. Moreover, the introduction of charged chelating ligands is of interest since it can overcome the limitations of an inherent architectural and chemical instability caused by the increased bond strength.[47]

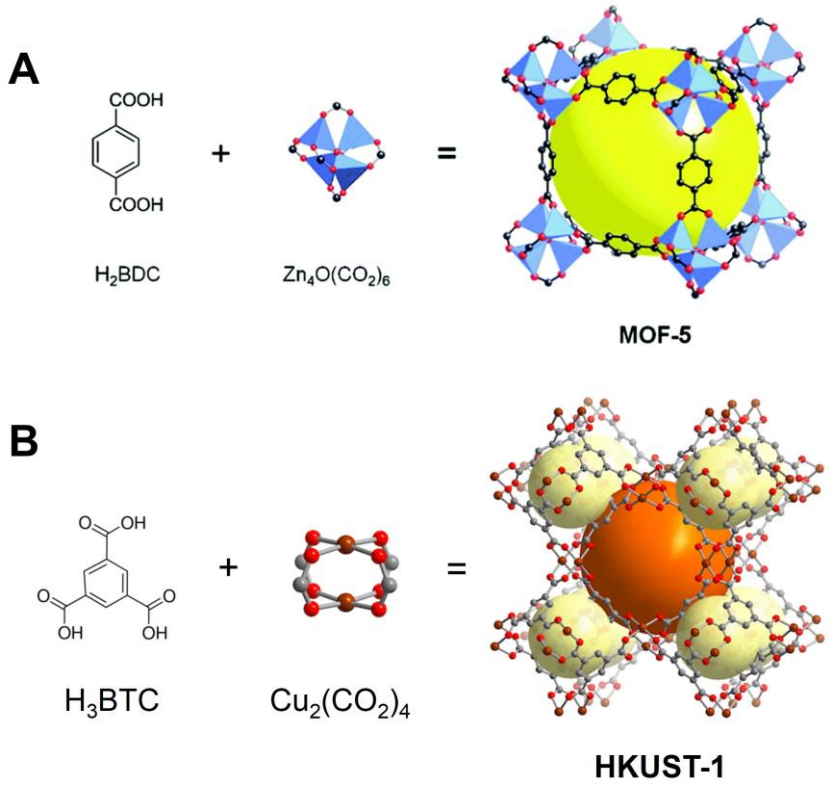

Figure 1.3. *Illustration of the crystal structures of the archetype MOFs, MOF-5, and HKUST-1. (A) The MOF-5 is composed of BDC ligands and $Zn_4O(CO_2)_6$ SBUs. Adapted with permission from ref. [32]. Copyright © 2017, The Royal Society of Chemistry. (B) Similarly, HKUST-1 consists of BTC ligands and $Cu_2O(CO_2)_4$ dimeric metal units. Image modified from ref. [48].*

Later, fascinating properties, namely breathing and swelling phenomena, were found in some MOFs. Such MOFs with flexible or dynamic frameworks have attracted a lot of attention from researchers.[49] Typically, the framework's flexibility is related to the interaction between host and guest molecules. However, this is not entirely true in flexible MOFs. Their flexibility or responsiveness can be triggered by external stimuli like light, electricity, heat, mechanical, or guest adsorption/desorption.[50,51] Due to these unique properties, flexible MOFs can be useful in separation processes, biomedicine, chemical sensing, and catalysis.[49] The rapid development of MOFs in the last two decades was mainly driven by observing a variety of fascinating properties and potential application prospects. Due to the variability of the components, geometry, size, and function, over 100,000 MOFs have been synthesized up to

date (Cambridge Crystallographic Data Center MOF collection), and over 500,000 are predicted.[52,53] However, only several stable and easy-to-prepare MOFs have been widely studied and applied, such as MOF-5, MIL series (MIL = Matériaux de l'Institut Lavoisier), HKUST-1, UiO-66 (UiO = Universitetet i Oslo), ZIF-8 (zeolitic imidazolate framework), and ZIF-67.

1.3.2 Surface-Mounted Metal-Organic Frameworks

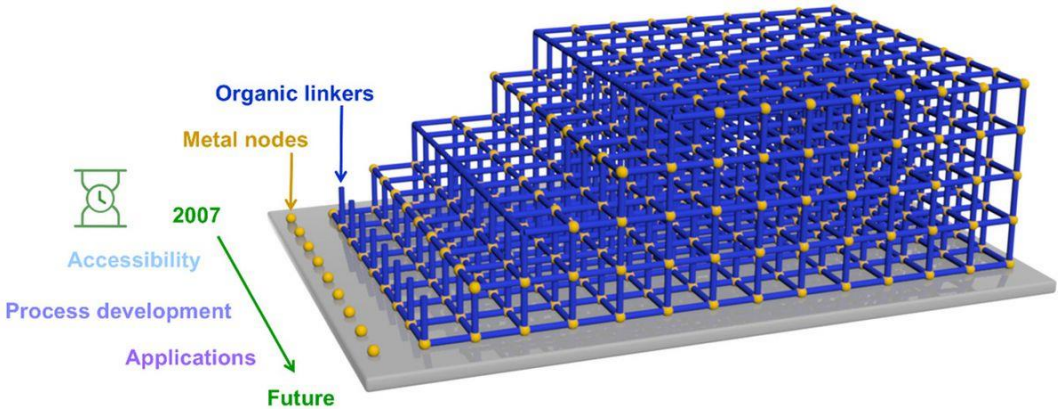

Figure 1.4. *Schematic diagram of a surface-mounted MOF thin film on the substrate, constructed by the connection of the organic linkers with the metal nodes. Reproduced with permission from ref. [54]. Copyright © 2021, American Chemical Society.*

In the past decade, surface-mounted MOF (SURMOF) thin films have gained much attention as another physical form of MOFs because of their importance for many applications such as chemical sensors, gas/liquid separation, and related electro-devices.[55] Numerous MOF film growth methods have been reported, commonly including direct growth/solvent thermal deposition, vapor assisted conversion, gas-phase deposition, electrochemical deposition, and liquid-phase (quasi-)epitaxy layer-by-layer (LPE-LbL).[56,57,58] However, the effective integration of MOF films into devices often requires tight control of key quality factors such as the precise control of surface roughness, crystal orientation, and the thickness of the deposited film. SURMOFs can be grown directly on supporting surfaces functionalized with self-assembled monolayers (SAMs) by the LbL method under relatively low temperatures and simple experimental conditions.[54] The obtained MOF films are crystalline, smooth, and well-oriented. Their thickness can be adjusted in the range of several ten nanometers to several micrometers by the number of deposited layers. In addition, SURMOF technology enables access to the flexible design of heterostructures and the introduction of target defects. The

SURMOF films prepared from LPE-LbL (*cf.* **Figure 1.4**) were first reported by C. Wöll and R. A. Fischer in 2007 and have subsequently received increasing attention.[59]

1.4 Metal-Organic Frameworks for Electrocatalysis

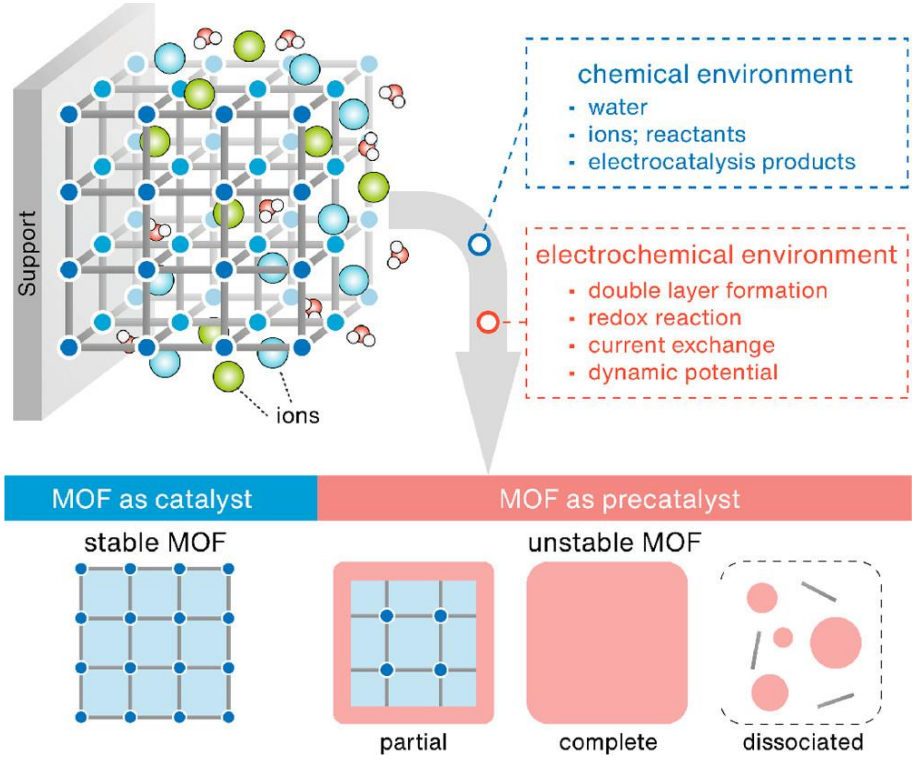

Figure 1.5. *Schematic representation of the possible states of a MOF in a specific chemical and electrochemical environment: catalyst or precatalyst. The precatalyst represents that the pristine MOFs underwent structure transformation and generation of active phases during the alkaline immersion and the electrochemical treatment. Reproduced with permission from ref. [61]. Copyright © 2021, American Chemical Society.*

Due to the unique advantages of MOFs, *e.g.*, high surface area, tunable pore size, and variable metal nodes / organic ligands, MOFs show great potential for applications in electrocatalysis.[60] Extensive literature has elucidated the easy modulation of the interactions between the active metal center and adjacent atoms of different coordination, thus altering the activity of the catalytic site and the magnitude of the adsorption energy toward the reaction intermediate.[53] In addition, MOFs with regular channels or pore structures allow an efficient mass transfer and adequate contact between the active site and the reactants. However, by nature, MOFs contain catalytically active metals, but these metal sites are usually combined with organic ligands, which are not exposed and thus inactive.[61] The low electronic conductivity and the weak

chemical stability of most MOFs greatly limit their applications in electrocatalysis. In other words, the role of MOFs in electrocatalysis is still worth confirming under certain electrochemical test conditions (potential, current, electrolyte, pH, *etc.*), as shown in **Figure 1.5**. Therefore, the deliberate introduction of defects or unsaturated active sites, size tuning, and improvement of conductivity are the focus of future research to improve the catalytic activity and expand the application area of MOFs.[53,62] Furthermore, it is meaningful to reveal the origin of catalytically active species and to analyze the relationship between structure and performance.

1.4.1 Pristine Metal-Organic Frameworks as Electrocatalysts

Given the inherent drawbacks of MOFs, such as low electrical conductivity values, excessive microporous structures, and the blockage of active metal sites by organic ligands, at present, the development of pristine MOF-based electrocatalysts is mainly focused on four mitigation strategies.

(1) **Improvement of conductivity.** The conductivity of electrocatalysts is one of the main parameters affecting the efficiency of electrocatalytic systems. The majority of the reported MOFs are semiconductors or insulators. Conductive MOFs were developed by introducing conjugated organic ligands to improve electrocatalytic performance. For instance, an effort in developing conductive MOFs was made by Feng *et al*.[63] They developed a reliable Langmuir-Blodgett (LB) approach to synthesize 2D supramolecular polymer monolayer sheets. The prepared triphenyl-fused nickel bis(dithiophene) complexes achieved an HER current density of 10 mA cm^{-2} at a lower overpotential of 333 mV. The efficient H_2 production is closely related to the 2D structure, the choice of conductive conjugated organic ligands, and synergistic effects between the metals, S, and N. Besides, combining MOFs with highly-conductive substrates (*e.g.*, graphene, activated carbon) is also a common strategy.[64]

(2) **Creation of unsaturated sites.** In catalysis, MOFs are ideal candidates for exploring structure-property relationships. Previous studies have shown that introducing defects or creating additional unsaturated metal sites in MOFs can lead to a higher number of catalytically active sites and higher catalytic performance.[65,66,67] Based on this strategy, Wang and colleagues used plasma etching to create more coordinatively unsaturated metal

sites in the chemically and thermally stable ZIF-67(Co). The electrocatalytic performance was enhanced significantly.[68]

(3) **Design of ultrathin nanosheets.** Most MOFs are rich in micropores, which is the reason for the ultra-high specific surface area. This feature is favorable for gas adsorption of small molecules but unfavorable for electrocatalytic reactions in a liquid environment because the micropores restrict the diffusion of reactants and product gas molecules. Ultra-thin two-dimensional nanosheet electrocatalysts are becoming an increasingly attractive research topic due to their unique physicochemical properties. Accordingly, developing ultrathin MOF nanosheets is an effective way to improve the accessibility of active metal sites and accelerate the reaction rate. For instance, in 2016, Zhao *et al.* first reported a series of ultrathin MOF nanosheets for the electrocatalytic oxygen evolution reaction (OER) with excellent activity.[69] Since then, 2D MOFs have attracted widespread interest in the field of electrocatalysis.

(4) **Generation of lattice strain.** Strain engineering is a common tool to achieve outstanding performances *via* the design of catalysts.[70] Current studies demonstrate that the electronic structure of the catalyst is among the main factors for performance. Introducing strain to the catalyst surface enables to precisely tune the electronic structure, and to further modify the adsorption strength ability of the active site toward reactants, reaction intermediates, and/or products. Recently, Liu *et al.* reported that the introduction of lattice strain in NiFe-MOFs allows for obtaining highly active bifunctional electrocatalysts.[71] The photoinduced lattice strain causes a redistribution of the atomic and electronic configurations of the Ni sites within the MOFs.

1.4.2 Metal-Organic Framework Derivatives as Electrocatalysts

"MOF-derivatives" are a general term for a large class of materials, but only MOF-derived electrocatalysts obtained in the benign routes (non-pyrolysis) are discussed here. In MOFs, the coordination bonds formed by metal ions (clusters) and organic ligands tend to dissociate under extreme conditions, resulting in the reconstruction of the thereby released metal ions or clusters in an ordered or disordered manner. The electronic interactions between metal centers and organic ligands are weaker in MOFs than that in conventional solid-state materials.[53] This explains the low stability. Even if the coordination bonds of some MOFs are strong in

concentrated acetic or alkaline electrolytes, the chemical stability does not imply their electrochemical stability.[61] In particular, at a very low or high bias voltage, the metal nodes in MOFs are likely to be reduced or oxidized, thus breaking the coordination bonds.[72,73] For example, carboxylate-based MOFs are relatively unstable under strongly alkaline conditions, since OH^- ions can split the coordination bonds that hold the carboxylate ligands to the metal sites, leading to the formation of metal hydroxides.[74,75,76] The obtained metal hydroxides play a key role in the subsequent electrocatalytic process. In addition to the alkaline hydrolysis, recently, Lee and co-workers systematically studied the transformation process of ZIF-67 during both cyclic voltammetry and amperometry.[77] Their *in-situ* spectroelectrochemistry results demonstrated that the strong transformation of tetrahedral Co sites in ZIF-67 to tetrahedral α-$Co(OH)_2$ and octahedral β-$Co(OH)_2$ occurs gradually during the electrochemical treatment, as illustrated in **Figure 1.6**. The active center of OER lies in CoOOH species, generated by the oxidation of α/β-$Co(OH)_2$, rather than from the metal nodes in ZIF-67.

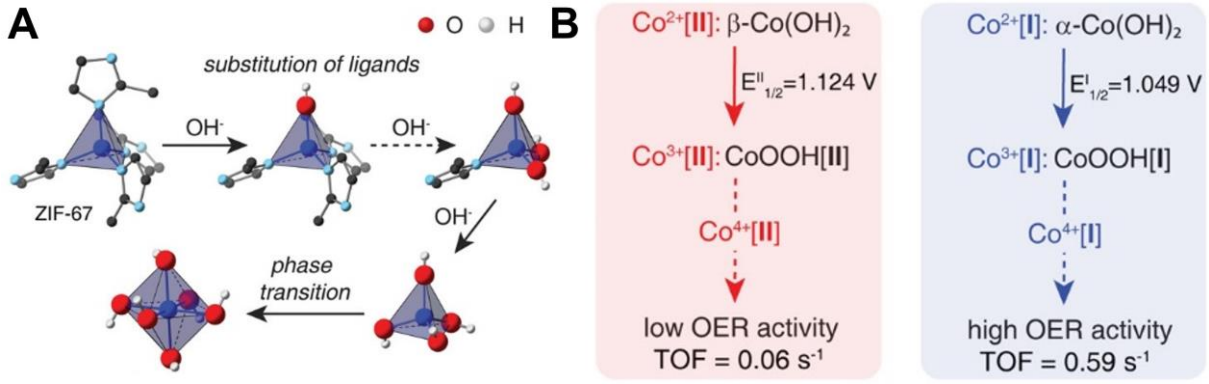

Figure 1.6. *Precatalytic transformation of ZIF-67 to α-$Co(OH)_2$ and β-$Co(OH)_2$, and the comparison of their further oxidation and OER activity. Reproduced with permission from ref. [77]. Copyright © 2020, American Chemical Society.*

Today, reports are appearing daily on the use of pristine MOFs as catalysts in electrocatalysis. We need to revisit these supposedly "stable" MOF electrocatalysts and consider the following questions: What is the real role of the MOFs: catalyst or precatalyst? What about the stability of MOFs in electrolytes and during the electrochemical treatment? What are the active catalytic species?

1.5 Aim

The overall goal of this work is to develop highly-active OER electrocatalysts through the SURMOF strategy. Throughout, the origin of active species and the relationship between structure and performance are methodically revealed.

Considering the SURMOF's advanced nature, such as high orientation and adjustable thickness, SURMOFs are ideal candidates for exploring structure-property relationships and derivation mechanisms, especially for introducing heterostructures. Therefore, the investigative content of this thesis can be grouped into three parts:

1. A series of *in-situ* and *ex-situ* methods were used to disclose the structural variations of the heterostructured SURMOFs during the alkaline immersion and electrochemical treatment. Additionally, the catalytic performance and the active species were considered.

2. It is well known that the electrode material and the electrolyte are two key elements dominating the electrocatalytic reactions of energy conversion systems. The effect of alkali metal cations on the electrified electrode/electrolyte interface and OER activity of the SURMOF derivatives were investigated by combining two *in-situ* techniques: Raman spectroscopy and a laser-induced current transient method.

3. The inherent properties of SURMOFs, such as highly-tunable coordination structures and tunable growth directions, allow easy access to effective strain modulation. A series of advanced oxygen evolution electrocatalysts were prepared by designing strained SURMOFs. The effect of strain on the electronic structure of SURMOFs and catalytic properties was investigated in detail.

2 Theory of Electrocatalysis

This chapter gives an overview of the electrochemistry fundamentals, including design principles of electrocatalysts, electrode kinetics, electrified interface, and mechanistic models of water splitting.

Parts of this chapter have been published in:

S. Hou,‡ R. M. Kluge,‡ R. W. Haid,‡ E. L. Gubanova, S. A. Watzele, A. S. Bandarenka, B. Garlyyev, A Review on Experimental Identification of Active Sites in Model Bifunctional Electrocatalytic Systems for Oxygen Reduction and Evolution Reactions. *ChemElectroChem* 8 (2021) 3433-3456;

J. Liu,‡ S. Hou,‡ W. Li, A. S. Bandarenka, R. A. Fischer, Recent Approaches to Design Electrocatalysts Based on Metal-Organic Frameworks and Their Derivatives. *Chemistry—An Asian Journal* 14 (2019) 3474-3501.

2.1 Design Principles of Electrocatalysts

There has been increasing research interest in electrochemistry with a growing need for renewable energy and environmentally sustainable systems.[78] Meanwhile, some new disciplines intersecting with electrochemistry are emerging and opening up new research and application fields. As an important part of electrochemical science, electrocatalysis is essential for sustainable energy conversion with the perspective of solving crucial environmental problems.[1,24,28] Compared to the traditional way of providing energy by burning fossil fuels (coal, oil, natural gas), electrocatalytic energy conversion technologies show clear intrinsic advantages to convert and store clean energy and produce valuable chemicals. Electrocatalytic reactions take place at the electrified electrode/electrolyte interface. The reaction rate is determined by the activity of the catalysts, the applied bias potential, and the electrolyte properties.[79,80] Typically, superior catalysts exhibit fast reaction kinetics, low overpotential, high selectivity, and good stability, enabling higher Faradaic efficiency and a low cost.[81,82] However, practically most electrochemical reactions involve multi-step electron or electron-

proton coupling reactions, which results in sluggish kinetics.[83] Therefore, detailed knowledge of the design principles is essential to developing efficient electrocatalysts.

2.1.1 The Sabatier Principle

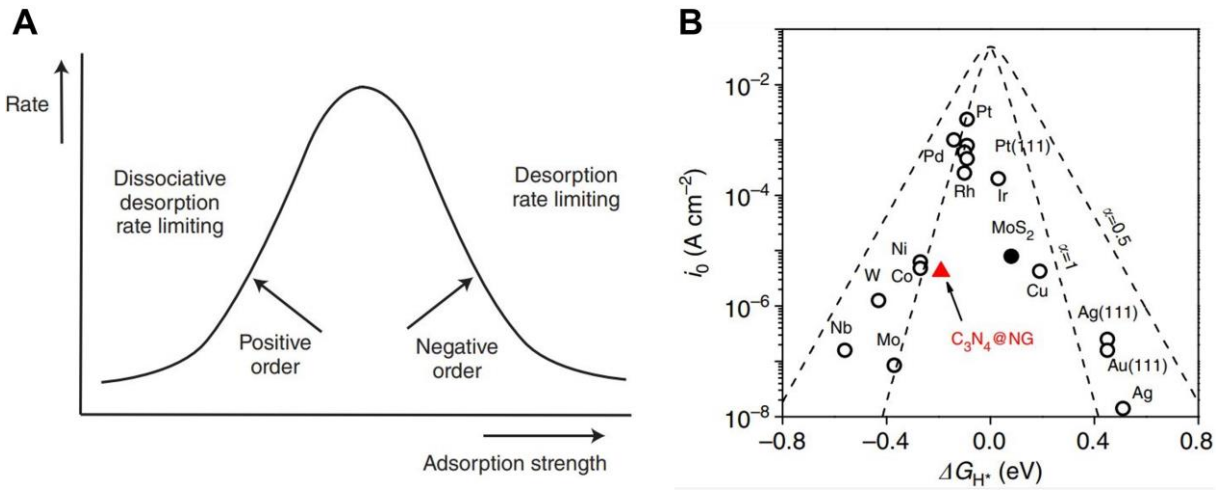

Figure 2.1. *(A) Illustration of the Sabatier principle. (B) Volcano plots for the relationship between the HER current density and the hydrogen adsorption free energy (ΔG_{H^*}) for pure metals, MoS_2, and C_3N_4@NG. Reproduced with permission from ref. [84]. Copyright © 2014, Nature Publishing Group.*

According to the Sabatier principle, the binding energy of the reactants onto the electrode surface should be "just right", namely, neither too strong nor too weak.[85,86,87] This principle was proposed by the French chemist Paul Sabatier in 1902. As shown in **Figure 2.1A**, for an electrocatalytic reaction, a too weak binding will result in limited interaction with the catalyst, *i.e.*, the reactants do not easily adsorb at the catalyst surface. On the other hand, a too strong binding will hinder the desorption of products from the catalyst surface, resulting in the blockage of available active sites. If the Sabatier principle is the only rate-describing factor of a certain reaction, it is possible to plot the reaction rate against the adsorption free energy of the intermediate. This is denoted as a so-called "volcano curve".[88] Taking the hydrogen evolution reaction (HER) as an example, it was Gerischer and Parsons who first proposed certain models predicting the "volcano"-type plot of the HER.[89,90,91] Subsequently, the first respective "volcano" plot was constructed by Trasatti based on the experimental data he collected.[92] However, given that there were no available experimental or theoretical data on hydrogen adsorption at that time, the energy of hydride formation (E_{M-H}) was used as the atomic-level parameter ("descriptor") instead of the energy of hydrogen adsorption. In recent years, the development of density functional theory calculations made the hydrogen binding

energy/hydrogen adsorption free energy (ΔG_{H^*}) readily available.[93,94,95] As shown in **Figure 2.1B**, the plots of HER activity as a function of hydrogen adsorption free energy for traditional pure metals, as well as MoS_2 and C_3N_4@NG demonstrate a volcano-type plot. Pt near the apex exhibits the closest value to $\Delta G_{H^*} = 0$ and the highest reaction current.[84] Therefore, the Sabatier principle is still an important theoretical basis for our understanding and prediction of electrocatalysts.

2.1.2 Electronic and Structural Effects in Electrocatalysis

Recent findings have demonstrated that the composition and the structure of the electrode material show a significant effect on the reaction rate and selectivity. The reaction selectivity indeed depends on the nature of the reaction intermediates and their stability, as well as on the relative speed of each successive step at the electrode interface.[96,97] Basically, the reaction rate of the active sites on the surface of the electrode material is closely related to two intrinsically interrelated effects, namely, electronic and structural effects.[98] The electronic effect mainly refers to the effect of the energy band and surface density of states of the electrode material on the activation energy of the reaction.[99,100] On the other hand, the structural effect indicates that the surface structure of the electrode materials can alter their interaction with the reactant molecules in the electrolyte, thus influencing the reaction rate.[101,102] In practical systems, electronic and structural effects overlap and cannot be completely distinguished. Usually, electronic effects are considered to be a more critical factor since variations of activation energy can cause changes in reaction rates of several orders of magnitude.[103]

Up to now, reported electrocatalysts mainly include metals and alloys as well as metal compounds, semiconductors, conducting polymers, and carbon-based materials; most of them are related to transition metals.[104,105] In the case of the same type of reaction system, different transition metal electrocatalysts can induce changes in the free energy of adsorption, which in turn affects the reaction rate.[106,107] As mentioned in **Figure 2.1B**, due to the discrepancy in the electronic properties of the electrode materials, the activity of different metals for the hydrogen formation reaction shows a volcano-type relationship with the binding energy or adsorption free energy.

Moreover, the design of alloys or multi-metal compounds is also a common strategy to reduce the reaction activation energy more effectively.[108] It has been shown that bi- and tri-metal

alloys can provide the intrinsic properties of individual metals and obtain synergies between different atoms. By carefully tailoring the composition and structure of the alloy, the physicochemical properties can be modulated to obtain the desired performance.[109] **Figure 2.2** shows maximal relative activities of Pt alloy catalysts for the oxygen reduction reaction (ORR) as a function of empirical radii of additive atoms.[110] Note that two clear maxima appear. This trend is closely related to lattice strain caused by the lattice parameter difference between the Pt shell and additive atoms. In the case of alloy catalysts, the electronic structure of the surface is significantly affected by the lattice strain.

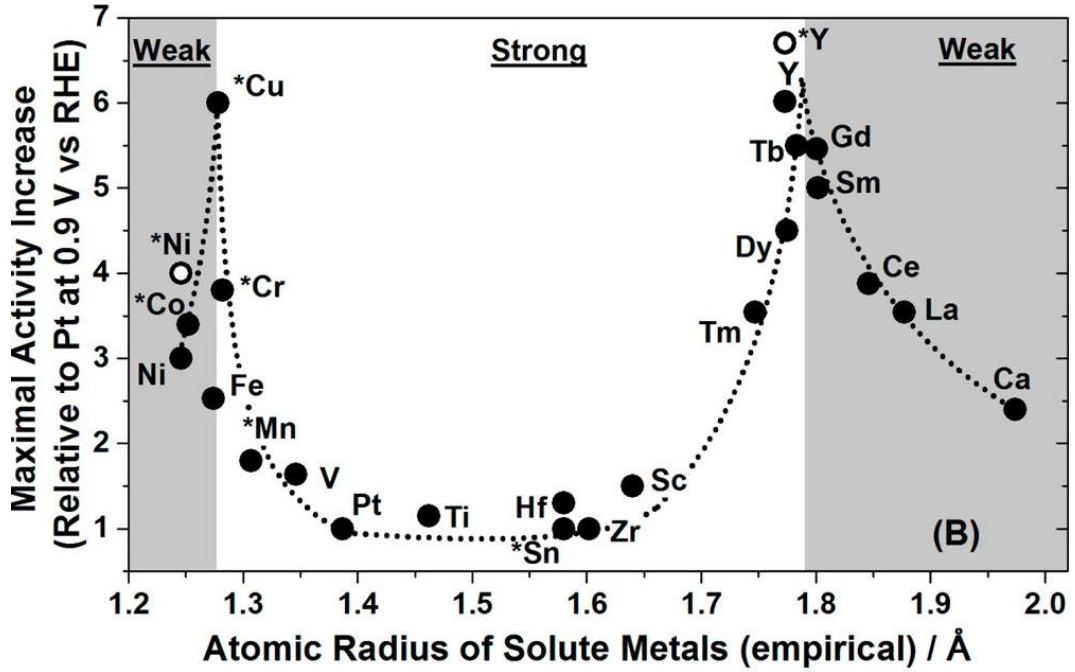

Figure 2.2. *Maximal activity toward the oxygen reduction reaction as a function of the empirical atomic radius of solute metals in Pt alloys. Reproduced with permission from ref. [110]. Copyright © 2016, American Chemical Society.*

As discussed earlier, another important reaction in electrocatalysis is the OER in alkaline solutions. Oxides and hydroxides of the transition metals (Mn, Fe, Co, Ni) exhibit relatively good properties toward the OER in alkaline and near-neutral electrolytes, so they are the subject of intensive research.[111] In particular, bi-metal-based NiFe (oxy)hydroxides have been considered as the most promising OER catalysts in alkaline conditions. Numerous studies have demonstrated trends in the OER activity as a function of Fe content and determined that a certain amount of Fe incorporation (*e.g.*, ~25%) maximizes activity.[112,113,114] Two options exist for the location of Fe^{3+} in NiFe (oxy)hydroxides: one is that the substituted Fe^{3+} sites become

more active in the lattice of γ-NiOOH due to changes in their electronic environment. The other is that the activity of the Ni^{3+} sites increases due to the change of their electronic properties after doping Fe^{3+} cations into the γ-NiOOH lattice. Bell and co-workers have demonstrated that all OER intermediates are too weakly adsorbed on pure γ-NiOOH, while pure γ-FeOOH exhibits too strong adsorption.[115] In the presence of doping (*cf.* **Figure 2.3**), a lower overpotential (0.43 V) can be achieved at the Fe sites surrounded by Ni next-nearest neighbors

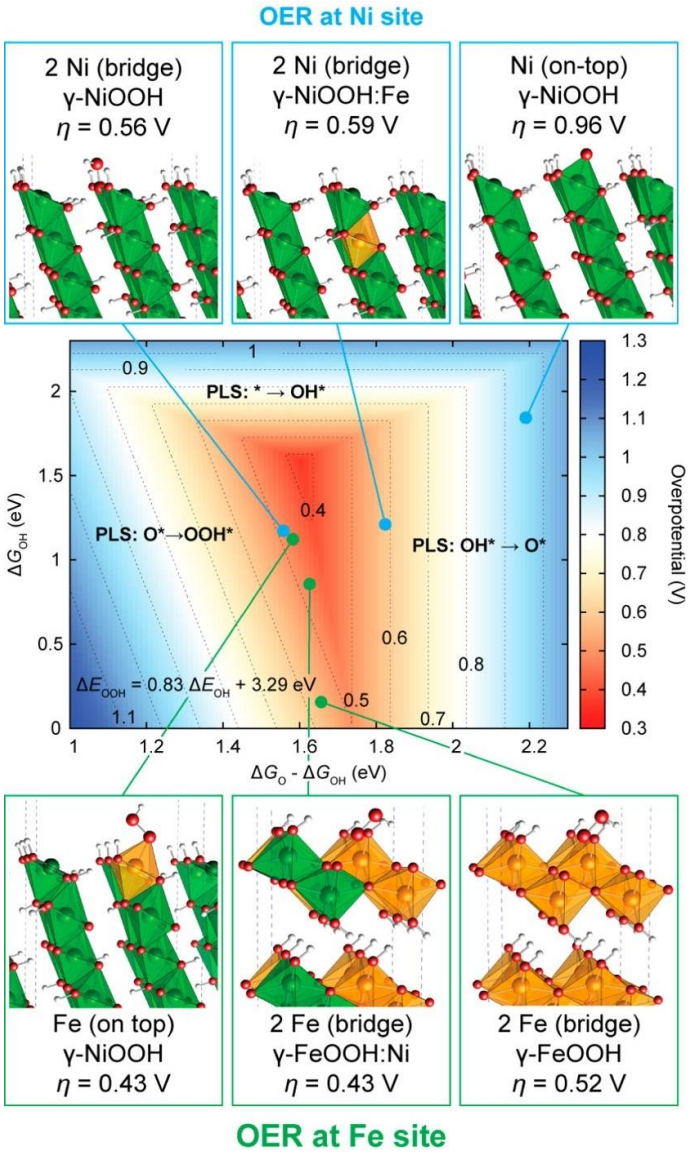

Figure 2.3. *Schematic representation of the OER activity "volcano" type plot for several proposed active sites on pure γ-NiOOH, pure γ-FeOOH, and mixed NiFe (oxy)hydroxides. Computed overpotentials are shown as a function of the Gibbs free energies of the OER reaction intermediates. The PLS is the potential limiting step of the intermediate formation during the OER process. Reproduced with permission from ref. [115]. Copyright © 2016, American Chemical Society.*

in γ-NiOOH or γ-FeOOH. Such Fe active sites exhibit near-optimal binding energy of the OER intermediate. Therefore, they speculated that Fe, but not Ni, represents the active site of the OER in the mixed NiFe (oxy)hydroxides.

Structural effects are of paramount importance for disclosing and understanding the contribution of different facets, such as steps, kinks, and surface atoms with higher/lower coordination numbers, to the electrocatalytic activity of the electrode.[98] The performance of an electrocatalyst significantly depends on the chemical structure (composition and valence state), geometric structure (morphology and size), and the atomic arrangement on the surface.[116,117] Moreover, several important electrocatalytic reactions, such as the HOR/HER, the ORR/OER, and the chlorine evolution reaction, are surface structure sensitive reactions in an acidic environment.[101] Therefore, the study of electrocatalytic surface structure effects can provide insight into the relationship between surface structure and the performance of electrocatalysts from a microscopic perspective. The structural effects of electrocatalysts have been intensively studied on model catalysts, *e.g.*, metal single crystals and well-defined shape-controlled nanoparticles. High-index facets with open surface structures and high surface energies usually exhibit higher catalytic activity for the HER than low-index facets where atoms are tightly packed.[118] In addition, to improve the catalyst utilization efficiency, nanosized electrocatalysts can yield larger specific surface areas. This can be crucial for high catalytic activity.[119] Further insight and knowledge into the study of the shape and size of nanostructured electrocatalysts will pave the way for a rational approach toward electrocatalyst design.

2.2 Electrode Kinetics

For an electrode process at a specific potential E, if the kinetics of the electron transfer is fast, it can be assumed that the concentrations of oxidized (C_O) and reduced (C_R) species on the electrode surface are in equilibrium with the electrode potential; namely, the forward and backward rates are equal:[120]

$$O + ne \underset{k_b}{\overset{k_f}{\rightleftharpoons}} R \tag{2.1}$$

where k_f and k_b represent the rate constants for the forward and backward reactions, respectively. In this case, the concentrations of oxidized and reduced species can be connected *via* the Nernst equation:

$$E = E^{0'} + \frac{RT}{nF} ln \frac{C_O}{C_R} \tag{2.2}$$

where $E^{0'}$ represents the formal potential of an overall reaction, R - the universal gas constant (~8.314 J K^{-1} mol^{-1}), T- the temperature, n - the electron transfer number, F - the Faraday constant (~96485 C mol^{-1}), C_O and C_R - the concentrations of oxidized and reduced species, respectively.

According to **Equation (2.1)**, the forward reaction rate (ν_f) is proportional to the concentration of oxidized species C_O at the vicinity of the electrode surface. Thus, the relationship between the ν_f and the forward current (cathodic current, i_c) can be expressed as:

$$\nu_f = k_f C_O = \frac{i_c}{\text{nFA}} \text{ or } i_c = nFAk_f C_O \tag{2.3}$$

Likewise, the backward current (anodic current, i_a) is a function of the rate ν_b:

$$\nu_b = k_b C_R = \frac{i_a}{\text{nFA}} \text{ or } i_a = nFAk_b C_R \tag{2.4}$$

Thus, the net reaction rate ν_{net} is

$$\nu_{net} = \nu_f - \nu_b = k_f C_O - k_b C_R = \frac{i}{nFA} \tag{2.5}$$

We can also obtain the net current i

$$i = i_c - i_a = nFA(k_f C_O - k_b C_R) \tag{2.6}$$

In the Arrhenius relationship, it is an experimental fact that the rate constants of most solution-phase reactions almost always vary with temperature, *i.e.*, $\ln k$ is linearly related to $1/\mathrm{T}$. Therefore, the above reaction rate constants can be written as:

$$k_f = k^0 e^{[-\alpha f(E-E^{0'})]} \tag{2.7}$$

and

$$k_b = k^0 e^{[(1-\alpha)f(E-E^{0'})]} \quad (2.8)$$

where k^0 is a standard rate constant, α is the transfer coefficient, and $f = F/RT$.

If the electrode/electrolyte interface is at equilibrium with a solution ($C_O^* = C_R^*$, in the bulk solution), the forward and backward reaction rates have the same value, *i.e.*, $E = E^{0'}$, and $k_f C_O^* = k_b C_R^*$, so that $k_f = k_b$.[120] Insertion of **Equations (2.7** and **2.8)** into **Equation 2.6** yields the complete current-potential characteristic:

$$i = nFA\left(k_f C_O^* - k_b C_R^*\right) = nFAk^0[C_O^* e^{-\alpha f(E-E^{0'})} - C_R^* e^{(1-\alpha)f(E-E^{0'})}] \quad (2.9)$$

This equilibrium also results in a zero net current, so that **Equation (2.9)** can be modified as

$$e^{f(E_{eq}-E^{0'})} = \frac{C_O^*}{C_R^*} \quad (2.10)$$

Note that this equation is an exponential form of the Nernst **equation (2.2)**, where E_{eq} is the equilibrium potential of an electrode.

However, there still exists a balanced faradaic activity, which can be expressed in the form of the exchange current i_0. The magnitude of i_0 is equal to either cathodic i_c) or anodic (i_a) currents.

$$i_0 = nFAk^0 C_O^* e^{-\alpha f(E_{eq}-E^{0'})} \quad (2.11)$$

If the exponential part of **Equation 2.11** is replaced by $\frac{C_O^*}{C_R^*}$ obtained from **Equation 2.10**, we can easily gain the simplified form:

$$i_0 = nFAk^0 {C_O^*}^{(1-\alpha)} {C_R^*}^{\alpha} \quad (2.12)$$

Therefore, the current i_0 is proportional to k^0 and can usually be substituted for k^0 in the kinetic equations. One advantage of using i_0 instead of k^0 is that the current can be described in terms of the deviation from the equilibrium potential, *i.e.*, the overpotential ($\eta = E - E_{eq}$). To obtain the current-overpotential relationship, **Equation (2.9)** is divided by **Equation (2.12)**.

$$\frac{i}{i_0} = \frac{nFA\left(k_f C_O - k_b C_R\right)}{nFAk^0 C_O^{*(1-\alpha)} C_R^{*\alpha}} = \frac{C_O e^{-\alpha f\left(E-E^{0\prime}\right)} - C_R e^{(1-\alpha)f\left(E-E^{0\prime}\right)}}{C_O^{*(1-\alpha)} C_R^{*\alpha}}$$

$$= \frac{C_O}{C_O^*} e^{-\alpha f(E-E^{0\prime})} \left(\frac{C_O^*}{C_R^*}\right)^{\alpha} - \frac{C_R}{C_R^*} e^{(1-\alpha)f(E-E^{0\prime})} \left(\frac{C_O^*}{C_R^*}\right)^{-(1-\alpha)} \quad (2.13)$$

Under conditions where the solution is well stirred or where the current is kept so low that there is no significant difference between the surface concentration and the bulk values (*i.e.*, $C_O = C_O^*$, $C_R = C_R^*$), **Equation (2.13)** can be rewritten by the substitution of $\frac{C_O^*}{C_R^*}$ with $e^{f(E_{eq}-E^{0\prime})}$,

$$i = i_0[e^{-\alpha f\eta} - e^{(1-\alpha)f\eta}] \quad (2.14)$$

This is the well-known Butler-Volmer equation for electrochemical kinetics.

2.3 Electrified Solid-Liquid Interfaces

2.3.1 The Electrical Double Layer

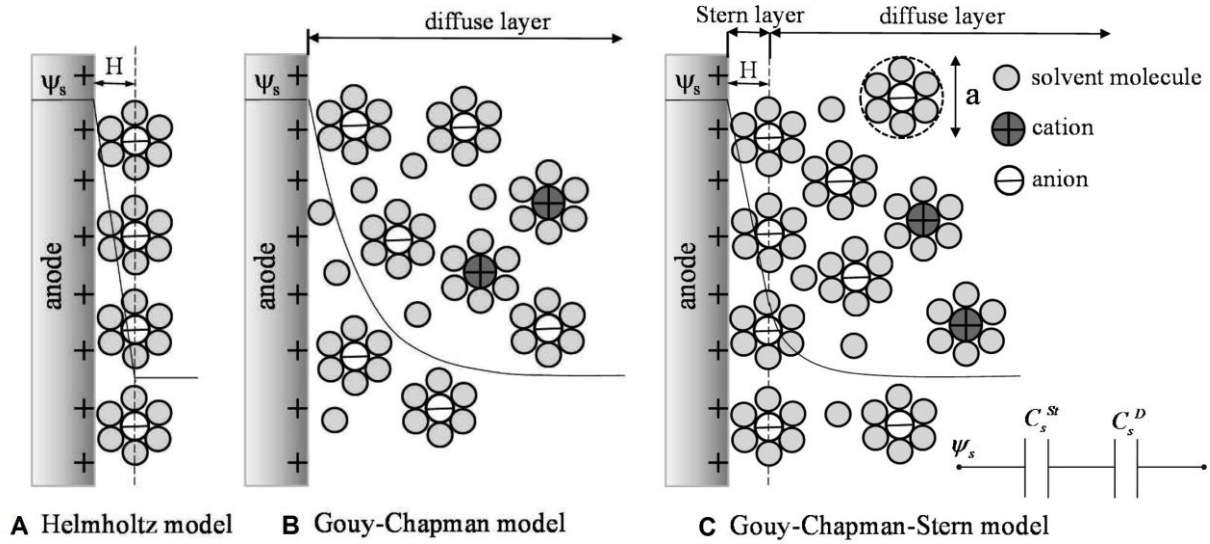

Figure 2.4. *Proposed models of the electrical double layer at a positively charged surface: (A) the Helmholtz model, (B) the Gouy-Chapman model, and (C) the Gouy-Chapman-Stern model. Reproduced with permission from ref. [121]. Copyright © 2011, American Chemical Society.*

When a metal electrode is in contact with an electrolyte, an interfacial region is formed at the electrified interface, which contains an excess of opposite-signed charge carriers. The region where free charges accumulate is called the electrical double layer (EDL).[121] As shown in

Figure 2.4A, a positively charged metal electrode surface exists with a layer of solvated anions in close contact. If the electrode side of the EDL is defined as the metal surface, the solution side is defined as the plane where the charge center of the excess ions (possibly solvated ions) is located. Accordingly, the distance (H) between the two charged layers is considered as the radius of the ion or the solvated ion. This simplest model is known as the compact double layer, namely, the well-known Helmholtz double layer model, first proposed by Helmholtz.[122] This structure is analogous to that of conventional dielectric capacitors. Undoubtedly the Helmholtz model is incomplete due to the lack of consideration of the fact that ions are mobile in the electrolyte solvent.[123] Gouy[124] and Chapman[125] developed an electrical double layer model and considered the ions' motions in the double layer. The key to the model they developed was the introduction of a new concept, the diffusion layer. As shown in **Figure 2.4B**, at the electrified electrode/electrolyte interface, the charge is strictly distributed on the electrode surface. However, it is different on the electrolyte side, where the interaction between different ions causes a lot of charges to diffuse into the bulk phase solution away from the interface. On the other hand, the presence of the inner Helmholtz layer is neglected in the Gouy-Chapman model. In 1924, Stern[126] proposed that the EDL should be a combination of the Helmholtz layer (also denoted as the Stern layer) and the diffuse layer. In addition, Stern added a new condition to the Gouy-Chapman model that the ions are of finite ionic size rather than point charge. In fact, there are still some shortcomings in the Gouy-Chapman-Stern model: (1) the anion or cation surfaces in the electrolyte are surrounded by solvent molecules, and in reality, the charge carriers are these "solvated ions"; (2) specific adsorption is capable of occurring at the electrified electrode/electrolyte interface, and if the adsorption force is greater than the electrostatic force, then even the charge with the same sign can be stabilized at the interface.

Subsequently, the Gouy-Chapman-Stern model was further modified by Grahame.[127] The Helmholtz layer (Stern layer) is divided into the inner Helmholtz plane (IHP) and the outer Helmholtz plane (OHP), as illustrated in **Figure 2.5**.[128] The layer closest to the electrode surface is formed by ions that exhibit strong chemical interactions with the electrode material. These polarizable anions tend to shed part of their solvent shell and specifically adsorb at the electrode surface. Thus, the IHP is introduced as the plane formed by the centers of the so-called specifically adsorbed ions. In addition, some ions are only electrostatically attracted close to the electrode surface and maintain their hydration shell. The OHP represents the locus of the

centers of the nearest solvated ions. The diffuse layer is adopted from the Gouy-Chapman model.

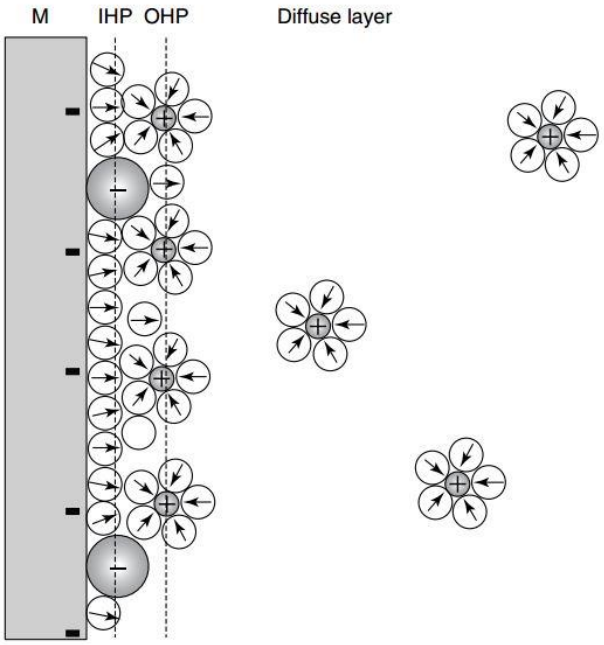

Figure 2.5. *Schematic representation of the electrical double layer model at a negatively charged metal-electrolyte solution interface. IHP is the inner Helmholtz plane and OHP is the outer Helmholtz plane. Reproduced with permission from ref. [128]. Copyright © 2008, Wiley-VCH Verlag GmbH & Co. KGaA.*

The electrical and chemical properties of the interface play a pivotal role in the rate of an electrochemical reaction. The development of EDL models helps to understand the relationship between the electrode surface and the electrolyte at the interface and elucidate the mechanisms of various electrochemical processes.

2.3.2 Influence of Electrolyte Composition

In most cases, heterogeneous catalysis involves five essential reaction steps: diffusion of reactant molecules to the catalyst surface, adsorption on the active surface, reaction on the surface, desorption of product molecules, and outward diffusion.[129,130] As a special branch of heterogeneous catalysis, electrocatalysis consists of multiple elementary reaction steps. The reaction process is determined by the adsorption and desorption equilibrium of intermediate species at the active sites in each elementary step.[131] One of the challenges of research in electrocatalysis is to understand how the physical or chemical state of the catalyst surface affects the adsorption and desorption equilibrium of intermediate species at each step and its

impact on the final catalytic performance. Numerous reports have considered the influence and modulation of the extrinsic physical properties or intrinsic electronic structure of catalysts on the kinetics of catalytic reactions. They mainly consist of the regulation of the crystal plane, defect engineering, strains, particle size, and surface modification.[98,101,119,132] An increasing amount of research also shows that understanding the influence of electrolyte composition is crucial for optimizing the performance of electrocatalytic systems. As shown in **Figure 2.6**, a catalytic system's activity is closely related to the composition of the electrolyte and the corresponding local disparate chemical environment.[133,134]

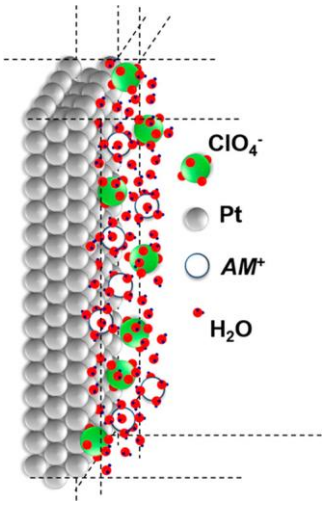

Figure 2.6. *Sketch of electrolyte ions on the surface of Pt electrode. AM^+: Li^+, Na^+, K^+, Rb^+, Cs^+. Reproduced with permission from ref. [133]. Copyright © 2018, American Chemical Society.*

Solvent Effect

As previously discussed in **section 2.3.1**, anions or cations in the electrolyte are surrounded by solvent molecules, and in reality, these "solvated ions" serve as the charge carriers. Therefore, the solvent type and property play an essential role in the catalytic reactions. In many electrocatalytic systems, aqueous solutions are used. Notably, for some reactions involving proton-coupled electron transfer or even using H_2O as a reactant, aqueous solutions are one of the most critical factors governing catalytic performance. Water exhibits many advantages that have led to its widespread use, such as low price, high sustainability, and availability.[134] Nonaqueous solvents are also frequently used in many catalytic systems. The absence of protons can inhibit some reactions that involve proton depletion, and aprotic solvents usually provide a higher potential window than water.[135,136]

Cation Effect

Cations present in the electrolyte, especially in neutral or alkaline solutions, can significantly impact the reaction rate.[137,138] The most prominent example of the cation effect is the influence of the alkali metal cations. For instance, Xue and co-workers found that for almost all investigated electrodes, such as Pt(111), Pt(221), and polycrystalline Pt (Pt(pc)), the electrochemical HER activity measured in alkaline electrolytes followed a strict trend Li^+ > Na^+ > K^+ > Rb^+ > Cs^+.[139] Note that regardless of the electrode surface structure, the HER current densities of all Pt electrodes in LiOH were about four times higher than those measured in CsOH solution, as shown in **Figure 2.7A**. This result indicates that the alkali metal cations strongly influence the HER activity of different Pt electrodes. In addition, Garlyyev and co-workers further explored the cation effects on the ORR activities of the Pt(221) and Pt(331) surfaces (*cf.* **Figure 2.7B**).[140] The ORR activity trend for both stepped single-crystal electrodes in 0.1 M alkaline electrolytes was as follows: $K^+ \gg Na^+ > Cs^+ > Rb^+ \approx Li^+$, which is different from the trend reported in the literature for Pt(111). The activity discrepancy between the Pt(221) and Pt(331) surfaces also demonstrated a strong dependence of alkali metal cation effects on the catalyst surface structure.

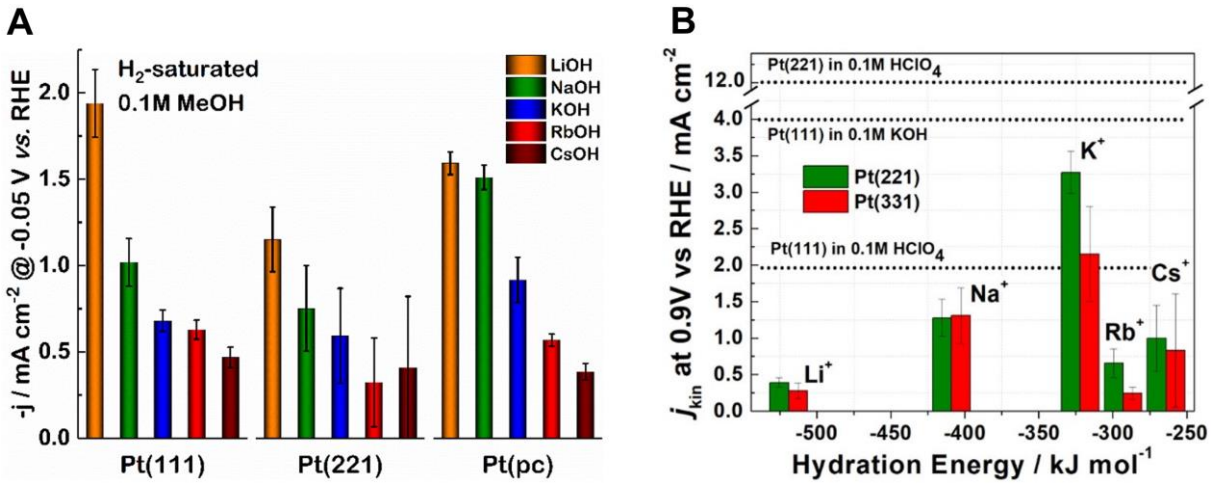

Figure 2.7. *(A) Bar chart showing the comparison of the HER activities on Pt(111), Pt(221) and Pt(pc) surfaces in H_2-saturated 0.1 M MeOH electrolytes (Me^+ = Li^+, Na^+, K^+, Rb^+, Cs^+). Reproduced with permission from ref. [139]. Copyright © 2018 Wiley-VCH Verlag GmbH & Co. KGaA, Weinheim. (B) Influence of the alkali metal cations on the ORR activities for both stepped single-crystal Pt(221) and Pt(331) electrodes. Reproduced with permission from ref. [140]. Copyright © 2018, American Chemical Society.*

Anion Effect

Anions are also important components of electrolytes. They can be specifically adsorbed onto the electrode surface or influence the local catalytic environment at the electrified electrode/electrolyte interface through chemical interactions with other electrolyte species.[128] For instance, layered double hydroxides (LDH) as promising OER catalysts contain nanosheets constructed with edge-sharing nickel oxide octahedra with varying amounts of ferric iron substituting at nickel sites, as presented in **Figure 2.8A**. Anions are incorporated into the interlayers for the charge balance. Zhou and co-workers demonstrated that intercalated anions in LDH alter the electronic structure of metal atoms exposed to the surface and significantly affect the OER activity.[141] **Figure 2.8B** shows a linear relationship between the OER onset potential of the NiFe-LDHs and the standard redox potentials of the intercalated anion, where NiFe-(H_2PO^{2-})-LDHs and NiFe-(F^-)-LDHs exhibit the best and the worst OER catalytic performance, respectively. In addition, Hunter and co-workers found that electrocatalytic water oxidation activity is a function of anion basicity. In other words, the Brewster or Lewis basicity of the anion plays a role in the mechanism of water oxidation.[142]

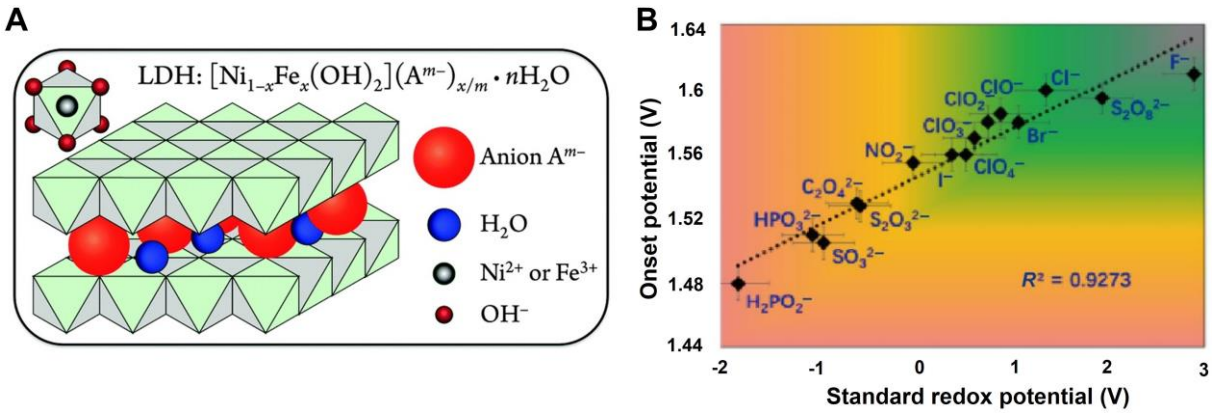

Figure 2.8. *(A) Illustration of a typical NiFe-LDH structure. Adapted with permission from ref. [142]. Copyright © 2016, The Royal Society of Chemistry. (B) Onset potential of the OER as a function of the standard redox potential of the intercalated anions in LDH. The onset potentials were extracted from the current density of 1 mA cm^{-2}. Adapted with permission from ref. [141]. Copyright © 2018, Tsinghua University Press and Springer-Verlag GmbH Germany.*

2.4 Electrochemical Water Splitting

From a technical point of view, water splitting is considered one of the most promising methods of hydrogen production owing to the multiple advantages of abundant resources, no greenhouse gas emissions, and good efficiency.[20,22,115] The IEA predicts that the market share of hydrogen production by electrocatalytic water splitting will reach ~22% in 2050.[143] In the past decades, the demand for hydrogen could be met by steam methane reforming and water-gas shift reaction. In contrast, the water electrolysis method becomes competitive only when electricity prices are low.[20, 144] Electrocatalytic water splitting has attracted strong interest in recent years by introducing the concept of the so-called "hydrogen economy". According to the operating temperatures and electrolytes, water electrolysis can be divided into alkaline, acidic polymer electrolyte membrane, and solid oxide electrolysis.[145] Typical electrocatalytic water splitting consists of two half-reactions: one is the hydrogen evolution reaction, and the other is the oxygen evolution reaction. Thermodynamic equilibrium voltage demonstrates that at standard conditions (1 bar and 25 ℃), a voltage of 1.23 V is required to electrolyze water into hydrogen and oxygen. Still, in reality, even with an excellent catalyst, a substantially larger overpotential is needed.[146] Therefore, developing efficient, stable, and affordable electrocatalysts is the key to achieving a large-scale industrial realization of this technology.

2.4.1 Hydrogen Evolution Reaction

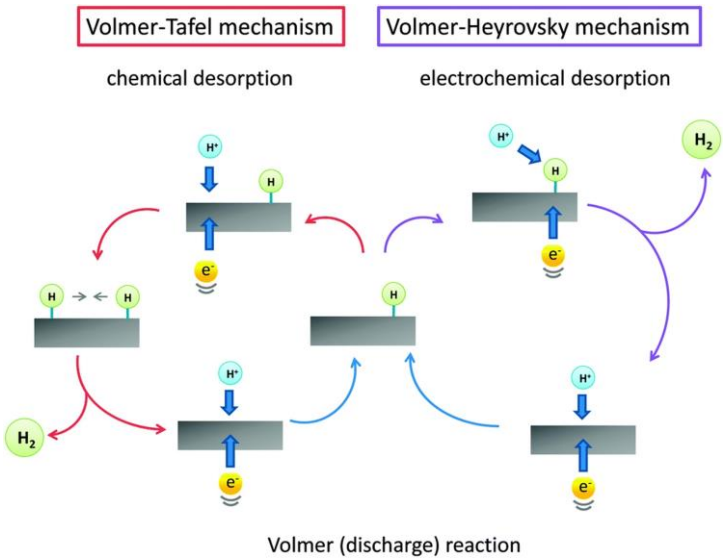

Figure 2.9. *Schematic illustration of the HER mechanism in acidic conditions. Reproduced with permission from ref. [147]. Copyright © 2014, The Royal Society of Chemistry.*

The HER is a hydrogen production process that occurs at the cathode of the electrolyzer and involves two-electron transfers.[147] The reaction mechanism of the HER strongly depends on the electrolyte pH. In an acidic solution, the generally accepted pathways for the HER are proceeded by either the Volmer-Tafel (chemical desorption) or the Volmer-Heyrovsky (electrochemical desorption) mechanism, as shown in **Figure 2.9**.[148]

The first step of the HER is known as the Volmer step: an electron is transferred through the electrode interface, and a proton gets reduced on the catalyst surface (M), forming an adsorbed hydrogen atom (H_{ads}). Subsequently, molecular H_2 is generated through two pathways, including a second proton/electron transfer step (Heyrovsky) or a chemical desorption step (Tafel).

$$\text{(Volmer) } H^+ + M + e^- \rightarrow M\text{-}H_{ads} \quad \text{.....(2.15)}$$

$$\text{(Heyrovsky) } M\text{-}H_{ads} + H^+ + e^- \rightarrow M + H_2 \quad \text{.....(2.16)}$$

$$\text{(Tafel) } 2M\text{-}H_{ads} \rightarrow H_2 + 2M \quad \text{.....(2.17)}$$

In alkaline solutions, due to the scarcity of protons, the reaction pathways for the HER can be represented as:

$$\text{(Volmer) } H_2O + M + e^- \rightarrow M\text{-}H_{ads} + OH^- \quad \text{.....(2.18)}$$

$$\text{(Heyrovsky) } M\text{-}H_{ads} + H_2O + e^- \rightarrow M + H_2 + OH^- \quad \text{.....(2.19)}$$

$$\text{(Tafel) } 2M\text{-}H_{ads} \rightarrow H_2 + 2M \quad \text{.....(2.20)}$$

At present, Pt and Pt group metal catalysts exhibit the best HER performance in most cases.[149] However, their high cost and limited availability question their large-scale application. It is therefore important to develop earth-abundant, non-noble metal-based catalysts. Many strategies and compounds have been explored in the past decade to develop efficient and affordable HER electrocatalysts, such as transition metal compounds, carbon-based or heteroatom-doped carbon materials, and conducting polymers.[20,147,148]

2.4.2 Oxygen Evolution Reaction

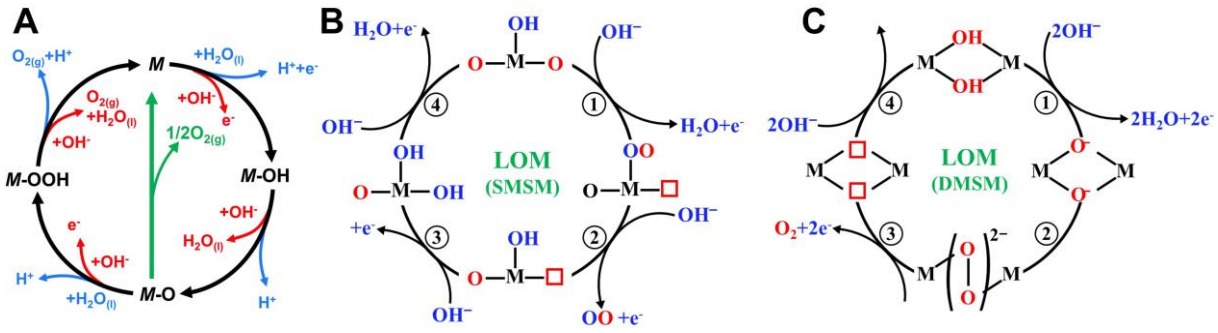

Figure 2.10. *Illustration of the OER mechanisms. (A) Adsorbate evolution mechanism (AEM) of OER on a single active site for acidic (blue route) and alkaline (red route) conditions. (B and C) Lattice-oxygen-participating mechanism (LOM) of OER in alkaline conditions, involving single-metal-site (SMSM) and dual-metal-site (DMSM). M represents the active site, and red squares are the oxygen vacancies. Reproduced with permission from ref. [53]. Copyright © 2021, John Wiley and Sons.*

Main losses in electrocatalytic water splitting occur at anodic half-reaction, namely the OER. The OER requires a high overpotential to complete the four electron-proton coupling reactions, which results in intractably sluggish kinetics.[148] OER electrocatalyst design plays a crucial role in efficient water splitting. Similar to HER, OER can be carried out in acidic and basic media, and the proposed adsorbate evolution mechanism (AEM) can be written as follows[148,150]:

In acidic solution:

$$M + H_2O \rightarrow M\text{-}OH + H^+ + e^- \quad (2.1)$$

$$M\text{-}OH \rightarrow M\text{-}O + H^+ + e^- \quad (2.2)$$

$$2M\text{-}O \rightarrow O_2 + 2M^+ + 2e^- \text{ or } M\text{-}O + H_2O \rightarrow M\text{-}OOH + H^+ + e^- \quad (2.3)$$

$$M\text{-}OOH \rightarrow M + O_2 + H^+ + e^- \quad (2.4)$$

In alkaline solution:

$$M + OH^- \rightarrow M\text{-}OH + e^- \quad (2.5)$$

$$M\text{-}OH + OH^- \rightarrow M\text{-}O + H_2O + e^- \quad (2.6)$$

$$2M\text{-}O \rightarrow O_2 + 2M^+ + 2e^- \text{ or } M\text{-}O + OH^- \rightarrow M\text{-}OOH + e^- \quad (2.7)$$

$$M\text{-}OOH + OH^- \rightarrow M + O_2 + H_2O + e^- \quad (2.8)$$

Since the OER process involves multiple electron transfers and several reaction intermediates (*e.g.*, M-OH, M-O, and M-OOH), the reaction mechanism of OER is also much more complex than that of HER.[151] It is widely accepted that OER can be performed through two different mechanisms: AEM and LOM (lattice oxygen oxidation mechanism or lattice oxygen-mediated mechanism).[152] Generally, AEM is assumed to undergo four consecutive concerted proton-electron transfer (CPET) reactions at the catalytically active metal sites.[153] For instance, in alkaline solutions, OH^- first adsorbs on the coordinatively unsaturated metal sites, followed by a deprotonation step to form M-O. Another OH^- will be adsorbed on the M-O site to generate the key intermediate of M-OOH. The final step involves the second deprotonation and the evolution of the O_2 molecule. Active metal sites are released and continue the reaction loop. As reported in the literature, the formation or decomposition of the M-OOH intermediate in OER is usually considered the rate-determining step (RDS), representing the transition state with the highest free energy for the whole reaction.[151] There are still some shortcomings of the AEM mechanism in practical OER studies. First, a theoretically considerable overpotential of 370 mV is observed in AEM. However, many reported onset overpotentials of OER on advanced electrocatalysts are much lower than the minimum value proposed by AEM.[152,154] In addition, numerous experimental studies have shown that the catalyst surface undergoes dynamic structural evolution during the reaction rather than retaining the structure. Accordingly, the AEM is not the only proposed mechanism for OER.[155,156,157]

Given the dynamic structural changes observed on the surface of OER catalysts, a lattice oxygen oxidation mechanism or lattice oxygen-mediated mechanism has been proposed for OER.[152,154] Arguably, this is directly related to the growing attempts to develop perovskite-based electrocatalysts. In the LOM pathway, the catalytic surface is no longer a stable platform but changes dynamically with the oxygen evolution process. The oxidation, exchange, and release of lattice oxygen ligands on the catalyst surface in the OER cycle are the basis for the LOM. As shown in **Figure 2.10B**, it is assumed that activated lattice oxygen around the active metal site can be directly coupled to deprotonated M-O intermediates to form M-OO species. The M-OO species can be further converted to O_2 molecules in a subsequent step. Note that the oxygen vacancies arising from the consumed lattice oxygen can be finally refilled by OH^-. This pathway is the so-called single-metal-site mechanism (SMSM).[158,159] Additionally, a dual-

metal-site mechanism (DMSM) has also been developed depending on the number of participated lattice oxygen around the active metal site.[152,160] In this mechanism, adjacent activated lattice oxygen atoms are capable of coupling to form the M-OO-M motif. Subsequently, the O_2 molecule is directly evolved, and OH^- refills the generated two oxygen vacancies. In the past decades, with the development of advanced techniques, such as ^{18}O isotope labeling and O-based X-ray spectroscopy, a large amount of work has been devoted to the study of the LOM for state-of-the-art OER electrocatalysts, including perovskite oxides, RuO_2, IrO_2, Zn-substituted CoO_2 plates, and $NiCo_2O_4$.[53,161,162]

Although the development of theoretical and experimental techniques has deepened our understanding of the OER catalytic mechanism, the design of efficient, robust electrocatalysts and the elucidation of the fundamental relationship between their catalytic activity and structure remain the focus of future research.

3 Experimental Part

This chapter provides an overview of the experimental techniques and instrumentation used for the synthesis and characterization of SURMOFs as well as for the investigation of the conversion mechanism and the electrochemical properties of the derivatives. For a more precise assessment of the catalytic activity, the mass loading of catalysts on the electrode was monitored by a gold quartz crystal microbalance.

3.1 Experimental Setups

3.1.1 Pump System for SURMOF Synthesis

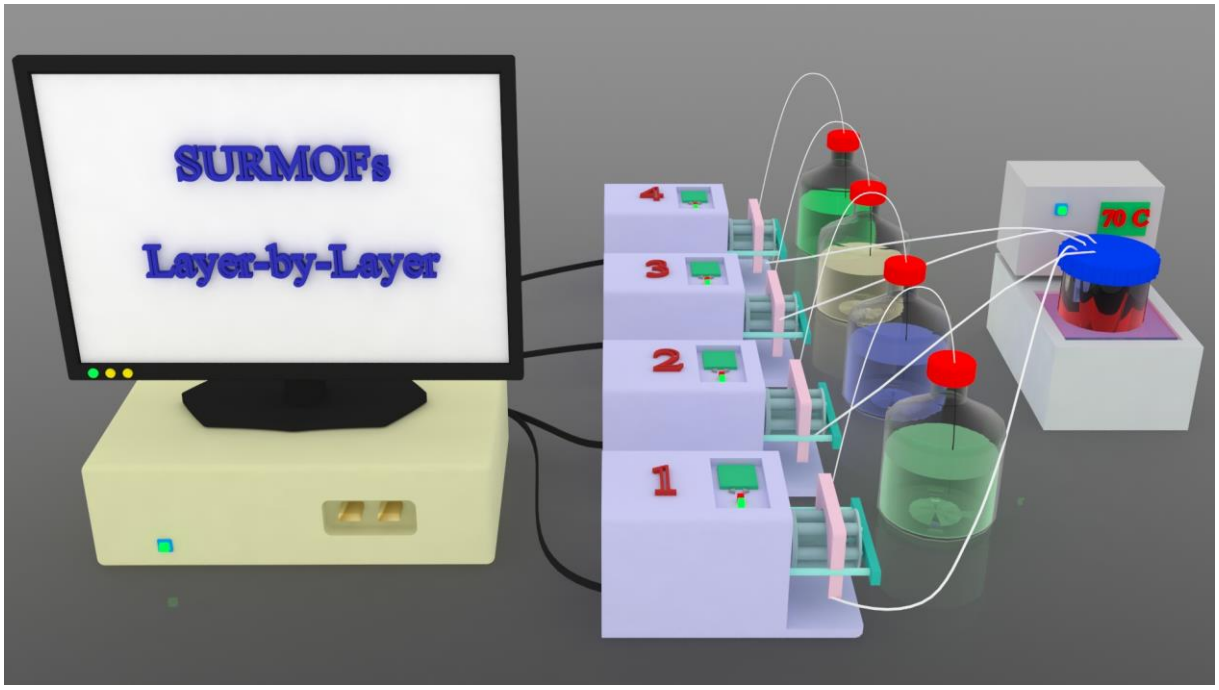

Figure 3.1. *Schematic diagram of the pump system for automatic layer-by-layer deposition of SURMOFs.*

As shown in **Figure 3.1**, a homemade pump system was used to grow MOF thin films (SURMOFs) on the functionalized gold substrates through a layer-by-layer deposition method. Initially, the gold substrates were modified by immersing them either in L-cysteine (1 mM) or 16-mercaptohexadecanoic acid (20 μM) and acetic acid (5 vol.%) mixed aqueous solution for 12 hours. After the functionalization process, the gold substrate was carefully rinsed three times with absolute ethanol to remove any soluble organic molecules before the next step. The

deposition of SURMOFs involved four immersions of the functionalized gold surface in each of the following solutions: metal ion source solution, ethanol, organic ligands, and again ethanol. The deposition process was controlled by a LabView program and the pump system. Referring back to **Figure 3.1**, it can be seen that pumps 1, 2, and 3 are responsible for the alternate injection of the metal ions, organic ligands, and ethanol solution into the reaction cell, respectively. In contrast, pump 4 takes the solution from the cell into the waste container. Finally, the obtained SURMOF thin film was washed with absolute ethanol three times and dried at room temperature.

3.1.2 Electrochemical Cell

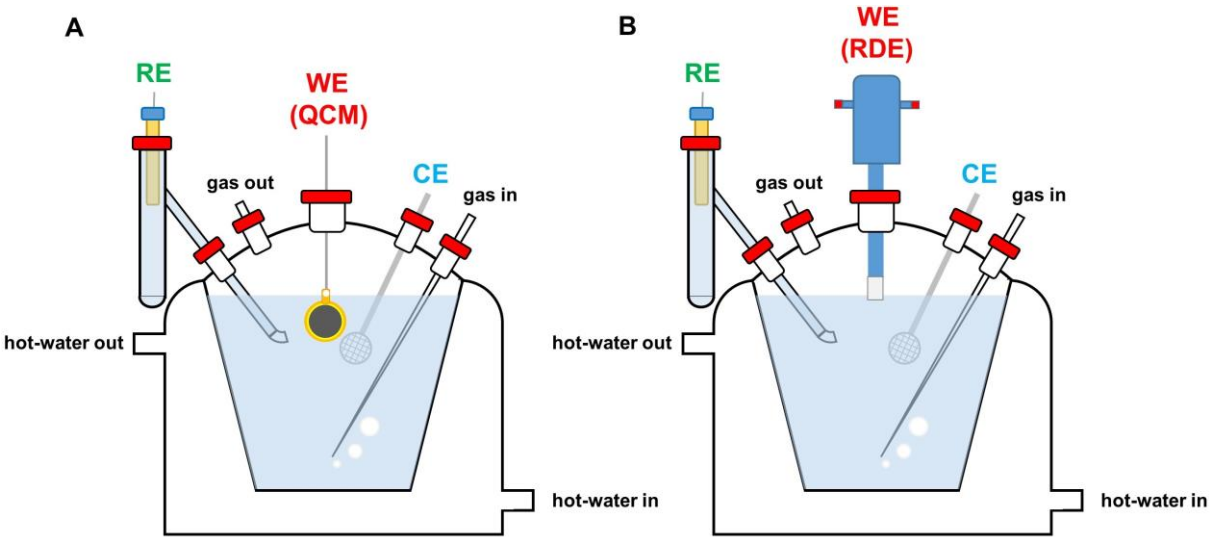

Figure 3.2. *Schematics of the electrochemical cells used for the quartz crystal microbalance (QCM) electrode (A) and the rotating disk (B) electrode. All electrochemical experiments were carried out in a three-electrode electrochemical cell (250 mL capacity) with a water jacket at room temperature or a set temperature.*

Electrochemical activation and activity testing experiments were performed using a three-electrode setup (*cf.* **Figure 3.2**) and a VSP-300 potentiostat (Bio-Logic, France). A SURMOF-deposited quartz crystal microbalance (QCM) gold substrate (10 mm diameter) or gold disk electrode (5 mm diameter) was used as the working electrode. A platinum mesh and a Hg/HgO (1 M NaOH, Bio-Logic, France) electrode served as the counter and reference electrodes, respectively. Prior to performing the electrochemical experiments, the glass cells were cleaned with piranha solution (peroxymonosulfuric acid) to remove trace amounts of organic residues. Specifically, the piranha solutions were freshly prepared by mixing concentrated sulfuric acid

(96% Suprapur™, Merck, Germany) with hydrogen peroxide (30% Suprapur™, Merck, Germany) in a ratio of 3:1. After the cleaning, the glass cells were rinsed several times using cold ultrapure water and near-boiling ultrapure water, respectively.

3.1.3 Setup for the LICT Measurement

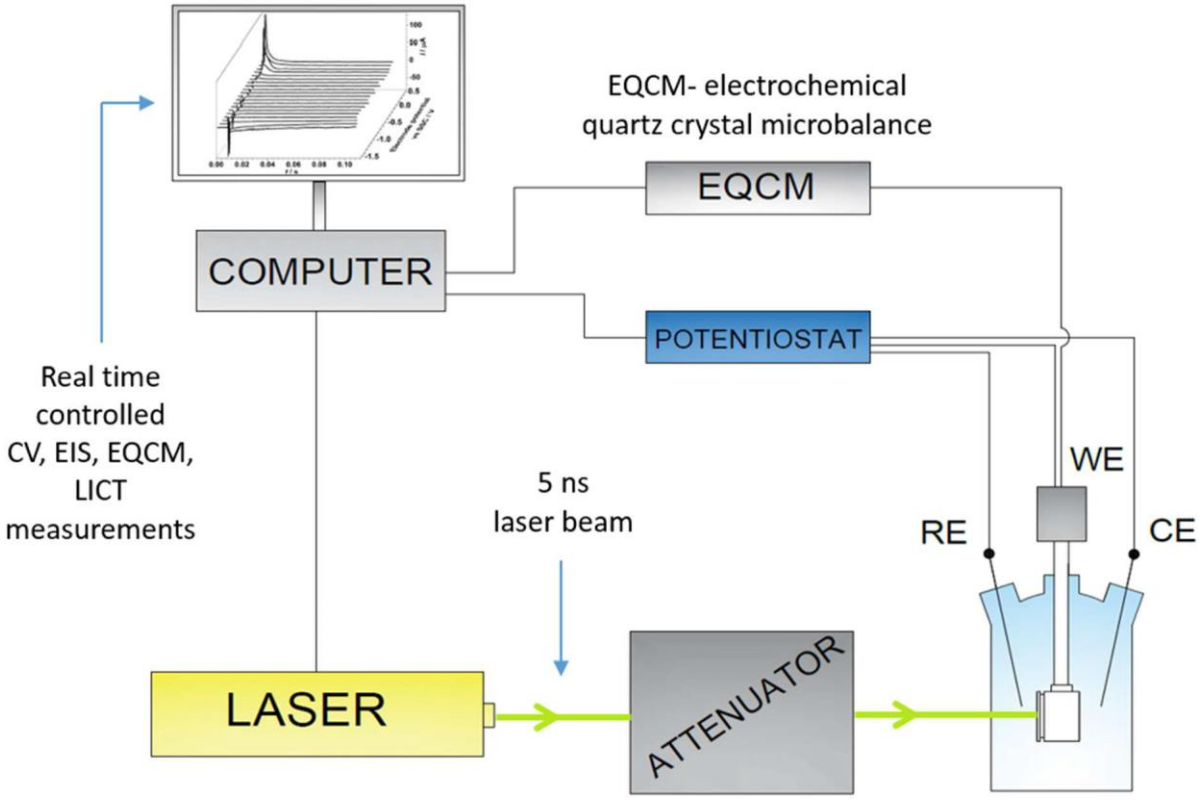

Figure 3.3. *Schematic illustration of the experimental setup for the real-time controlled electrochemical measurements. Reproduced with permission from ref. [163]. Copyright © 2017, American Chemical Society.*

As depicted in **Figure 3.3**, a Quanta-Ray INDI pulsed Nd:YAG laser with a 5-8 ns laser pulse and a wavelength of 532 nm was used in the laser test system. To avoid damaging the electrodes due to the high laser energy, an attenuator (Newport Corp.) was placed between the laser and the electrochemical cell, achieving a low energy density of *ca.* 12.5 mJ cm^{-2}. A SURMOF-coated AT-cut Au quartz crystal chip (Stanford Research Systems) was installed in a PTFE holder and served as the working electrode in the above presented three-electrode configuration (*cf.* **Figure 3.3**). The current transients were obtained by recording the current variation with time on a potentiostat (Bio-Logic, France) during the laser illumination. An "auto" setting of the current range and a recording period 0.4 ms was used. Prior to the LICT measurement,

SURMOF electrodes were derived and activated in another homemade cell through the alkaline immersion and the electrochemical cycling. This transformation process promotes the dissociation of the ligand molecules, thus avoiding interference of ligands with the EDL structure in subsequent laser tests. For LICT measurements, a fresh electrolyte was used, and the working electrode was oriented towards the quartz window of the cell (ø = 30 mm) to facilitate vertical laser irradiation. The experimental electrode potential range was set between 0.81 and 1.21 V *vs* RHE with an increasing step of 20 mV.

3.1.4 *In-situ* Raman Cell

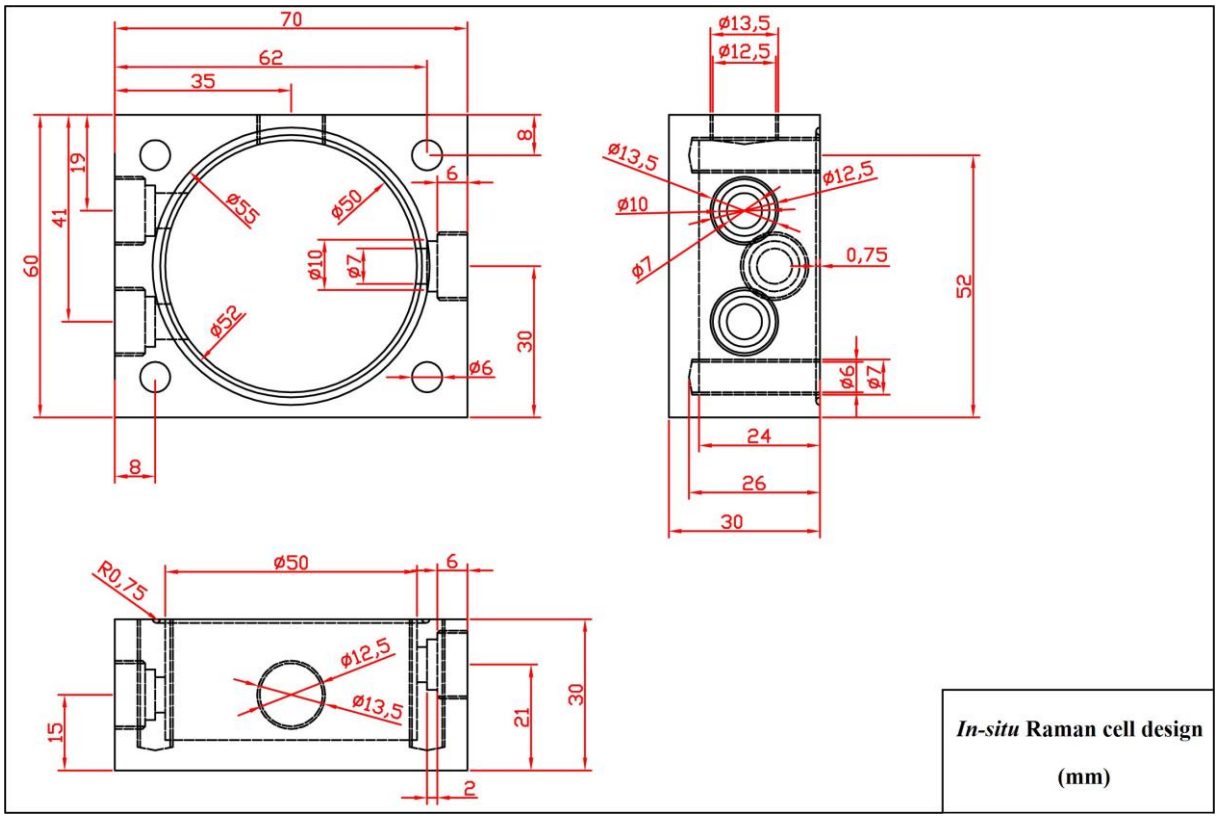

Figure 3.4. *Schematics of in-situ Raman cell design. The drawing of the design shows three regular views: top (the left), front (the bottom), and side (the right).*

The *in-situ* Raman measurement was performed in a homemade polytetrafluoroethylene (PTFE) cell with a quartz window (50 mm diameter). To attain high efficiency in collecting Raman scattered radiation, a SURMOF-deposited gold QCM chip was placed close to the quartz window while ensuring that it was immersed in the electrolyte. The QCM chip used as the working electrode was connected to the potentiostat (Autolab 302N) by a gold wire. A platinum

mesh and a Hg/HgO (1 M NaOH) were used as the counter and reference electrodes, respectively.

3.1.5 Rotating Disk Electrode

A gold rotating disk electrode (RDE) was used to evaluate the electrochemical surface area by impedance measurements. Prior to the SURMOF synthesis, a gold RDE was polished using the alumina slurry on a microcloth and subsequently rinsed with distilled water to clean off the alumina particles. The SURMOF-coated RDE was mounted to the Pine research MSR rotator with a constant rotation speed during electrochemical measurements, which creates a forced convection electrolyte flow. When an RDE is held at a reaction potential, the reactants are consumed rapidly at the electrode surface, which leads to a quick decrease in the concentration of reactants near the electrode. Thus, the reaction rate is governed by the diffusion rate of reactants. The rotation speed of the RDE determines the thickness of the "dynamically stable" layer (diffusion layer), where the concentration of reactants is maintained.[164] The smaller the diffusion layer, the faster reactants in the bulk solution can diffuse to the electrode surface. This means that more abundant reactants are available, and a higher reaction current can be obtained.[165] The thickness of the diffusion layer (δ) can be calculated as follows [166]:

$$\delta = 1.61 D^{1/3} \omega^{-1/2} \upsilon^{1/6} \tag{3.1}$$

Here, D is the diffusion coefficient ($cm^2\ s^{-1}$), ω – rotation rate (rpm), and υ – the kinematic viscosity of the liquid ($cm^2\ s^{-1}$). Mass transport limited current density (J_{lim}) can be calculated according to the Levich-equation[167,168]:

$$J_{lim} = 0.620 n F A D^{2/3} \upsilon^{-1/6} \omega^{1/2} C_0 \tag{3.2}$$

where n represents the number of electrons transferred in a half-reaction, F – the Faraday constant ($C\ mol^{-1}$), A – the electrode area (cm^2), and C_0 – the concentration of the electroactive species ($mol\ cm^{-3}$).

Figure 3.5. *Photograph of a gold rotating disk electrode (5 mm diameter). Adapted with permission from ref. [169].*

3.1.6 Quartz Crystal Microbalance Electrode

The activity per unit mass is a relevant parameter for evaluating and comparing catalytic activity at a specific overpotential.[170] Hence, for comparison, the activity per mass is adopted in this thesis. It can assess the mass loading on the electrodes using a QCM electrode, which is widely considered as a sensitive and precise technique to monitor small mass variations by measuring the frequency change of a quartz crystal resonator (*e.g.*, a 5 MHz crystal has a mass sensitivity of 17.7 ng $(cm^2 \cdot Hz)^{-1}$, and a 10 MHz crystal has a theoretical mass sensitivity of 4.4 ng $(cm^2 \cdot Hz)^{-1}$).[171] According to Sauerbrey's equation, the change of the quartz resonance frequency (Δf) is a function of mass change (Δm) on the quartz crystal.[172]

$$\Delta f = -\left(\frac{2f_0^2}{A\sqrt{\mu\rho}}\right)\Delta m = -C_f \Delta m \tag{3.3}$$

where f_0 is the fundamental frequency of quartz crystal (Hz), A – the piezoelectrically active crystal area (cm^2), μ – the shear modulus of quartz for AT-cut crystal (2.947×1011 g cm^{-1} s^{-2}), ρ – the density of quartz (2.648 g cm^{-3}), and C_f – the calibration constant.

Therefore, QCM is an important tool in electrochemical research for measuring the changes in mass loading on the electrode during the electrochemical test.

3.2 Synthesis of SURMOFs

For the SURMOF synthesis, the metal ion sources and a deprotonated organic ligand solution were firstly prepared. In the case of the heterostructured SURMOFs, 0.25 mmol $NiCl_2 \cdot 6H_2O$ (99.3%, Alfa Aesar) and 0.25 mmol $FeCl_3$ (98%, abcr GmbH & Co. KG, Germany) were

dissolved in 1.0 L absolute ethanol under stirring, respectively. Compared to the heterostructured SURMOFs, a small difference in concentration of the metal ion sources should be noted in the preparation of NiFe mixed SURMOFs, where 0.125 mmol $NiCl_2 \cdot 6H_2O$ and 0.125 mmol $FeCl_3$ were dissolved together in 1.0 L absolute ethanol as a mixed metal ions source. Since the ligand molecules are poorly soluble in ethanol, 0.185 mmol of Terephthalic acid (TA, 98%, Sigma-Aldrich) was dissolved in a mixed solution containing ethanol (1.02 L), distilled water (60 mL), and Et_3N (Triethylamine, 0.8 mL), followed by continuous stirring for 24 hours. The addition of Et_3N and prolonged stirring can promote the deprotonation of ligands.

SURMOFs were synthesized in a homemade pump system, which was kept at a temperature of 70 ℃. The functionalized gold electrode was placed at the bottom of the glass cell to ensure that it was well submerged in the injected reaction solutions. For more details on the operating mode of the pump system, please refer to **section 3.1.1**. In heterostructured SURMOFs, Ni-[TA] SURMOFs were obtained by repeating the deposition process after 15 or 30 cycles. Then Ni ion sources were replaced by Fe ion sources in the subsequent 15 or 30 cycles.

3.3 Electrochemical Measurements

All electrochemical experiments, such as cyclic voltammetry (CV) activation, OER testing, electrochemical impedance spectroscopy (EIS), performance measurements for stability assessment and estimation of apparent activation energy, were performed using a three-electrode setup and a VSP-300 potentiostat (Bio-Logic, France). All the potentials in this thesis were converted to a reversible hydrogen electrode (RHE) scale. In addition, before electrochemical experiments, SURMOF films were first derived by immersing them in an alkaline solution for 3 minutes. This enabled partial leaching of the ligands and access to the initially reconstructed derivatives.

OER tests were conducted in O_2-saturated 0.1 M alkali metal hydroxide solutions. Initially, the CV scans were performed within a potential range of 1.14 and 1.54 V *vs* RHE at a scan rate of 20 mV s^{-1} for 40 cycles to ensure complete conversion of SURMOFs in alkaline electrolytes. Afterward, the OER polarization curves were recorded by CV over a potential range of 1.10 to 1.75 V *vs* RHE, with a scan rate of 5 mV s^{-1} for five cycles. The mass loading of the pristine SURMOFs and the catalysts derived after the OER were detected by a BEL-QCM & BEL-Flow device. Thus, all catalytic activities were normalized according to the catalysts' mass loading

on the gold QCM electrodes. All OER polarization curves were obtained with an automatically corrected 85% iR-compensation unless otherwise stated.

The electrochemical active surface area (ECSA) is a critical parameter to gauge the performance of the catalyst.[173] Quick and accurate assessment of the ECSA of electrocatalysts remains a challenging task because of the complexity of the research object and the limitations of the assessment methods. In this thesis, adsorption capacitance obtained from the impedance measurements was used to determine the ECSA accurately. The EIS was collected on a SURMOF-coated gold RDE and a rotator (Pine Research Instrumentation) in argon-saturated 0.1 M KOH solution. Firstly, SURMOFs were transformed into highly-active catalysts after the alkaline immersion and electrochemical activation. To reduce the 'sample history' effects, linear sweep voltammetry was performed at a slow scan rate of 0.5 mV s^{-1} until the potential rose to the starting potential of the EIS measurement. Then, the EIS was measured between 1.50 and 1.65 V *vs* RHE in 10 mV steps with a frequency range of 30 kHz to 10 Hz and a detection amplitude of 10 mV. All impedance data were analyzed by using the EIS Data Analysis 1.3 software.

The apparent activation energy (E_a) is a crucial parameter used to evaluate catalyst activity. A temperature-dependent catalytic activity was measured by CV under four different temperatures (303.65, 313.15, 323.15, and 333.15 K), which could be achieved by a circulating thermostatic water bath. Note that water at the set temperature flowed through the jacket of the electrochemical cell for 30 minutes before starting the polarization curve acquisition. The E_a can be obtained according to the Arrhenius equation:[174]

$$\frac{\partial \log i}{\partial \frac{1}{T}} = -\frac{E_a}{2.3R} \tag{3.4}$$

where i is the reference point current (mA), T – the temperature (K), and R – the universal gas constant (~8.314 J K^{-1} mol^{-1}). The current reference points were extracted from an overpotential range of 250 to 300 mV in the OER polarization curves.

3.4 Characterization Techniques

3.4.1 X-ray Photoelectron Spectroscopy

X-ray Photoelectron Spectroscopy (XPS), also known as Electron Spectroscopy for Chemical Analysis (ESCA), is a conventional surface characterization tool. In principle, it can characterize the composition of materials and the chemical state in which each component is located. XPS also allows quantitative acquisition of the relative content of each chemical state. This enables XPS to be widely used in various fields of materials research.[175] XPS spectra are obtained by irradiating a solid surface with an X-ray beam and measuring the kinetic energy of the electrons emitted from the top 1-10 nm of the material. The commonly used X-ray source is the Al-Kα-ray monochromatic source with an energy of 1486.6 eV, which excites the electron leap in the inner energy level of an atom and makes it escape from the sample surface. The main principle of XPS is the photoelectric effect. Albert Einstein was awarded the Nobel Prize in 1923 for his discovery of the principle of the photoelectric effect. Its fundamental equation is:

$$E_{binding} = E_{photon} - (E_{kinetic} + \phi) \tag{3.5}$$

where $E_{binding}$ is the electron binding energy, E_{photon} is the photon (X-ray) energy, $E_{kinetic}$ is the measured kinetic energy of the photoelectron, and ϕ is the work function of the solid surface.

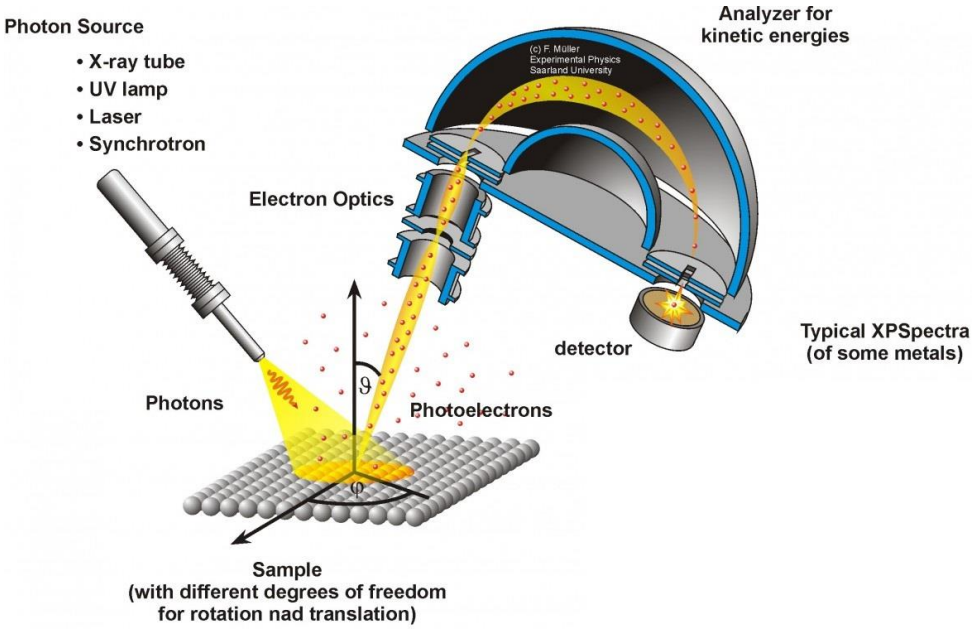

Figure 3.6. *Schematic view of a typical XPS surface analysis technique. The XPS instrument includes a photo source, an ultra-high vacuum (UHV) stainless steel chamber, an electron collection lens, a*

magnetic shield, an analyzer for kinetic energies, and an electron detector. Adapted with permission from ref. [176].

In this thesis, XPS analysis was conducted on a Kratos Axis Ultra DLD spectrometer under a vacuum of 1×10^{-12} mbar. A monochromatic Al Kα X-ray source ("hv" = 1486.58 eV) produces an X-ray beam for the XPS measurement. To study the composition and chemical state at the surface of the catalysts, the high-resolution spectra were determined by a fixed analyzer with an energy of 20 eV. Finally, all collected spectra were analyzed using the XPS Peak software.

3.4.2 X-ray Diffraction

X-ray Diffraction (XRD) is a versatile analytical technique that provides access to the qualitative and quantitative identifications of crystalline phases as well as unit cell dimensions in materials. Regarding the fundamental principles of XRD,[177] it is based on constructive interference of monochromatic X-rays and a crystalline sample. X-rays are the optical radiation produced by the leap of electrons in the inner shells of atoms under the bombardment of high-speed moving electrons, mainly including continuous X-rays and characteristic X-rays. In the XRD equipment, X-rays are produced by cathode ray tubes, which are filtered to produce monochromatic radiation. When a monochromatic X-ray beam is directed towards a crystal, the electrons around the atoms in the crystal will vibrate due to the periodic changes in the electric field of the X-rays. Based on the periodicity of the crystal structure, the scattered waves of individual atoms (electrons of atoms) in the crystal can interfere with each other and superimpose, which is called diffraction. If Bragg's law ($n\lambda = 2d\sin\theta$) is fulfilled, the interaction of the incident rays with the sample will constructively interfere, producing a diffracted beam. The diffraction pattern generated by each crystal reflects the atomic distribution inside the crystal. XRD has traditionally been used to analyze bulk samples, but it is also possible to use XRD for thin-film analysis, *e.g.*, grazing incidence XRD (GIXRD). In a GIXRD measurement, the grazing angle of incidence is fixed because this mode avoids the strong signal from the substrate and obtains a stronger signal from the film itself.

In this thesis, GIXRD patterns of all thin-film samples were collected on an X'Pert PRO PANanalytical instrument. The procedure used for the GIXRD measurements includes a 2θ range of 5 to 35 °and a slow-scanning step of 0.125 °per min.

3.4.3 Grazing-Incidence Wide-Angle X-ray Scattering

Grazing-incidence wide-angle X-ray scattering (GIWAXS) is a popular technique used to investigate nanostructured thin films. It can provide information on crystalline lattice spacing, degree of crystallinity, and orientation distributions.[178]

The SURMOF thin films and their derivatives were studied using GIWAXS at P03 beamline, PETRA III, DESY in Hamburg (Germany). The X-ray wavelength is 0.99 Å, which corresponds to an energy of 12.57 keV. In the beamline, the sample detector distance (SDD) and an incident angle are 180 mm and 0.2 °, respectively. All GIWAXS data were analyzed by using the Matlab-based software GIXSGUI (written by Zhang Jiang, Argonne National Laboratory, USA). To obtain a more precise peak position, the resulting curves after tube-cut or cake-cut were finally fitted with Gaussian functions.

3.4.4 Raman Spectroscopy

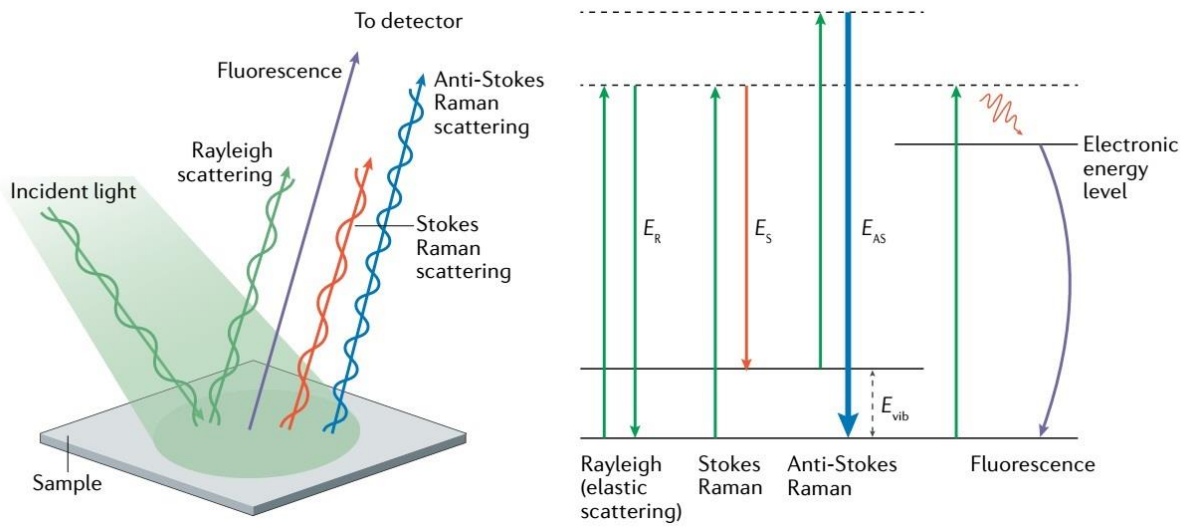

Figure 3.7. *Diagram of Raman scattering and energetic transitions. Stokes and anti-Stokes Raman scatterings are inelastic. In the case of Stokes scattering, a lower frequency (longer wavelength) than the initial radiation can be observed, representing that part of the photon's energy is absorbed by the molecule. In turn, if a molecule initially in a vibrationally excited state interacts with a photon and temporarily reaches a virtual energy state, then returns to the initial ground state. The scattered photon obtains more energy. This is the anti-Stokes Raman scattering. Reproduced with permission from ref. [179]. Copyright © 2021, Springer Nature Limited.*

Raman spectroscopy is an important analytical method based on the Raman scattering effect, which was discovered by the Indian scientist C. V. Raman in 1928. Regarding the definition of Raman scattering, when the high-intensity incident light from a laser beam source is scattered by molecules, most of the scattered light has the same wavelength (color) as the incident laser, and this scattering is called Rayleigh scattering. However, a small amount (about $1/10^{\wedge 9}$) of the scattered light exhibits a wavelength (color) different from that of the incident light, and the change in wavelength is determined by the chemical structure of the test sample. This scattering mode is referred to as Raman scattering. Raman spectroscopy provides detailed information on the chemical structure, phase and morphology, crystallinity, and molecular interactions of a sample.[179]

In this work, Raman spectroscopy analysis was conducted on the Renishaw inVia Reflex Raman microscope with a 532 nm laser source. All *in-situ* Raman measurements were performed with a potentiostat (Autolab PGSTAT302N). A SURMOFs-coated QCM electrode, a Pt wire, and a Hg/HgO (1 M NaOH) were assembled as a three-electrode configuration in a homemade spectro-electrochemical cell, which has been described in **section 3.1.4**.

3.4.5 Time-of-Flight Secondary Ion Mass Spectrometry

Time-of-flight secondary ion mass spectrometry (ToF-SIMS) has emerged as a powerful technique for high-resolution surface analysis, such as quantitative characterizations of inorganic, organic, and biological materials.[180] In SIMS, a pulsed primary ion beam is used to remove material from the top monolayer of the sample by sputtering. Atomic and molecular secondary ions result from pulsed primary ion beams (Cs^+, Ga^+) impinging on the surface of samples. They will be accelerated into a reflection type ToF mass spectrometer. The ToF analyzer can be used over a large mass range, making the instrument well-suited for detecting the composition of large sample surfaces. In addition, depth profiling is commonly used in ToF-SIMS by combining high current, low energy caesium, and sputtering argon sources.

To study the distribution of chemical species on the surface and in the depth of the SURMOFs and derivatives, ToF-SIMS was performed on a TOF.SIMS5 instrument (ION-TOF GmbH, Münster, Germany) equipped with a liquid metal ion gun (LMIG) and a reflective time-of-flight analyzer. An ultrahigh vacuum base pressure (below 5×10^{-9} mbar) was maintained throughout the ToF-SIMS measurement. The depth profiling and high-resolution mapping were executed

with the Bi source in the "high current bunched" mode, which provides 0.7 ns Bi_1^+ primary ion pulses at 25 keV energy. In static SIMS experiments, the primary ion beam was rastered over a 500 × 500 μm^2 field-of-view area on each sample, and 128 × 128 data points were recorded. In-depth profiling, a 500 × 500 μm^2 pit was eroded using 1 keV oxygen erosion, and a central 200 × 200 μm^2 with 64 × 64 pixels was acquired for analysis. Note that all captured signal strengths are normalized to their maximum for a clearer comparison.

3.4.6 Transmission Electron Microscopy

A transmission electron microscope (TEM) is a very useful microscopy tool in the fields of materials, physics, chemistry, and life sciences. This technique uses an accelerated electron beam to pass through very thin samples, enabling the observation of features such as structure and morphology. In this work, TEM and high-resolution TEM images were obtained using an FEI Titan Themis at 300 kV accelerating voltage (Department of Chemistry, Ludwig Maximilian University of Munich (LMU)). The SURMOFs and corresponding derivatives were carefully scraped off the gold substrates and then dispersed in ethanol solution by sonication for TEM characterization. The final obtained ink was evenly deposited on the copper grids and dried naturally in the air.

3.4.7 Field Emission Scanning Electron Microscopy

Field emission scanning electron microscope (FE-SEM) is another large precision instrument for high-resolution morphological observation. It features a large depth of field, high resolution, intuitive imaging, strong stereoscopic sense, and a wide magnification range. Compared to conventional SEM, FE-SEM produces higher-resolution images with less electrostatic distortion. In this thesis, microstructure images were obtained on a high-resolution FE-SEM (Zeiss Gemini NVision 40) with an accelerating voltage of 5 kV and a working distance of 3.5 mm.

3.4.8 Atomic Force Microscope

Atomic force microscopy (AFM) is a versatile and powerful technique for studying nanoscale samples, first developed by Binnig, Quate, and Gerber in 1985.[181,182] It is capable of imaging virtually any type of surface, including polymers, ceramics, glass, and biological samples. Moreover, AFM can operate in air, liquid, or ultra-high vacuum and provides accurate and non-

destructive measurements regarding morphological, chemical, optical, electrical, magnetic, and mechanical properties of the sample surfaces with a very high resolution. AFM consists of a micromachined silicon or silicon nitride cantilever with an extremely sharp tip. When the tip approaches the scanned sample surface, a small deflection of the flexible cantilever occurs due to the very weak Pauli repulsive forces between the tip and sample surface atoms. The force (F) between the tip and the sample deflection (x) of the cantilever follows Hooke's law:

$$F = -kx \tag{3.6}$$

where k is a force constant factor of the cantilever.

A series of cantilever deflections caused by variations in sample height will be tracked by a laser beam reflected from the backside of the AFM cantilever. A position-sensitive photodiode can be used to monitor the changes and control the height of the tip above the surface by using a feedback loop, hence achieving a constant interaction force. According to the interaction force between the AFM tip and the surface, AFM mainly includes three basic modes of imaging surface topography: contact mode, non-contact mode, and tapping mode.

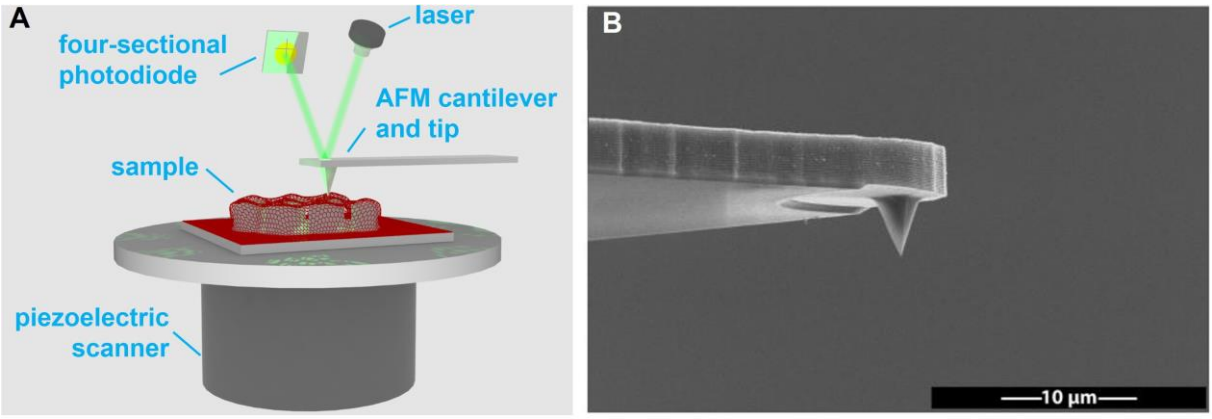

Figure 3.8. *(A) Schematic diagram of AFM and (B) a typical SEM image of a tip on the AFM microcantilever. Reproduced with permission from ref. [183]. Copyright © 2017, Rights managed by AIP Publishing.*

In this thesis, a multimode EC-STM/AFM instrument (Veeco Instruments Inc.) was adopted to study the sample morphology with a Nanoscope IIID controller. As for the AFM measurements, the tapping mode (AFM tip, Bruker RTESP-300) was used and operated at a scan rate of 0.5 Hz with a scan area of $2 \times 2\ \mu m^2$.

4 Results and Discussion

4.1 Metamorphosis of Heterostructured SURMOFs Enables a Record Mass Activity towards Oxygen Evolution Reaction

This part elaborates a facile strategy to prepare the highly active oxygen evolution electrocatalysts by the *in-situ* structural transformation and self-activation of heterostructured SURMOFs. In particular, the combination of the SURMOFs growth and positioning technology with the metamorphosed perspectives of the alkaline-unstable SURMOFs offers deep insights into understanding the transformation mechanisms and the structure-performance relationships.

This research has been published in:

S. Hou, W. Li, S. Watzele, R. M. Kluge, S. Xue, S. Yin, X. Jiang, M. Döblinger, A. Welle, B. Garlyyev, M. Koch, P. Müller-Buschbaum, C. Wöll, A. S. Bandarenka, R. A. Fischer, Metamorphosis of Heterostructured Surface-Mounted Metal-Organic Frameworks Yielding Record Oxygen Evolution Mass Activities. *Advanced Materials* 33 (2021) 2103218.[184]

4.1.1 Motivation

The majority of MOF compositions comprise the low-cost first-row transition metals such as Mn(II)/Mn(III), Fe(III), Co(II), Ni(II), Cu(II), Zn(II), *etc*. as well as inexpensive and commercially accessible organic ligands (mostly carboxylates).[67,148] These compositional features make MOFs promising earth-abundant candidates and precursors in the field of heterogeneous catalysis and electrocatalysis. Despite a recent surge in research findings, major problems remain unsolved regarding MOF-based electrocatalysts, *e.g.*, stability in extreme conditions, the origin of the active sites, and the structure-activity correlations.[72,73,74,75] Accordingly, the optimal ways to advance MOF-based electrocatalysts are being debated.

Since most MOFs are sensitive to water exposure and water molecules are in opulence under water splitting conditions, the MOF stability in aqueous electrolytes becomes a crucial factor in the study of MOF-related electrocatalysis.[53] Recent research has used a variety of advanced physicochemical approaches to elucidate the existence of active species in electrochemically tested (SUR)MOF catalysts.[75,77,185,186] As a result, the stated active species were assumed to form from MOF-derived metal hydroxides during the oxygen electrocatalytic process in alkaline electrolytes. Albeit recent efforts aimed at revealing catalytic species, comprehensive knowledge of the transformation mechanisms and the structure–performance correlations remain elusive.

Thanks to the highly tunable film thickness, controllable growth orientation, and binder-free processing, SURMOFs technology offers an effective strategy to design unique structures and accessible active sites at the molecular level.[54,55,56] In this work, the heterostructured SURMOFs were precisely constructed on the gold QCM electrode, offering intrinsic advantages for investigating transformation mechanism studies and performance optimization.

4.1.2 Mass Detection and Electrochemical Mass Activities

As described in **Chapter 3.1.1**, a series of mixed-metal, heterostructured SURMOFs have been fabricated through a stepwise layer-by-layer deposition method, including the Ni|Fe-[TA]-SURMOFs, NiFe-[TA]-SURMOFs, and Fe|Ni-[TA]-SURMOFs. The normalized mass activity was adapted in this work to accurately assess and compare the intrinsic electrocatalytic activity of these as-prepared electrodes. Prior to and after the electrochemical measurement, a QCM chip was used to record the mass loading of the electrodes. As shown in **Figure 4.1A**, the

remarkable discrepancy in the mass loading for the pristine SURMOFs and Catalysts (SURMOFs after the electrochemical tests) indicates that SURMOF components partially leached out, and SURMOFs were transformed into SURMOF derivatives. Subsequently, the SURMOF derivative obtained after electrochemical cycling is denoted as 'Catalyst'. We first evaluated the electrochemical behavior of these derived Catalysts in a three-electrode setup using the typical OER polarization curves (*cf.* **Figure 4.1B**). Note that the Ni|Fe-[TA]-Catalyst exhibits higher oxygen evolution activity (~2.90 kA g^{-1} at the overpotential of 300 mV) than that of NiFe-[TA]-Catalyst (~0.58 kA g^{-1}), Fe|Ni-[TA]-Catalyst (~0.28 kA g^{-1}) and Ni-[TA]-Catalyst (~0.25 kA g^{-1}). The activity trend suggests that the heterostructure formed by rationally arranging Ni and Fe-based SURMOFs greatly influences the OER electrocatalytic performance. Hence, in terms of the heterostructured strategy, it would provide more access to the design and development of MOF-based electrocatalysts. In addition, the Ni|Fe-[TA]-Catalyst demonstrates a remarkably fast reaction kinetics with the lowest Tafel slope of 44.3 mV dec^{-1} as shown in **Figure 4.1D**, while NiFe-[TA]-Catalyst, Fe|Ni [TA] Catalyst and Ni-[TA]-Catalyst exhibit higher Tafel slope values of 54.2, 60.8, and 87.1 mV dec^{-1}, respectively. Impressively, the Ni|Fe-[TA]-Catalyst attains a mass activity of 3.15 kA g^{-1} at a 300 mV overpotential, exceeding other recent state-of-the-art OER electrocatalysts (*cf.* **Figure 4.1E** and **Table 4.1**).

According to the remarkable mass variation and the unprecedented high oxygen evolution activity, studies on the conversion mechanism of SURMOFs into highly-active catalysts are pivotal for understanding the structure-performance relationship. Therefore, several key fundamental questions were posed and aimed at giving answers: What is the real role of the SURMOFs? Catalyst or pre-catalyst? How about the stability for SURMOFs in the alkaline electrolyte or during the electrochemical treatment? What are the active catalytic species? Where do they originate from? What is involved in the structural transformation process? Why does the heterostructure have a significant impact on catalytic activity?

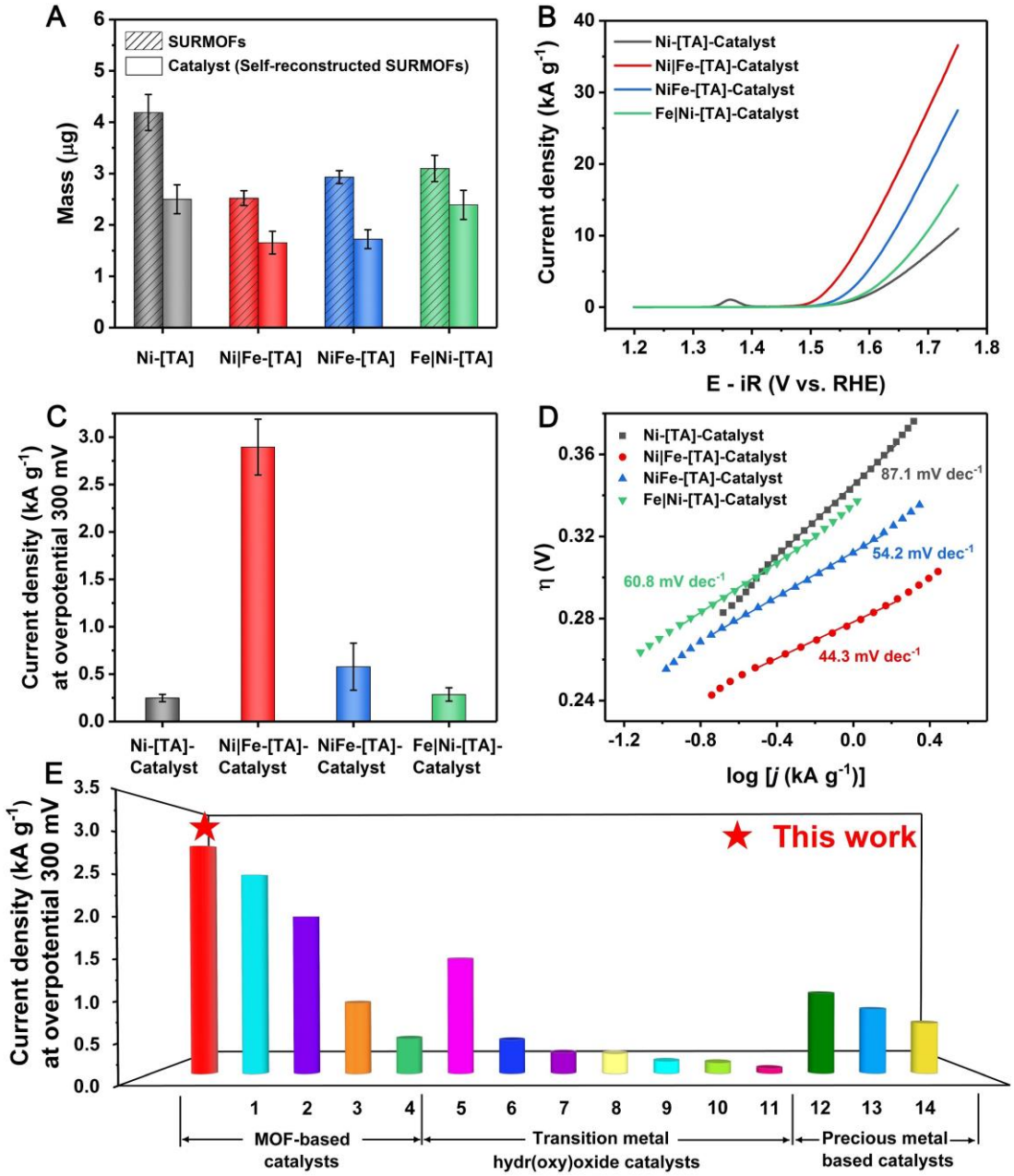

Figure 4.1. *(A) The mass loading of SURMOFs and Catalysts recorded by the Au QCM electrodes. Hereafter, the Catalysts represent the self-reconstructed SURMOFs after electrochemical cycling. (B) Typical OER polarization curves of Catalysts measured in 0.1 M O_2-saturated KOH with a scan rate of 5 mV s^{-1}. (C and D) Comparison of mass activities at an overpotential of 300 mV for all Catalysts and the corresponding Tafel slopes. (E) Electrochemical performance comparison of Ni|Fe-[TA]-Catalyst with benchmarked data of state-of-the-art catalysts. (1) 50Ni50Co-SURMOFD 10 cycles,[187] (2) Lattice-strained 4.3%-MOF,[71] (3) NiFe-BTC-GNPs,[188] (4) [M(BDC)] nanosheets (M = Ni^{2+}, Co^{2+}),[69] (5) Cu-Ni-Fe Hydr(oxy)oxide,[189] (6) NiFe-LDH@NiCu,[190] (7) δ-FeOOH NSs/Nickel foam,[191] (8) NiFe LDH nanomesh,[192] (9) CoMn LDH,[193] (10) $Ni_{0.8}Fe_{0.2}O_xH_y$,[194] (11) γ-CoOOH Nanosheets,[195], (12) $Rh_{22}Ir_{78}$/VXC,[196] (13) Ir-network,[197] and (14)Co–IrCu ONC/C.*[198]

Table 4.1. Comparison of the electrocatalytic performance based on mass activity for the recently reported OER catalysts.

Catalyst	Current density (A g^{-1}) at an overpotential of 300 mV	pH	E_{onset} V *vs* RHE	Ref.
Ni|Fe-[TA]-Catalyst	**~2900**	**13**	**~1.45**	**This work**
50Ni50Co-SURMOFD 10 cycles	2530	13	~1.47	[187] *J. Am. Chem. Soc.* 141 (2019) 5926-5933.
Lattice-strained 4.3%-MOF	2000 A g_{metal}^{-1}	13	~1.43	[71] *Nat. Energy* 4 (2019) 115-122.
FeCoNi-ATNs	1931 at 330 mV	14	1.465	[199] *Adv. Energy Mater.* 9 (2019) 1901312.
Cu-Ni-Fe hydr(oxy)oxide	1464.5	14	~1.40	[189] *Angew. Chem. Int. Ed.* 58 (2019) 4189-4194.
NiFe-BTC-GNPs	905	14	~1.43	[188] *Energy Environ. Sci.* 13 (2020) 3447-3458.
NiFe-MOF	547.8	14	-	[200] *Adv. Funct. Mater.* 31 (2021) 2102066.
P─$Ni_{0.75}Fe_{0.25}Se_2$	328.19 at 500 mV	14	-	[201] *Adv. Sci.*, 8 (2021) 2101775.
NiFe-LDH@NiCu	429.1	14	1.326	[190] *Adv. Mater.* 31 (2019) 1806769.
MIL-53(FeNi)/NF	76.07 at 252 mV	14	~1.45	[202] *Adv. Energy Mater.* 8 (2018) 1800584.
NiCo-UMOFNs	50 at 250 mV	14	1.42	[69] *Nat. Energy* 1 (2016) 16184.

$Co_{0.7}Fe_{0.3}CB$	643.4 at 320 mV	14	~1.49	[203] *Adv. Funct. Mater.* 30 (2020) 1909889.
NiFe LDH nanomesh	257.8	14	~1.47	[192] *Nano Energy* 53 (2018) 74-82.
$Ni_{0.8}Fe_{0.2}O_xH_y$	140 ±30	14	~1.50	[194] *Chem. Mater.* 29 (2017) 120-140.
$Ni_{50}Fe_{50}$-DAT	~1200	14	~1.48	[204] *ACS Catal.* 6 (2016) 1159-1164.
δ-FeOOH NSs/NF	267	14	~1.47	[191] *Adv. Mater.* 30 (2018) 1803144.
CoMn LDH	159	14	~1.50	[193] *J. Am. Chem. Soc.* 136 (2014) 16481-16484.
γ-CoOOH NS	66.6	14	1.47	[195] *Angew. Chem. Int. Ed.* 54 (2015) 8722-8727.
$NiSe_2$	88.7	14	~1.42	[205] *Electrochim. Acta* 295 (2019) 92-98.
$CaCu_3Ru_4O_{12}$	1942 A g_{Ru}^{-1} at 270 mV	0	~1.37	[206] *Nat. Commun.* 10 (2019) 3809.
RuO_2 NSs	520 A g_{Ru}^{-1} at 230 mV	0	~1.40	[207] *Energy Environ. Sci.* 13 (2020) 5143-5151.
$Rh_{22}Ir_{78}$/VXC	1020 A g_{metal}^{-1}	0	~1.47	[196] *ACS Nano* 13 (2019) 13225-13234.
RuO_2 particle	600 A g_{Ru}^{-1} at 250 mV	1	~1.40	[208] *Chem. Sci.* 6 (2015) 190-196.

Co-IrCu ONC/C	640 A g_{Ir}^{-1}	1	~1.46	[198] *Adv. Funct. Mater.* 27 (2017) 1604688.
Ir-network	817 A g_{Ir}^{-1}	1	~1.47	[197] *J. Mater. Chem. A* 8 (2020) 1066-1071.

4.1.3 Monitoring the Properties of the Ni|Fe-[TA] Electrode during the Evolution Process

To unlock the structural transformation mechanism and the quantitative correlation between the inherent MOF structures and the real active sites, in the following, a variety of *ex-situ* and *in-situ* approaches were used to investigate the nature of the active species and the structural evolution of SURMOFs throughout the alkaline hydrolysis and electrochemical treatments.

The hydrolytic stability of MOFs significantly depends on the strength of the metal-ligand bonds, which can be typically speculated from the principle of hard and soft acids and bases. Typically, a hard Lewis acid-hard Lewis base tie-up demonstrates high hydrolytic stability.[53] Pertaining to carboxylic acid-based MOFs, the O^{2-} in the carboxylate ligands is a relatively hard Lewis base.[209] At the same time, transition metal ions (*e.g.*, Fe^{2+}, Ni^{2+}, Co^{2+}, Cu^{2+}, and Zn^{2+}) in moderate oxidation states are classified into the borderline of the hard and soft acids. Accordingly, numerous transition metal-carboxylic acid MOFs should exhibit a limited alkaline hydrolysis resistance under an extreme experimental environment.

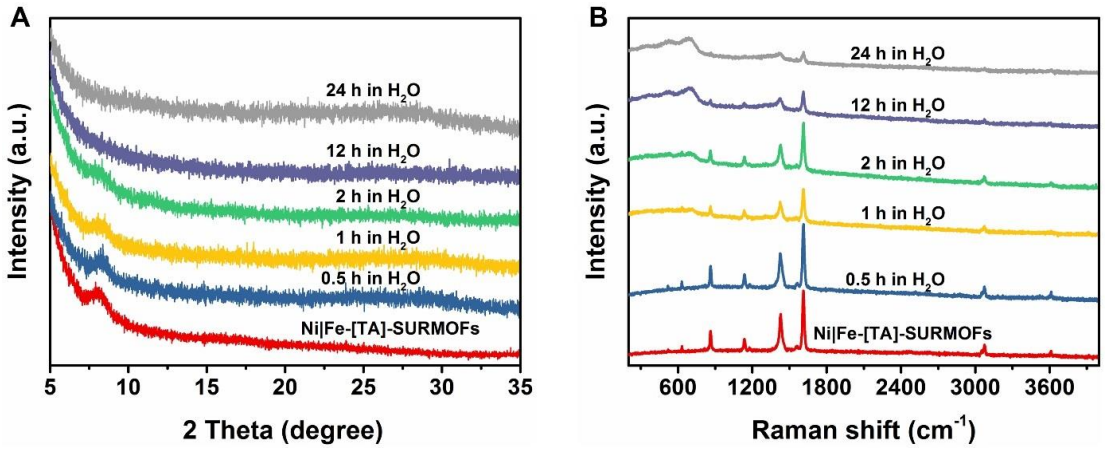

Figure 4.2. *The investigation of hydrolytic stability of Ni|Fe-[TA]-SURMOFs. (A and B) GIXRD data and Raman spectra of Ni|Fe-[TA]-SURMOFs (60 layers) collected in deionized water. The electrode was dried with Ar gas flow before each GIXRD and Raman measurements.*

As shown in **Figure 4.2**, the hydrolytic stability of Ni|Fe-[TA]-SURMOFs against the immersion time was investigated *via ex-situ* XRD and *ex-situ* Raman. The faint changes in the intensities of Raman and XRD peaks unveil the relative stability of the SURMOFs when the immersion time is less than one hour. Nevertheless, the XRD peak pertained to the SURMOFs became invisible after immersing in water for 12 hours, indicating the decomposition of the SURMOF crystalline structures under a long-term water immersion. This conclusion can be further determined based on the weakened Raman peaks against the immersion time. It is of note that two newly emerged Raman peaks at around 526 cm^{-1} and 690 cm^{-1} after the immersion in water for 24 hours should be attributed to the γ-FeOOH species since the hydrolysis reaction results in the decomposition of superficial Fe-[TA] in the heterostructured Ni|Fe-[TA]-SURMOFs and the generation of FeOOH under the alkaline environment.[210,211]

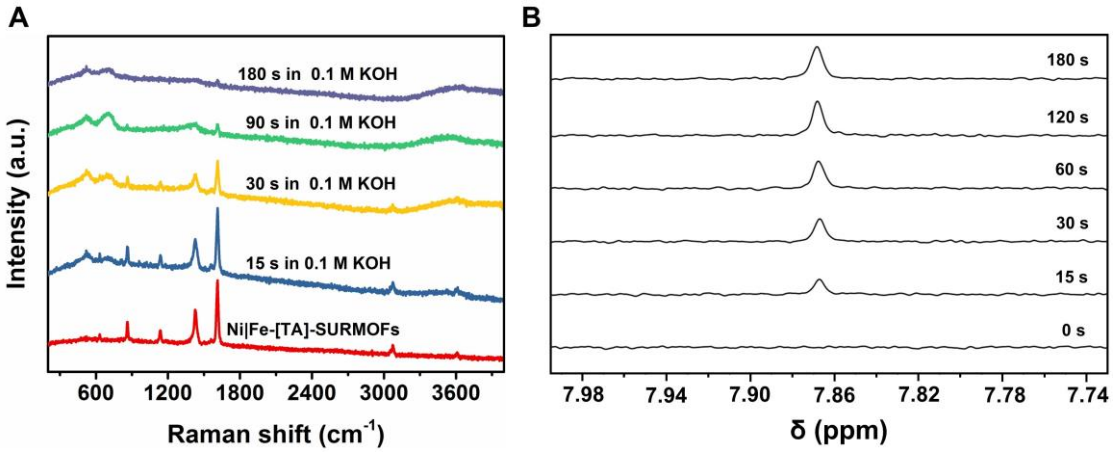

Figure 4.3. *(A) Raman spectra collected during the 3-min immersion in 0.1 M KOH for Ni|Fe-[TA]-SURMOFs electrode within a wavenumber region of 200-4000 cm^{-1}. The electrode was promptly washed three times with deionized water after each KOH immersion process and dried with Ar gas flow. (B) ^{1}H NMR spectra obtained by immersing Ni|Fe-[TA]-SURMOF electrode into the 0.1 M KOH/D_2O electrolyte with gradient time slots (0, 15, 30, 60, 120, 180 s).*

Although SURMOFs are relatively stable in water, their dissociation and transformation processes in alkaline electrolytes remain enigmatic. Given that Raman spectroscopy can provide more derivative details in terms of ligands and metal intermediate species, the alkaline hydrolysis experiment was carried out by recording the Raman spectra. As shown in **Figure 4.3A**, a rapid decomposition for the Ni|Fe-[TA]-SURMOFs can be observed by gradually weakening peaks during the alkaline immersion. This result further confirms the truth of alkaline-unstable characteristics for Ni|Fe-[TA]-SURMOFs. Nuclear magnetic resonance

(NMR) spectroscopy was performed during the alkaline immersion treatment to explore the process of structural transformation more intuitively, as shown in **Figure 4.3B**. The gradually increasing NMR peak intensity indicates the dissolution of ligands in SURMOFs over time. In particular, the characteristic ligand NMR peak showed a clear enhancement within 2 min and then remained almost constant. This result further reveals the rapid decomposition and ligand dissolution of the SURMOFs under an alkaline environment.

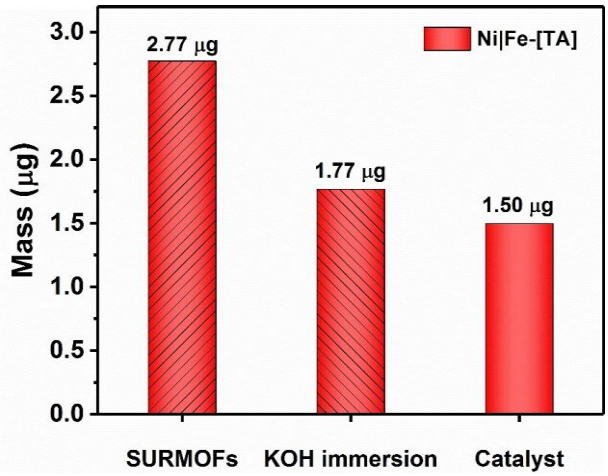

Figure 4.4. *Mass detection of Ni|Fe-[TA]-SURMOFs, Ni|Fe-[TA]-SURMOFs immersed in 0.1 M KOH solution for 3 min (defined as KOH immersion), and Ni|Fe-[TA]-Catalyst. All mass loadings were recorded by the gold QCM electrode. In particular, the samples of KOH immersion and Ni|Fe-[TA]-Catalyst were taken out from the KOH electrolyte, followed by three times washing with deionized water and a drying step with argon.*

Additionally, QCM measurements were taken to track the mass changes for the SURMOFs during the structural evolution process. As shown in **Figure 4.4**, remarkable mass loading discrepancies can be observed for Ni|Fe-[TA]-SURMOFs, Ni|Fe-[TA]-SURMOFs immersed in 0.1 M KOH solution for 3 min (defined as KOH immersion), and Ni|Fe-[TA]-Catalyst. In detail, after 3 minutes of immersion in 0.1 M KOH solution, the mass loading on the QCM electrode reduced from ~2.77 to ~1.77 μg, indicating that the as-prepared SURMOFs were unstable in the alkaline electrolyte. This result was consistent with the finding in Raman and XRD characterizations. Subsequently, a CV test was conducted to promote the structural evolution of the SURMOFs further. A further decrease in mass loading was observed after the electrochemical activation. These preceding characterizations provide sufficient evidence to confirm the transformation of SURMOFs in terms of components and structure during both

alkali immersion and electrochemical cycling. However, the deeper derivation mechanism remains puzzling.

4.1.4 The Hypothesis of the Transformation Mechanism

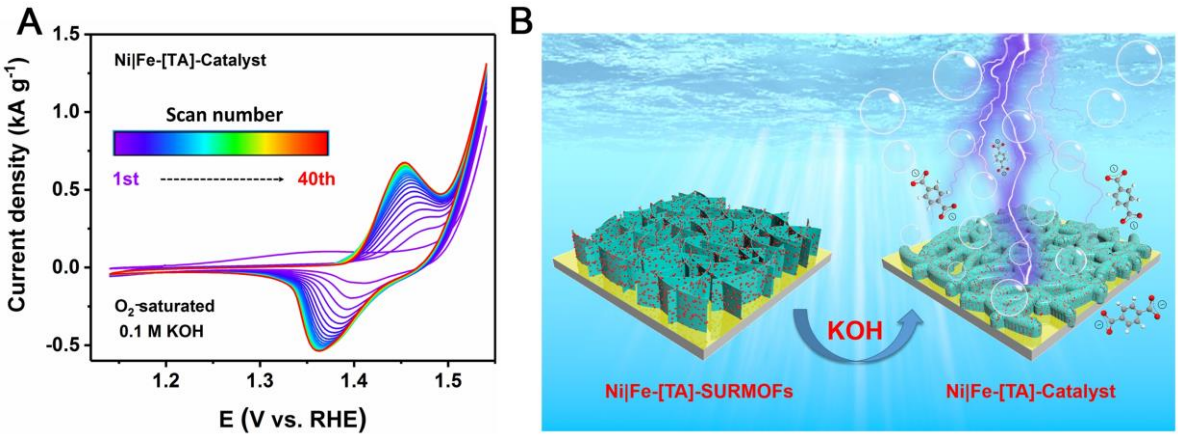

Figure 4.5. *(A) Characteristic CV curves of the Ni|Fe-[TA]-Catalyst electrode collected with a scan rate of 20 mV s^{-1} for 40 cycles in an O_2-saturated 0.1 M KOH solution. (B) Schematic hypothesis showing the transformation mechanism of heterostructured SURMOFs into Catalysts during alkaline hydrolysis and electrochemical cycling processes.*

Figure 4.5A shows the electrochemical activation treatment. An anodic peak in the first cycle's polarization curve was observed within the potential range of 1.25 to 1.46 V *vs* RHE, corresponding to the oxidation of SURMOFs. After that, the oxidation current increased further in the higher potential range (1.46-1.54 V), indicating that more SURMOF species were oxidized. As the number of cycles increased, the characteristic redox pair peaks can be observed, assigned to reversible redox transitions between Ni^{2+} and Ni^{3+} species.[114,212] Moreover, the redox current densities gradually reached an extreme value until the 35^{th} cycle. This finding is attributed to the continuous exposure of Ni^{2+}-Ni^{3+} species and an increase in the number of available catalytic active sites. Therefore, this is significant for referring SURMOFs as "Catalyst" after electrochemical cycling. According to this evidence, we put forward a mechanism for the transformation of pristine SURMOFs into the highly-active electrocatalysts, as shown in **Figure 4.5B**. A two-step sequential derivatization process is involved, including an impregnation treatment in the alkaline electrolyte and the electrochemical activation. The former leads to the dissociation of the coordination bonds between the ligands and the metal clusters as well as the replacements of organic ligands by the OH^-/H_2O through the alkaline hydrolysis reaction. At the same time, the latter treatment facilitates the reconstruction of the

retained metal hydroxides and the exposure of the active sites. Hence, we denote the transformation process as the SURMOF metamorphosis.

4.1.5 Elucidation of the Transformation Mechanism

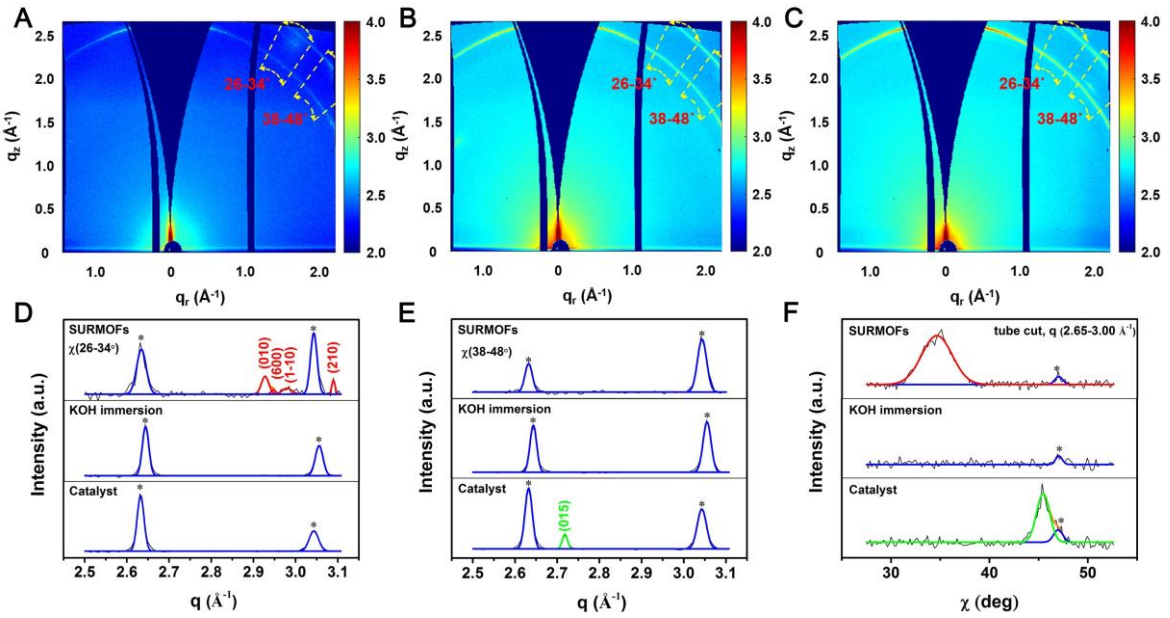

Figure 4.6. *2D GIWAXS patterns for the Ni|Fe-[TA]-SURMOFs (A), after 3 min immersion in 0.1 M KOH solution (B), and after the OER test (C). Cake cuts at angles between (D) χ = 26-34 °and (E) 38-48 °extracted from the above 2D GIWAXS data. (F) Tube cuts performed in a q range of 2.65-3.00 Å^{-1}. All curves were fitted using the Gaussian functions. These peaks marked with a star (*) in D-F belong to the diffraction peaks (blue lines) of the electrode substrates.*

From the nature of SURMOF metamorphosis, it is apparent that the composition change and active site exposure should be closely related to the structural variation. To directly characterize the crystalline structure and orientation of SURMOFs during the derivatization process, GIWAXS and GIXRD were carried out on the samples. As shown in **Figure 4.6A-C**, 2D GIWAXS patterns show two significant diffraction rings at scattering vectors of q = 2.64 Å^{-1} and 3.04 Å^{-1}, corresponding to the scattering signals from the QCM substrate. Note that two pronounced Bragg diffraction spots can be observed in the scattering patterns (*cf.* **Figure 4.6A** and **C**) of Ni|Fe-[TA]-SURMOFs and Ni|Fe-[TA]-Catalyst. They represent the generation of crystalline phases on the pristine SURMOFs and their NiFe hydroxide derivatives, respectively.[69, 213] These diffraction spots reflect the highly preferred crystallographic orientations associated with the substrate.[214] To compare quantitatively, the cake cuts of the GIWAXS patterns were performed as shown in **Figure 4.6D** and **E**. Several peaks located at q

= 2.93, 2.95, 2.98, and 3.09 $Å^{-1}$, respectively, can be observed, corresponding to the (010), (600), (110), and (210) Bragg peaks of Ni|Fe-[TA]-SURMOFs. However, these diffraction signals vanished after 3 min KOH immersion, which is associated with the destruction of the crystalline structure of SURMOFs in alkaline electrolytes. After electrochemical cycling, a new diffraction peak at q = 2.72 $Å^{-1}$ can be found in the line-cut profile of Ni|Fe-[TA]-Catalyst (*cf.* **Figure 4.6E**), representing the (015) diffraction peak of NiFe-LDH.[213] Furthermore, the properties of preferential orientation for the samples were investigated through the tube cuts on the reshaped 2D GIWAXS patterns (*cf.* **Figure 6.2** in the Appendix). The Ni|Fe-[TA]-SURMOFs exhibit a preferential orientation around $\chi = 34.5°$, which corresponds to a broad orientation distribution. In contrast, no orientation peak can be detected in the tube cut pattern of the Ni|Fe-[TA]-KOH immersion sample, pointing to the structural collapse of higher-order SURMOFs and the formation of amorphous nickel/iron hydroxides. At the same time, a sharp peak at $\chi = 45.4°$ with a small orientation distribution is observed in the Ni|Fe-[TA]-Catalyst, as shown in **Figure 4.6E**. This experimental evidence reveals a two-step evolution process of the pristine SURMOFs into Catalyst: 1) The crystalline SURMOFs transform into amorphous NiFe hydroxides during an ephemeral alkaline immersion treatment; 2) A minority of NiFe-LDH with high crystallographic orientation is produced after the electrochemical activation. Additionally, similar crystalline structure variations are further clarified by the GIXRD patterns. In **Figure 4.7**, a characteristic peak that appeared at around 9 ° in the SURMOF sample can be indexed to the previously reported Ni-[TA] MOFs. This peak vanished after the electrochemical cycling, suggesting the structural transformation of SURMOFs into amorphous electrocatalysts. Generally, amorphous structures demonstrate more structural defects, which are favorable to catalytic reactions.

SEM and AFM experiments were carried out on all samples to monitor morphologic changes during the SURMOF metamorphosis process. **Figures 6.3** and **6.4** in the Appendix show that the Ni-[TA]-SURMOFs and Fe-[TA]-SURMOFs exhibit ultrathin nanosheet and nanocluster morphologies, respectively. Interestingly, these two different structures are appropriately preserved in the heterostructured Ni|Fe-[TA]-SURMOFs and Fe|Ni-[TA]-SURMOFs (*cf.* **Figures 4.7C** and **6.6C**) since the Ni-[TA] and Fe-[TA] can be synthesized through a stepwise layer-by-layer deposition process. In the case of the heterostructured Ni|Fe-[TA]-SURMOFs, 15 layers of Ni-[TA] were initially deposited on the gold substrate, followed by a deposition of 15 layers of Fe-[TA] on top. Therefore, this is what "Ni|Fe" in the formula represents. These

morphologies further confirm the distinctive superiority of the LBL method for the construction of heterostructured SURMOFs. By contrast, the NiFe-[TA]-SURMOFs exhibit a significantly different morphology in **Figure 6.5C**, as evidenced by the uniform thin film composed of MOF nanoparticles. After the OER testing, remarkable morphological variations were observed in all samples (*cf.* **Figures 4.7D**, **6.3D**, **6.5D**, and **6.6D**). In particular, the interconnected nanofiber networks covered on the gold substrate can be observed in the Ni|Fe-[TA]-Catalyst, which should be derived from the nanosheet structures in the pristine SURMOFs.

In addition, AFM characterization provides more information on the roughness and thickness variations of the pristine SURMOFs and the derived electrocatalysts. **Figures 4.7E, 4.7F**, **6.5E**, **6.5F**, **6.6E**, **6.6F**, and **Table 4.2** show that the Catalysts' surface is smoother than the pristine SURMOFs. For example, when the Ni|Fe-[TA]-SURMOFs were converted to the Ni|Fe-[TA]-Catalyst, the roughness average was reduced from ~49.0 nm to ~26.9 nm, and the average height was decreased from ~244.3 to ~131.4 nm. Thus, AFM images offer further support for the decomposition and the reconstruction of SURMOFs in alkaline electrolytes.

Table 4.2. Surface roughness results of all samples measured by AFM.

Sample	Roughness average R_a (nm)	Average height (nm)	Maximum height (nm)	Roughness factor
Ni|Fe-[TA]-SURMOFs	49.0	244.3	417	1.80
Ni|Fe-[TA]-Catalyst	26.9	131.4	199	1.06
NiFe-[TA]-SURMOFs	35.7	150.5	319	2.02
NiFe-[TA]-Catalyst	11.3	91.1	205	1.19
Fe|Ni-[TA]-SURMOFs	36.1	190.2	401	1.35
Fe|Ni-[TA]-Catalyst	18.5	68.1	150	1.15

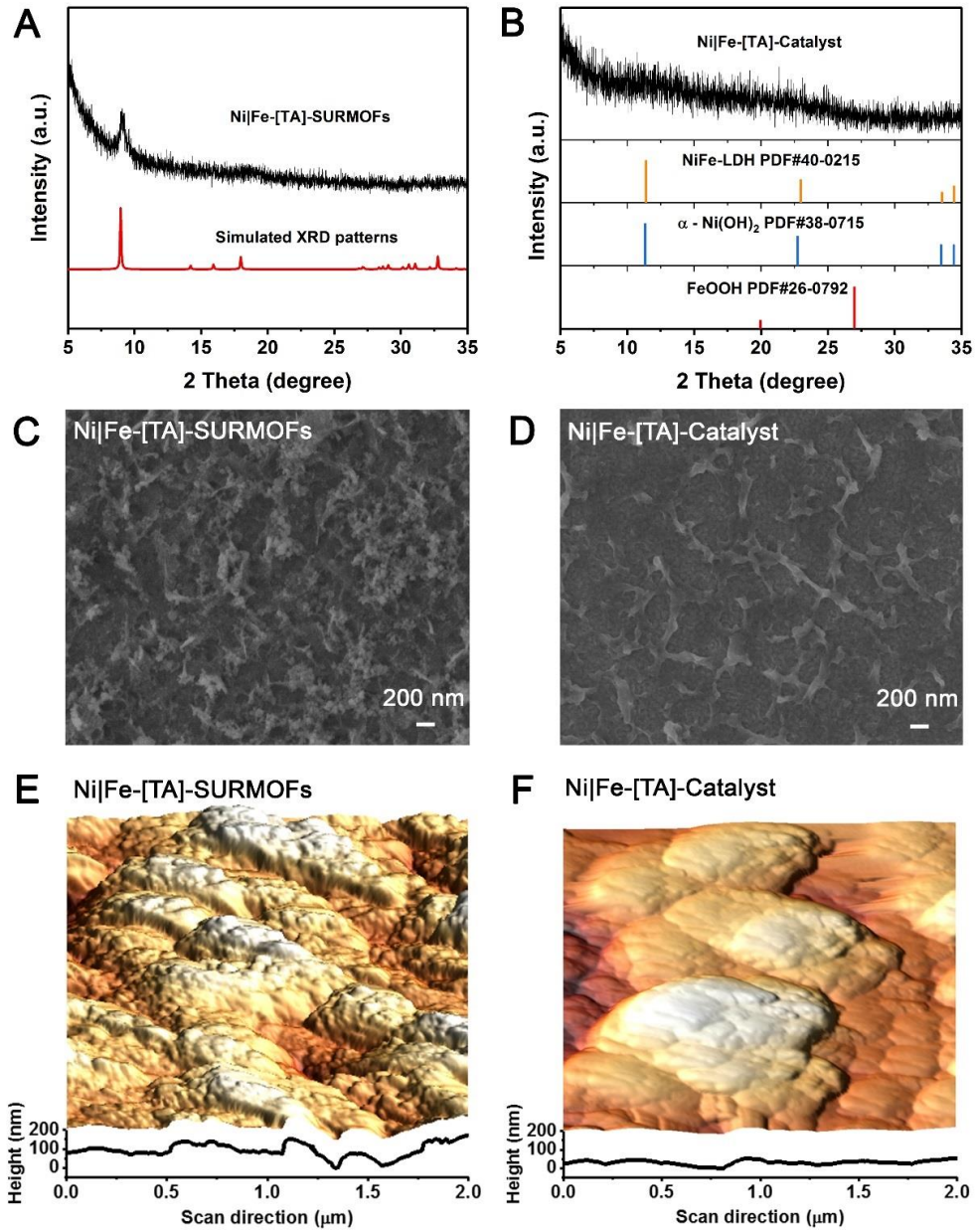

Figure 4.7. *The comparison of structures and morphologies for pristine Ni|Fe-[TA]-SURMOFs and Ni|Fe-[TA]-Catalyst using the GIXRD, SEM, and AFM.*

The TEM image shown in **Figure 4.8A** demonstrates that the ultrathin nanosheets can be observed in the Ni|Fe-[TA]-SURMOFs, corresponding to the 2D Ni-[TA] SURMOFs. Benefiting from the ultrathin morphology, these nanosheets are embedded in a matrix with uniformly sized nanoparticles, which should be Fe-[TA] nanoparticles according to the SEM image in **Figure 6.4A**. By contrast, the TEM image of the Ni|Fe-[TA]-Catalyst (*cf.* **Figure 4.8D**) shows a similar matrix of nanoparticles, but the nanosheets are not observed anymore, indicating the structural transformation of SURMOFs after the OER testing. The diffraction

patterns of both samples (insets of **Figure 4.8A** and **D**) exhibit wide diffraction rings on an intense diffuse background. Note that the latter demonstrates a large amorphous material component. According to the d-values in the diffraction patterns, the structures of the SURMOFs and the $Fe_{0.67}Ni_{0.33}OOH$ (PDF# 00-014-0556) can be confirmed. Meanwhile, the crystallite sizes of Ni|Fe-[TA]-SURMOFs and Ni|Fe-[TA]-Catalyst are estimated to be around 2.2 nm and 1.1 nm, respectively. The presence of nanosheets is further confirmed by the high-resolution TEM image, as shown in **Figure 4.8B**. At the same time, lattice fringes are not discernible due to low crystallinity and beam sensitivity. Moreover, the distribution of O, Fe, and Ni elements was investigated by the energy-dispersive X-ray spectroscopy (EDX) elemental mappings. The Fe and Ni overlap elemental mapping image (*cf.* **Figure 4.8C**) shows a much stronger Fe signal than that of the Ni, which is in line with the heterostructures in Ni|Fe-[TA]-SURMOFs. After electrochemical cycling, the EDX elemental mappings demonstrate O, Fe, and Ni uniform distribution in the Ni|Fe-[TA]-Catalyst (*cf.* **Figure 4.8F**).

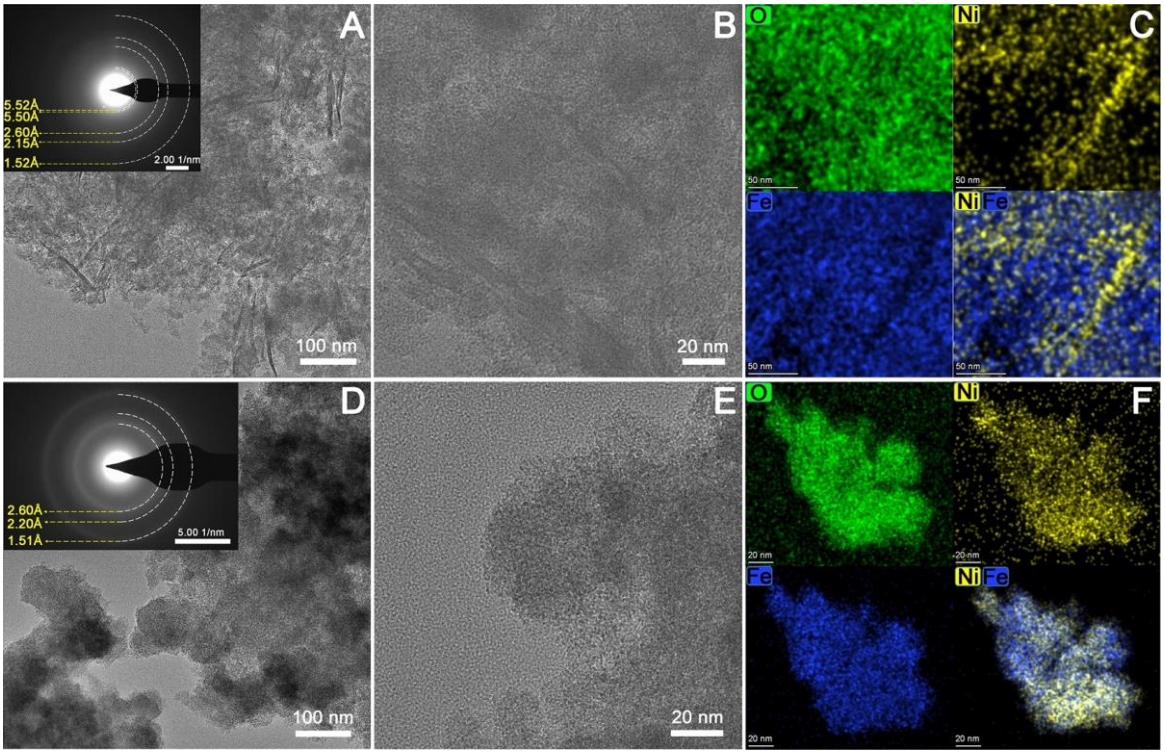

Figure 4.8. *(A and B) TEM and High-Resolution TEM images of the pristine Ni|Fe-[TA]-SURMOFs. The inset in (A) denotes the selected area electron diffraction (SAED) pattern. (C) EDX mappings in STEM mode of O, Ni, and Fe elements in the pristine Ni|Fe-[TA]-SURMOFs. (D and E) TEM and High-Resolution TEM images of Ni|Fe-[TA]-Catalyst. The inset in (D) denotes the SAED pattern. (F) EDX mappings in STEM mode of O, Ni, and Fe elements in Ni|Fe-[TA]-Catalyst.*

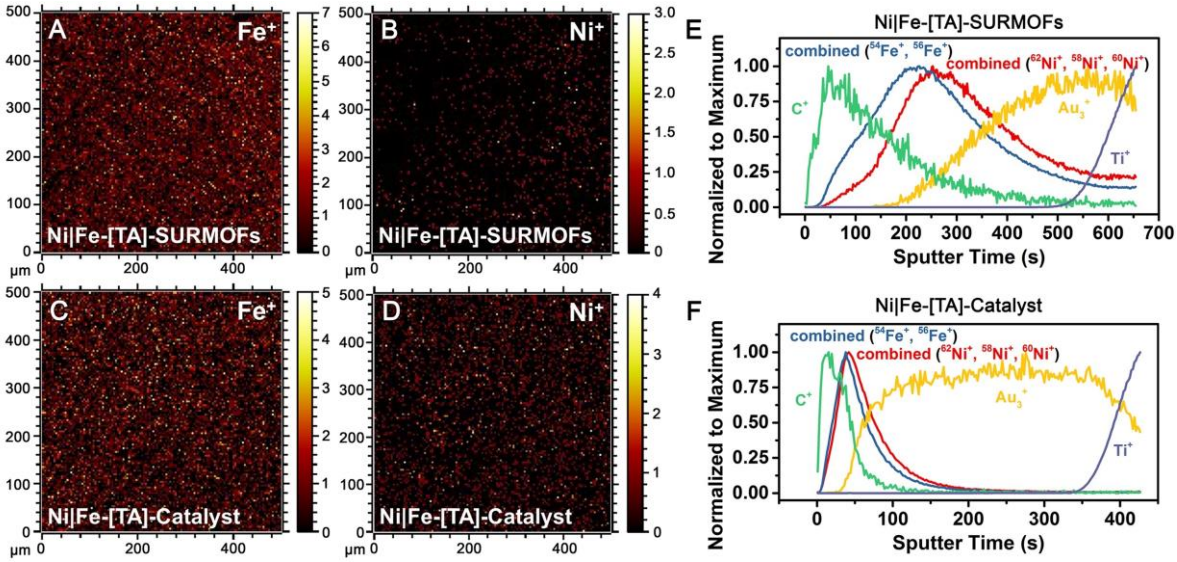

Figure 4.9. *ToF-SIMS analysis. (A-D) Chemical mapping of Fe and Ni signals collected from the topmost layer of the pristine Ni|Fe-[TA]-SURMOFs and the Ni|Fe-[TA]-Catalyst. (E and F) The depth profile characterization of the pristine Ni|Fe-[TA]-SURMOFs and the Ni|Fe-[TA]-Catalyst by probing C^+, Fe^+, Ni^+, Au^{3+}, and Ti^+ secondary ion fragments. The ToF-SIMS spectra have been normalized to the maximum.*

ToF-SIMS was further used in this work to elucidate the changes in species distribution during the reconstruction process. As shown in **Figure 4.9A** and **B**, Fe^+ and Ni^+ signals collected from the surface of the Ni|Fe-[TA]-SURMOFs exhibit significant differences, where the Fe^+ signal is apparently stronger than the Ni^+ signal, yet an opposite trend toward the Fe^+ and Ni^+ signals presents on the Fe|Ni-[TA]-SURMOFs (*cf.* **Figure 6.6A** and **B**). This difference can be attributed to the achievement of well-designed heterostructures. For example, the bottom-layer Ni-[TA] nanosheets are mostly covered by the top layer Fe-[TA] nanoparticles in the Ni|Fe-[TA]-SURMOF thin film, resulting in a stronger Fe-signal in the ToF-SIMS surface chemical mapping image. Thus, this leads to a better understanding of why the signal intensities of Fe^+ and Ni^+ are similar in the NiFe-[TA]-SURMOFs (*cf.* **Figure 6.5A** and **B**). Interestingly, the signal ratio of Fe:Ni species reduces dramatically from 16.5:1 to 1.98:1 when the Ni|Fe-[TA]-SURMOFs are converted into the Ni|Fe-[TA]-Catalyst (*cf.* **Figure 4.9C**, **D** and **Table 4.3**). The reason behind this should be the reconstruction and the re-distribution of Ni and Fe species during alkaline immersion treatment and electrochemical activation. Once again, our hypothesis is proved to be reasonable. Furthermore, ToF-SIMS depth profiles were conducted by the erosion treatment with 1 keV oxygen plasma sputtering. As a result, the distribution of C, Ni, and Fe species in SURMOFs and their derived catalysts can be determined. In the case

of Ni|Fe-[TA]-SURMOFs, the Fe^+ signal can be probed within the initial 25 s, while the curve of the Ni^+ signal markedly lags behind that of the Fe^+ signal, which is consistent with the design concept of heterostructural SURMOFs. In addition, NiFe-[TA]-SURMOFs and Fe|Ni-[TA]-SURMOFs show different occurrence time patterns of Ni^+ and Fe^+ signals (*cf.* **Figures 6.5E** and **6.6E**), which are in good agreement with their Ni and Fe species distribution. However, after electrochemical cycling, large distribution differences for Ni and Fe species can be found in the catalysts derived from heterostructured SURMOFs, *i.e.*, Ni|Fe-[TA]-Catalyst and Fe|Ni-[TA]-Catalyst. Ni^+ and Fe^+ signals can be detected almost simultaneously in both derived catalysts (*cf.* **Figures 4.9F** and **6.6F**). Therefore, these observations coincide nicely with a reconstruction process for heterostructured SURMOFs.

Table 4.3. Signal ratios of Fe and Ni acquired by static SIMS probing of the top few nanometers in the selected regions.

Sample	Fe:Ni signal ratio
Ni|Fe-[TA]-SURMOFs	16.5
Ni|Fe-[TA]-Catalyst	1.98
NiFe-[TA]-SURMOFs	0.52
NiFe-[TA]-Catalyst	1.72
Fe|Ni-[TA]-SURMOFs	0.04
Fe|Ni-[TA]-Catalyst	0.50

To expound on the surface chemical states and chemical composition in the pristine SURMOFs and derived electrocatalysts, XPS analysis was performed in this work. As shown in **Figure 4.10A**, the C 1s high-resolution spectra can be resolved into three peaks, corresponding to C-C

(284.8 eV), C-O (~286.7 eV), and O=C-O (~288.5 eV) bonds, respectively.[215,216,217] The presence of these peaks in the Ni|Fe-[TA]-Catalyst also confirms the residues of ligands since they are characteristic bonds of the [TA] ligand. Moreover, a new peak at 293 eV appears in Ni|Fe-[TA]-Catalyst, which can be attributed to the K^+, stemming from the KOH electrolyte.[216] In the O 1s spectra (*cf.* **Figure 4.10B**), four peaks corresponding to Ni(Fe)-oxygen bonds, Ni(Fe)-hydroxyl, C-O bonds, and O=C-O group can be observed in sequence according to the binding energy from low to high.[218,219] Note that a significant increase in the content of the Ni(Fe)-oxygen bonds and Ni(Fe)-hydroxyl is found after electrochemical activation. The content of C-O bonds and O=C-O groups remarkably decreases in the Ni|Fe-[TA]-Catalyst (*cf.* **Table 4.4**). This comparison suggests a partial and gradual dissociation of the organic ligands to the electrolyte during the immersion and electrochemical cycling in 0.1 M KOH. Meanwhile, more hydroxyl species or water would fill the vacant sites created by the dissociation of the ligands, leading to the formation of metal hydroxides. In the high-resolution Fe 2p spectrum of Ni|Fe-[TA]-SURMOFs (*cf.* **Figure 4.10C**), the Fe $2p_{3/2}$ and $2p_{1/2}$ peaks at 710.7 eV and 723.9 eV are observed with two corresponding satellite peaks, clearly determining the presence of Fe^{3+}.[220] After electrochemical activation, the Fe $2p_{3/2}$ peak of the Ni|Fe-[TA]-catalyst is positively shifted by about 0.7 eV compared to the peak in the initial Ni|Fe-[TA]-SURMOFs. This shift is related to the changes in the coordination environment of SURMOFs during the alkaline hydrolysis and electrochemical cycling, leading to a replacement of $[TA]^{2-}$ ligand with OH^-/O^{2-}.[75,221] In general, the positive shift in binding energy represents a decrease in the electron density around the center of Fe^{3+}.[75,221,222,223] The high-resolution Ni 2p spectra exhibit significant differences in the SURMOFs and the derived electrocatalysts. In the case of the Ni 2p spectrum of Ni|Fe-[TA]-Catalyst (*cf.* **Figure 4.10D**), a characteristic Ni $2p_{3/2}$ peak appears at a high binding energy of *ca.* 857.0 eV, corresponding to the Ni^{3+} species. However, it is not present in the SURMOFs because the electrochemical cycling produces the high oxidation state of Ni. Another Ni $2p_{3/2}$ peak located at 856.2 eV is assigned to the Ni^{2+} species in the SURMOFs,[224] yet the corresponding peak in the Catalyst appears at 856.0 eV. Moreover, the intensity of Ni 2p signals becomes remarkably higher after the OER, which suggests that more Ni species diffuse from the inner layer into the surface of electrocatalysts. This finding further reveals that the structural evolution and self-activation in an alkaline solution can expose more active Ni species to the surface of Catalysts. In addition, similar XPS variations are observed in the transformation process of other SURMOFs (*cf.* **Figures 6.9** and **6.10**). As shown in **Table 4.5**, the lowest Ni^{2+}:Ni^{3+} atomic ratio of 0.68:1 is obtained for Ni|Fe-[TA]-Catalyst based on

the peak area ratios of the Ni $2p_{2/3}$. In contrast, the Ni^{2+}:Ni^{3+} ratios are 1.08:1 and 2.49:1 for NiFe-[TA]-Catalyst and Fe|Ni-[TA]-Catalyst, respectively. It is worth noting that the content of Ni^{3+} species in the Catalysts is in good agreement with the trend of their OER performance. Analogously, the high oxidation state of nickel in NiFe-based double hydroxides has been reported to improve the electrocatalytic activity for water oxidation.[225]

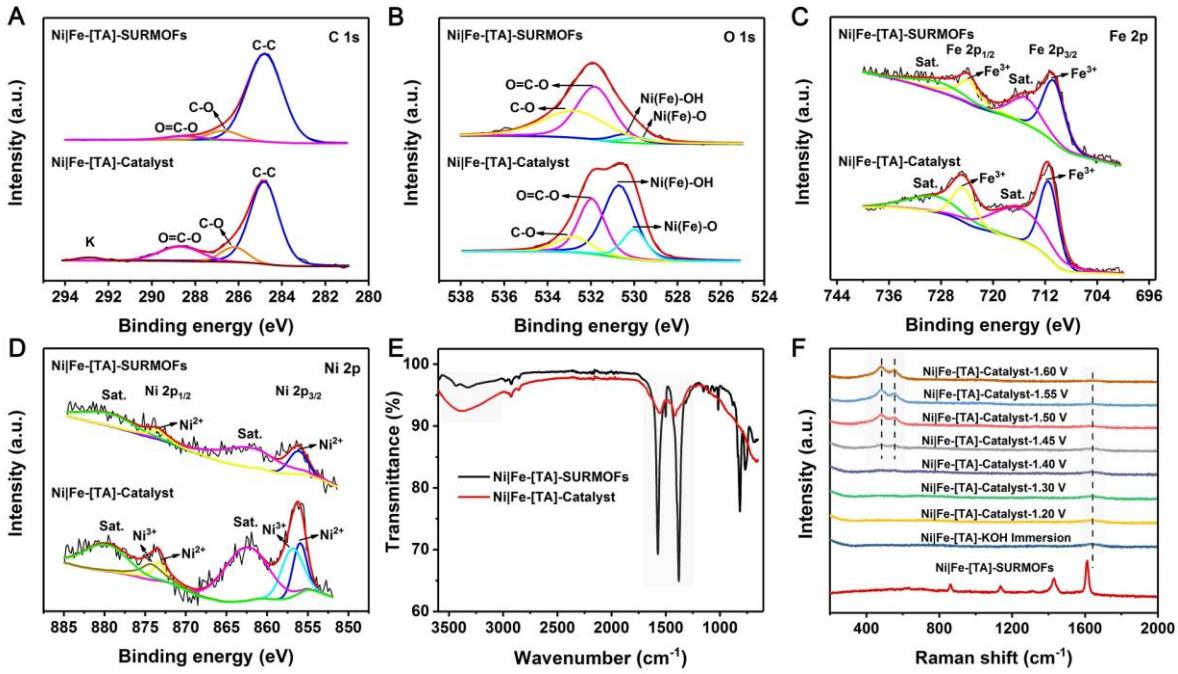

Figure 4.10. *Spectral characterizations. (A-D) High-resolution XPS spectra of C 1s, O 1s, Fe 2p, and Ni 2p for Ni|Fe-[TA]-SURMOFs and Ni|Fe-[TA]-Catalyst. (E) ATR-FTIR spectra for Ni|Fe-[TA]-SURMOFs and Ni|Fe-[TA]-Catalyst. (F) In-situ Raman spectra for the study of structural transformation during the immersion and OER processes.*

In **Figures 4.10E**, **6.9E**, and **6.10E**, the ATR-FTIR spectra provide further insight into the transformation mechanism. In the pristine Ni-Fe-[TA]-SURMOFs, two peaks located at 1571 cm^{-1} and 1378 cm^{-1} are observed, which are attributed to the asymmetric stretching and symmetric stretching vibrations of the carboxyl group, respectively.[71,187,216] The wavenumber of the two peaks demonstrates the coordination bonds between $[TA]^{2-}$ ligands and metal ions in SURMOFs. However, the intensity of these characteristic peaks dramatically decreases after the OER testing, indicating the dissociation of coordination bonds and partial leaching of organic ligands. Note that the existence of residual $[TA]^{2-}$ can also be detected by these faint FTIR peaks. In addition, a broad peak appeared in a range of 3000-3550 cm^{-1} can be found, which is attributed to the O-H stretching vibration of water molecules.[226]

Table 4.4. O 1s binding energies and peak area ratios of the oxygen-containing functional groups in all samples.

Sample	Surface groups							
	C-O		O=C-O		Ni(Fe)-OH		Ni(Fe)-O	
	Peak (eV)	Area (%)	Peak (eV)	Area (%)	Peak (eV)	Area (%)	Peak (eV)	Area (%)
Ni|Fe-[TA]-SURMOFs	532.73	42.87	531.81	47.93	530.42	5.50	529.83	3.70
Ni|Fe-[TA]-Catalyst	532.79	10.83	531.96	29.20	530.69	45.71	529.70	14.26
NiFe-[TA]-SURMOFs	532.41	25.79	531.53	44.16	530.60	11.52	529.89	18.53
NiFe-[TA]-Catalyst	532.83	7.96	532.05	15.16	530.94	41.96	529.82	34.92
Fe|Ni-[TA] -SURMOFs	533.44	32.51	532.03	46.76	531.09	17.48	529.96	3.26
Fe|Ni-[TA]-Catalyst	532.55	8.63	531.61	12.85	530.93	56.17	529.98	22.35

Table 4.5. XPS binding energies, peak areas, and atomic ratios of Ni $2p_{2/3}$ at different valences in the pristine SURMOFs and the derived electrocatalysts.

Sample	Ni^{2+} $2p_{2/3}$		Ni^{3+} $2p_{2/3}$		Ni^{2+} / Ni^{3+} Atom Ratio
	BE (eV)	Area	BE (eV)	Area	
Ni|Fe-[TA]-SURMOFs	856.76	2093	--	--	--
Ni|Fe-[TA]-Catalyst	856.00	1569	856.96	2304	0.68
NiFe-[TA]-Catalyst	855.82	3755	857.23	3474	1.08

Fe|Ni-[TA]-Catalyst	855.60	105479	857.09	42442	2.49

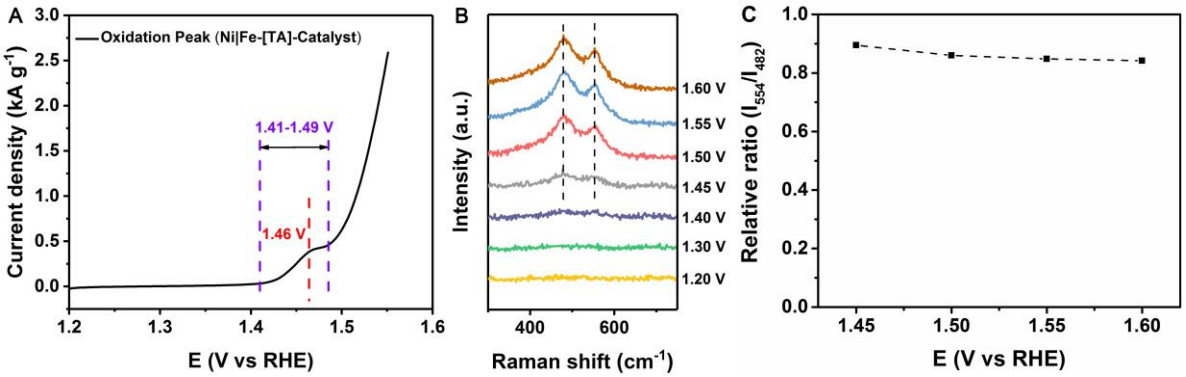

Figure 4.11. *(A) Characteristic anodic polarization curve of Ni|Fe-[TA]-Catalyst. (B) In-situ Raman spectra collected in 0.1 M KOH within a potential region of 1.20-1.60 V vs RHE. (C) The intensity ratio of the Raman peaks at 554 (stretching vibration of Ni−O) and 482 (bending vibration of Ni−O) cm^{-1}. All intensity values were extracted from (B).*

In-situ Raman measurements were performed on the Ni|Fe-[TA]-Catalyst, as shown in **Figures 4.10F** and **11**. Four Raman shift peaks at 1610, 1430, 1140, and 863 cm^{-1} can be detected in the Ni|Fe-[TA]-SURMOFs, corresponding to coordinated organic ligands in the pristine SURMOFs.[75] Subsequently, an alkaline immersion treatment in 0.1 M KOH for 3 min results in the disappearance of these peaks, which indicates the destruction of coordination bonds and the leaching of organic ligands. Moreover, a faint peak appears at ~1637 cm^{-1} representing the uncoordinated carboxylate groups of $[TA]^{2-}$.[216] When the applied potential is increased above 1.40 V *vs* RHE, two distinct Raman peaks can be probed at around 482 and 554 cm^{-1}, corresponding to the bending and stretching vibration modes of the Ni-O bond in NiOOH.[227,228] In comparison with the CV results (*cf.* **Figure 4.11A**), the potential at which the Raman peak appears is strongly related to the generation of Ni species in the high oxidation state. Besides, the Raman spectrum provides access to evaluate the structural disorder in NiOOH according to the intensity ratio of the two Ni-O Raman peaks (I_{554}/I_{482}).[229,230] All values of I_{554}/I_{482} are over 0.84 in the potential range of 1.45-1.60 V *vs* RHE, which suggests that abundant defects present in SURMOF-derived LDH-type catalysts. Indeed, defect engineering is an efficient approach to tuning the catalytic performance and controlling the structure of active sites.

4.1.6 Assessment of Derived Catalysts by Means of Electroactive Surface Area and Apparent Activation Energy

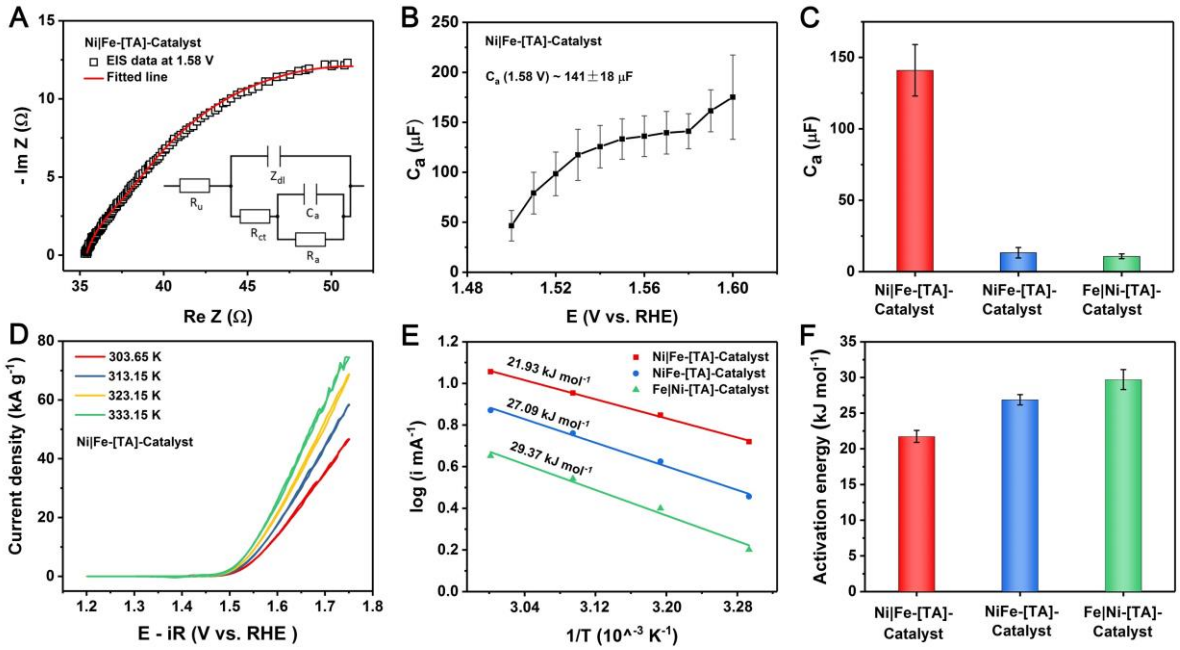

Figure 4.12. *(A) Electrochemical impedance spectrum of Ni|Fe-[TA]-Catalyst collected at the potential of 1.58 V vs RHE. These square points represent measured impedance values, while the fitted data (red line) was obtained according to the equivalent electric circuit shown in the inset. (B) Adsorption capacitances of the Ni|Fe-[TA]-Catalyst electrode as a function of the electrode potentials. (C) Comparison of the adsorption capacitances for three Catalysts. (D) CV curves of the Ni|Fe-[TA]-Catalyst electrode measured at different temperatures. (E) Arrhenius plots showing the exchange current as a function of the inverse of temperature. The calculation details refer to* ***Equation (3.4)*** *in* ***section 3.3*** *and the slop values in (E) represent the activation energy. (F) The calculated activation energy of the three Catalysts. All error bars were obtained from multiple parallel experiments.*

The electrochemical active surface area (ECSA) is a critical parameter to gauge the performance of the catalyst. There are some methods available to determine the ECSA, such as hydrogen underpotential deposition (HUPD), CO stripping, double layer capacitance, Brunauer–Emmett–Teller (BET), and electrochemical impedance spectroscopy (EIS).[173] However, quick and accurate assessment of the ECSA of electrocatalysts remains a challenging task because of the complexity of the research object and the limitations of the assessment methods. For instance, the ECSA can be measured by cycling the electrode in the non-Faradaic regions, in which no charge-transfer reactions occur. Still, absorption and desorption processes can take place. It is important to keep in mind that not all electrochemically active sites are

catalytically active, and inactive porous species can dramatically contribute to the whole double layer capacitance. In this work, the adsorption capacitances obtained from the impedance measurements were used to accurately determine the ECSA, which has been extensively verified by a series of Ni-, Co-, Fe-, Pt-, and Ir-based oxides in previous work.[231] This technique takes advantage of reversibly adsorbed OER reaction intermediates, which can be probed through so-called adsorption capacitance from the equivalent electric circuit (EEC). As shown in the inset of **Figure 4.12A**, the EEC, also known as Armstrong-Henderson EEC, consists of the electrolyte resistance (R_s), a double layer impedance (Z_{dl}), a charge transfer resistance (R_{ct}), adsorption resistance (R_a), and the adsorption capacitance (C_a).[232,233] For more details on the impedance measurements, please refer to **section 3.3**. **Figure 4.12A** shows a representative Nyquist plot, which was measured at 1.58 V *vs* RHE and fitted by the EEC model. Similarly, all Nyquist plots obtained in the potential range of 1.50-1.60 V *vs* RHE were fitted, and the corresponding adsorption capacitances were extracted from the fitted results, as shown in **Figure 4.12B**. Remarkably, it can be noticed that C_a increases with increasing potential, indicating a gradual activation of the catalytic active centers and exposure of more active sites. At 1.58 V, most of the catalytic sites become active, and C_a reaches a plateau. Afterward, the adsorption capacitance is divided by the specific adsorption capacitance (C_a'), which is taken from the literature (C_a' of NiFe @ 1.58 V: ~435 µF cm^{-2}).[231] According to the relation $C_a' = C_a/ECSA$, an ECSA of ~0.32 cm^2 is gained.[231] This value is ~1.7 times the geometric surface area of the electrode (0.196 cm^2), which indicates that the derived Ni|Fe-[TA]-Catalyst intrinsically owns abundant active sites. By contrast, Fe|Ni-[TA]-Catalyst and NiFe-[TA]-Catalyst show much lower C_a values, as can be seen in **Figure 4.12C**. The ECSA results clarify the strong correlation between the number of active sites and the catalytic activity.

In addition, to further quantify the intrinsic electrocatalytic performance of the derived catalysts, the investigation of apparent activation energy provides another means by OER measurements at different temperatures. For example, the CV curves of Ni|Fe-[TA]-Catalyst electrode were collected at 303.65, 313.15, 323.15, and 333.15 K, respectively. The temperature rises cause an increase in current density, as shown in **Figure 4.12D**. Based on the Arrhenius equation $\frac{\partial \log i}{\partial \frac{1}{T}} = -\frac{E_a}{2.3R}$, the related current plots extracted from the low current region for each catalyst show a linear relationship with the reciprocal of temperature, where the slope of the Arrhenius plot represents their apparent activation energy.[174] In **Figure 4.12F**, Ni|Fe-[TA]-Catalyst displays

the lowest average apparent activation energy (E_a = ~21.73 kJ mol^{-1}), indicating the superb OER reaction kinetics, while the higher E_a values are observed in NiFe-[TA]-Catalyst (~26.88 kJ mol^{-1}) and Fe|Ni-[TA]-Catalyst (~29.70 kJ mol^{-1}).

4.1.7 A Long-Term Stability Study

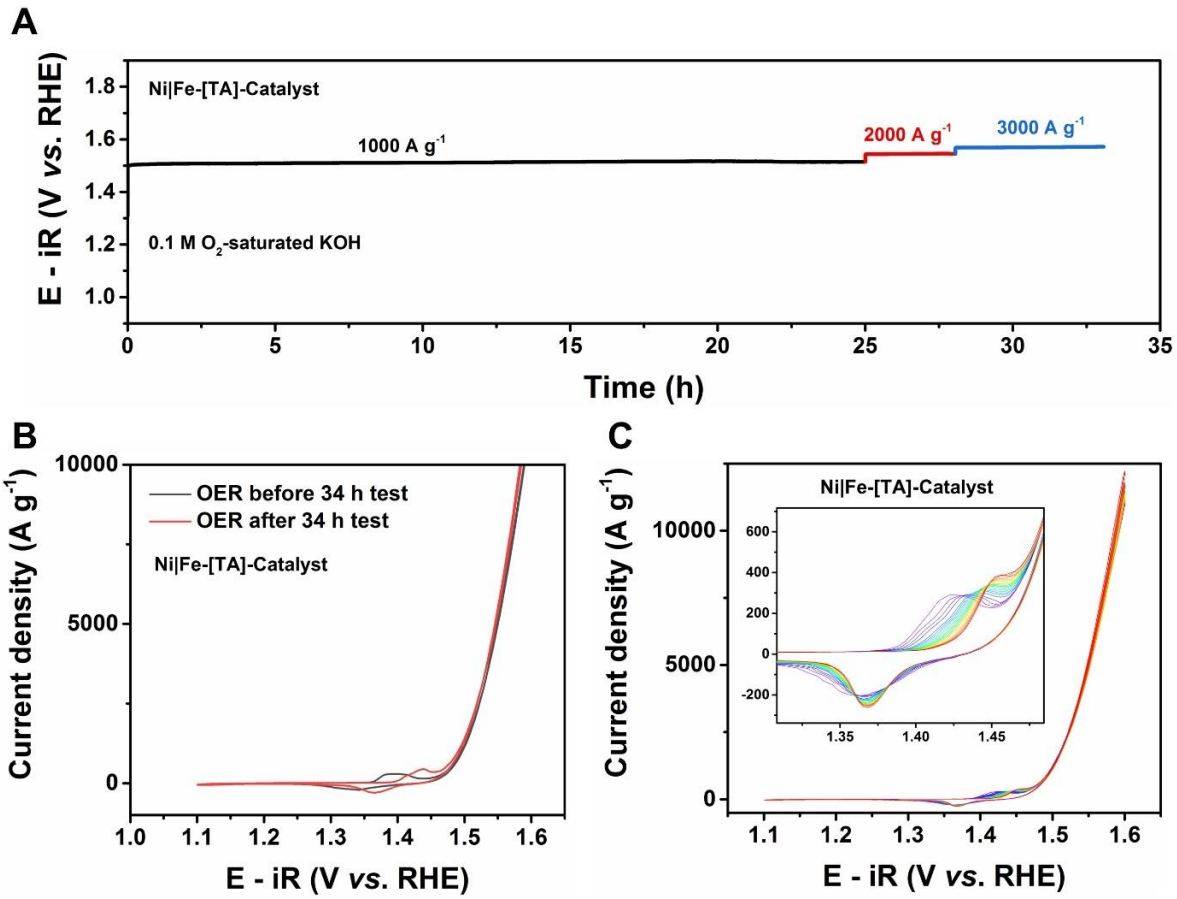

Figure 4.13. *(A) Catalytic stability test on Ni|Fe-[TA]-Catalyst at current densities of 1000, 2000, and 3000 A g^{-1} in O_2-saturated 0.1 M KOH. (B) Comparison of CV curves before and after a 34 hours chronopotentiometry measurement. (C) Long-term CV cyclings recorded with a scan rate of 5 mV s^{-1} for 400 cycles. Enlarged redox peaks were shown in the insert.*

The stability of the derived electrocatalysts and their properties after the long-term measurement were investigated; and the results are shown in **Figures 4.13** and **4.14**. The Ni|Fe-[TA]-Catalyst was initially obtained after the SURMOFs metamorphosis. Then, chronopotentiometry experiments were performed at three current densities of 1.0 kA g^{-1}, 2.0 kA g^{-1}, and 3.0 kA g^{-1} for more than 34 hours. Note that outstanding long-term stability was found based on the negligible degradation of the polarization curve. Moreover, the redox peaks

of Ni^{2+}/Ni^{3+} show dramatic differences before and after the long-term chronopotentiometry experiments. The positive shift for the oxidation peak is attributed to the aging process.[230] To further reveal the aging process of the Ni|Fe-[TA]-Catalyst, the durability was also examined *via* CVs (*cf.* **Figure 4.13C**). A gradual positive shift for the oxidation peak can be clearly seen during the 400-cycle measurement. Meanwhile, the OER current density exhibits a slight increase compared to that in the first cycle. Subsequently, the properties of the Ni|Fe-[TA]-Catalyst after the long-term measurement were studied by the SEM, XRD, Raman, and XPS characterizations. The interconnected nanofiber networks can be maintained compared to the morphology observed after electrochemical activation (*cf.* **Figure 4.7D**), suggesting excellent structural stability. However, no distinct XRD peak is still present in the GIXRD pattern. *Ex-situ* Raman spectrum clarifies the Ni-O vibrations of the NiOOH by two peaks at around 478 and 545 cm^{-1}. Based on the XPS spectra, the residual ligands and abundant metal (oxy)hydroxides can be determined. These characterizations provide sufficient evidence to elucidate the outstanding structural and catalytic stability of the SURMOF derivatives.

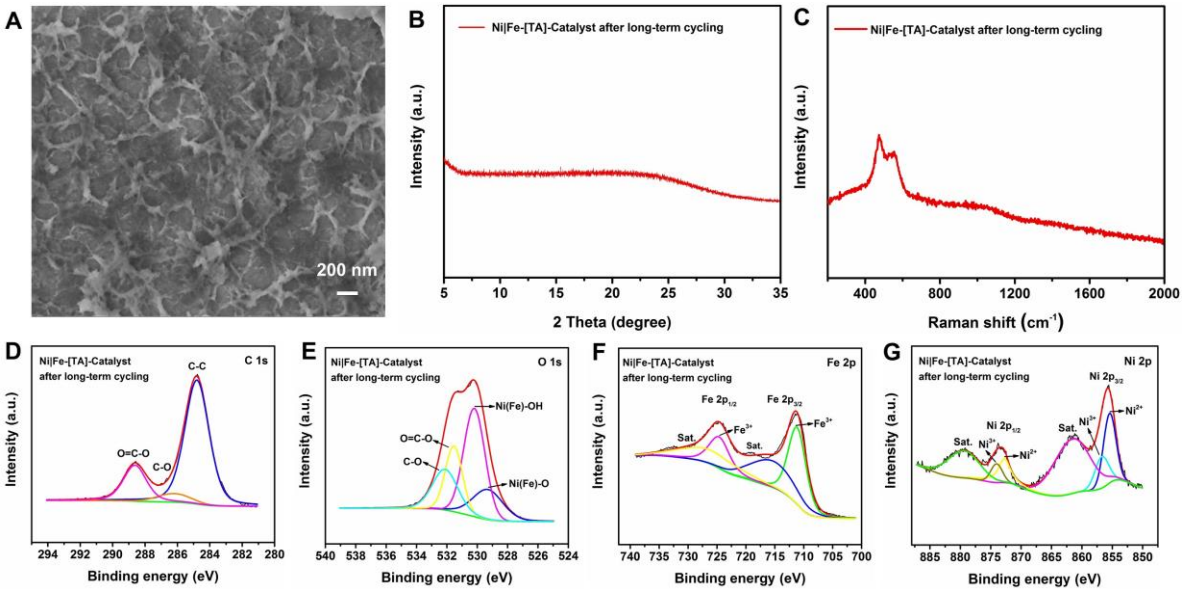

Figure 4.14. *(A) Morphological characterization for the Ni|Fe-[TA]-Catalyst electrode after the 34 hours catalytic stability test. GIXRD data (B) Raman spectrum (C), and XPS spectra (D-G) of the Ni|Fe-[TA]-Catalyst after long-term cycling.*

4.2 Elucidating the Cation Effects on Electrocatalytic Oxygen Evolution Reaction Activities of SURMOF Derivatives

Following the last work, a deep understanding of the reaction mechanisms of SURMOF derived NiFe(OOH) electrocatalyst at the electrified electrode/electrolyte interface is expounded in this part. The key objective is to reveal the impact of alkali metal cations (*i.e.*, Li^+, Na^+, K^+, and Cs^+) on the oxygen evolution reaction (OER) activities of SURMOF derivatives by the advanced *in-situ* Raman and LICT techniques.

This part is based on the following publication:

S. Hou, L. Xu, X. Ding, R. M. Kluge, T. K. Sarpey, R. W. Haid, B. Garlyyev, S. Mukherjee, J. Warnan, M. Koch, S. Zhang, W. Li, A. S. Bandarenka, R. A. Fischer, Dual In-situ Laser Techniques Underpin the Role of Cations in Impacting Electrocatalysts. *Angewandte Chemie International Edition* 2022, accepted, https://doi.org/10.1002/ange.202201610.

4.2.1 Motivation

In the last section, the catalytic species as NiFe (oxy)hydroxide in the SURMOF derivatives were identified, and a more detailed understanding of the structural transformation mechanisms and the structure-performance relationships was provided. The derived NiFe (oxy)hydroxides show a unique crystalline-amorphous phase, a large electroactive surface area, and low apparent activation energy. We found that the NiFe (oxy)hydroxides obtained by the SURMOFs strategy manifest an unprecedented high oxygen evolution activity. This conceptual approach of applying SURMOFs as precursors for advanced catalyst fabrication differs from other reported NiFe-based MOFs. Despite many MOFs, at least the carboxylate-based MOFs, can be (long-term) unstable under alkaline conditions, numerous papers still reported them as working electrocatalysts and investigated the catalytic mechanisms based on the MOF structures.[53,148] The SURMOFs strategy demonstrates how to use this intrinsic liability as a particular advantage. Instead of aiming to overcome the instability issue in aqueous media, this property is used to derive high-performing NiFe (oxy)hydroxide-type electrocatalysts.

In addition, understanding the electrode/electrolyte interface processes is essential to optimize the performance of electrocatalytic systems such as electrolyzers, fuel cells, or metal-air batteries.[234,235,236] However, the chemistry at the surface of the SURMOF-derived catalysts during the OER process remains enigmatic. It has been reported that non-covalent interactions between hydrated cations in the electrolyte and adsorbed reactants or reaction intermediates at the electrified electrode/electrolyte interface can occur and further significantly affect the OER activity.[237,238] The activity is usually proportional to the cation size, and differences in cation size can also be expressed in terms of the hydration energies, electronegativities, and Lewis acidities.[239,240,241] Nonetheless, some reoccurring discrepancies make the above rule less plausible. For example, Michael and co-workers[242] indicated that the activity of NiOOH in purified electrolytes follows a trend of $Cs^+ > K^+ \approx Na^+ \approx Li^+$. Garcia and co-workers[233] pointed out a different trend in the cation enhancement effect on the OER activity of NiOOH, *i.e.*, $Cs^+ > Na^+ > K^+ > Li^+$. Hence, it is essential to investigate the deeper interfacial mechanisms. Furthermore, in the alkali metal group, smaller cations with high electronegativity significantly affect the hydration shell layer and interfacial water structure through stronger non-covalent interactions. Yet, the knowledge about the cation effect on the EDL structure is still limited.

Hence, the effect of the nature of cationic species in the electrolyte on the oxygen evolution reaction (OER) activity of SURMOF derivatives was studied. Several *in-situ* techniques, such as *in-situ* Raman spectroscopic experiments and a profound methodology called laser-induced current transient technique, were carried out to reveal the reaction kinetics at the electrified electrode/electrolyte interface.

4.2.2 Fundamental Characterization of the Transformation Mechanism of SURMOFs

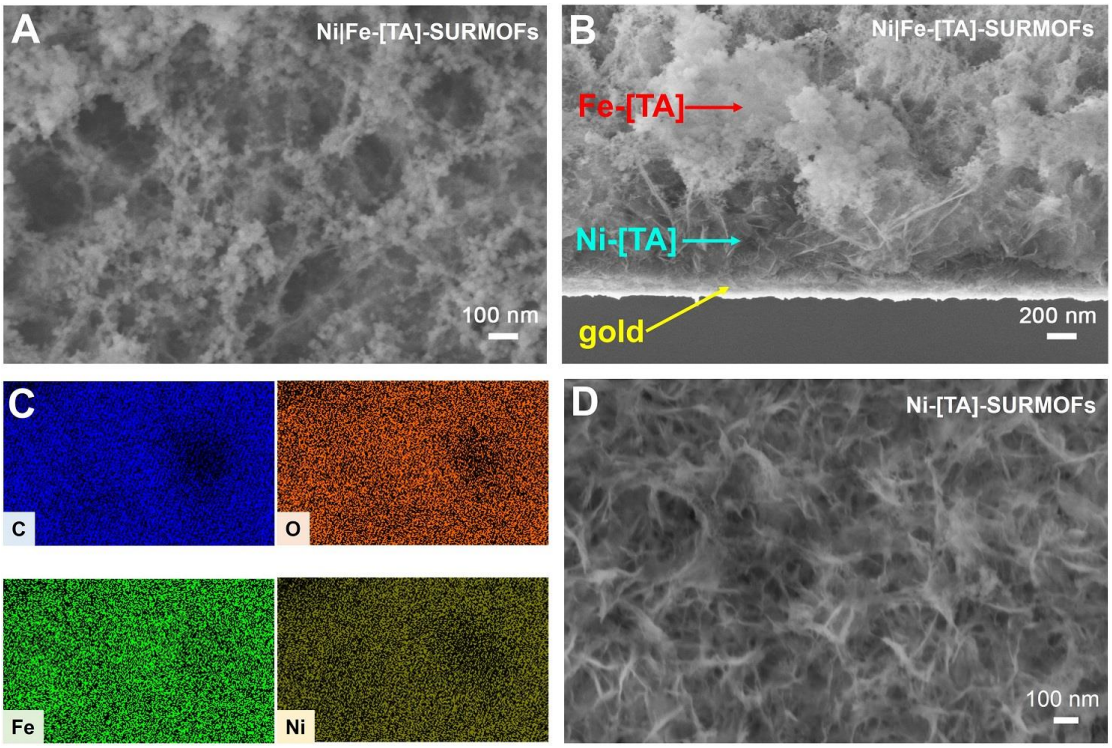

Figure 4.15. *Morphological characterization for the Ni|Fe-[TA]-SURMOFs: top-view (A) and cross-section (B) SEM images. (C) EDS mapping images of C, O, Fe, and Ni in the Ni|Fe-[TA]-SURMOFs. (D) SEM image of the Ni-[TA]-SURMOFs (45 layers) growth on the gold QCM electrode.*

In **Figure 4.15A** and **B**, the top-view and cross-section SEM images reveal the heterostructure in the Ni|Fe-[TA]-SURMOFs due to the two different morphological species. Moreover, the stronger signal intensity of Fe species can be observed in energy dispersive spectroscopy (EDS) mapping images (*cf.* **Figure 4.15C**) compared to that of Ni. According to the morphology of Ni-[TA]-SURMOFs in **Figure 4.15D**, it can be inferred that in the heterostructured SURMOFs, the nanosheets in the bottom layer correspond to Ni-[TA], and the nanoparticles in the surface layer represent Fe-[TA]. However, the heterostructure of Ni|Fe-[TA]-SURMOFs was decomposed and transformed into hierarchical network morphologies after the alkaline

hydrolysis and electrochemical treatments in MOH (M^+ = Li^+, Na^+, K^+, Cs^+). The similar SEM images observed in **Figure 4.16** indicate that the effect of alkaline electrolytes on the surface morphology of the derived catalysts is negligible.

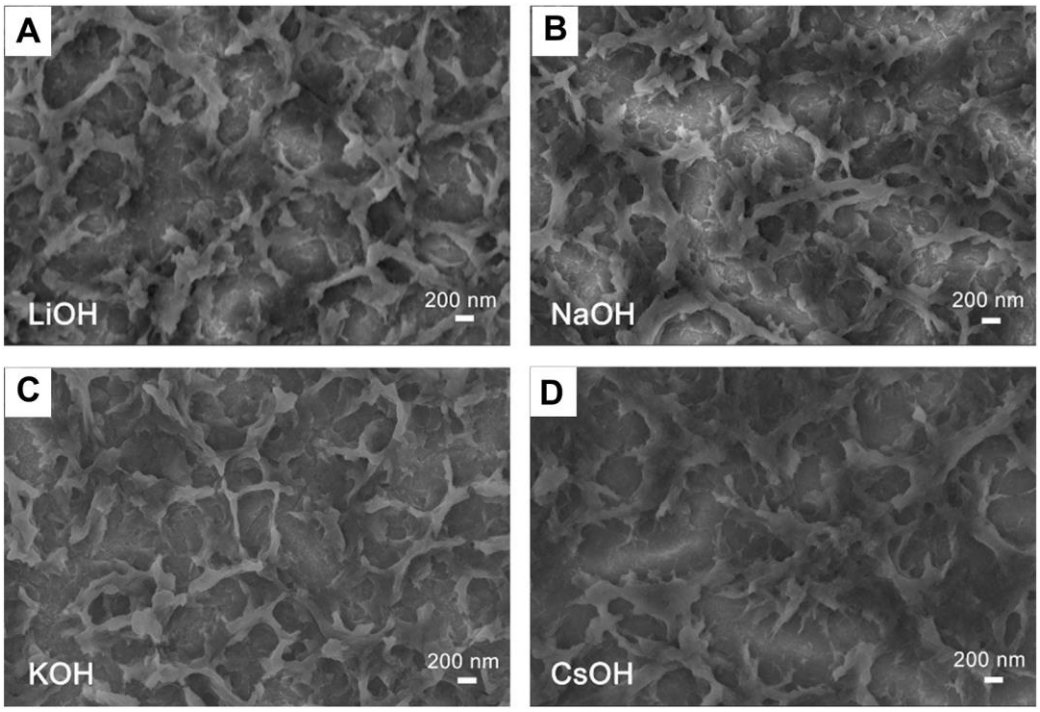

Figure 4.16. *Morphological characterization for the Catalyst samples obtained after the OER tests in various alkaline electrolytes (0.1 M LiOH (A), NaOH (B), KOH (C), and CsOH (D)).*

In addition, the GIXRD was used to monitor the changes in the crystalline structure. In **Figure 6.12**, a pronounced peak can be observed in the as-prepared SURMOFs, which matches well with the simulated XRD pattern of the Ni-[TA].[69] At the same time, it disappeared after the electrochemical activation in the presence of different alkali metal cations, indicating a crystalline phase transformation of the SURMOFs into the amorphous structure. XPS was conducted on all samples to investigate further the discrepancies between the pristine SURMOFs and the derived catalysts, as shown in **Figure 4.17**. The existence of organic ligands in both pristine SURMOFs and the derived catalysts can be determined by the characteristic peaks of C=C, C-C, C=O, and O-C=O bonds in high-resolution XPS spectra of C 1s.[216] The O 1s spectra can be resolved into four peaks, corresponding to the O=C-O group, C-O bonds, Ni(Fe)-oxygen bonds, and Ni(Fe)-hydroxyl species, respectively.[218] Note that the relative contents of organic groups (O=C-O group and C-O bonds) dramatically decreased after OER, while for the Ni(Fe)-oxygen bonds and Ni(Fe)-hydroxyl species, an opposite trend was observed in the derived catalysts (*cf.* **Figure 4.17B** and **Table 4.6**). The results reveal the

leaching of most organic ligands and the generation of NiFe(oxy)hydroxide species during the transformation process. Interestingly, there are two prominent peaks in the Ni 2p spectrum (*cf.* **Figure 4.17D**) of SURMOFs at *ca.* 856.56 and *ca.* 874.47 eV, corresponding to the Ni^{2+} species in Ni $2p_{3/2}$ and Ni $2p_{1/2}$, respectively. However, two distinct peaks that appeared at a higher binding energy of *ca.* 857 eV and *ca.* 873 eV in the derived catalysts are attributed to the newly generated high-oxidation state Ni species.[224] All the XPS results confirmed our hypothesis that the pristine SURMOFs would transform to the NiFe(oxy)hydroxide species in various electrolytes after the electrochemical cycling.

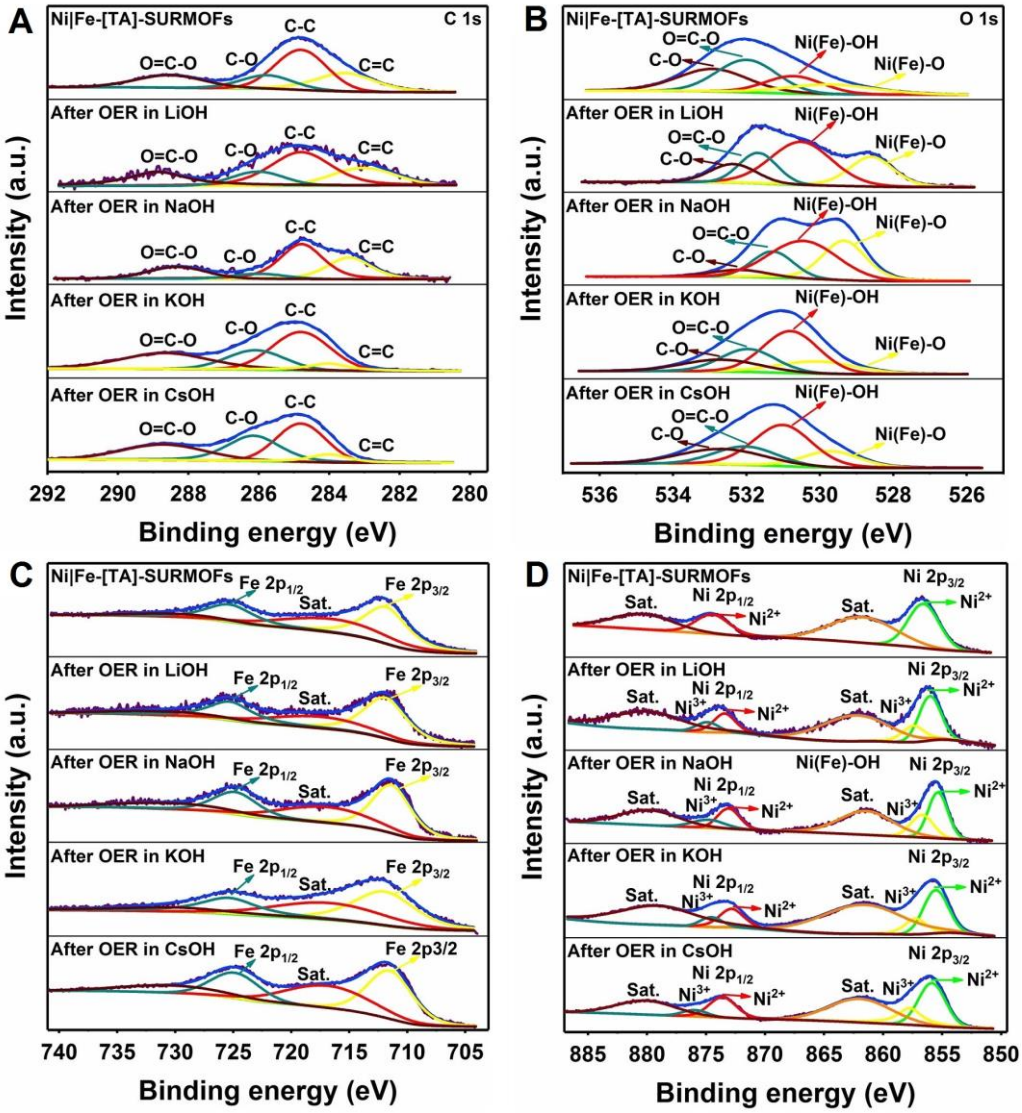

Figure 4.17. *High-resolution XPS showing the comparisons of C 1s, O 1s, Fe 2p, and Ni 2p spectra in the pristine Ni|Fe-[TA]-SURMOFs and these Catalyst thin films after the electrochemical cycling in different electrolytes.*

Table 4.6. XPS binding energies and peak area ratios of O 1s for Ni|Fe-[TA]-Catalysts in different electrolytes.

Samples	Surface groups							
	C-O		O=C-O		Ni(Fe)-OH		Ni(Fe)-O	
	Peak (eV)	Area (%)	Peak (eV)	Area (%)	Peak (eV)	Area (%)	Peak (eV)	Area (%)
Ni|Fe-[TA]-SURMOFs	532.91	30.6	531.99	34.7	530.72	18.5	529.72	16.2
Ni|Fe-[TA]-Catalyst in LiOH	532.36	13.7	531.68	18.5	530.51	44.4	528.60	23.4
Ni|Fe-[TA]-Catalyst in NaOH	532.19	6.4	531.28	18.0	530.46	43.3	529.34	32.3
Ni|Fe-[TA]-Catalyst in KOH	532.69	16.3	531.95	22.9	530.80	42.5	530.08	18.3
Ni|Fe-[TA]-Catalyst in CsOH	532.65	21.8	532.02	19.3	531.01	42.3	529.69	16.6

4.2.3 Electrochemical Characterization and Stability

To unravel the electrolyte cation effect on the oxygen evolution activity, the SURMOF electrodes were initially activated by CV cycling in different cationic electrolytes at a high scan rate of 20 mV s^{-1}. As shown in **Figure 4.18**, there is a distinguishable redox couple peak, reflecting a reversible redox transition between Ni^{2+} and Ni^{3+} species.[114,212] An increase in the faradaic current can be observed with the increasing number of cycles. Afterward, both the Ni^{2+}/Ni^{3+} redox peak and OER current density become stabilized. This result indicates that the transformation of SURMOFs into the metal (oxy)hydroxides is almost completed after the electrochemical activation treatment. Moreover, the oxygen evolution current densities measured at 1.54 V *vs* RHE in 0.1 M MOH (M^+ = Li^+, Na^+, K^+, Cs^+) electrolytes closely correlate with the cations. The highest current density is obtained in 0.1 M CsOH, while the SURMOF derivative demonstrates the lowest OER activity in 0.1 M LiOH. More details regarding the cation effect on the catalytic activity will be discussed in the OER testing results.

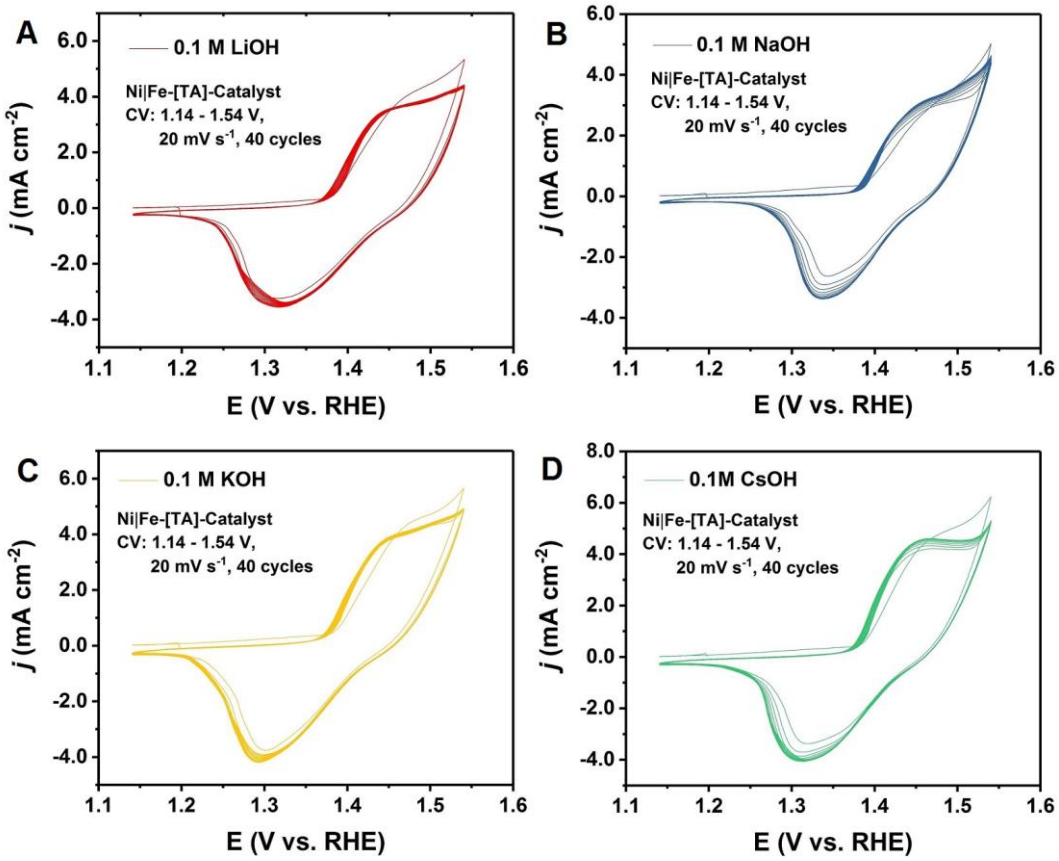

Figure 4.18. *The electrochemical activation of Ni|Fe-[TA]-SURMOF precatalysts in the presence of various cations at a scan rate of 20 mV s^{-1} for 40 cycles within a potential range of 1.14-1.54 V vs RHE.*

In **Figure 4.19A**, the OER activity of the Ni|Fe-[TA]-Catalyst was evaluated in the presence of various cations at a slow scan rate of 5 mV s^{-1}. All OER polarization curves were normalized according to the mass loading of the catalysts on the QCM electrode to accurately assess and compare the intrinsic electrocatalytic activity. The significant performance discrepancy can be seen intuitively in **Figure 4.19A** and **C**. The OER current densities obtained at overpotential η = 300 mV increase in the order of LiOH (~360 A g^{-1}), NaOH (~602 A g^{-1}), KOH (~701 A g^{-1}), and CsOH (~802 A g^{-1}), which exactly follow the size of the cations. Similarly, the corresponding Tafel slopes show an opposite trend to the mass activity (*cf.* **Figure 4.19B**): Li^+ (~96 mV dec^{-1}) > Na^+ (~79 mV dec^{-1}) > K^+ (~78 mV dec^{-1}) > Cs^+ (~72 mV dec^{-1}). According to the literature, the enhancement effect of cations can be achieved through the interaction of hydrated alkali metal cations with the OH species adsorbed at the catalyst interface in the form of OH_{ad}-$M^+(H_2O)_n$ or OH_{ad}-(H_2O)-$M^+(H_2O)_n$.[237] The interaction directly correlates with the hydration energies of metal ions. The smaller cations with higher electronegativities exhibit higher hydration energy, leading to stronger interactions with the electrode surface. As shown

in **Figure 4.19D**, the OER electrocatalytic activities at both 1.53 and 1.63 V *vs* RHE increase linearly with the decreasing hydration energies from Li^+ to Cs^+. The strong interaction with the catalyst surface would restrict some reactants from reaching the active sites, thus resulting in low activity.

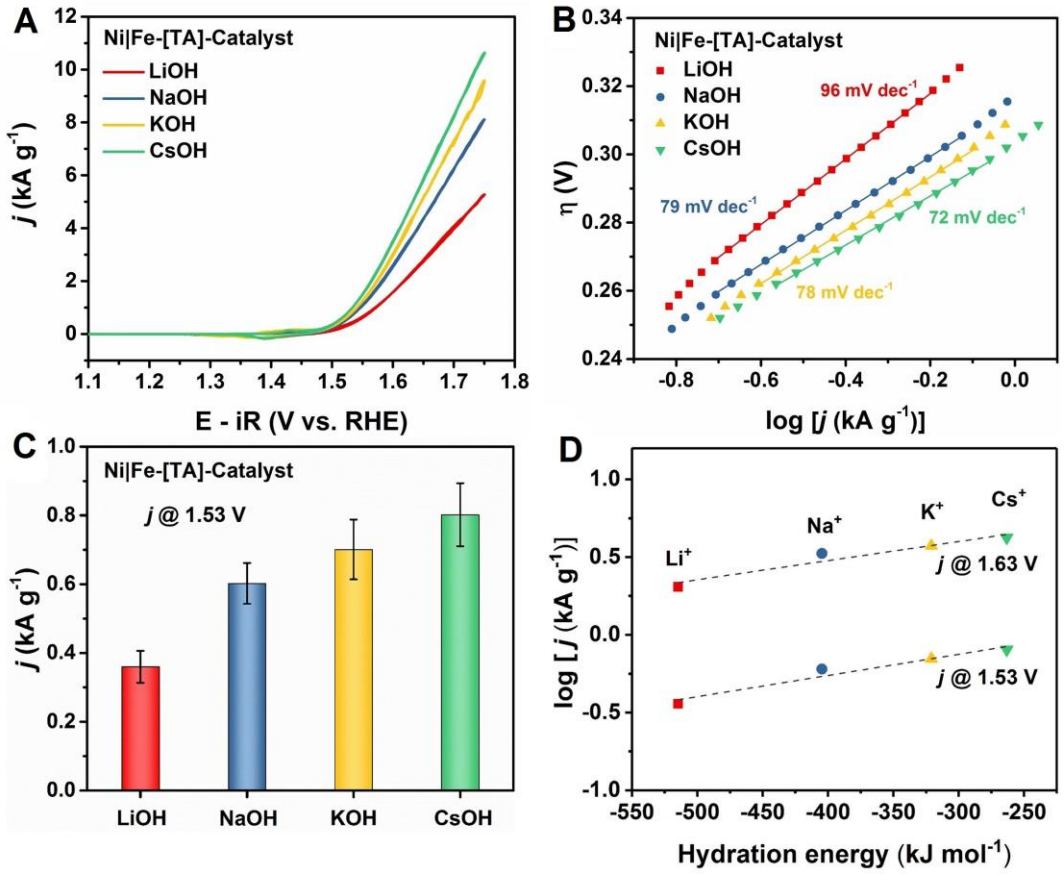

Figure 4.19. *(A) Typical OER polarization curves of the Ni|Fe-[TA]-Catalyst measured in 0.1 M O_2-saturated MOH (M^+ = Li^+, Na^+, K^+, Cs^+) with a scan rate of 5 mV s^{-1}. (B) The corresponding Tafel plots of the presented data in (A). (C) The mass activities of the Ni|Fe-[TA]-Catalyst in the presence of various cations. (D) Linear relationships between the alkali metal cation hydration energies and the electrochemical activities obtained at 1.53 and 1.63 V vs RHE.*

Stability tests were conducted to evaluate the property of the SURMOF-derived catalysts in the presence of different cations, as shown in **Figure 4.20**. A much higher overpotential can be achieved at a current density of 10 mA cm^{-2} in 0.1 M LiOH compared to other cations. The lowest overpotential is found for 0.1 M CsOH. It is worth noting that all chronopotentiometry curves show outstanding long-term stability, which highlights the robust nature of SURMOF-derived catalysts.

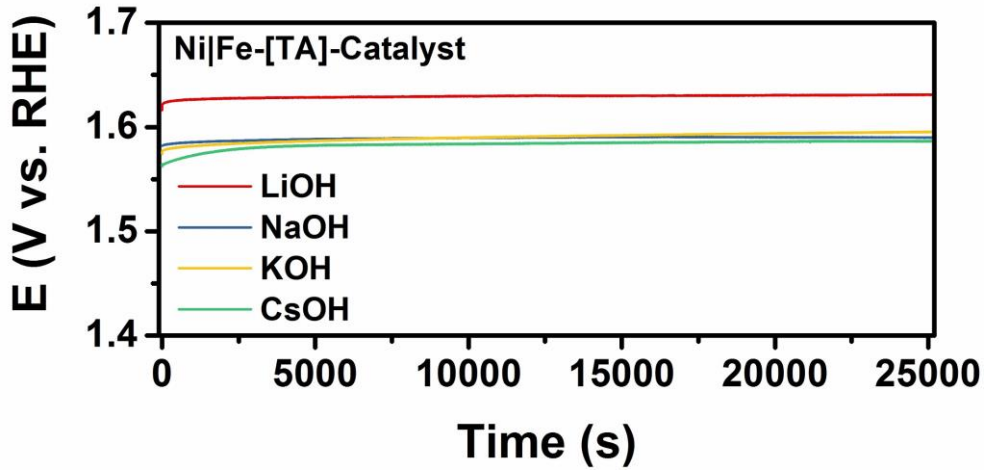

Figure 4.20. *Chronopotentiometry curves for the study of stability on the Ni|Fe-[TA]-Catalyst in different electrolytes. All tests were performed with a constant current density of 10 mA cm^{-2}.*

4.2.4 Investigating Cation Effects by *in-situ* Raman Spectroscopy

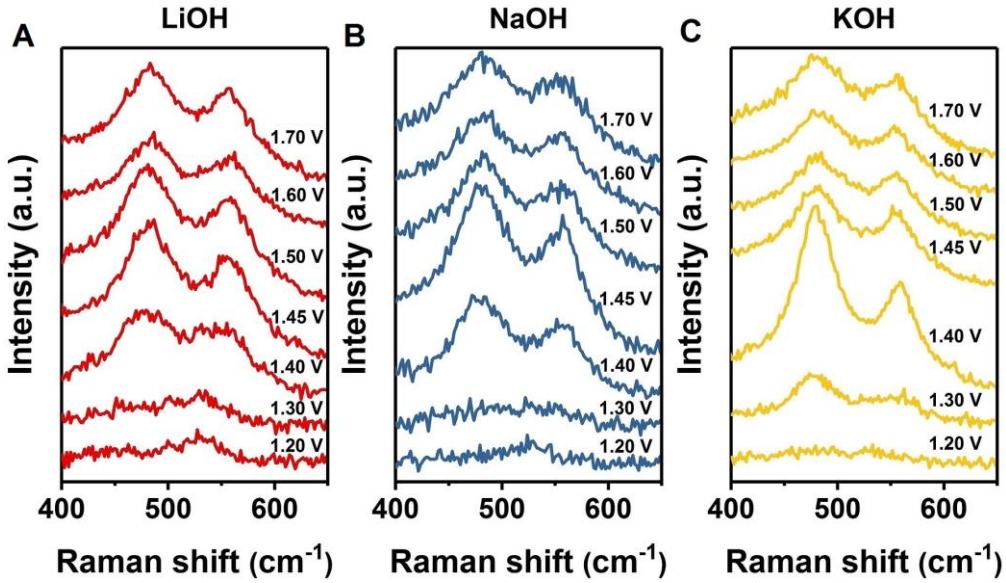

Figure 4.21. *In-situ Raman spectra of the Ni|Fe-[TA]-Catalyst electrode recorded in 0.1 M LiOH (A), NaOH (B), and KOH (C) under different applied potentials from 1.20 to 1.70 V vs RHE.*

To gain deeper insight into the reason underlying these changes, a potential-dependent *in-situ* Raman spectroscopic technique was used to investigate the cation effect and the variations in the chemical structure of the SURMOFs and derived catalysts. The *in-situ* Raman spectrum was recorded in two wavenumber ranges of 400-650 cm^{-1} and 800-1200 cm^{-1}, respectively. **Figures 4.21** and **4.22A** show that two characteristic Raman peaks are probed at around 480 and 560 cm^{-1} when the applied potential increases above 1.4 V *vs* RHE. They correspond to the

bending and stretching vibration modes in NiOOH (in high oxidation states: +3.3 to +3.7), respectively.[229,233,242] To accurately evaluate and compare the Raman shifts in different electrolytes, all Raman spectra collected at 1.70 V *vs* RHE were fitted using the Gaussian functions (*cf.* **Figure 4.22B**). The Raman shift in CsOH appears at about 479.04 and 557.82 cm^{-1}, while the same feature can be observed in LiOH at about 481.32 and 558.39 cm^{-1}, thus indicating a clear positive shift. According to the literature, a longer Ni-O bond in the NiOOH structure can induce a lower Raman shift.[233,242,243] Afterward, the Raman shifts of the bending vibration of the Ni-O bond were extracted from all electrolytes. The cation-dependent Raman shifts for the Ni-O bending from Cs^+ to Li^+ are inversely proportional to the mass activities, as shown in **Figure 4.22C** and **D**. The linear correlation reflects the significant influence of electrolyte components on the OER reaction intermediates. Koper and co-workers reported a similar result of cation-dependent Raman shifts in the NiOOH catalyst.[233] They hypothesized that Cs^+ with the largest ionic size could interact with Ni-OO^- species to form Ni-OO-Cs^+ intermediates and enhance their stability, which leads to a higher catalytic activity.

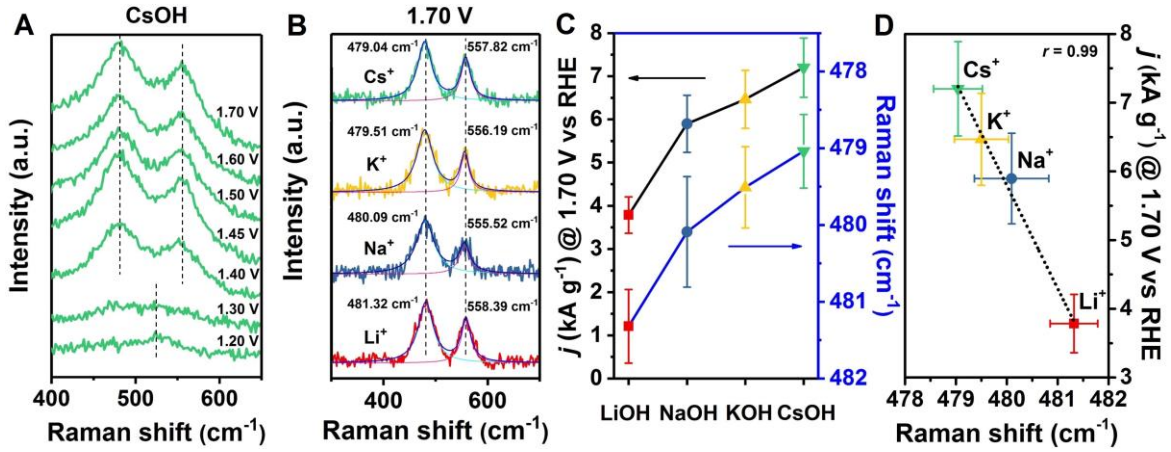

Figure 4.22. *(A) In-situ Raman spectra of the Ni|Fe-[TA]-Catalyst electrode recorded under different applied potentials in 0.1 M CsOH. (B) Corresponding Raman spectra measured at 1.70 V vs RHE in the presence of different cations. All curves were fitted using the Gaussian functions for a more precise peak position. Two well-defined Raman peaks appeared at ~480 and ~560 cm^{-1} correspond to the bending and stretching vibrations of Ni-O, respectively. (C and D) In the presence of different alkali metal cations, the electrocatalytic activities achieved at 1.70 V vs RHE (solid black line in C) as a function of the Raman peaks at ~480 cm^{-1} (solid blue line in C).*

Additionally, a broad Raman peak at 800-1200 cm^{-1} represents the vibration mode of the O-O bond in the reactive oxygen intermediate $NiOO^-$.[228] It can be seen that the signal appears at

potentials above 1.40 V *vs* RHE, and this trend is similar to the bending and stretching vibration modes of NiOOH.

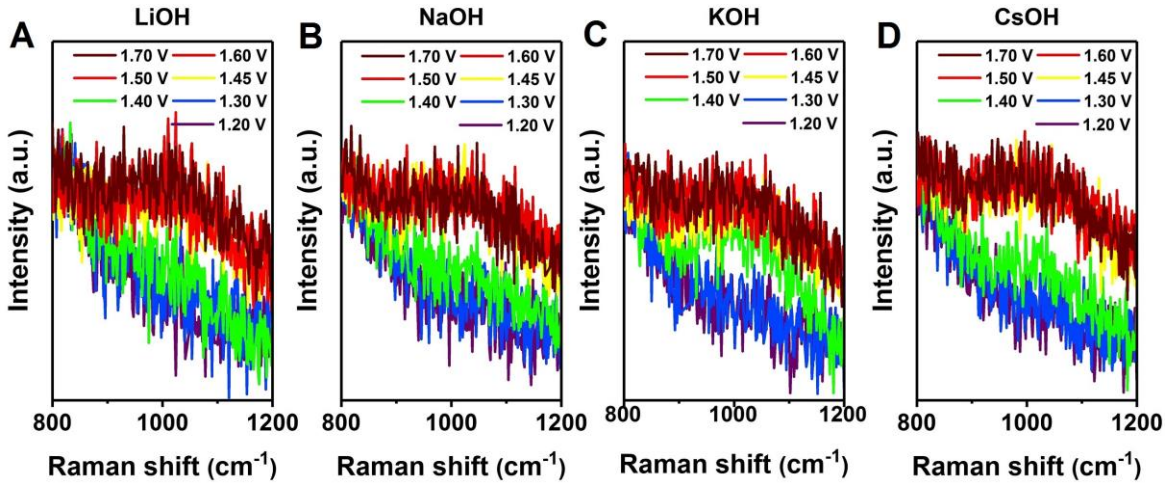

Figure 4.23. *In-situ* Raman spectra of the Ni|Fe-[TA]-Catalyst electrode recorded in 0.1 M MOH electrolytes under various applied potentials from 1.20 to 1.70 V *vs* RHE. The frequency range of the Raman spectra (800-1200 cm^{-1}) represents the active structure OO^{-} in NiOOH.

4.2.5 Probing Cation Effects on the Interfacial Water Layer by the Laser-Induced Current Transient Technique

The LICT technique has recently been explored for *in-situ* analysis of the electrode/electrolyte interface.[163,244,245,246,247] In detail, an Nd:YAG laser, an attenuator, a custom-made cell, a QCM chip fixed in a PTFE holder, and a potentiostat constitute the LICT setup used in this work (*cf.* **Figure 4.24A**). When the laser irradiates the electrode surface, the temperature rapidly increases, which induces a disordered state of the originally well-ordered water dipoles in the EDL. Subsequently, as a result of the rapid relaxation, sharp positive or negative current transients can be expected. Moreover, the degree of order of the interfacial water molecules (rigidity or looseness) can be evaluated by the potential of maximum entropy (PME), which reflects the EDL structure and the interfacial energy barriers.[248,249] In general, the interfacial water molecules are maximally disordered at the PME, whereas moving away from the PME, the network of water molecules in the EDL becomes organized and rigid. Accordingly, at potentials close to the PME, the reactants reach the active sites more easily due to a smaller interfacial energy barrier.[250,251] As shown in **Figures 4.24A** and **4.25**, the extreme values of the sharp positive and negative current transients are obtained by LICT measurements. Based

on the sign of current transients, the orientation of the water dipoles and the excess charge on the electrode surface can be demonstrated. The reason is that the sharp temperature jump after laser pulse irradiation breaks the ordered structure of interfacial water molecules, which results in a current-time plot in the relaxation time frame.[251] As the applied potential increases, the sign of the current transient changes from negative to positive. This indicates that the sign of the net surface charge at the electrode interface is reversed, corresponding to a change in the orientation of the interfacial water molecules. The transition point of the current signal can be represented using the PME at which the interfacial water layer is at its maximum disorder.

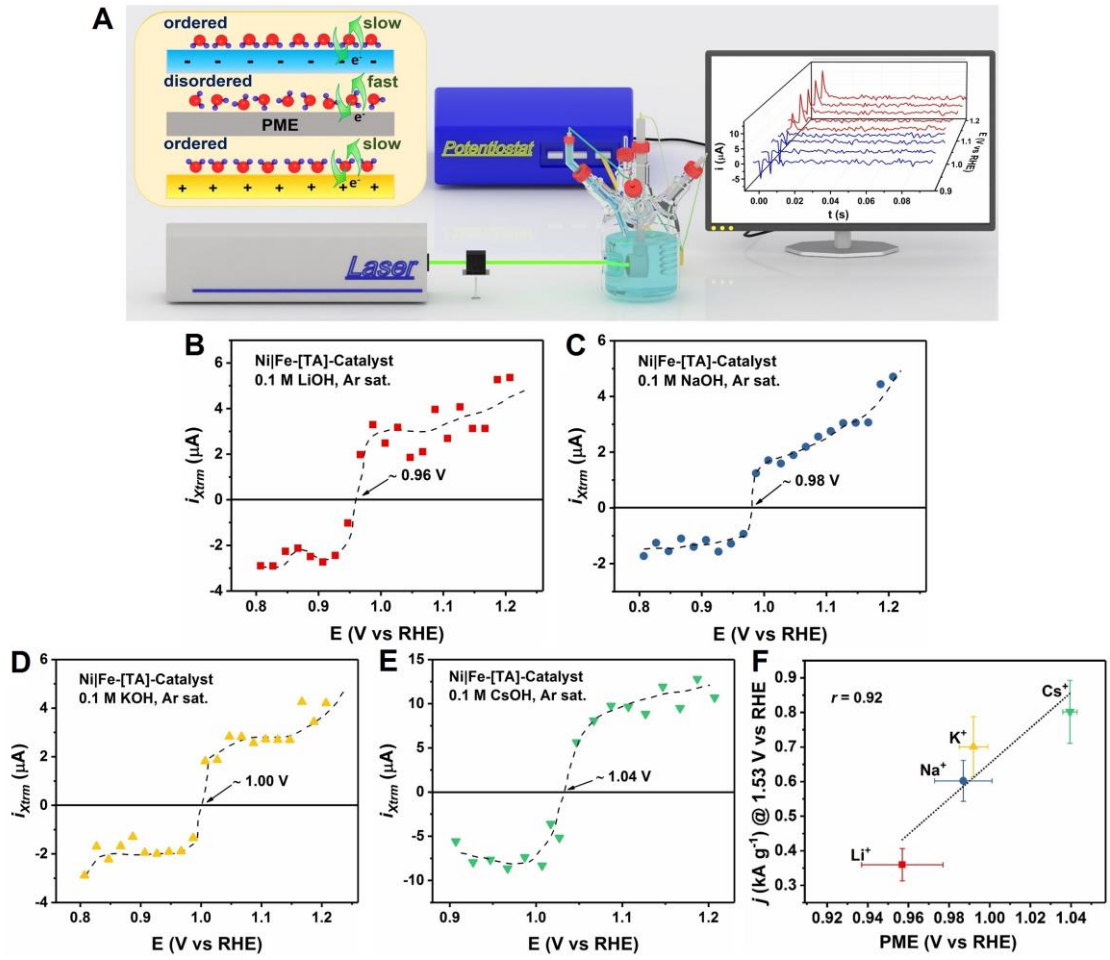

Figure 4.24. *(A) Schematic illustration of the laser-induced current transient (LICT) experiment. The potential of maximum entropy (PME) for the Ni|Fe-[TA]-Catalyst was determined using the LICT setup in Ar-saturated 0.1 M MOH electrolytes. The correlation between the interfacial water layer structure and PME is shown in the inset, indicating the PME as a key descriptor of the maximum disorder for water dipoles. The computer monitor presents the current transient results for the Ni|Fe-[TA]-Catalyst in Ar-saturated 0.1 M CsOH under varying potentials from 0.81 to 1.21 V vs RHE. (B-E) The maximal current transients collected during the LICT measurement under various electrochemical potentials in*

Ar-saturated 0.1 M MOH. (F) The electrocatalytic activities achieved at 1.53 V vs RHE plotted as a function of the PME for the Ni|Fe-[TA]-Catalyst electrode in the presence of different alkali metal cations.

With this in mind, 3D plots of current transients in various electrolytes were collected, as shown in **Figures 4.24A** and **4.25**. All maximal current transients extracted from the 3D plots during the LICT measurement under various electrochemical potentials are presented in **Figure 4.24B-E**. Following the trend of the PME for various electrolytes, the most positive PME value (~1.04 V *vs* RHE) can be obtained in 0.1 M CsOH electrolyte. This result indicates a significant correlation between the PME and the electrolyte composition. Furthermore, a linear dependence of the OER activity on the PME is visible, as shown in **Figure 4.24F**. This suggests that the large Cs^+ cation can alter the degree of order of the interfacial water molecules and further improve the kinetics of the oxygen evolution reaction.

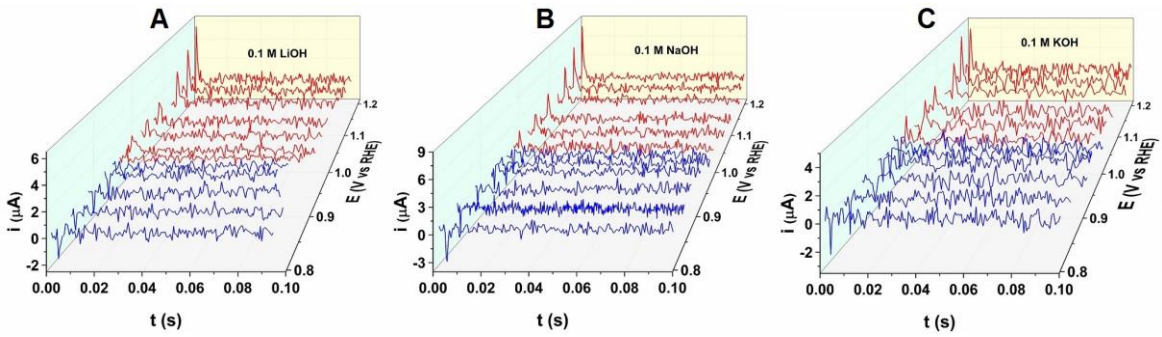

Figure 4.25. *3D plots of current transients observed during the LICT measurement at various electrochemical potentials in different electrolytes. The PME can be determined by the potential at which the current transient changes its sign from negative to positive or from positive to negative.*

4.3 Strain Modulation Approach in SURMOFs to Design Advanced Oxygen Evolution Electrocatalysts

Due to the tunable nature of MOF structures, a strain modulation approach can easily be introduced into the SURMOF methodology by altering the ligand or the coordination environment. Hence, in this part, a simple strain engineering method by preparing NiFe-SURMOFs with various organic ligands was set forth. This work mainly focuses on the effect of strain on the catalytic activity and properties of the derivatives.

This study has been published in:

W. Li, S. Xue, S. Watzele, S. Hou, J. Fichtner, A. L. Semrau, L. Zhou, A. Welle, A. S. Bandarenka, R. A. Fischer, Advanced Bifunctional Oxygen Reduction and Evolution Electrocatalyst Derived from Surface-Mounted Metal-Organic Frameworks. *Angewandte Chemie International Edition* 59 (2020) 5837-5843.[215]

4.3.1 Motivation

The first two works meticulously investigated the mechanism of SURMOF derivatization and the effect of electrolyte components on the catalytic activity. Recent studies show that tuning the lattice strain in catalysts can lead to a remarkable improvement in their catalytic activity.[70,71] However, efficient strain modulation is relatively complicated for catalysts due to low precision and uncontrollability. In turn, the intrinsic properties of SURMOFs, such as the highly tunable coordination structure or the controllable growth orientation, provide a promising template for the strain design.

With this in mind, a strain modulation approach was used for SURMOFs to design advanced oxygen evolution electrocatalysts.

4.3.2 Preparation of NiFe-[TA] (X) SURMOFs

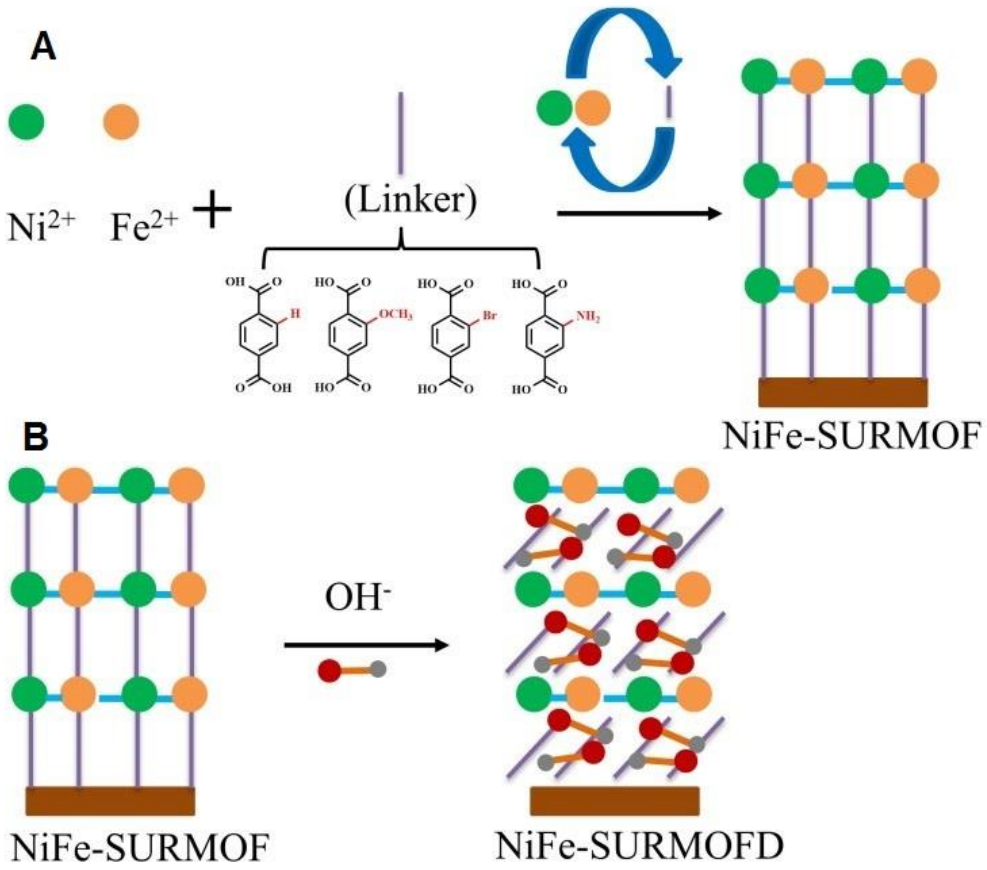

Figure 4.26. *(A) Schematic illustration of the preparation strategy for the NiFe-[TA] (X) SURMOFs (X= NH_2, H, OCH_3, or Br). (B) Structure transformation of NiFe-SURMOF into NiFe-SURMOF derivatives (denoted as SURMOFD) in an alkaline electrolyte.*

In this work, a series of NiFe-[TA] (X) SURMOFs ("X" represents the organic groups of NH_2, H, OCH_3, or Br as one substituent on the benzene ring of [TA]) were initially synthesized through a facile layer-by-layer deposition approach, as shown in **Figure 4.26A**. To visually monitor the growth process of SURMOFs, a gold QCM electrode was used with the Q-sense instrument. As depicted in **Figure 4.27**, the measured frequency suggests the SURMOF growth to consist of two regimes: nucleation and growth. An almost linear growth curve can be observed after the nucleation, which takes ~140 minutes. Impressively, the partial magnification of the growth curve demonstrates a typical four-step synthesis process, *i.e.*, metal ion solution, ethanol, ligand solution, and ethanol. As a result of the dissociation of coordination bonds and partial leaching of organic ligands, the as-prepared SURMOF electrode was transformed into NiFe-based (oxy)hydroxides (denoted as SURMOFDs) in an alkaline electrolyte.

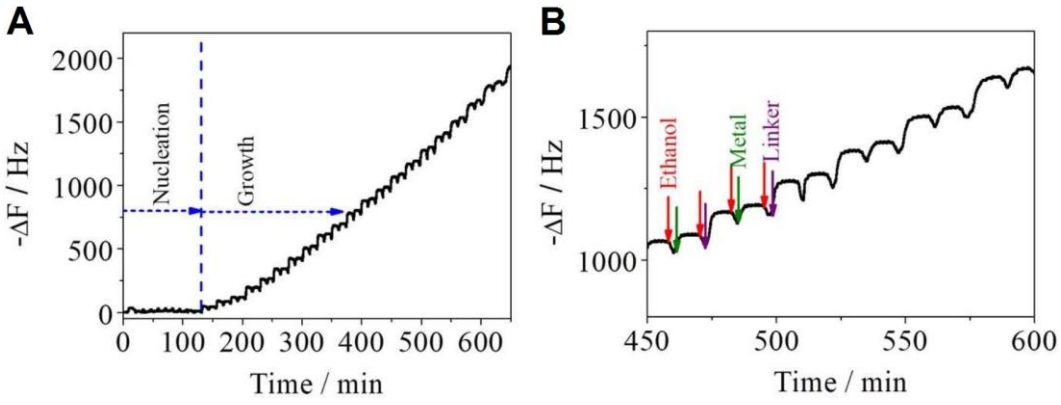

Figure 4.27. *Layer-by-layer deposition of the SURMOFs monitored by a quartz crystal microgravimetry. (A) Frequency change (ΔF) as a function of the deposition time. (B) Partial magnification of (A). A tandem synthesis process can be determined in (B), including the four steps: metal ion solution, ethanol, ligand solution, and ethanol.*

4.3.3 Investigation of the OER Activity of SURMOFDs

To minimize the effect of electrolyte resistance and suppress the formation of large oxygen bubbles, Pt microelectrode was used as a substrate to study the intrinsic activity of the SURMOF derivatives. Initially, the SURMOFs were synthesized on a Pt microelectrode with a nickel/iron feeding ratio of 6:1. Given the small geometry of the microelectrodes, the determination of the mass loading of the derived catalysts is limited. Therefore, the number of deposition cycles of SURMOFs was optimized to achieve an optimal OER activity, which was

normalized to the geometric electrode surface area. As shown in **Figure 4.28A**, NiFe-[TA] SURMOFs of 10, 30, and 60 cycles prepared by the LbL deposition method are converted to SURMOFDs in an alkaline solution. The anodic current density at an overpotential of 300 mV increases from 0.09 to 1.43 A cm^{-2} when the deposition cycles of the pristine SURMOF are increased from 10 to 30. This activity increase can be assigned to the higher mass loading in the 30-cycle SURMOF derivative. However, when the number of deposited layers is increased to 60, the OER anodic current density does not increase accordingly but rather decreases to ~1.16 A cm^{-2} at an overpotential of 300 mV. This decrease in activity could be attributed to the increased resistance of the electrocatalyst film, which hinders the effective charge transfer during the OER process. In addition, a corresponding Tafel slope of *ca.* 27 mV dec^{-1} can be observed in **Figure 4.28B**. A 30-cycle SURMOF with a Ni/Fe feeding ratio of 6:1 will be studied in the following research.

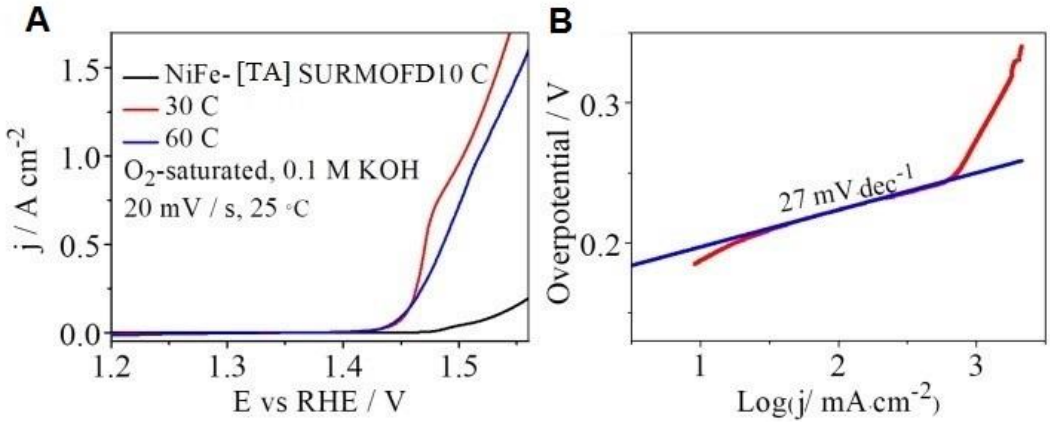

Figure 4.28. *(A) Effect of deposition cycle on the OER activity. (B) Tafel plot of NiFe-[TA] SURMOFD 30 C. Herein, the "C" represents the deposition cycle.*

To assess the electrocatalytic activity, the products of OER were analyzed on a rotating ring disc electrode (RRDE), where constant potentials of 0.7, 0.2, and 1.5 V *vs* RHE were applied to a Pt ring. The onset potential of the OER can be determined through the polarization curve recorded on the Pt ring with a constant potential of 0.7 V *vs* RHE. In **Figure 4.29A**, an increase in current density on the ring can be observed at a working electrode (WE) potential above 1.45 V *vs* RHE, which represents the onset potential of the OER on the NiFe-[TA] SURMOFD 30 C (denoted as 1-H). A constant potential of 0.2 V *vs* RHE is used to study the possible oxidation side reaction of H_2O to H_2O_2 (*cf.* **Figure 4.29B**). Similarly, no significant current changes are observed on the ring at WE potentials below 1.45 V *vs* RHE, indicating that a four-electron

process occurs at the 1-H surface, *i.e.*, water is directly oxidized to O_2. Furthermore, OER activities obtained for the SURMOF derivatives with different ligands are compared, as shown in **Figure 4.30A**. All derived catalysts were denoted according to the ligand species in the pristine SURMOFs, including 1-NH_2, 1-H, 1-OCH_3, and 1-Br. Among all catalysts, 1-NH_2 exhibits the highest OER current density of ~0.86 A cm^{-2} at an overpotential of 300 mV, followed by 1-H (~0.70 A cm^{-2}), 1-OCH_3 (~0.50 A cm^{-2}), and 1-Br (~0.46 A cm^{-2}). This interesting declining variation suggests that the ligands in SURMOFs have a significant effect on the catalytic activity of the derivatives. However, this has to be further investigated in the future. Tafel analysis of the catalysts can be used to evaluate electrocatalytic kinetics. As shown in **Figure 4.30B**, 1-NH_2 shows a smaller Tafel slope of ~26 mV dec^{-1} in comparison to that of 1-H (~28 mV dec^{-1}), 1-OCH_3 (~29 mV dec^{-1}), and 1-Br (~48 mV dec^{-1}).

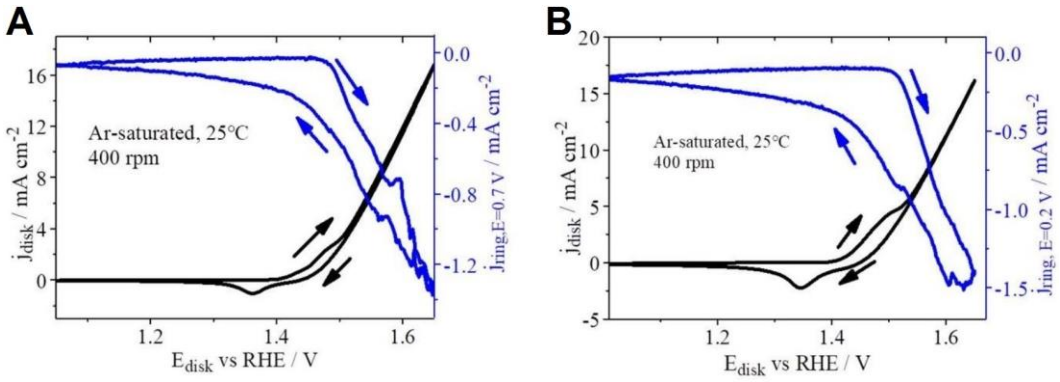

Figure 4.29. *Rotating ring disk electrode (RRDE) measurement of 1-H in Ar-saturated 0.1 M KOH solution at a rotation speed of 400 rpm. A Pt ring with different constant potentials of (A) 0.7 V vs RHE and (B) 0.2 V vs RHE was used in the RRDE.*

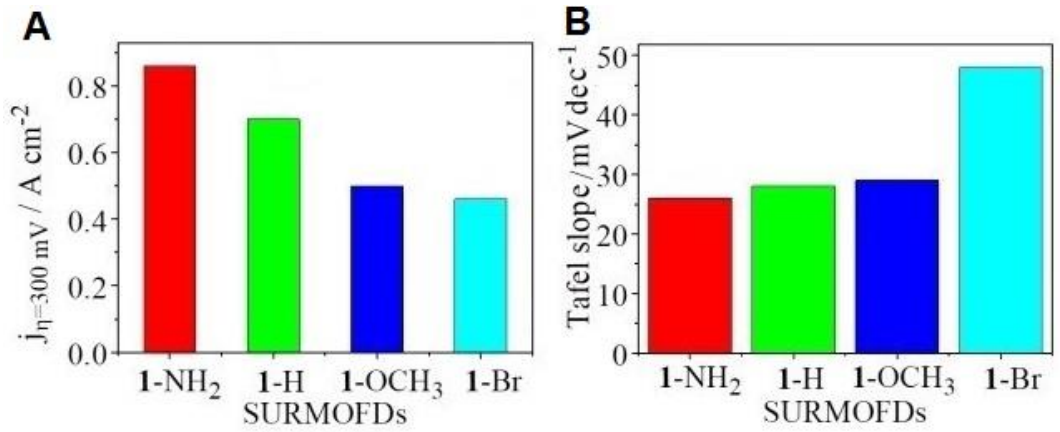

Figure 4.30. *(A) Comparison of OER activities at an overpotential of 300 mV for 1-NH_2, 1-H, 1-OCH_3, and 1-Br derivatives. (B) The corresponding Tafel plots of all derived catalysts.*

4.3.4 Defect Strain in SURMOFDs

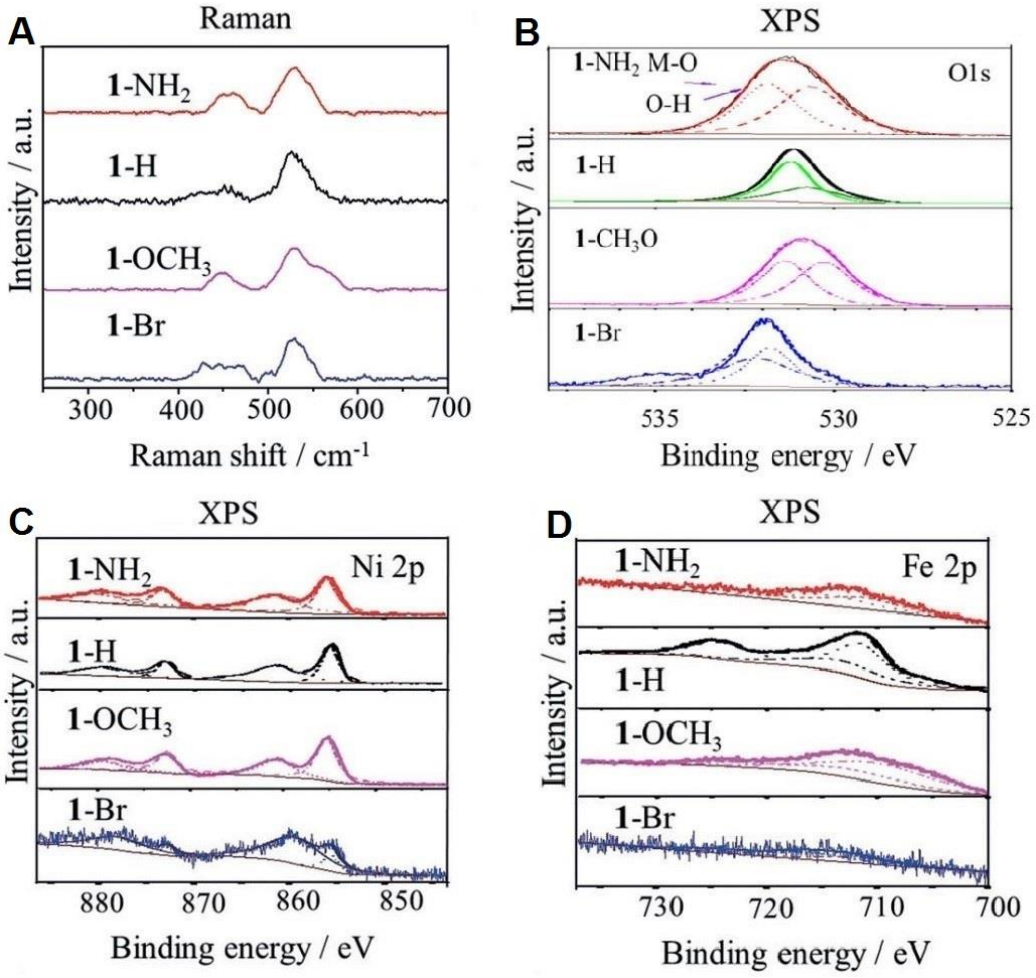

Figure 4.31. *(A) Raman spectra of 1-NH_2, 1-H, 1-OCH_3, and 1-Br derivatives. (B-D) Comparison of the XPS spectra of SURMOFDs: for O 1s, Ni 2p, and Fe 2p, respectively.*

To deepen the understanding of catalyst mechanisms and performance-structure relationships, a series of characterizations of the catalysts were performed. In the Raman spectra (*cf.* **Figure 4.31A**), the peaks of Ni-O bonds (Ni-O, Ni-OH) in 1-Br appear at 455 cm^{-1} and 533 cm^{-1}, whereas a slight red shift can be observed for 1-NH_2 (corresponding peaks at 449 cm^{-1} and 527 cm^{-1}). According to the literature, the change in strain can induce phonon softening of the material, leading to a red shift in the Raman spectrum.[252,253,254] Tuning the lattice strain in catalysts can remarkably improve their catalytic activity. Hence, the observed Raman red shifts of the different derivatives indicate the existence of "defective strain", which depends on the type of derivatives. Furthermore, XPS analysis provided more insights into the defective strain. As shown in **Figure 4.31B**, the O 1s spectra show positive shifts for 1-OCH_3 (530.8 eV), 1-H (531.0 eV), and 1-NH_2 (531.5 eV), which corresponds to the Ni(Fe)-OH species in derivatives.

This indicates that the effect of ligands in SURMOFs can be inherited into the derived catalysts, resulting in significant differences in catalytic activity.[255] For 1-Br, the binding energy of the Ni $2p_{3/2}$ peaks are 0.1 eV and 0.9 eV lower compared to the corresponding Ni $2p_{3/2}$ peaks of 1-OCH_3 and 1-NH_2, respectively. The Fe $2p_{3/2}$ peak of 1-Br shows higher binding energy than 1-OCH_3 and 1-NH_2. Therefore, shifts of the binding energies indicate the change of bond lengths of Ni-O or Fe-O in the derivatives caused by the defective strain.[71,256,257]

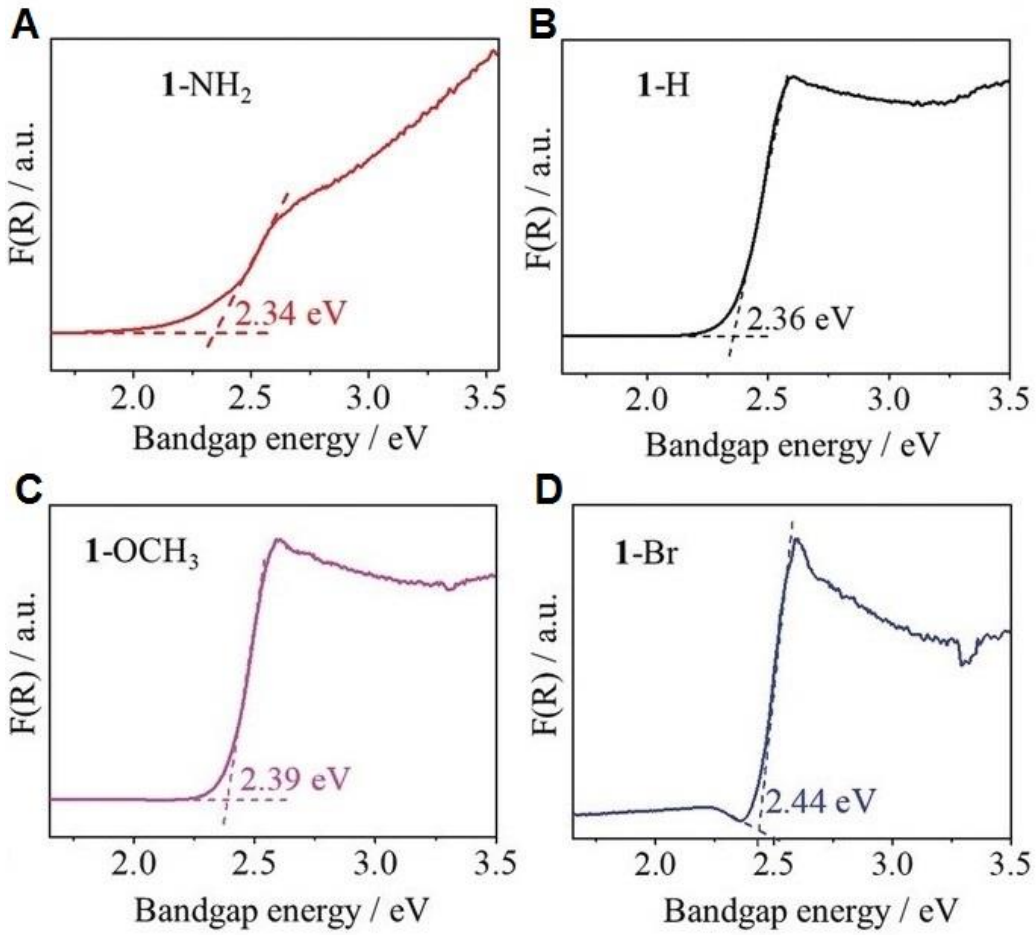

Figure 4.32. *Bandgap energies of the derived catalysts measured by UV/Vis diffuse reflectance spectra.*

Furthermore, UV/Vis diffuse reflectance spectra were performed to investigate the bandgap energies of all derived catalysts. In **Figure 4.32**, 1-Br exhibits a higher bandgap (2.44 eV) in comparison to 1-NH_2 (2.34 eV), 1-H (2.36eV), and 1-OCH_3 (2.39 eV). The positive shift of the bandgap energy represents an increase in defective strain. According to the d-band theory,[258,259] the d-band center shifts toward the Fermi level, leading to a less filled anti-bonding state.[260] Consequently, the partially filled anti-bonding orbitals can provide more active sites for the adsorption of oxygen species.

It is highly challenging to directly predict the overall activity of the SURMOFDs and their active sites with density functional theory calculations. Note that electron affinity is a key factor in the evaluation of a catalyst, especially in the MOF system, because electron affinity stands for the ability of a molecule to gain electrons. Interlayer ligands with low electron affinity can increase the density of non-occupied states in transition metals and further boost their OER activity. The calculated electron affinities for various ligands are listed in **Figure 4.33**. The numbers given on the left and right in parentheses represent the vertical electron affinity and absolute electron affinity, respectively. [TA]-NH_2 shows the lowest electron affinity (0.18 eV). In contrast, a high electron affinity (0.66 eV) is observed for [TA]-Br. Interestingly, this result is consistent with the trend of catalytic activities for the corresponding SURMOF derivatives. Only [TA]-OCH_3 shows a higher electron affinity than [TA]-H, while their OER activity trends are in the opposite direction, even though their electron affinity values are close. Therefore, we speculate that the influence of ligands in the pristine SURMOFs can be inherited and expressed by the catalytic activity of the derivatives. Ligand engineering provides new pathways for the design and development of MOF-based electrocatalysts.

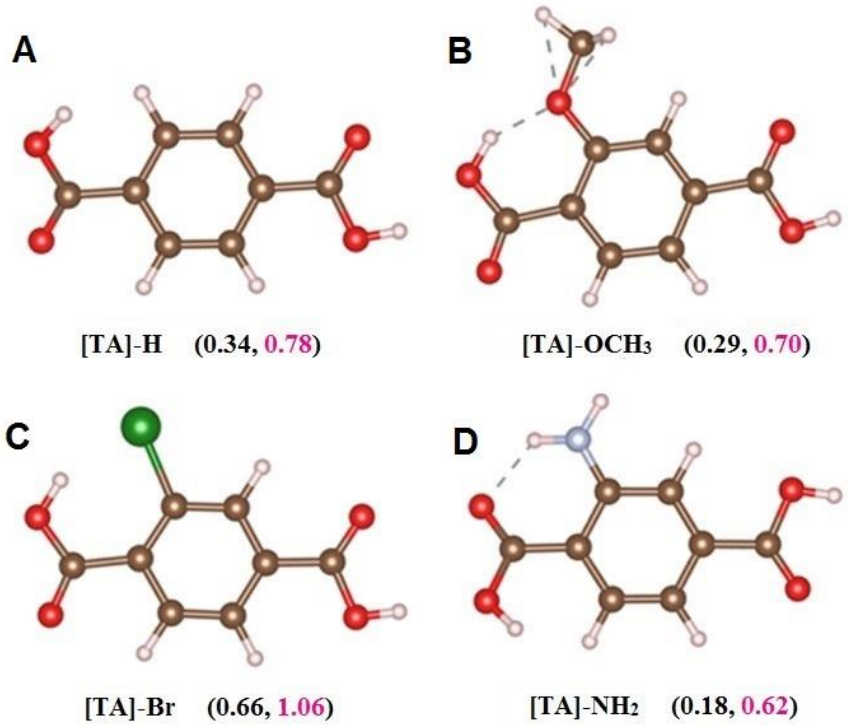

Figure 4.33. *Calculations of the electron affinities for various ligands.*

5 Conclusion and Perspective

In this work, a series of heterostructured and strained SURMOFs were prepared through a stepwise LbL deposition process and analyzed for their OER performance. The objective was to understand the SURMOF precatalysts' transformation mechanisms, the structure-performance relationships, and the electrified electrode/electrolyte interface influence. The conclusions from the study are summarized in the following paragraphs.

In **section 4.1**, heterostructured NiFe-based SURMOFs consisting of deprotonated terephthalic acid ($[TA]^{2-}$) ligands were synthesized, and structural and compositional variants were explored to optimize the OER performance. The experiments demonstrated that unprecedentedly high oxygen evolution activity of electrocatalysts could be developed by *in-situ* structural transformations and self-activation of heterostructured SURMOFs. The derived electrocatalyst exhibited a record mass activity of ~2.90 kA g^{-1} at an overpotential of 300 mV, superior to the benchmark values of precious and non-precious metal electrocatalysts. Given the unstable nature of our SURMOFs in alkaline media, this work turned this intrinsic lability as a particular advantage to derive high performing electrocatalysts, rather than aiming to overcome the instability issue. A series of *in-situ* and *ex-situ* methods disclose that during the alkaline immersion and electrochemical measurements, morphology transformation, structural metamorphosis, and self-activation for SURMOFs have been confirmed to lead to the production of highly-active catalytic species -NiFe (oxy)hydroxides- and the leaching of organic ligands. These derived NiFe (oxy)hydroxides show a unique crystalline-amorphous phase, large electroactive surface area, and low apparent activation energy.

In **section 4.2**, considering that electrode materials and electrolytes are two key factors that dominate the electrocatalytic reaction of energy conversion systems, the effect of the cationic species in the electrolyte on the OER activity of NiFe SURMOF derivatives was investigated. The LICT technique and the *in-situ* Raman spectroscopy were carried out to reveal the reaction mechanisms and kinetics at the electrified electrode/electrolyte interface. Electrochemical data show that the activity of OER is sensitive to alkali metal cations in the following order, $Cs^+ > K^+ > Na^+ > Li^+$. Raman spectra disclose that the OER activities in different alkali metal

hydroxide electrolytes follow the variations in the Raman shifts of Ni-O bending vibration, which correspond to the length discrepancies of the Ni-O bonds in the high-valence Ni intermediates. This result reflects the strong interaction between the large alkali metal cation and the charged intermediates. Further insights concerning the cation-dependent electrical double layer structures were obtained from the LICT technique. Using the PME obtained from LICT measurements, the optimal potential to convert formerly oriented water dipoles in the electrical double layer into a disordered state was assessed. It is found that the cation-dependence of the OER activity is in line with the trend of the PMEs, elucidating the fact that the large Cs^+ cations can significantly affect the structure of the interfacial water layer resulting in improved OER kinetics.

Strain engineering of catalysis is an effective method of affecting the adsorption/desorption properties of reactants, intermediates, and products by modifying the electronic structure. The intrinsic properties of the SURMOF's highly tunable coordination structure provide an ideal template for strain design. In **section 4.3**, a series of strained SURMOFs were designed by the rational introduction of functional groups (-Br, -OCH_3, and -NH_2) onto organic ligands. Significant electronic structure differences were observed in the SURMOFs prepared by the "strain modulation" approach. Moreover, the strained SURMOF derivatives show a remarkable activity towards the OER, with the 1-NH_2 presenting the highest anodic current density of ~0.86 A cm^{-2} among all tested OER catalysts at an overpotential of 300 mV, followed by 1-H (0.70 A cm^{-2}), 1-OCH_3 (0.50 A cm^{-2}), and 1-Br (0.46 A cm^{-2}). This trend of catalytic activity exhibits a close correlation with the electron affinity of the organic ligands.

It is well-known that heterogeneous (electro-)catalysts are dynamic materials and are typically not in a thermodynamic equilibrium state. The catalyst performance is connected to the chemical kinetics of the catalyst fabrication process. In line with this knowledge, it was demonstrated that the morphologic transformation, the structural metamorphosis, and the self-activation of SURMOFs are independent of the precatalyst choices (*e.g.*, heterostructure and strain) and their transformation chemistry in an alkaline medium. In total, the here presented SURMOF method for deriving LDH-type materials can produce highly active electrocatalysts as (binder-free) coatings in a precisely controllable fashion. The methodologies in this work regarding the metamorphosis mechanism of SURMOFs and the interfacial mechanism will likely be transferable to the design and investigation of other state-of-the-art catalysts. Finally, it should be underlined that the evolution of SURMOFs is a complex process, and further efforts

need to be devoted to this field. Of course, more advanced technological and theoretical approaches are also eagerly waiting to be developed and applied to SURMOF-based electrocatalysis. Feeding abundant material and catalytic parameters to a computer, the state-of-the-art machine learning (ML) or artificial intelligence (AI) may provide us with more blueprints in the near future, such as a predictive catalytic model with near-ideal efficiency.

6 Appendix

6.1 Figures

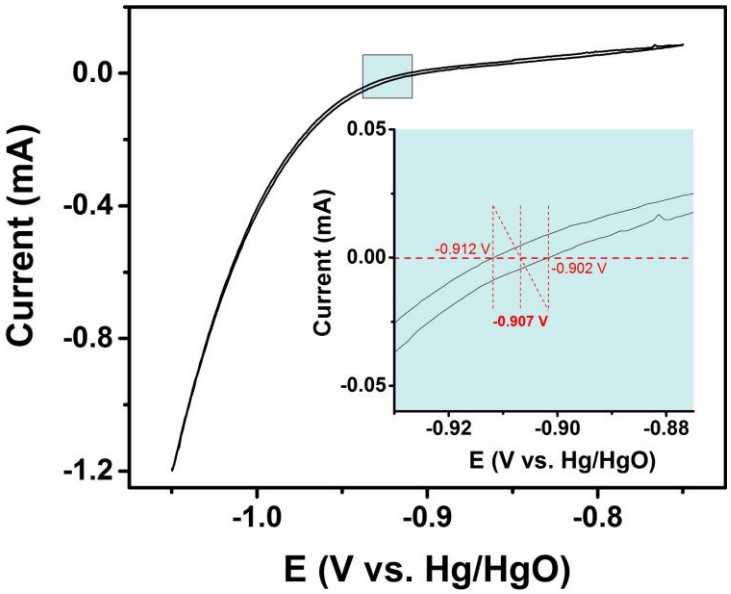

Figure 6.1. *Potential calibration for the Hg/HgO (1.0 M high-purity NaOH) reference electrode. In detail, the calibration experiment was conducted in high-purity H_2 saturated 0.1 M NaOH (pH = 13.1) electrolyte with a three-electrode setup. A Pt wire and a Pt mash were used as the working and counter electrodes, respectively. The Pt wire was placed close to the reference electrode (Hg/HgO). The HER curves were recorded by CV at a scan rate of 5 mV s^{-1} within a potential region of -0.75 to -1.05 V vs Hg/HgO. Two potentials can be obtained from the intersections with the x-axis. The thermodynamic potential of HER was calculated as -0.907 V according to the average value of the above intersections. Hence, the conversion of potential can be indicated as $E_{RHE} = E_{Hg/HgO} + 0.134\ V + 0.059*pH$.*

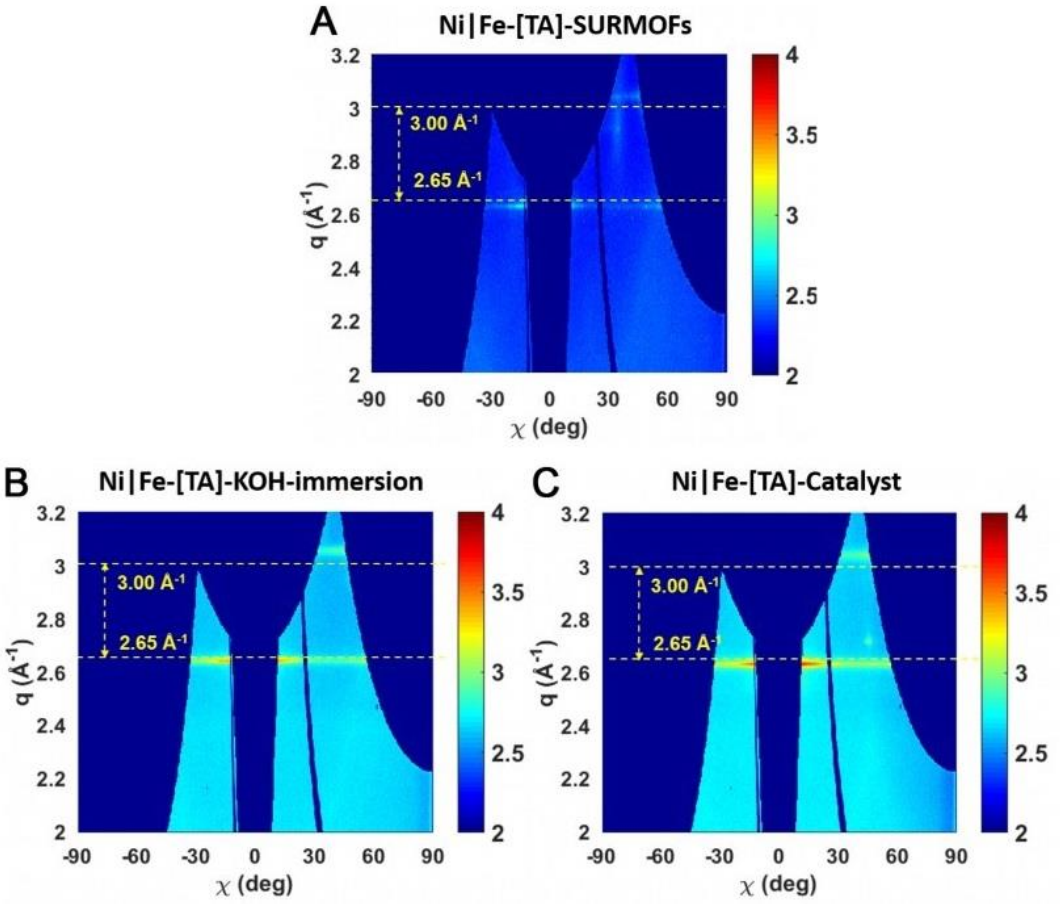

Figure 6.2. *Reshaped 2D GIWAXS patterns of Ni|Fe-[TA]-SURMOFs (A), Ni|Fe-[TA]-KOH-immersion sample (B), and Ni|Fe-[TA]-Catalyst (C).*

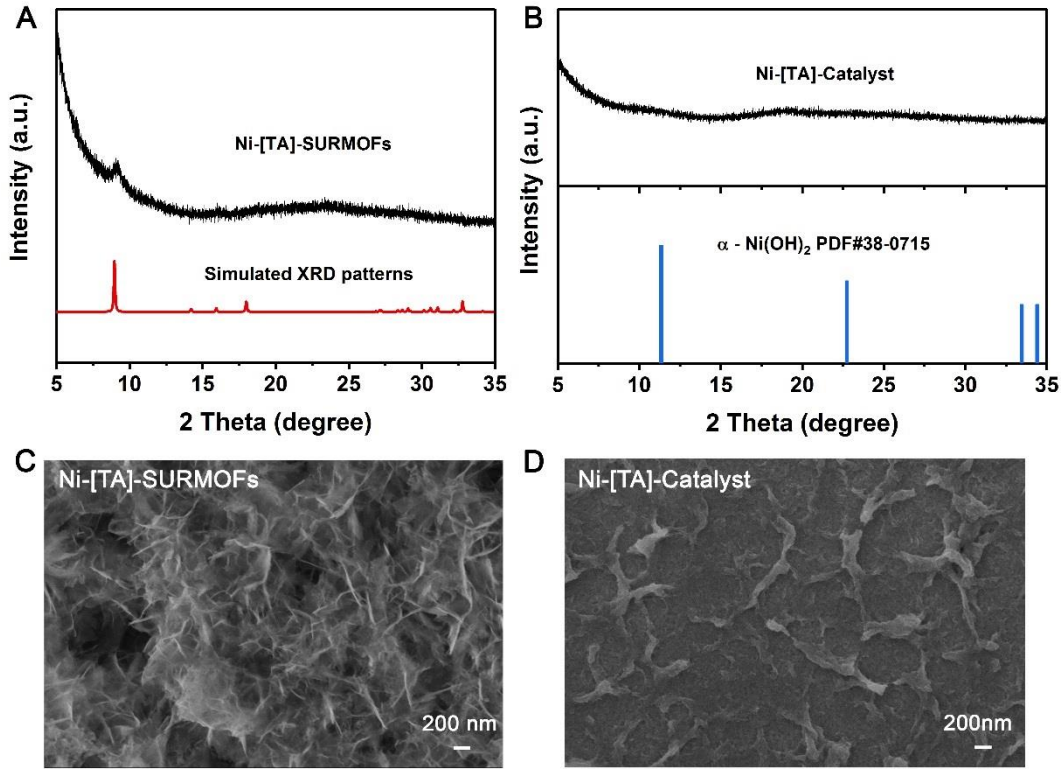

Figure 6.3. *GIXRD patterns and SEM images of Ni-[TA]-SURMOFs (A and C) and Ni-[TA]-Catalyst (B and D).*

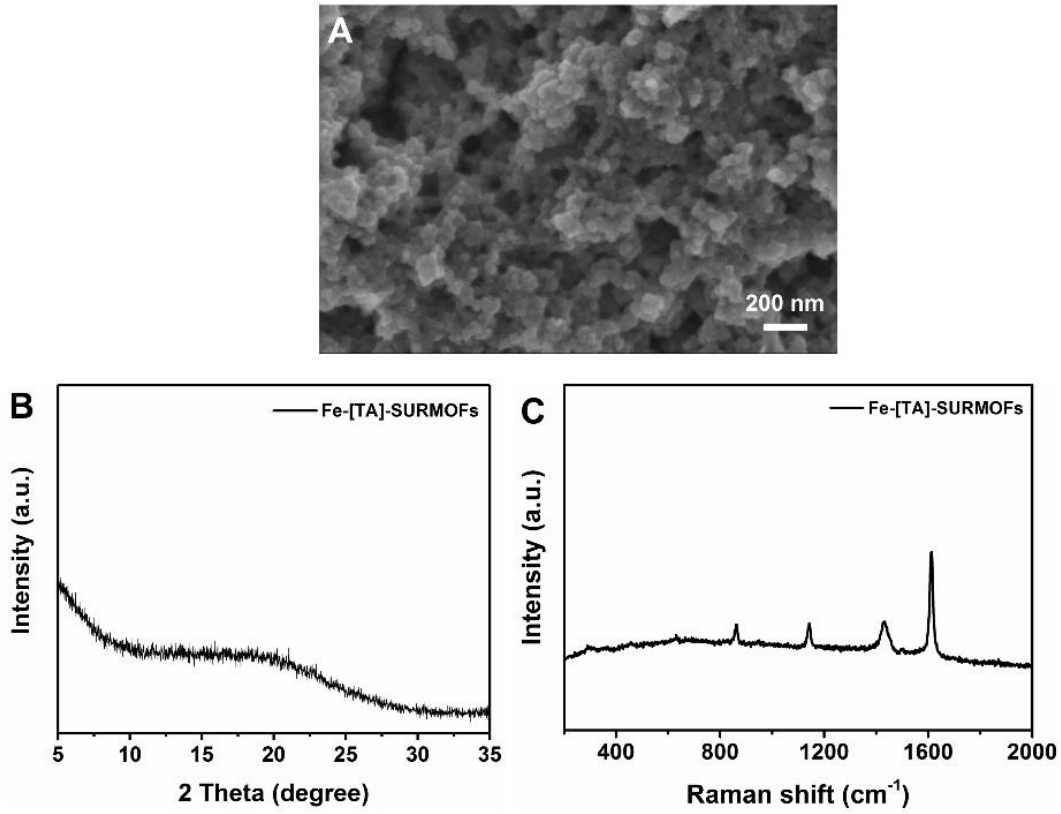

Figure 6.4. *SEM image (A), GIXRD pattern (B), and Raman spectrum (C) of the as-prepared Fe-[TA]-SURMOFs.*

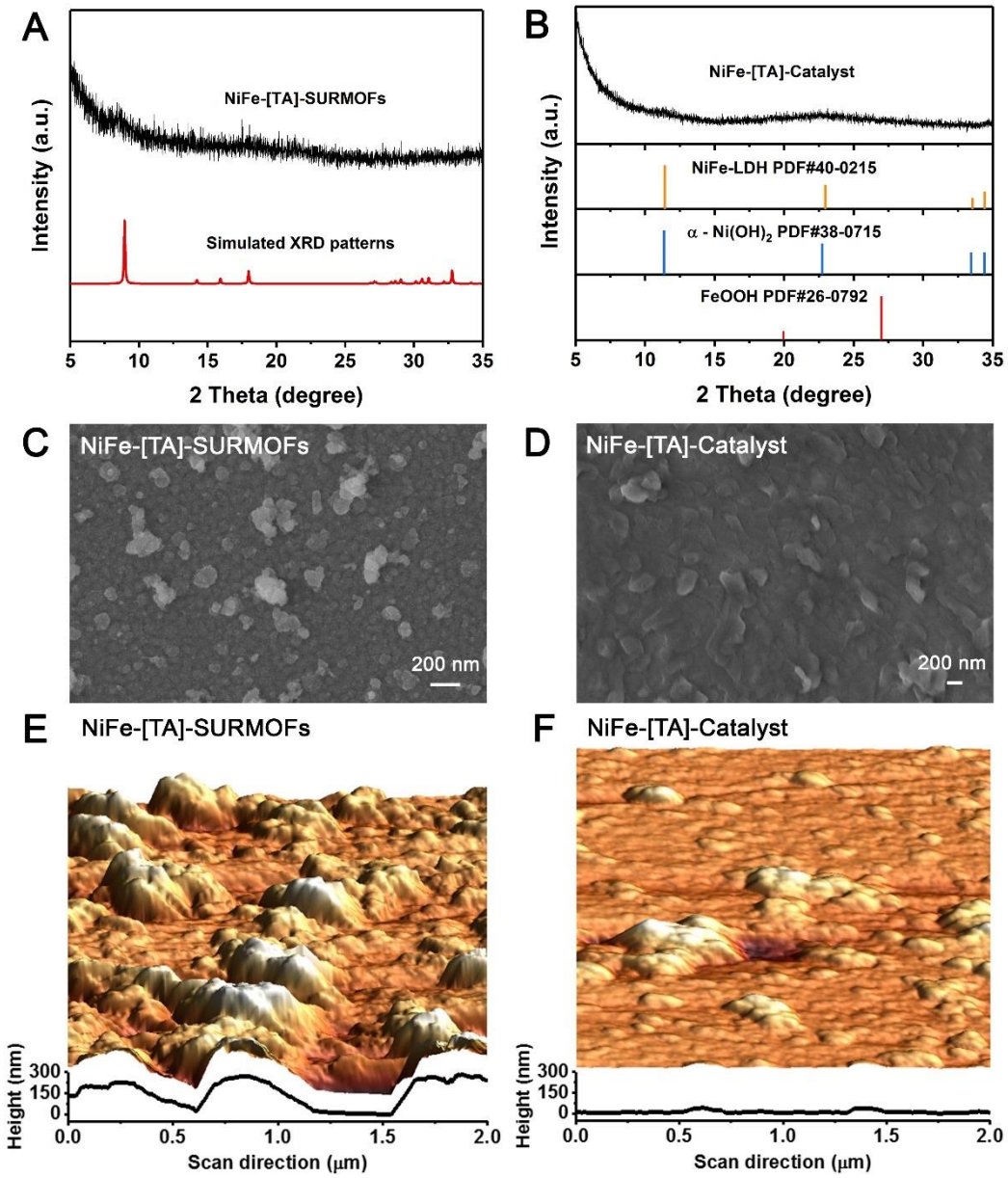

Figure 6.5. *The studies of structures and morphologies for pristine NiFe-[TA]-SURMOFs and NiFe-[TA]-Catalyst using the GIXRD, SEM, and AFM.*

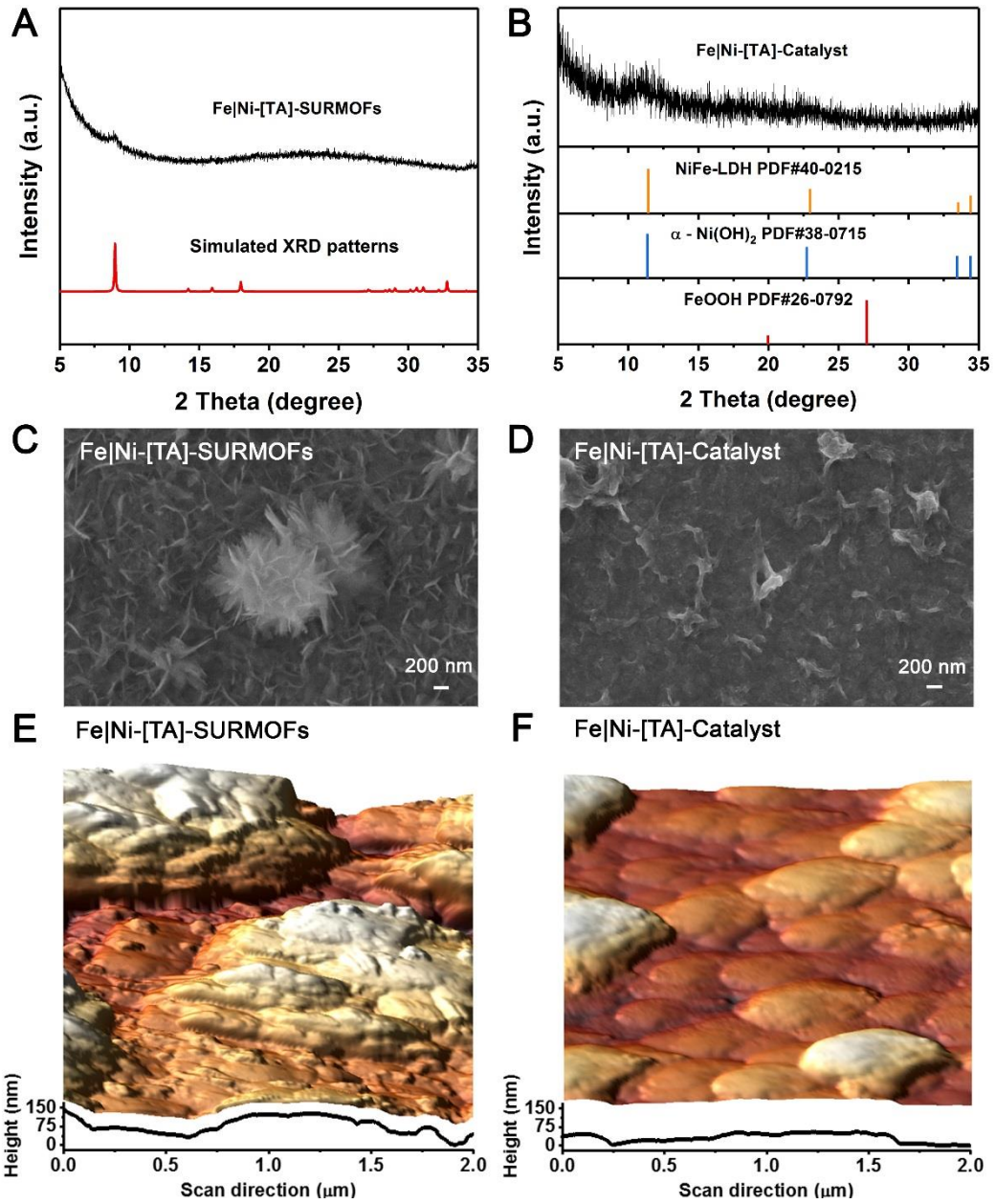

Figure 6.6. *The comparison of structures and morphologies for pristine Fe|Ni-[TA]-SURMOFs and Fe|Ni-[TA]-Catalyst using the GIXRD, SEM, and AFM.*

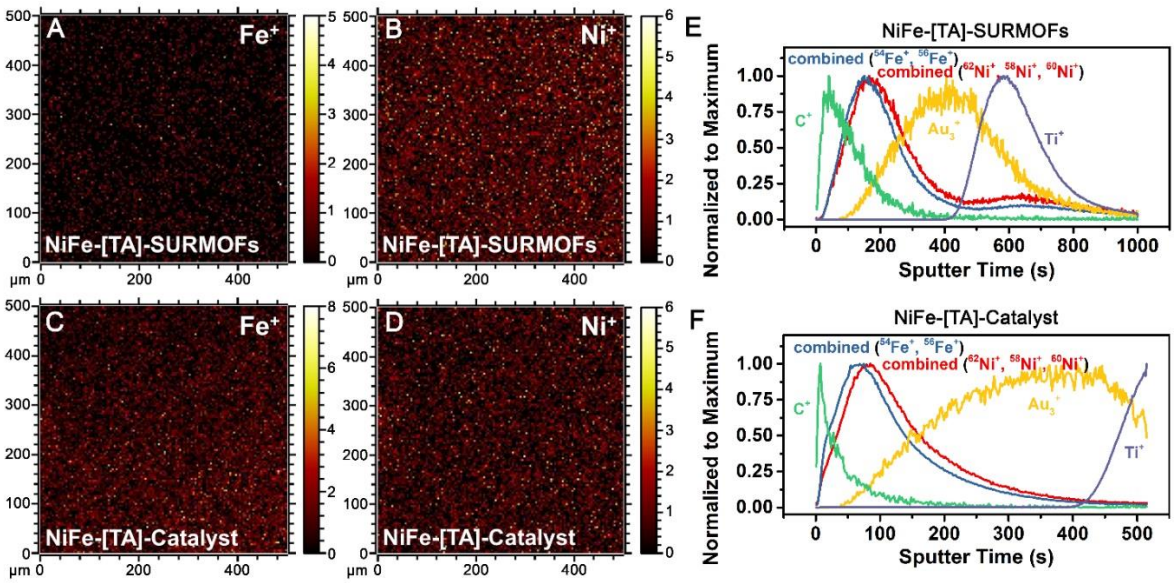

Figure 6.7. *(A-D) ToF-SIMS chemical mapping analysis for Fe and Ni signals collected from the topmost layer of the NiFe-[TA]-SURMOFs and NiFe-[TA]-Catalyst thin films. (E and F) Normalized secondary ion fragment spectra of* C^+, Fe^+, Ni^+, Au_3^+ *and* Ti^+ *obtained by sputtering along with the depth profile of the NiFe-[TA]-SURMOFs and NiFe-[TA]-Catalyst thin films.*

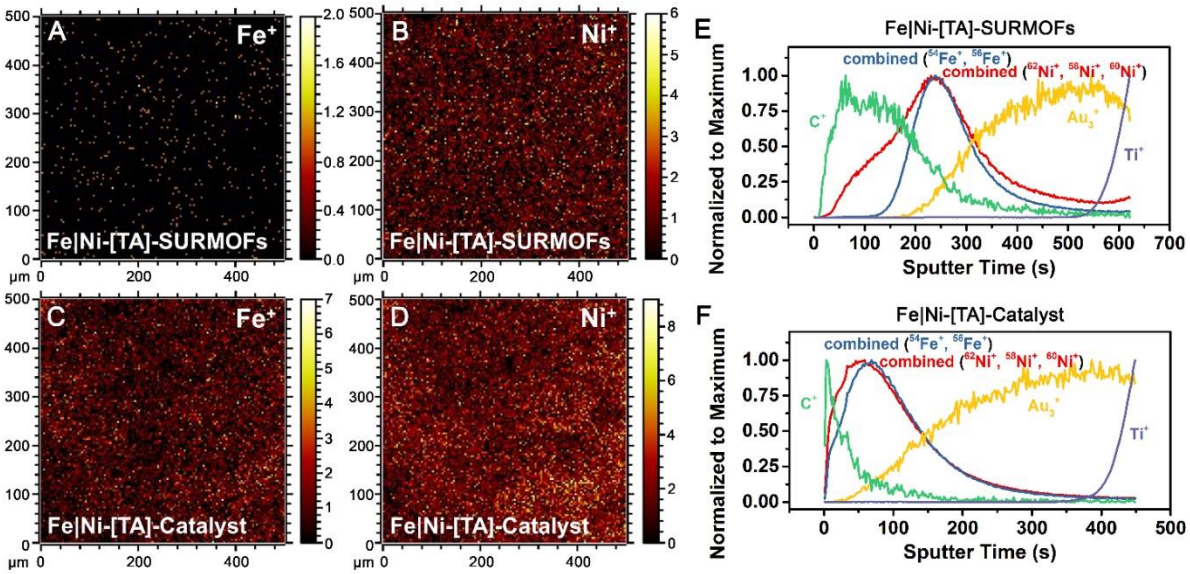

Figure 6.8. *(A-D) ToF-SIMS chemical mapping analysis for Fe and Ni signals probed in the topmost layer of the Fe|Ni-[TA]-SURMOFs and Fe|Ni-[TA]-Catalyst thin films. (E and F) Normalized secondary ion fragment spectra of C^+, Fe^+, Ni^+, $Au_3{}^+$, and Ti^+ obtained by sputtering along with the depth profile of the Fe|Ni-[TA]-SURMOFs and Fe|Ni-[TA]-Catalyst thin films.*

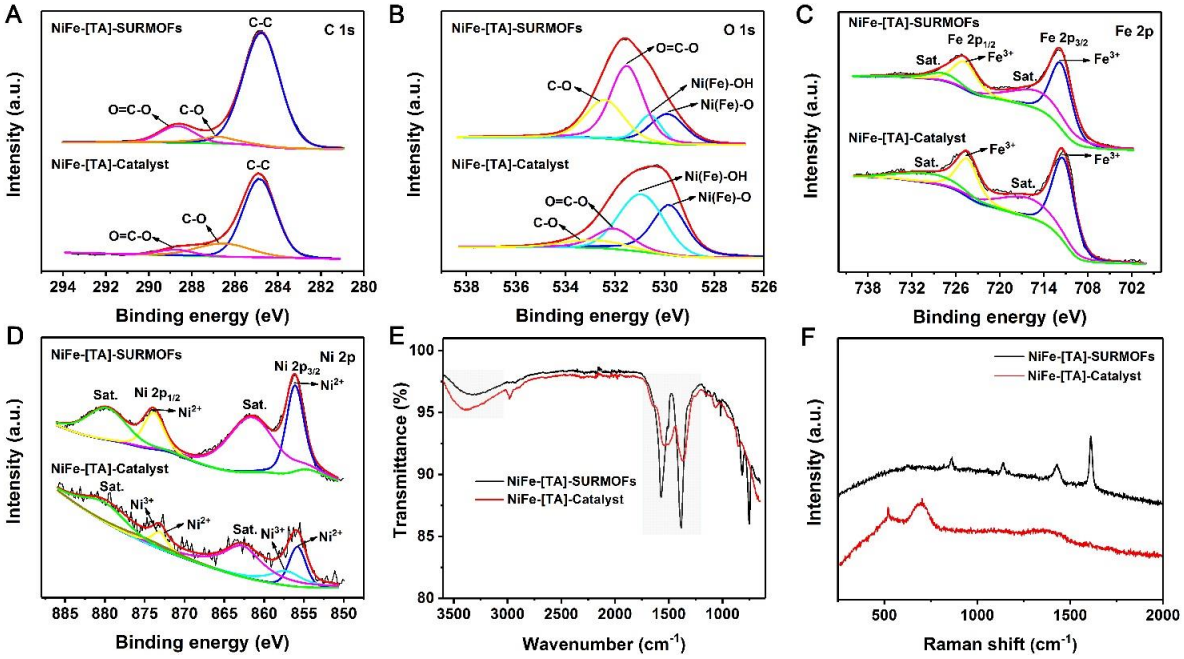

Figure 6.9. *Spectral characterization of the NiFe-[TA]-SURMOFs and NiFe-[TA]-Catalyst by high-resolution XPS C 1s (A), O 1s (B), Fe 2p (C), and Ni 2p (D) spectra. ATR-FTIR (E) and ex-situ Raman (F) measurements on the NiFe-[TA]-SURMOFs and NiFe-[TA]-Catalyst.*

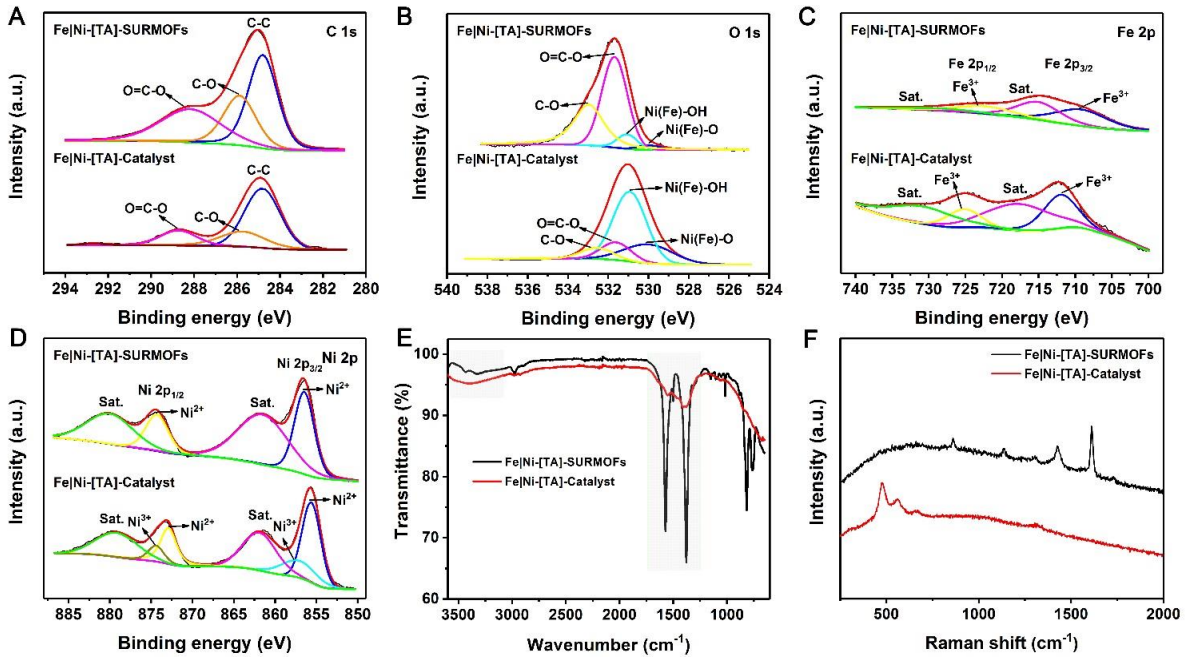

Figure 6.10. *High-resolution XPS C 1s (A), O 1s (B), Fe 2p (C), and Ni 2p (D) spectra of the Fe|Ni-[TA]-SURMOFs and Fe|Ni-[TA]-Catalyst. ATR-FTIR (E) and ex-situ Raman (F) spectra of the Fe|Ni-[TA]-SURMOFs and Fe|Ni-[TA]-Catalyst.*

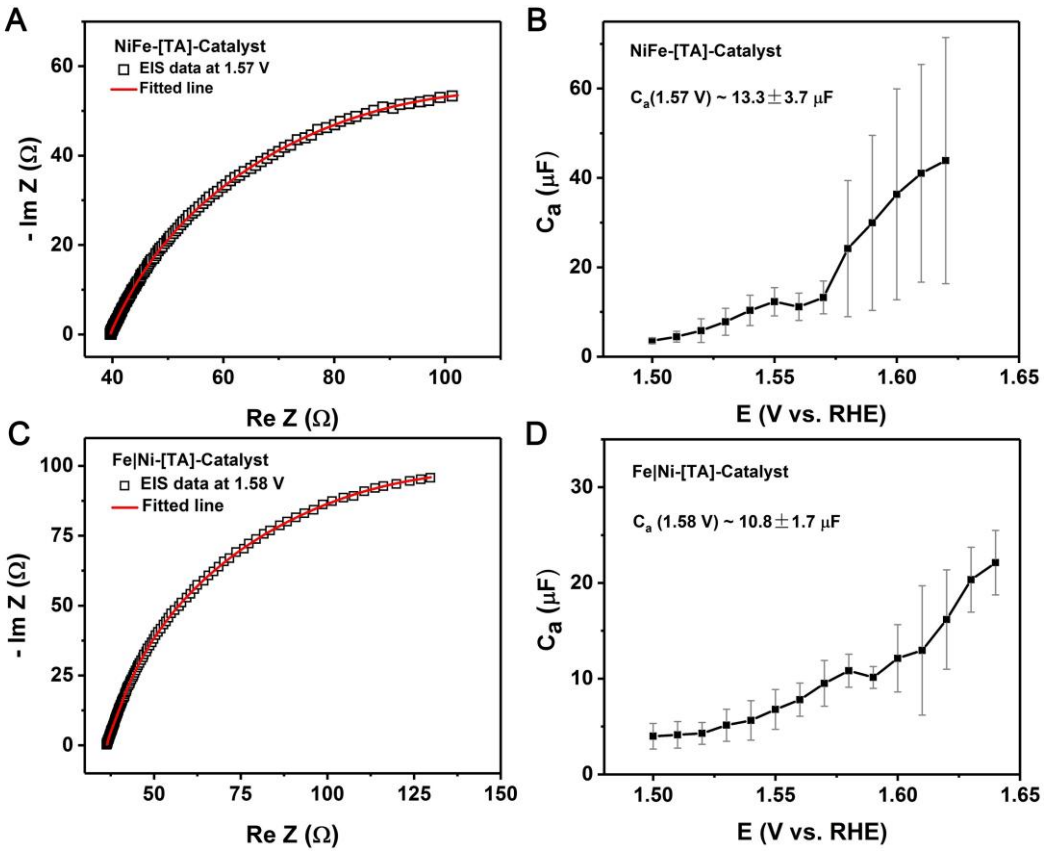

Figure 6.11. *Electrochemical impedance data of the NiFe-[TA]-Catalyst (A) and the Fe|Ni-[TA]-Catalyst (C) electrodes measured at the potentials of 1.57 and 1.58 V vs RHE, respectively. Adsorption capacitances of the NiFe-[TA]-Catalyst (B) and Fe|Ni-[TA]-Catalyst (D) electrodes at different bias potentials.*

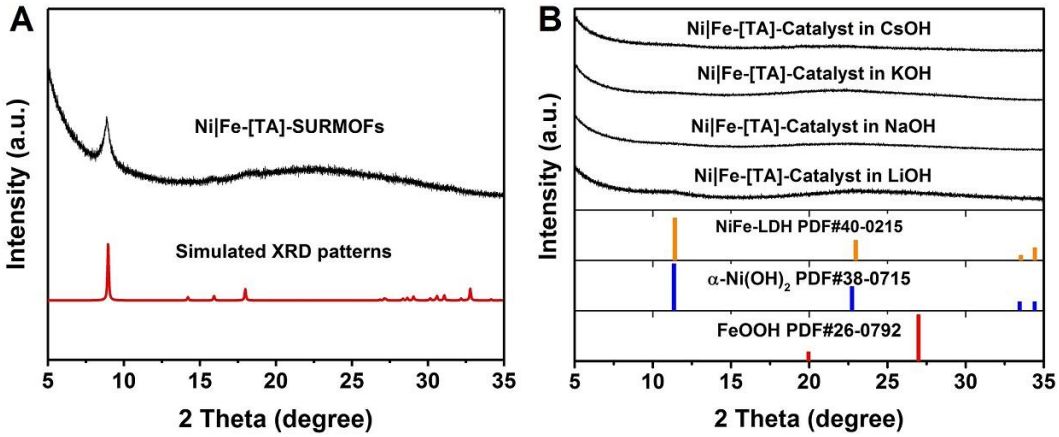

Figure 6.12. *GIXRD patterns of the Ni|Fe-[TA]-SURMOFs (A) and corresponding Catalysts (B) prepared by immersion and electrochemical cycling in O_2-saturated 0.1 M LiOH, NaOH, KOH, and CsOH electrolytes.*

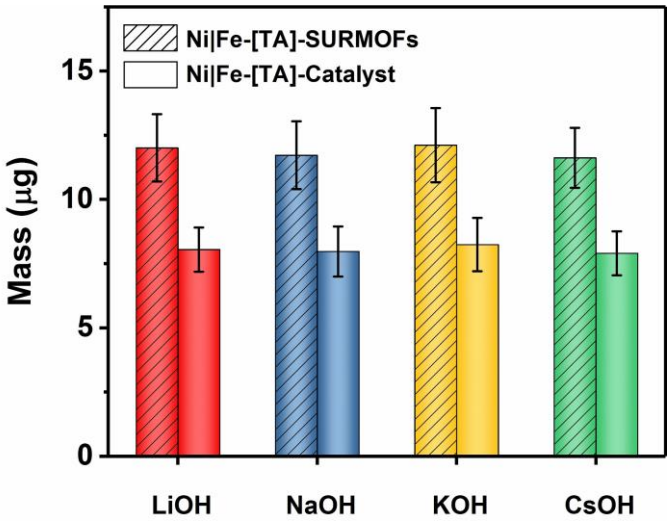

Figure 6.13. *Comparison of the mass loading on the Au QCM electrodes for the pristine Ni|Fe-[TA]-SURMOFs and the Ni|Fe-[TA]-Catalysts derived in various electrolytes.*

6.2 Abbreviations and Symbols

A	electrode surface area
A	piezoelectrically active crystal area
AEM	adsorbate evolution mechanism
AFM	atomic force microscopy
AM	alkali metal
bdc or BDC	1,4-benzenedicarboxylate
BET	Brunauer–Emmett–Teller
btc or BTC	1,3,5-benzenetricarboxylate
C	capacitance/capacitor
C_0	the concentration of the electroactive species
C_a	adsorption capacitance
C_a'	specific adsorption capacitance
C_f	calibration constant
C_O	oxidized species
C_R	reduced species
CV	cyclic voltammetry
D	diffusion coefficient

DOE	department of energy (USA)
DMSM	dual-metal-site mechanism
E	potential
E_a	apparent activation energy
$E_{binding}$	electron binding energy
EDS	energy dispersive spectroscopy
E_{eq}	equilibrium potential
ECSA	electrochemically active surface area
EDL	electric double layer
EEC	equivalent electric circuit
EIS	electrochemical impedance spectroscopy
$E_{M\text{-}H}$	the energy of hydride formation
$E_{kinetic}$	measured kinetic energy of the photoelectron
E_{photon}	photon (x-ray) energy
Et_3N	triethylamine
$E^{0'}$	the formal potential of an overall reaction
F	Faraday constant
F	force

f_0	the fundamental frequency of quartz crystal
G	Gibbs free energy
GIWAXS	grazing-incidence wide-angle X-ray scattering
GIXRD	grazing incidence X-ray diffraction
H_{ads}	adsorbed hydrogen
HER	hydrogen evolution reaction
HUPD	hydrogen underpotential deposition
i	net current
i_c	cathodic current
i_a	anodic current
IEA	international energy agency
IHP	inner Helmholtz plane
ImZ	the imaginary part of the impedance
iR	ohmic drop
j	current density
J_{lim}	mass transport limited current density
k	a force constant factor of the cantilever
k^0	standard rate constant

k_b	the backward reaction rate constant
k_f	the forward reaction rate constant
LB	Langmuir-Blodgett
LbL	layer-by-layer
LDH	layered double hydroxides
LICT	laser-induced current transient
LOM	lattice-oxygen-participating mechanism
LPE	liquid-phase (quasi-)epitaxy
M	metal electrode
MMO	mercury/mercurous oxide reference electrode
MMT	million metric tons
MOFs	metal-organic frameworks
MOH	alkali metal hydroxides
NMR	nuclear magnetic resonance
n	electron transfer number
OER	oxygen evolution reaction
OHP	outer Helmholtz plane
ORR	oxygen reduction reaction

pc	polycrystalline
PLS	potential limiting step
PME	the potential of maximum entropy
PTFE	polytetrafluoroethylene
QCM	quartz crystal microbalance
R	universal gas constant
R	resistance
R_a	adsorption resistance
R_{ct}	charge transfer resistance
RDE	rotating disk electrode
Re	the real part of the complex impedance
RHE	reversible hydrogen electrode
RRDE	rotating ring disk electrode
R_s	electrolyte resistance
rpm	revolutions per minute
SAMs	self-assembled organic monolayers
SBUs	secondary building units
SDD	the sample detector distance

SEM	scanning electron microscope
SMSM	single-metal-site mechanism
STM	scanning tunneling microscopy
SURMOFDs	surface-mounted metal-organic framework derivatives
SURMOFs	surface-mounted metal-organic frameworks
T	temperature
TA	terephthalic acid
TEM	transmission electron microscope
ToF-SIMS	time-of-flight secondary ion mass spectrometry
UiO	Universitetet i Oslo
UHV	ultra-high vacuum
WE	working electrode
x	deflection of the cantilever
XPS	X-ray photoelectron spectroscopy
XRD	X-ray diffraction
Z_{dl}	double layer impedance
ZIF	zeolitic imidazolate framework
α	transfer coefficient

δ	the thickness of the diffusion layer
ω	rotation rate
μ	shear modulus of quartz for AT-cut crystal
ρ	density of quartz
ϕ	the work function of the solid surface
υ	kinematic viscosity of the liquid
ν_b	rate of the backward path
ν_f	rate of the forward path
ν_{net}	net reaction rate
η	overpotential
Δf	change of the quartz resonance frequency
ΔG_{H^*}	adsorption free energy
Δm	mass change

6.3 Publications

RESEARCH ARTICLE

ADVANCED MATERIALS
www.advmat.de

Metamorphosis of Heterostructured Surface-Mounted Metal–Organic Frameworks Yielding Record Oxygen Evolution Mass Activities

Shujin Hou, Weijin Li, Sebastian Watzele, Regina M. Kluge, Song Xue, Shanshan Yin, Xinyu Jiang, Markus Döblinger, Alexander Welle, Batyr Garlyyev, Max Koch, Peter Müller-Buschbaum, Christof Wöll, Aliaksandr S. Bandarenka,* and Roland A. Fischer**

Materials derived from surface-mounted metal–organic frameworks (SURMOFs) are promising electrocatalysts for the oxygen evolution reaction (OER). A series of mixed-metal, heterostructured SURMOFs is fabricated by the facile layer-by-layer deposition method. The obtained materials reveal record-high electrocatalyst mass activities of ≈2.90 kA g^{-1} at an overpotential of 300 mV in 0.1 M KOH, superior to the benchmarking precious and non-precious metal electrocatalysts. This property is assigned to the particular in situ self-reconstruction and self-activation of the SURMOFs during the immersion and the electrochemical treatment in alkaline aqueous electrolytes, which allows for the generation of NiFe (oxy)hydroxide electrocatalyst materials of specific morphology and microstructure.

1. Introduction

Electrochemical water splitting offers an attractive means for producing renewable hydrogen fuel, which is promising for carbon-neutral energy provision schemes owing to its high energy density.[1–5] However, the main cause of low efficiency in this process is the anodic half-reaction,[6,7] namely, the oxygen evolution reaction (OER), which shows sluggish kinetics. Hence, exploring highly efficient and cost-effective earth-abundant electrocatalysts is a desirable solution to cope with these issues.[8] Non-noble electrocatalysts, such as transition-metal oxides, hydroxides, sulfides, and phosphides, have been regarded as promising alternatives. Among them, Ni-based and Fe-incorporated Ni-based compounds exhibit high OER activity in alkaline media.[9–13]

Metal oxo/hydroxo materials derived from surface-mounted metal–organic frameworks (SURMOFs) have shown promising OER performances due to the highly tuneable film thickness, controllable growth orientation and binder-free processing.[14–16] Thus, the layer-by-layer deposition of ultrathin SURMOFs on conductive substrates offers an effective strategy to design highly active

S. Hou, Dr. S. Watzele, R. M. Kluge, Dr. S. Xue, Dr. B. Garlyyev, Prof. A. S. Bandarenka
Physics of Energy Conversion and Storage
Physik-Department
Technische Universität München
James-Franck-Str. 1, 85748 Garching, Germany
E-mail: bandarenka@ph.tum.de

S. Hou, Dr. W. Li, Prof. A. S. Bandarenka, Prof. R. A. Fischer
Catalysis Research Center TUM
Ernst-Otto-Fischer-Straße 1, 85748 Garching, Germany
E-mail: wj.li@tum.de; roland.fischer@tum.de

Dr. W. Li, Prof. R. A. Fischer
Chair of Inorganic and Metal–Organic Chemistry
Department of Chemistry
Technische Universität München
Lichtenbergstraße 4, 85748 Garching, Germany

The ORCID identification number(s) for the author(s) of this article can be found under https://doi.org/10.1002/adma.202103218.

DOI: 10.1002/adma.202103218

S. Yin, X. Jiang, Prof. P. Müller-Buschbaum
Lehrstuhl für Funktionelle Materialien
Physik-Department
Technische Universität München
James-Franck-Str. 1, 85748 Garching, Germany

Dr. M. Döblinger
Department of Chemistry
Ludwig-Maximilians-Universität München
Butenandtstr. 5–13 (E), 81377 München, Germany

Dr. A. Welle, Prof. C. Wöll
Institut für Funktionelle Grenzflächen (IFG)
Karlsruhe Nano Micro Facility (KNMF)
Karlsruher Institut für Technologie (KIT)
76021 Karlsruhe, Germany

M. Koch
Department of Chemistry
Technische Universität München
Lichtenbergstraße 4, 85748 Garching, Germany

Prof. P. Müller-Buschbaum
Heinz Maier-Leibnitz Zentrum (MLZ)
Technische Universität München
Lichtenbergstr. 1, 85748 Garching, Germany

electrocatalysts and enables precise adjustment of defects and accessible active centres at the molecular level. Interestingly, heterostructured systems generally exhibit a higher catalytic activity than their uniformly structured counterparts, attributed to synergistic effects of the electrode structure/composition and interface properties.[17–21] Herein, we demonstrate taking advantage of both, the opportunities of SURMOF heterostructure growth and of their unique metamorphosis to yield metal oxo/hydroxo materials of special morphology and microstructure. We measured record oxygen evolution mass activities of ≈2.90 kA g^{-1} at the overpotential of 300 mV in 0.1 M KOH, superior to the benchmarking precious and nonprecious metal electrocatalysts. To the best of our knowledge, this is the highest reported mass activity for NiFe-based electrocatalysts.

SURMOFs have been reported to yield highly active electrocatalysts toward water oxidation, but the electrochemical stability or transformations and the origin of active species in MOF-based catalytic systems remain elusive.[22,23] Recent studies focus on the elucidation of the active species in MOF-based catalytic systems, and discover the presence of metal hydroxides in the electrochemically tested (SUR)MOF catalysts via a series of advanced physicochemical techniques.[24–27] Therefore, the stated active species were presumed to originate from MOF-derived metal hydroxides during the oxygen electrocatalytic process in alkaline electrolytes. Despite some recent efforts devoted to elucidate the catalytic species, an in-depth understanding of the transformation mechanisms and the structure–performance relationships remains open.

In this work, we use heterostructured NiFe-based SURMOFs composed of deprotonated terephthalic acid ($[TA]^{2-}$) linkers and exploit variants in structure and composition to optimize the OER performance. The experiments show that heterostructured SURMOFs undergo specific in situ reconstruction and self-activation process during the alkaline immersion and the electrochemical measurements, resulting in metal hydroxides and oxyhydroxides together with a partial leaching of the organic linkers. We propose using SURMOFs as precursors allowing for access to a parameter space of catalyst fabrication, which is beyond existing synthetic concepts.

2. Results and Discussion

The NiFe-based SURMOFs have been prepared through a stepwise layer-by-layer deposition process on functionalized gold substrates, as illustrated in Figure S1 in the Supporting Information. Three different types of samples have been prepared. The first type, heterostructured Ni|Fe-[TA]-SURMOFs, have been prepared using a two-step procedure. Initially, 15 layers of Ni-[TA] have been deposited on the gold substrate, followed by a deposition of 15 layers of Fe-[TA] on top. Note that "Ni|Fe" in the formula indicates the Ni-containing layers being the bottom layers and the Fe-containing layers being the top layers. The second type of sample is a mixed-phase NiFe-[TA]-SURMOFs prepared by simultaneous layer-by-layer deposition of both Ni- and Fe-layers in the presence of $[TA]^{2-}$. The third sample, Fe|Ni-[TA]-SURMOFs have been obtained by initially depositing 15 layers of Fe-[TA] followed by 15 layers of Ni-[TA]. More details are given in the experimental section. According to structural engineering, heterostructures do not solely induce the electron transfer between different components to expose more active sites, but also facilitate the mass diffusion by rationally constructing well-defined nanostructures.[28,29] In this light, the three NiFe-based SURMOFs and 30-layer monometallic Ni-[TA]-SURMOFs are further investigated to explore their catalytic performance for water oxidation.

To accurately evaluate the electrocatalytic performance, the activity of as-prepared electrodes is normalized to the catalyst's mass and geometric surface area of the electrode, respectively.[30] Before and after the electrochemical measurement, the electrodes' mass loading is recorded by a quartz crystal microbalance (QCM). Note that in **Figure 1**A the mass loading of SURMOF electrodes dramatically decreases after OER activity measurements in 0.1 M KOH solution. This indicates that components of the SURMOFs partially leached out, and the SURMOFs are transformed into SURMOF derivatives. We will refer to the SURMOFs after electrochemical cycling as "Catalysts." Hence, the derivatives of Ni|Fe-[TA]-SURMOFs, NiFe-[TA]-SURMOFs, Fe|Ni-[TA]-SURMOFs, and Ni-[TA]-SURMOFs are in the following denoted as Ni|Fe-[TA]-Catalyst, NiFe-[TA]-Catalyst, Fe|Ni-[TA]-Catalyst and Ni-[TA]-Catalyst, respectively. As shown in Figure 1B,C and Figure S2A (Supporting Information), the Ni|Fe-[TA]-Catalyst records a remarkable current density of ≈2.90 kA g^{-1} at the overpotential of 300 mV, which is nearly 5, 10 and 12 times higher than the mass activities of NiFe-[TA]-Catalyst (≈0.58 kA g^{-1}), Fe|Ni-[TA]-Catalyst (≈0.28 kA g^{-1}), and Ni-[TA]-Catalyst (≈0.25 kA g^{-1}), respectively. Moreover, the same catalytic activity trend based on the geometric current density can be found in Figure S2C,D in the Supporting Information, reiterating the remarkable OER performance of Ni|Fe-[TA]-Catalyst. These results suggest that the heterogeneous structure constructed by rationally adjusting the arrangement of Ni and Fe-based SURMOFs has a significant influence on the OER electrocatalytic performance. The corresponding Tafel slopes are utilized to study OER kinetics (Figure 1D; Figure S2D, Supporting Information). In the case of mass activity, the Ni|Fe-[TA]-Catalyst exhibits the lowest Tafel slope of ≈44.3 mV dec^{-1} compared to NiFe-[TA]-Catalyst (≈54.2 mV dec^{-1}), Fe|Ni [TA] Catalyst (≈60.8 mV dec^{-1}), and Ni-[TA]-Catalyst (≈87.1 mV dec^{-1}), further verifying the better OER reaction kinetics of Ni|Fe-[TA]-Catalyst. As shown in Figure 1E, Figure S3 (Supporting Information), Tables S1 and S2 (Supporting Information), the Ni|Fe-[TA]-Catalyst achieves an activity of ≈2.90 kA g^{-1} at the overpotential of 300 mV, outperforming other most recent state-of-the-art OER electrocatalysts. Moreover, the electrocatalytic activity of the Fe-[TA]-Catalyst is shown in Figure S4 in the Supporting Information, exhibiting a low intrinsic activity of ≈0.029 kA g^{-1}. However, due to the unstable characteristics of FeOOH at high biases,[31,32] the polarization curve of the Fe-[TA]-Catalyst exhibits a declining trend at an increased number of cycles.

In the following, we utilize various ex situ and in situ techniques to shed light on the nature of the active surface species and the structural evolution of SURMOFs during the electrochemical treatment. Initially, QCM measurements are carried out to monitor the mass changes during the structural evolution of SURMOFs. As shown in Figure S5 in the Supporting Information, the mass loading on the QCM electrode decreases from ≈2.77 to ≈1.77 μg after the immersion in 0.1 M KOH

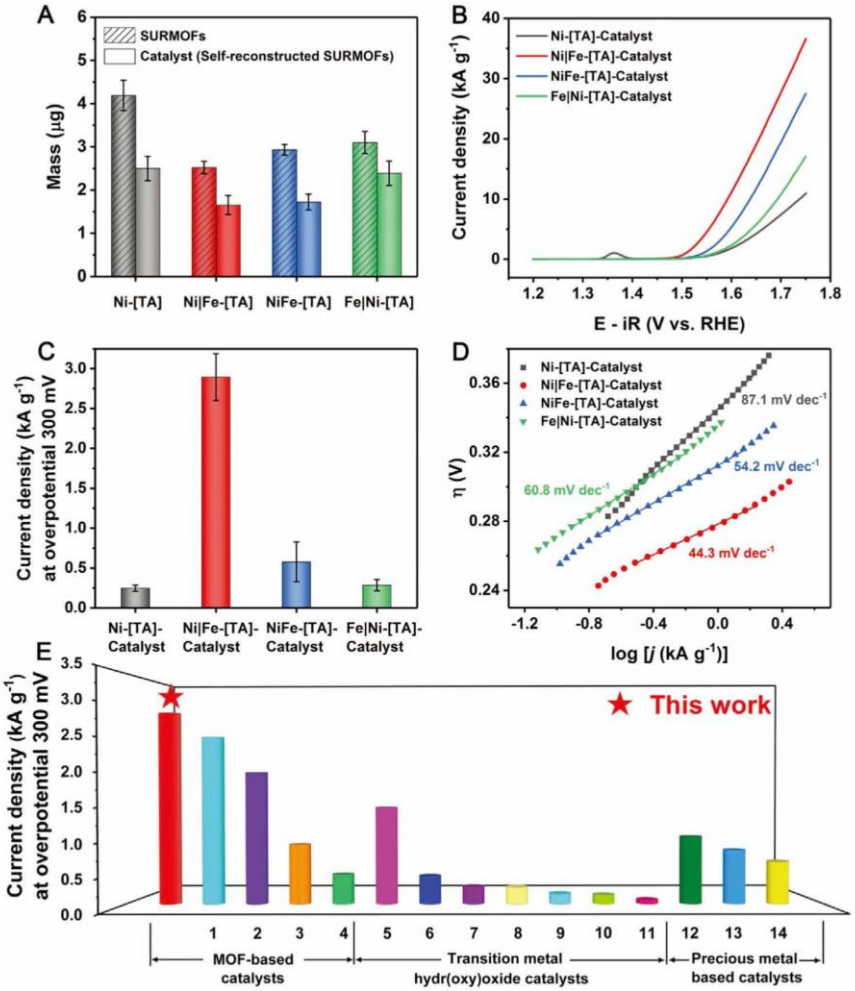

Figure 1. A) The mass loading of SURMOFs and Catalysts (self-reconstructed SURMOFs after electrochemical cycling) measured on the Au QCM electrodes. B) Polarization curves of Catalysts collected in 0.1 M O_2-saturated KOH with a scan rate of 5 mV s^{-1}. Current densities are normalized to the Catalyst mass. C) Comparison of mass activities at an overpotential of 300 mV for these Catalysts. D) The corresponding Tafel plots of all Catalysts. E) Comparison of the OER mass activity of Ni|Fe-[TA]-Catalyst with benchmarked data of state-of-the-art catalysts. 1–4) MOF-based catalysts, 5–11) transition metal (oxy)hydroxide catalysts and 12–14) precious-metal-based catalysts are compared at an overpotential of 300 mV: 1) 50Ni50Co-SURMOFD 10 cycles,[14] 2) lattice-strained 4.3%-MOF,[33] 3) NiFe-BTC-GNPs,[34] 4) [M(BDC)] nanosheets (M = Ni^{2+}, Co^{2+}),[35] 5) Cu–Ni–Fe hydr(oxy) oxide,[36] 6) NiFe-LDH@NiCu,[37] 7) δ-FeOOH NSs/nickel foam,[38] 8) NiFe LDH nanomesh,[39] 9) CoMn LDH,[40] 10) $Ni_{0.8}Fe_{0.2}O_xH_y$,[41] 11) γ-CoOOH nanosheets,[42] 12) $Rh_{22}Ir_{78}$/VXC,[43] 13) Ir-network,[44] and 14) Co–IrCu ONC/C.[45] For more details on the experimental conditions, please refer to Table S1 in the Supporting information.

solution for 3 min, revealing that the as-prepared SURMOFs are unstable in an alkaline medium. Meanwhile, the ex situ Raman and NMR spectra confirmed the rapid leaching of the organic linkers and the generation of FeOOH species during the 3 min KOH immersion process (Figures S6 and S7, Supporting Information). After that, cyclic voltammetry (CV) is performed to promote further the structural evolution of the SURMOFs (**Figure 2**A). It is found that the polarization curve of the first cycle shows an anodic peak in the potential range of 1.25–1.46 V versus the reversible hydrogen electrode (RHE). This increase in faradaic current can be assigned to the oxidation of SURMOF species.[16,26] Furthermore, the oxidation current increases in a higher potential range (1.46–1.54 V), suggesting that more SURMOF species are oxidized. With the increasing number of cycles, a distinguishable redox couple peak corresponding to the reversible redox transition between Ni^{2+} and Ni^{3+} species can be observed.[16,46,47] Notably, both the Ni^{2+}/Ni^{3+} redox peak and the OER current gradually increase and stabilize after the 35th cycle. This can be ascribed to the continuous exposure of Ni^{2+}–Ni^{3+} species and an increasing number of accessible catalytically active sites. Therefore, it is meaningful to denote the SURMOFs after the electrochemical

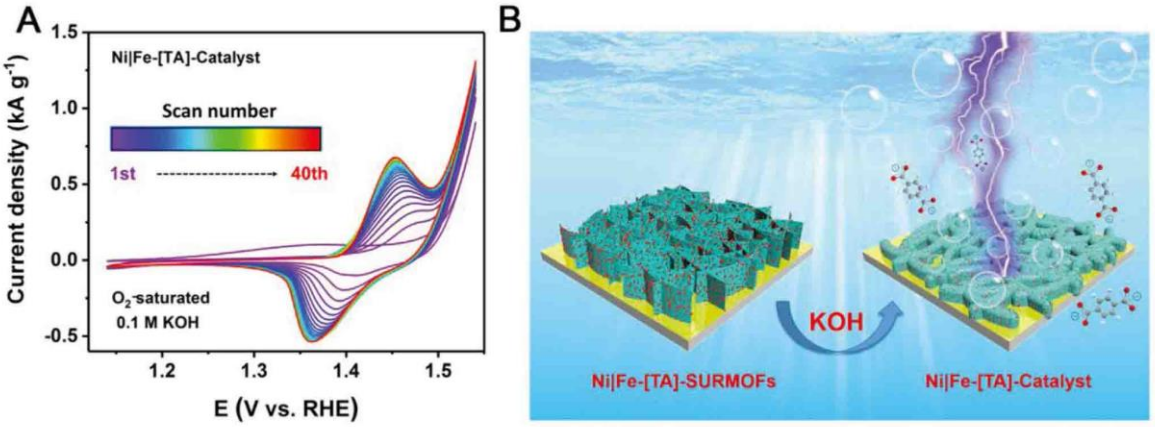

Figure 2. A) Cyclic voltammogram of Ni|Fe-[TA]-Catalyst electrode recorded with scan rate 20 mV s^{-1} for 40 cycles in 0.1 M KOH solution. B) Schematic illustration showing the transformation process of heterostructured SURMOFs into Catalysts in alkaline electrolyte.

cycling as "Catalysts." According to these facts, we propose a mechanism for the structural evolution of SURMOFs into Catalysts, as shown in Figure 2B. Heterostructured SURMOFs are undergoing an in situ self-reconstruction process in the alkaline electrolyte. In the case of the alkaline-unstable SURMOF thin films, the coordinate bonds between metal nodes and organic linkers can be dissociated in the KOH electrolyte, thereby leading to the replacements of organic linkers by the OH^-/H_2O. In this process of SURMOF metamorphosis, phase structural transition facilitates the generation of disordered NiFe hydroxides, which generally possess abundant defects. Subsequently, CV cycling accelerates the reconstruction and self-activation processes, leading to the exposure of a higher number/density of active sites, which significantly improve the OER activity.

From the electrochemical data, it becomes apparent that a change in composition takes place after electrochemical cycling. The increase in OER current implies a higher number of active sites being available. The latter translates into structural changes. To directly access the crystalline structure and orientation of the SURMOFs during this structural evolution, grazing-incidence wide-angle X-ray scattering (GIWAXS) is performed on these samples. **Figure 3** illustrates the 2D GIWAXS patterns and the corresponding line-cut profiles of the Ni|Fe-[TA]-SURMOFs, the Ni|Fe-[TA]-SURMOFs after 3 min immersion in 0.1 M KOH solution (denoted as KOH immersion), and the Ni|Fe-[TA]-Catalyst. In the 2D GIWAXS data (Figure 3A–C; Figure S9, Supporting Information), two significant diffraction rings at scattering vectors of q = 2.64 and 3.04 $Å^{-1}$ are visible for all samples, which are dominated by the scattering signals of the QCM substrate. More importantly, two pronounced Bragg diffraction spots in the scattering patterns are present in the 2D GIWAXS data (Figure 3A,C), corresponding to the generation of crystalline phases on the as-prepared SURMOFs and its NiFe hydroxide derivatives, respectively.[35,48] These diffraction spots manifest a high degree of preferential crystallographic orientation pertaining to the substrate.[49] Furthermore, from cake-cuts of the GIWAXS patterns, the (010), (600), (1-10), and (210) Bragg peaks located at q = 2.93, 2.95, 2.98, and 3.09 $Å^{-1}$, respectively, are present in the Ni|Fe-[TA]-SURMOFs (Figure 3D,E; Table S4, Supporting Information), indicating its high crystallinity. Note that these crystalline structures of the SURMOFs are destroyed after 3 min KOH-immersion procedure, as indicated by the loss of the (010), (600), (1-10), and (210) diffraction signals. After the electrochemical treatment, a new diffraction peak located at q = 2.72 $Å^{-1}$ appears in the line-cut profile of Ni|Fe-[TA]-Catalyst (Figure 3E; Table S5, Supporting Information), corresponding to the (015) diffraction peak of NiFe layered double hydroxide (NiFe-LDH).[48] Additionally, a preferential orientation located at around χ = 34.5° with a broad orientation distribution can be observed for Ni|Fe-[TA]-SURMOFs (Figure 3F; Figure S10A, Supporting Information). In contrast, there is no orientation peak in the tube cut pattern of the Ni|Fe-[TA]-KOH immersion sample, indicating a structural collapse of high-order MOFs and the generation of amorphous NiFe hydroxide. On the Ni|Fe-[TA]-Catalyst, a sharp peak at χ = 45.4° with a narrow orientation distribution is detected in the tube cut pattern (Figure 3F; Figure S10C, Supporting Information). From these observations, one can conclude that the evolution process from the as-prepared SURMOFs to the Catalyst involves two steps. The first step includes the phase transition of crystalline SURMOFs into amorphous NiFe hydroxide during the KOH immersion treatment. Afterward, NiFe-layered double hydroxide (LDH) material with crystallographic orientation is generated after the electrochemical activation.

To elucidate the structural transformation of the SURMOFs, especially the existence of morphological structures during the derivation process, scanning electron microscopy (SEM), atomic force microscopy (AFM) and transmission electron microscopy (TEM) are performed on the freshly prepared samples. Interestingly, the heterostructures can be easily inferred from the hierarchical ultrathin nanosheet array and nanoclusters in Ni|Fe-[TA]-SURMOFs and Fe|Ni-[TA]-SURMOFs (Figures S12C and S14C, Supporting Information), where the ultrathin nanosheets represent Ni-[TA]-SURMOFs and nanoclusters are from Fe-[TA] -SURMOFs. A more detailed discussion is given in the Supporting Information. After the OER test, significant morphology changes are observed for all

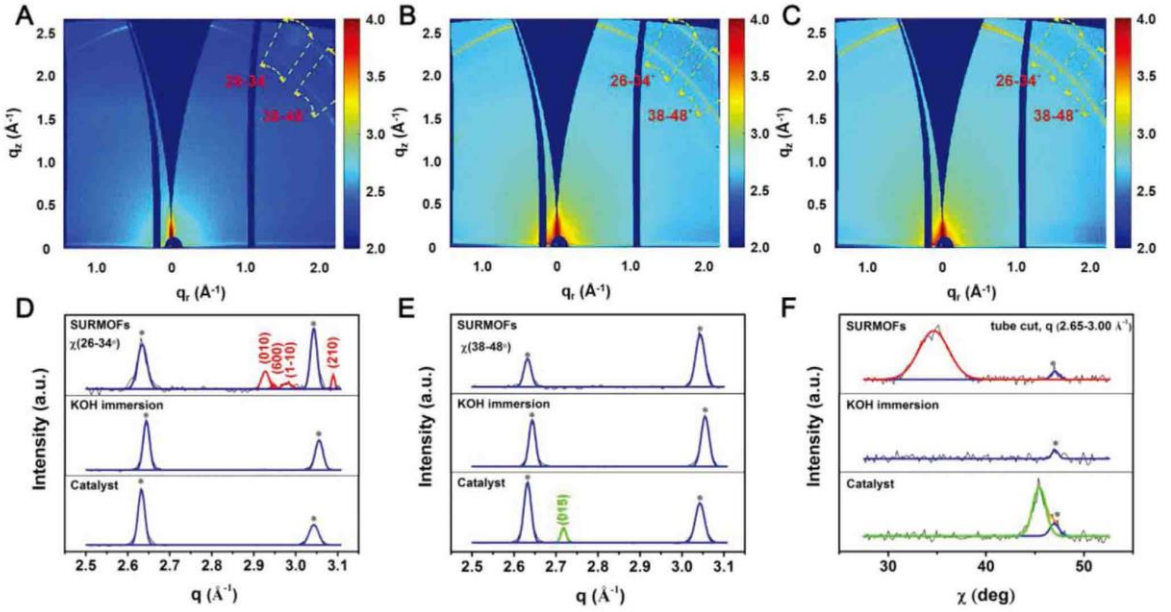

Figure 3. A–C) 2D GIWAXS data of the Ni|Fe-[TA]-SURMOFs in the as-prepared state (A), after 3 min immersion in a 0.1 M KOH solution (B) and after electrochemical cycling until the Ni|Fe-[TA]-Catalyst is obtained (C). D,E) Cake cuts performed at angles between $\chi = 26–34°$ (D) and 38–48° (E) derived from the 2D GIWAXS data. F) Tube cuts in a q range of 2.65–3.00 Å^{-1}. All Peaks are fitted with Gaussian functions. The peaks denoted with a star (*) can be assigned to the diffraction peaks (blue lines) of the substrates. The red lines represent oriented Ni|Fe-[TA]-SURMOFs crystals and the green lines represent oriented NiFe layered-double-hydroxides crystals.

samples as shown in the SEM images (Figures S11D, S12D, S13D, and S14D, Supporting Information). These interconnected nanofiber networks, which cover the gold substrate, are derived from the nanosheet structures of the pristine SURMOFs after the OER test. Moreover, AFM images reveal the decreased roughness and thickness in these SURMOF derivatives compared with the initial SURMOF-coated electrodes (Figures S12E,F, S13E,F, and S14E,F and Table S6, Supporting Information), which provide further support for the reconstruction of the SURMOFs in the alkaline electrolyte. From the TEM image shown in **Figure 4**A, the ultrathin nanosheets can be observed in the Ni|Fe-[TA]-SURMOFs, corresponding to the 2D Ni-[TA]-SURMOFs. Benefiting from the unique ultrathin morphology, these nanosheets are embedded in a matrix of nanoparticles with uniform sizes, where the nanoparticles should be attributed to the Fe-[TA] according to the SEM image in Figure S12C in the Supporting Information. In Figure 4D, the TEM image of the Ni|Fe-[TA]-Catalyst shows a similar matrix of nanoparticles, however the nanosheets are not observable anymore, suggesting the structural transformation of SURMOFs after the OER test. The diffraction patterns of both samples show broad diffraction rings on a strong diffuse background, and the latter indicates a large amorphous material fraction. The d-values in the inset of Figure 4A are very similar with the structure of SURMOFs, while the *d*-values obtained from the stronger diffraction rings in inset of Figure 4D are in agreement with $Fe_{0.67}Ni_{0.33}OOH$ (PDF#00-014-0556). The high-resolution TEM image in Figure 4B further reveals the presence of nanosheets, whereas lattice fringes are not visible due to low crystallinity and beam sensitivity. In addition, energy-dispersive X-ray spectroscopy (EDX) elemental mappings are used to study the elementary distribution of O, Fe, and Ni. In overlap elemental mappings of Fe and Ni (Figure 4C), the Fe signal is much stronger than the Ni, which is in good agreement with the heterostructures in Ni|Fe-[TA]-SURMOFs. After the OER test, EDX elemental mappings in STEM mode show the uniform distribution of O, Fe, and Ni in the Ni|Fe-[TA]-Catalyst (Figure 4F).

To gain deeper insight into the self-reconstruction process of heterostructured SURMOFs, time-of-flight secondary ion mass spectrometry (ToF-SIMS) is conducted to ascertain the evolution of chemical species at both surface and bulk of catalyst thin film. As representatively shown in **Figure 5**A,B for Ni|Fe-[TA]-SURMOFs, the intensity of the Fe^+ signal is much stronger than that of the Ni^+. The opposite trend in Fe^+ and Ni^+ signal intensities is found for Fe|Ni-[TA]-SURMOFs (Figure S17A,B, Supporting Information). This result can be ascribed to the achievement of well-designed heterostructures, e.g., the bottom-layer Ni-[TA] in Ni|Fe-[TA]-SURMOFs is covered by the top-layer Fe-[TA], leading to a stronger Fe-signal in the surface chemical mapping image. After the electrochemical activation, the signal ratio of Fe:Ni species significantly decreases from 16.5:1 to 1.98:1 when Ni|Fe-[TA]-SURMOFs are transformed into Ni|Fe-[TA]-Catalyst (Figure 5C,D; Table S7, Supporting Information). Therefore, it is reasonable to assume a self-reconstruction and re-distribution of Ni and Fe species in the pristine SURMOFs during the electrochemical treatment in alkaline media. In addition, ToF-SIMS depth profiles are measured to ascertain the distribution of C, Ni and Fe species

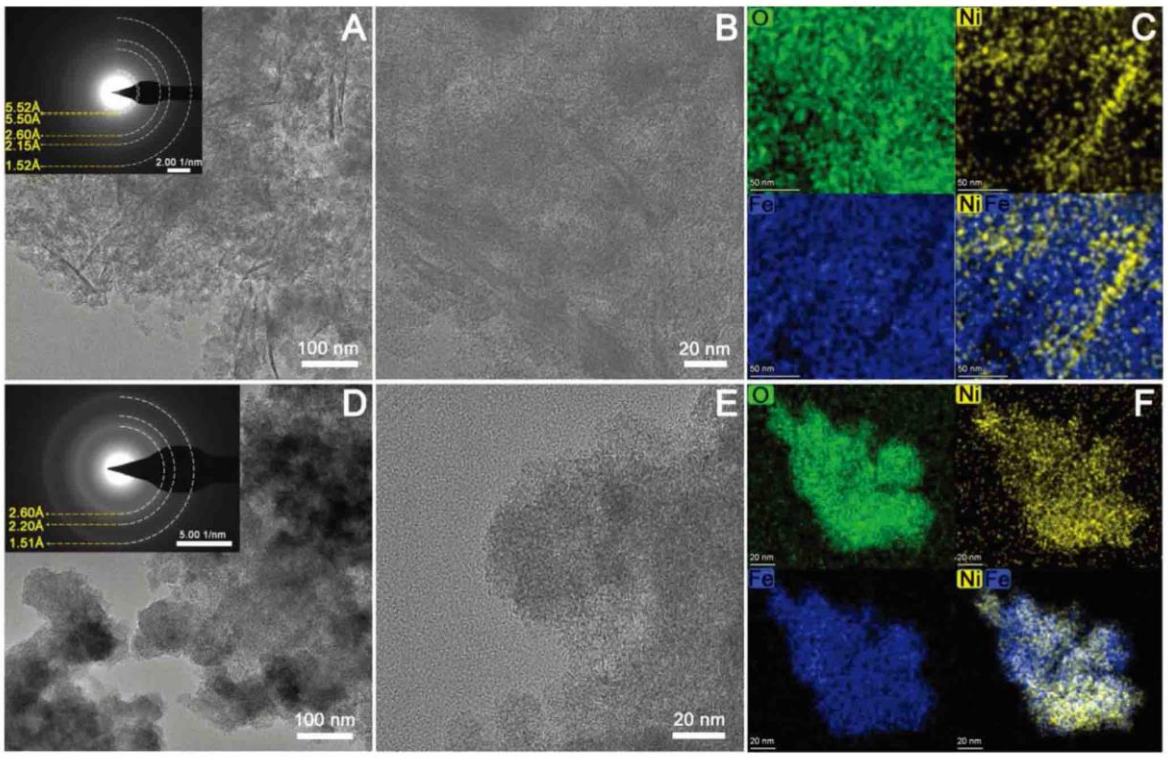

Figure 4. A,B) TEM and HRTEM images of Ni|Fe-[TA]-SURMOFs. The inset in (A) represents the selected-area electron diffraction (SAED) pattern. C) EDX elemental mappings in STEM mode of O, Fe, and Ni in Ni|Fe-[TA]-SURMOFs. D,E) TEM and HRTEM images of Ni|Fe-[TA]-Catalyst. The inset in (D) represents the SAED pattern. F) EDX elemental mappings in STEM mode of O, Fe, and Ni in Ni|Fe-[TA]-Catalyst.

in the bulk of SURMOFs and their derived Catalysts. For Ni|Fe-[TA]-SURMOFs, a Fe^{+} signal can be detected in the initial 25 s. Afterward, the intensity rapidly increases to reach its maximum with a subsequent decrease as the sputtering further proceeds (Figure 5E). In comparison, the curve of Ni^{+} signal lags behind that of Fe^{+} signal, which is in good agreement with the heterostructural design concept. However, after electrochemical activation, the distribution of Ni- and Fe-species changes dramatically in the Ni|Fe-[TA]-Catalyst as shown in Figure 5F. Therefore, these observations coincide well with a self-reconstruction process.

X-ray photoelectron spectroscopy (XPS) analysis is performed to explore the surface chemical states and chemical composition of the as-prepared electrodes. As shown in **Figure 6A**, the C 1s spectrum of Ni|Fe-[TA]-SURMOFs deconvolutes into three peaks at binding energies of 284.8, 286.7, and 288.5 eV, which are attributed to C—C, C—O, and O=C—O bonds, respectively. These groups are expected since the organic linkers have been used in the synthesis process.[15,50,51] Corresponding peaks are also detected in the C 1s spectrum of Ni|Fe-[TA]-Catalyst, revealing the existence of residual organic linkers after OER. A new peak at 293 eV appears due to the presence of K^{+}, stemming from the KOH electrolyte.[50] Thus, the C 1s spectrum provides additional evidence for the residues of organic linkers in the derived catalysts. In the O 1s spectrum of the Ni|Fe-[TA]-SURMOF, two peaks at 531.7 and 532.9 eV can be assigned to O=C—O groups and C—O bonds of the organic linkers (Figure 6B).[52,53] The intensity of both peaks significantly decreases after electrochemical activation. In contrast, the intensity of the other two peaks at 529.7 and 530.2 eV dramatically increases, corresponding to Ni(Fe)-oxygen bonds and Ni(Fe)-hydroxyl species, respectively.[50,54] This comparison demonstrates that organic linkers partially and gradually leaches into the electrolyte during the immersion in KOH and the electrochemical potential cycling. In addition, the relative content of Ni(Fe)-hydroxyl species increases after KOH immersion and electrochemical measurements, suggesting that a large number of Ni(Fe)-hydroxyl species are produced during electrochemical activation in KOH electrolyte (Table S8, Supporting Information). The high-resolution Fe 2p spectrum of Ni|Fe-[TA]-SURMOFs shows the Fe $2p_{3/2}$ and $2p_{1/2}$ peaks at 710.7 and 723.9 eV with two corresponding satellite peaks (Figure 6C), clearly indicating the presence of Fe^{3+}.[55] The Fe $2p_{3/2}$ peak of Ni|Fe-[TA]-Catalyst is positively shifted by ≈0.7 eV in comparison to the corresponding peak of the initial Ni|Fe-[TA]-SURMOFs, due to the dissociation of the organic linkers from the metal–organic coordination bond after the electrochemical process, resulting in a replacement of $[TA]^{2-}$ with OH^{-}/O^{2-}.[24,56] As such, the positively shifted binding energy indicates the decreased electron density in Fe^{3+} centers, owing to the change in coordination environment of Fe^{3+}.[24,56–58] Analogously, in the case of the Ni 2p spectrum of Ni|Fe-[TA]-SURMOFs (Figure 6D), two

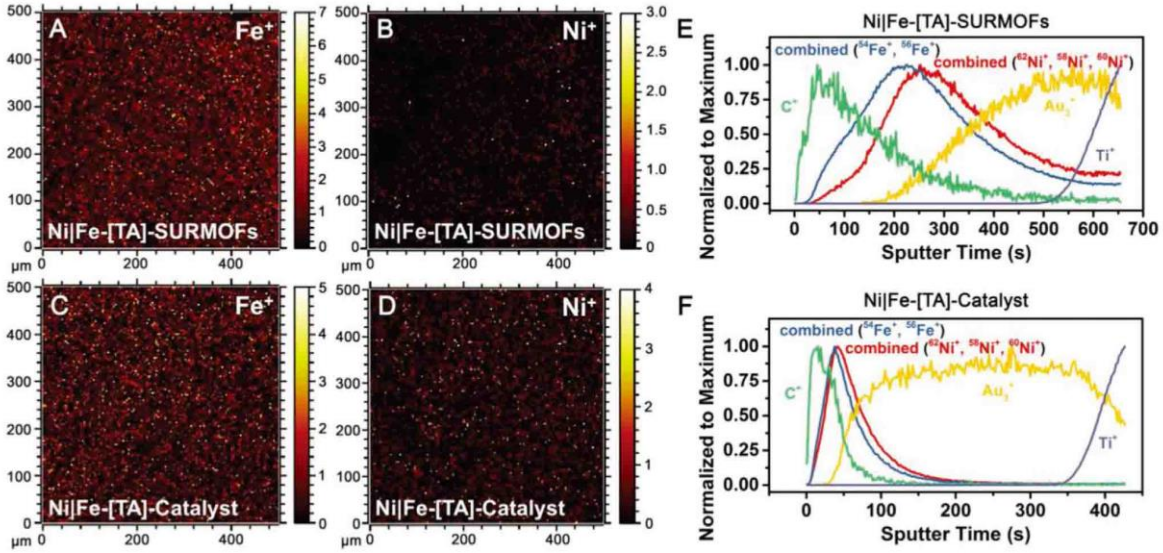

Figure 5. A–D) ToF-SIMS chemical mapping of Fe and Ni signals in the probed topmost layer of Ni|Fe-[TA]-SURMOFs and Ni|Fe-[TA]-Catalyst. E,F) Normalized ToF-SIMS intensities of C^+, Fe^+, Ni^+, Au^{3+}, and Ti^+ secondary ions along the depth profile of the Ni|Fe-[TA]-SURMOFs and Ni|Fe-[TA]-Catalyst. The Ti acts as an adhesion promoter underneath the gold electrode.

characteristic peaks are present at 856.2 and 874.1 eV, corresponding to Ni $2p_{3/2}$ and Ni $2p_{1/2}$, respectively, which can be assigned to Ni^{2+}, indicating the existence of pure Ni-[TA] SURMOFs.[59,60] Moreover, the intensity of Ni 2p signals significantly increases after OER, indicating that more inner-layer Ni species diffused to the surface layer of catalysts. Initially, in Ni|Fe-[TA]-SURMOFs, the Ni-[TA] nanosheets are covered by large numbers of Fe-[TA] clusters. The structural evolution and

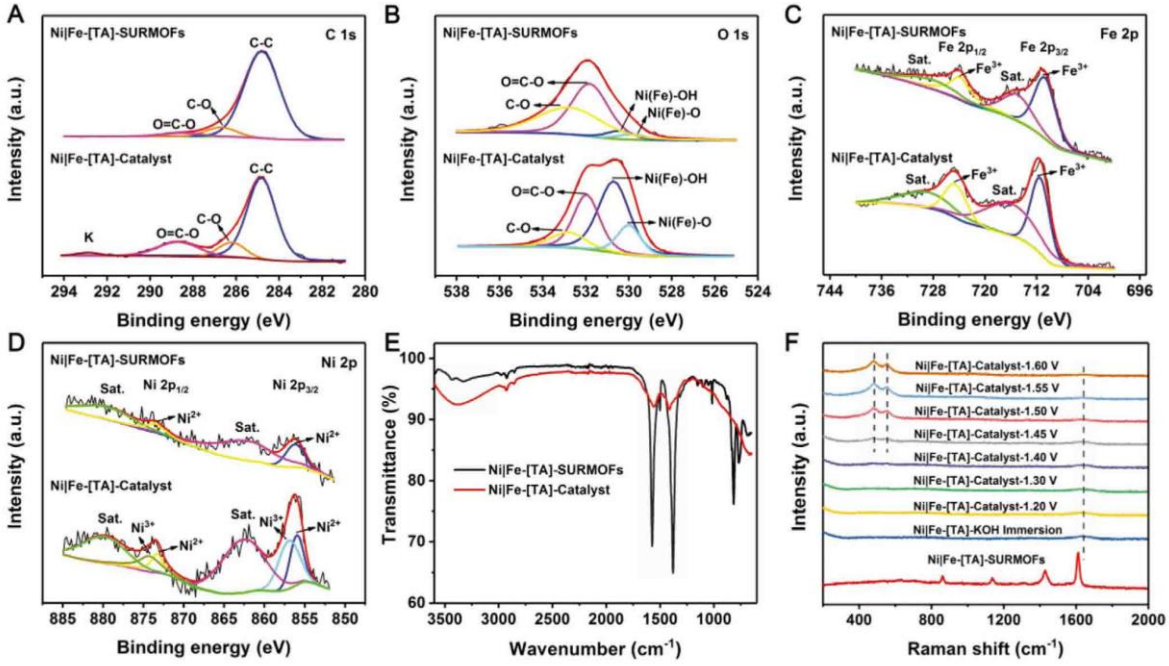

Figure 6. Spectral measurements on Ni|Fe-[TA]-SURMOFs and Ni|Fe-[TA]-Catalyst. a–d) High-resolution XPS spectra of C 1s (A), O 1s (B), Fe 2p (C), and Ni 2p (D). E) FT-IR spectra. F) In situ Raman spectra collected during the OER process in 0.1 M KOH within a low-wavenumber region of 200–2000 cm^{-1}.

self-activation in alkaline solution expose more active Ni species to the surface of catalysts. The high-resolution Ni 2p XPS spectrum of Ni|Fe-[TA]-Catalyst differs from that of the pristine SURMOFs. The Ni $2p_{3/2}$ spectrum can be deconvoluted into two distinct peaks. A peak located at 856.0 eV is assigned to the Ni^{2+} species in $Ni(OH)_2/NiO_x$, where the binding energy is slightly higher than that of the Ni^{2+} peak in pure $Ni(OH)_2/NiO_x$ (≈855.4 eV) reported in the literature.[24,56,61,62] This higher binding energy found here indicates a lower electron density of Ni^{2+} centers in the derived Catalysts. In detail, the strong electron-withdrawing ability of the bridging $[TA]^{2-}$ linkers in the SURMOFs can induce a decrease of the electron density of the Ni^{2+}-centers via a weakened electron–electron repulsion between the p-orbitals ($2p^6$) of the own O atoms of linkers and the fully occupied π-symmetry (t_{2g}) d-orbitals of the Ni^{2+} species, leading to the increase in the binding energy of Ni^{2+}.[35,56] Accordingly, the residual $[TA]^{2-}$ linkers and Fe^{3+} dopants (Ni^{2+}-X-Fe^{3+}, X = O^{2-}, or $[TA]^{2-}$) play an important role in the positive shift of Ni $2p_{3/2}$ spectrum in $Ni(OH)_2/NiO_x$ phase. Another characteristic peak at a higher binding energy of ≈857.0 eV is ascribed to Ni^{3+} species. The lowest Ni^{2+}:Ni^{3+} atomic ratio of 0.68:1 was obtained for Ni|Fe-[TA]-Catalyst. In comparison, for NiFe-[TA]-Catalyst and Fe|Ni-[TA]-Catalyst, a ratio of 1.08:1 and 2.49:1 is measured, respectively (Table S9, Supporting Information). This result indicates that more Ni^{3+} species are generated in Ni|Fe-[TA]-Catalyst during the potential cycling, which agrees with the trend of their OER performance. In the literature, it was reported that the high-oxidation state of Ni in NiFe-based double hydroxides can enhance the electrocatalytic activities toward water oxidation.[63]

Furthermore, Fourier transform infrared (FT-IR) spectroscopy results reveal that the chemical structures of these as-prepared SURMOFs drastically changed after the electrochemical process. As shown in Figure 6E, two peaks at 1571 and 1378 cm^{-1} assigned to the asymmetric stretching and symmetric stretching vibrations of the carboxyl groups in pristine Ni|Fe-[TA]-SURMOFs are observed, demonstrating the successful coordination of $[TA]^{2-}$ linkers with the metal ions in SURMOFs.[14,33,50] The intensity of the characteristic peaks of the carboxyl group significantly decreases after OER, suggesting partial leaching of organic linkers and the existence of residual $[TA]^{2-}$. Another broadened peak in the range of 3000–3550 cm^{-1} can be ascribed to O—H stretching vibration, which is characteristic for water molecules.[64]

Ex situ and in situ Raman spectroscopy are used to systematically investigate the structural self-reconstruction process from SURMOFs to catalysts during the OER process. Ni|Fe-[TA]-SURMOFs show four Raman shift peaks at 1610, 1430, 1140, and 863 cm^{-1} (Figure 6F), corresponding to coordinated organic linkers of pristine SURMOFs.[24] Interestingly, these peaks disappear after immersion into KOH for 3 min, indicating the destruction of the coordination of metal nodes and organic linkers after immersion in alkaline electrolyte. Meanwhile, a broad peak appears at ≈1637 cm^{-1}, which can be assigned to the uncoordinated carboxylate groups of $[TA]^{2-}$.[50] To further reveal the nature of the catalysts' active sites, an in situ electrochemical Raman spectroscopy is conducted. For potential below 1.40 V, the spectra remain unchanged. However, when the potential is increased to 1.45 V, two distinct Raman peaks evolve at around 482 and 554 cm^{-1}, which are attributed to Ni—O vibrations of the surface intermediate oxyhydroxide NiOOH.[65,66] The intensities of both peaks increase with increasing potentials and stabilize when the applied potential exceeded 1.50 V (Figure S20, Supporting Information). In addition, the intensity ratio of the two Ni—O Raman peaks (I_{554}/I_{482}) can be used to evaluate the structural disorder of NiOOH.[67,68] As shown in Figure S21 in the Supporting Information, in situ Raman experiment elucidates the high intensity ratio (≥0.84) of I_{554}/I_{482} in the OER potential region of 1.45–1.60 V versus RHE, suggesting abundant defects in the SURMOF derived NiOOH catalyst. Therefore, we can conclude that the generated Ni(Fe)-hydroxyl species, residual organic linkers and high oxidation state of Ni play a critical role in improving the OER performance.

The electroactive surface area (ECSA) of Catalysts and their density of active sites can be a decisive factor for their performance in the real application. However, the assessment of the ECSA is a nontrivial task in the case of metal oxides. In our previous work, we demonstrated an effective strategy to estimate the ECSA by analyzing the adsorption capacitance of OER species, which were reversibly adsorbed on the catalyst surface.[69] Therefore, electrochemical impedance spectroscopy (EIS) measurements are carried out at potentials close to the onset of the OER on the as-prepared catalysts. The EIS data were fitted and evaluated with the equivalent electric circuit (EEC) model shown in **Figure 7**A. The EEC used in this work, also known as Armstrong-Henderson EEC, accounts for the electrolyte resistance (R_s), a double layer impedance (Z_{dl}), a charge transfer resistance (R_{ct}), adsorption resistance (R_a), and the adsorption capacitance (C_a).[70,71] A representative Nyquist plot measured at 1.58 V is shown and fitted according to the EEC model (Figure 7A). As an outcome of the fit, the adsorption capacitances C_a for the different catalyst films are presented in Figure 7B, Figure S22B,D (Supporting Information) as a function of the applied potential. It can be seen that the C_a increases with increasing potentials, indicating the gradual activation of catalytically active centers (active sites). Remarkably, on Ni|Fe-[TA]-Catalyst, this activation occurs already at potentials lower than 1.50 V, while state-of-the-art NiFe catalysts do not show any increase in C_a at potentials below 1.55 V.[69] This is an additional indicator for the superior catalytic performance of this SURMOF derived catalyst. For a rough estimation of the ECSA, the adsorption capacitance is evaluated at 1.58 V and divided by the specific adsorption capacitance of NiFe at the same potential, i.e., C_a' (NiFe @ 1.58 V) ≈ 435 µF cm^{-2}. This yields an ECSA of ≈0.32 cm^2, which is ≈1.7 times higher than the geometric surface area of the substrate (≈0.196 cm^2). In other words, the synthesized Ni|Fe-[TA]-Catalyst has intrinsically a high density of active sites normalized to the geometric surface area, which is an additional reason for its outstanding activity. This is also reflected by significantly outperforming the Fe|Ni-[TA]-Catalyst and NiFe-[TA]-Catalyst, which show much lower C_a values, as can be seen in Figure 7C.

To further study the intrinsic electrocatalytic activity of prepared catalysts, the OER reaction kinetics are accessed by CV measurements at different temperatures. Noticeably, the temperature rises from 303.65 to 333.15 K results in an increased current density for the Ni|Fe-[TA]-Catalyst (Figure 7D), confirming the temperature dependence of OER performance. The

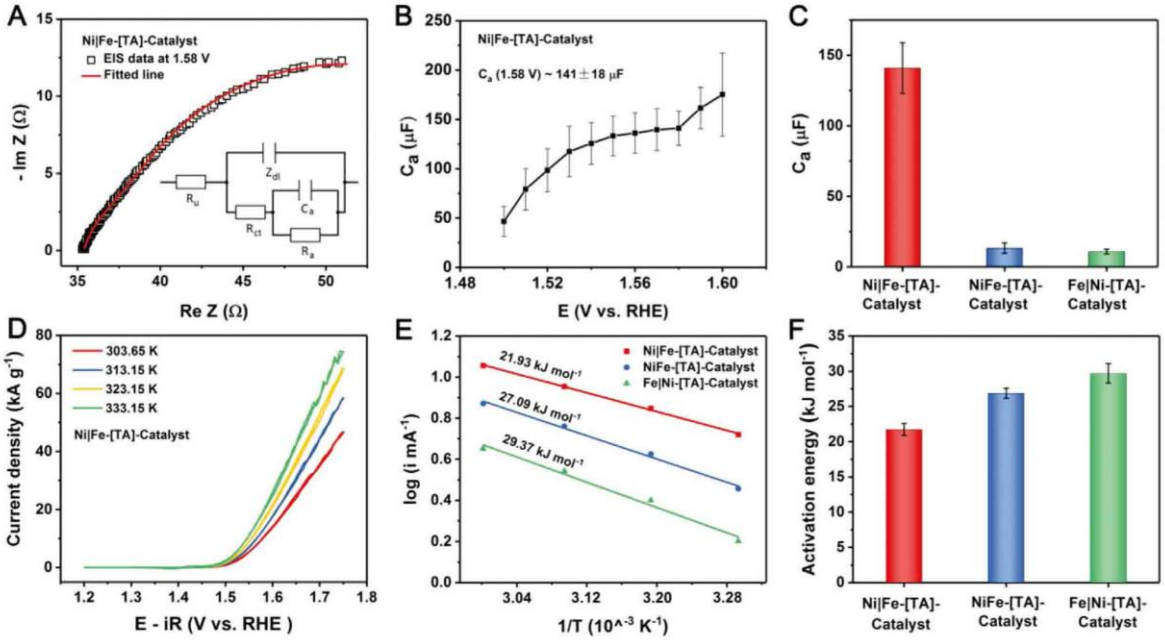

Figure 7. A) EIS data (black squares) of a Ni|Fe-[TA]-Catalyst electrode recorded at a potential of 1.58 V. The data were fitted (red line) according to the equivalent electric circuit shown in the inset. B) Adsorption capacitances of the Ni|Fe-[TA]-Catalyst electrode as a function of potential, recorded in a potential range from 1.50 to 1.60 V in Ar-saturated 0.1 M KOH. C) Comparison of the adsorption capacitances of the three different Catalysts. D) Polarization curves of Ni|Fe-[TA]-Catalyst electrode measured under various temperatures with a scan rate of 5 mV s^{-1} in O_2-saturated 0.1 M KOH. E) Arrhenius plot of the apparent exchange current as a function of temperature and F) calculated activation energy for all catalysts. The error bars were obtained from at least three independent experiments.

related Arrhenius plots extracted at the low current region for each of the different catalysts are linearly fitted as presented in Figure 7E. Their apparent activation energy is calculated via the slope of the Arrhenius plot.[72] Figure 7F displays the average apparent activation energy value (≈21.73 kJ mol^{-1}) for Ni|Fe-[TA]-Catalyst, which is significantly smaller than that for NiFe-[TA]-Catalyst (≈26.88 kJ mol^{-1}) and Fe|Ni-[TA]-Catalyst (≈29.70 kJ mol^{-1}).

Chronopotentiometry experiments at three different current densities of 1.0, 2.0, and 3.0 kA g^{-1} confirm the high stability of the Ni|Fe-[TA] Catalyst for more than 34 h (Figure S23A, Supporting Information). Interestingly, the polarization curve after the 34-hour long-term test displays a slight increase in comparison with that before the long-term test (Figure S23B, Supporting Information). The redox peaks of Ni^{2+}/Ni^{3+} show a significantly positive shift, which can be due to the aging process.[68] The durability of the Ni|Fe-[TA]Catalyst is also examined via CVs. As shown in Figure S23C in the Supporting Information, similar trends of current increase and positive shift of redox peaks are obtained during the 400-cycle measurement, further confirming the aging process. Consistently, SEM, XRD, Raman, and XPS characterizations are performed to investigate the chemical properties of Ni|Fe-[TA]-Catalyst after the long-term test. In Figure S24 in the Supporting Information, the similar interconnected nanofiber networks can be found from the SEM image and no distinct XRD peak presents in the GIXRD pattern. Two peaks in the Raman spectra appear at around 478 and 545 cm^{-1}, corresponding to Ni—O vibrations of the NiOOH. XPS analysis displays that partial organic links and abundant metal hydroxides construct the SURMOF derivatives. These pieces of evidence reveal the excellent structural and catalytic stability.

3. Conclusion

We have developed a facile strategy to prepare highly active LDH-type electrocatalysts of unique morphology and microstructure by reconstruction and self-activation of heterostructured SURMOFs. A series of ex situ and in situ experiments are carried out to reveal the details of the structural evolution process. The results confirm that KOH immersion and electrochemical potential cycling transform the alkaline-unstable NiFe heterostructured SURMOFs into electrocatalytically active derivatives. This transformation is characterized by the partial leaching of organic linkers and the generation of NiFe hydroxides/oxyhydroxides. Among the series of evaluated SURMOF derived catalysts in this study, the Ni|Fe-[TA]-Catalyst, which is formed from heterostructured Ni|Fe-[TA]-SURMOFs, shows the highest OER activity with a mass activity of ≈2.90 kA g^{-1} at an overpotential of 300 mV. We ascribe this excellent performance to the unique crystalline–amorphous phase obtained, which features a high content of Ni species in a higher oxidation state, a large electroactive surface area and a low apparent activation

energy. In this work, we do not only study the origin of catalytic activity for SURMOF-derived materials systematically, but we also show a promising route to design and fabricate high-efficiency electrocatalysts via the in situ reconstruction of heterostructured SURMOFs in alkaline electrolytes. In summary, our results suggest SURMOF technology to provide a novel parameter space LDH-type electrocatalyst fabrication to be further exploited and holds promise for further OER efficiency optimizations. More variations in the SURMOF fabrication can be envisaged, also including different electrode substrate materials and 3D shaped structures, which all-together may cause different kinds of kinetically controlled morphology transformation, structural metamorphosis, and self-activation.

Supporting Information

Supporting Information is available from the Wiley Online Library or from the author.

Acknowledgements

Financial support from the International Graduate School of Science and Engineering of Technical University of Munich (project number 11.01), German Research Foundation (DFG) under Grant No. 355784621, under Germany's Excellence Strategy-EXC 2089/1-390776260, are gratefully acknowledged. S.H. and S.X. acknowledge financial support from the China Scholarship Council. W.J.L. is grateful for the support of an Alexander von Humboldt Fellowship for Postdoctoral Researchers. R.M.K. acknowledges DFG project BA 5795/4-1 for funding. A.S.B. is thankful for the financial support from the DFG project BA 5795/5-1. The authors thank Dr. Ke Zhang and Dr. Christian Jandl for providing XPS data and Dr. Matthias Schwartzkopf for the help with setting up the beamline P03 at DESY.

Open access funding enabled and organized by Projekt DEAL.

Conflict of Interest

The authors declare no conflict of interest.

Data Availability Statement

Research data are not shared.

Keywords

heterostructure, NiFe (oxy)hydroxides, oxygen evolution reaction, structural transformation, surface-mounted metal–organic frameworks

Received: April 27, 2021
Published online: August 1, 2021

[1] Q. Zhang, E. Uchaker, S. L. Candelaria, G. Cao, *Chem. Soc. Rev.* **2013**, *42*, 3127.
[2] T. R. Cook, D. K. Dogutan, S. Y. Reece, Y. Surendranath, T. S. Teets, D. G. Nocera, *Chem. Rev.* **2010**, *110*, 6474.
[3] D. Wu, K. Kusada, S. Yoshioka, T. Yamamoto, T. Toriyama, S. Matsumura, Y. Chen, O. Seo, J. Kim, C. Song, S. Hiroi, O. Sakata, T. Ina, S. Kawaguchi, Y. Kubota, H. Kobayashi, H. Kitagawa, *Nat. Commun.* **2021**, *12*, 1145.
[4] H. Mistry, A. S. Varela, S. Kühl, P. Strasser, B. R. Cuenya, *Nat. Rev. Chem.* **2016**, *1*, 16009.
[5] H. Zhang, J. Nai, L. Yu, X. W. Lou, *Joule* **2017**, *1*, 77.
[6] M. Dincă, Y. Surendranath, D. G. Nocera, *Proc. Natl. Acad. Sci. USA* **2010**, *107*, 10337.
[7] S. Laha, Y. Lee, F. Podjaski, D. Weber, V. Duppel, L. M. Schoop, F. Pielnhofer, C. Scheurer, K. Müller, U. Starke, K. Reuter, B. V. Lotsch, *Adv. Energy Mater.* **2019**, *9*, 1803795.
[8] W. T. Hong, M. Risch, K. A. Stoerzinger, A. Grimaud, J. Suntivich, Y. Shao-Horn, *Energy Environ. Sci.* **2015**, *8*, 1404.
[9] F. Dionigi, P. Strasser, *Adv. Energy Mater.* **2016**, *6*, 1600621.
[10] L.-A. Stern, L. Feng, F. Song, X. Hu, *Energy Environ. Sci.* **2015**, *8*, 2347.
[11] Y. Guo, T. Park, J. W. Yi, J. Henzie, J. Kim, Z. Wang, B. Jiang, Y. Bando, Y. Sugahara, J. Tang, Y. Yamauchi, *Adv. Mater.* **2019**, *31*, 1807134.
[12] H. Zhang, W. Zhou, J. Dong, X. F. Lu, X. W. Lou, *Energy Environ. Sci.* **2019**, *12*, 3348.
[13] J. Zhao, J. J. Zhang, Z. Y. Li, X. H. Bu, *Small* **2020**, *16*, 2003916.
[14] W. Li, S. Watzele, H. A. El-Sayed, Y. Liang, G. Kieslich, A. S. Bandarenka, K. Rodewald, B. Rieger, R. A. Fischer, *J. Am. Chem. Soc.* **2019**, *141*, 5926.
[15] W. Li, S. Xue, S. Watzele, S. Hou, J. Fichtner, A. L. Semrau, L. Zhou, A. Welle, A. S. Bandarenka, R. A. Fischer, *Angew. Chem., Int. Ed.* **2020**, *59*, 5837.
[16] S. Begum, T. Hashem, M. Tsotsalas, C. Wöll, M. H. Alkordi, *Energy Technol.* **2019**, *7*, 1900967.
[17] F. Malara, A. Minguzzi, M. Marelli, S. Morandi, R. Psaro, V. Dal Santo, A. Naldoni, *ACS Catal.* **2015**, *5*, 5292.
[18] C. C. McCrory, S. Jung, J. C. Peters, T. F. Jaramillo, *J. Am. Chem. Soc.* **2013**, *135*, 16977.
[19] Y. Guo, J. Tang, H. Qian, Z. Wang, Y. Yamauchi, *Chem. Mater.* **2017**, *29*, 5566.
[20] R. Subbaraman, D. Tripkovic, D. Strmcnik, K.-C. Chang, M. Uchimura, A. P. Paulikas, V. Stamenkovic, N. M. Markovic, *Science* **2011**, *334*, 1256.
[21] S. Xue, R. W. Haid, R. M. Kluge, X. Ding, B. Garlyyev, J. Fichtner, S. Watzele, S. Hou, A. S. Bandarenka, *Angew. Chem., Int. Ed.* **2020**, *59*, 10934.
[22] Z. Xue, K. Liu, Q. Liu, Y. Li, M. Li, C.-Y. Su, N. Ogiwara, H. Kobayashi, H. Kitagawa, M. Liu, G. Li, *Nat. Commun.* **2019**, *10*, 5048.
[23] L. Heinke, C. Wöll, *Adv. Mater.* **2019**, *31*, 1806324.
[24] Q. Qian, Y. Li, Y. Liu, L. Yu, G. Zhang, *Adv. Mater.* **2019**, *31*, 1901139.
[25] M. Liu, L. Kong, X. Wang, J. He, X. H. Bu, *Small* **2019**, *15*, 1903410.
[26] W. Zheng, M. Liu, L. Y. S. Lee, *ACS Catal.* **2019**, *10*, 81.
[27] S. Zhao, C. Tan, C.-T. He, P. An, F. Xie, S. Jiang, Y. Zhu, K.-H. Wu, B. Zhang, H. Li, J. Zhang, Y. Chen, S. Liu, J. Dong, Z. Tang, *Nat. Energy* **2020**, *5*, 881.
[28] G. Zhao, K. Rui, S. X. Dou, W. Sun, *Adv. Funct. Mater.* **2018**, *28*, 1803291.
[29] A. R. Akbashev, L. Zhang, J. T. Mefford, J. Park, B. Butz, H. Luftman, W. C. Chueh, A. Vojvodic, *Energy Environ. Sci.* **2018**, *11*, 1762.
[30] J. Kibsgaard, I. Chorkendorff, *Nat. Energy* **2019**, *4*, 430.
[31] D. Y. Chung, P. P. Lopes, P. Farinazzo Bergamo Dias Martins, H. He, T. Kawaguchi, P. Zapol, H. You, D. Tripkovic, D. Strmcnik, Y. Zhu, S. Seifert, S. Lee, V. R. Stamenkovic, N. M. Markovic, *Nat. Energy* **2020**, *5*, 222.
[32] S. Zou, M. S. Burke, M. G. Kast, J. Fan, N. Danilovic, S. W. Boettcher, *Chem. Mater.* **2015**, *27*, 8011.
[33] W. Cheng, X. Zhao, H. Su, F. Tang, W. Che, H. Zhang, Q. Liu, *Nat. Energy* **2019**, *4*, 115.

[34] P. Thangavel, M. Ha, S. Kumaraguru, A. Meena, A. N. Singh, A. M. Harzandi, K. S. Kim, *Energy Environ. Sci.* **2020**, *13*, 3447.
[35] S. Zhao, Y. Wang, J. Dong, C.-T. He, H. Yin, P. An, K. Zhao, X. Zhang, C. Gao, L. Zhang, J. Lv, J. Wang, J. Zhang, A. M. Khattak, N. A. Khan, Z. Wei, J. Zhang, S. Liu, H. Zhao, Z. Tang, *Nat. Energy* **2016**, *1*, 16184.
[36] Z. Cai, L. Li, Y. Zhang, Z. Yang, J. Yang, Y. Guo, L. Guo, *Angew. Chem., Int. Ed.* **2019**, *58*, 4189.
[37] Y. Zhou, Z. Wang, Z. Pan, L. Liu, J. Xi, X. Luo, Y. Shen, *Adv. Mater.* **2019**, *31*, 1806769.
[38] B. Liu, Y. Wang, H. Q. Peng, R. Yang, Z. Jiang, X. Zhou, C. S. Lee, H. Zhao, W. Zhang, *Adv. Mater.* **2018**, *30*, 1803144.
[39] J. Xie, J. Xin, R. Wang, X. Zhang, F. Lei, H. Qu, P. Hao, G. Cui, B. Tang, Y. Xie, *Nano Energy* **2018**, *53*, 74.
[40] F. Song, X. Hu, *J. Am. Chem. Soc.* **2014**, *136*, 16481.
[41] M. B. Stevens, L. J. Enman, A. S. Batchellor, M. R. Cosby, A. E. Vise, C. D. M. Trang, S. W. Boettcher, *Chem. Mater.* **2017**, *29*, 120.
[42] J. Huang, J. Chen, T. Yao, J. He, S. Jiang, Z. Sun, Q. Liu, W. Cheng, F. Hu, Y. Jiang, Z. Pan, S. Wei, *Angew. Chem., Int. Ed.* **2015**, *54*, 8722.
[43] H. Guo, Z. Fang, H. Li, D. Fernandez, G. Henkelman, S. M. Humphrey, G. Yu, *ACS Nano* **2019**, *13*, 13225.
[44] A. W. Jensen, G. W. Sievers, K. D. Jensen, J. Quinson, J. A. Arminio-Ravelo, V. Brüser, M. Arenz, M. Escudero-Escribano, *J. Mater. Chem. A* **2020**, *8*, 1066.
[45] T. Kwon, H. Hwang, Y. J. Sa, J. Park, H. Baik, S. H. Joo, K. Lee, *Adv. Funct. Mater.* **2017**, *27*, 1604688.
[46] M. W. Louie, A. T. Bell, *J. Am. Chem. Soc.* **2013**, *135*, 12329.
[47] L. Trotochaud, S. L. Young, J. K. Ranney, S. W. Boettcher, *J. Am. Chem. Soc.* **2014**, *136*, 6744.
[48] F. Dionigi, Z. Zeng, I. Sinev, T. Merzdorf, S. Deshpande, M. B. Lopez, S. Kunze, I. Zegkinoglou, H. Sarodnik, D. Fan, A. Bergmann, J. Drnec, J. F. Araujo, M. Gliech, D. Teschner, J. Zhu, W. X. Li, J. Greeley, B. R. Cuenya, P. Strasser, *Nat. Commun.* **2020**, *11*, 2522.
[49] A. Z. Chen, M. Shiu, J. H. Ma, M. R. Alpert, D. Zhang, B. J. Foley, D. M. Smilgies, S. H. Lee, J. J. Choi, *Nat. Commun.* **2018**, *9*, 1336.
[50] W. Li, F. Li, H. Yang, X. Wu, P. Zhang, Y. Shan, L. Sun, *Nat. Commun.* **2019**, *10*, 5074.
[51] Y. Shi, Y. Yu, Y. Liang, Y. Du, B. Zhang, *Angew. Chem., Int. Ed.* **2019**, *58*, 3769.
[52] J. Chen, P. Zhuang, Y. Ge, H. Chu, L. Yao, Y. Cao, Z. Wang, M. O. L. Chee, P. Dong, J. Shen, M. Ye, P. M. Ajayan, *Adv. Energy Mater.* **2019**, *29*, 1903875.
[53] Z. Xue, Y. Li, Y. Zhang, W. Geng, B. Jia, J. Tang, S. Bao, H.-P. Wang, Y. Fan, Z.-w. Wei, Z. Zhang, Z. Ke, G. Li, C.-Y. Su, *Adv. Energy Mater.* **2018**, *8*, 1801564.
[54] Q. Zhang, N. M. Bedford, J. Pan, X. Lu, R. Amal, *Adv. Energy Mater.* **2019**, *9*, 1901312.
[55] Z. Cai, D. Zhou, M. Wang, S. M. Bak, Y. Wu, Z. Wu, Y. Tian, X. Xiong, Y. Li, W. Liu, S. Siahrostami, Y. Kuang, X. Q. Yang, H. Duan, Z. Feng, H. Wang, X. Sun, *Angew. Chem., Int. Ed.* **2018**, *57*, 9392.
[56] W. He, H.-M. Gao, R. Shimoni, Z.-Y. Lu, I. Hod, *ACS Appl. Energy Mater.* **2019**, *2*, 2138.
[57] F. Kong, W. Zhang, L. Sun, L. Huo, H. Zhao, *ChemSusChem* **2019**, *12*, 3592.
[58] J. Y. Chen, L. Dang, H. Liang, W. Bi, J. B. Gerken, S. Jin, E. E. Alp, S. S. Stahl, *J. Am. Chem. Soc.* **2015**, *137*, 15090.
[59] D. Zhu, C. Guo, J. Liu, L. Wang, Y. Du, S. Z. Qiao, *Chem. Commun.* **2017**, *53*, 10906.
[60] P. Wen, P. Gong, J. Sun, J. Wang, S. Yang, *J. Mater. Chem. A* **2015**, *3*, 13874.
[61] L. Trotochaud, J. K. Ranney, K. N. Williams, S. W. Boettcher, *J. Am. Chem. Soc.* **2012**, *134*, 17253.
[62] S. L. Candelaria, N. M. Bedford, T. J. Woehl, N. S. Rentz, A. R. Showalter, S. Pylypenko, B. A. Bunker, S. Lee, B. Reinhart, Y. Ren, S. P. Ertem, E. B. Coughlin, N. A. Sather, J. L. Horan, A. M. Herring, L. F. Greenlee, *ACS Catal.* **2017**, *7*, 365.
[63] O. Diaz-Morales, I. Ledezma-Yanez, M. T. M. Koper, F. Calle-Vallejo, *ACS Catal.* **2015**, *5*, 5380.
[64] F. L. Li, P. Wang, X. Huang, D. J. Young, H. F. Wang, P. Braunstein, J. P. Lang, *Angew. Chem., Int. Ed.* **2019**, *58*, 7051.
[65] B. S. Yeo, A. T. Bell, *J. Phys. Chem. C* **2012**, *116*, 8394.
[66] S. Lee, K. Banjac, M. Lingenfelder, X. Hu, *Angew. Chem., Int. Ed.* **2019**, *58*, 10295.
[67] S. Lee, L. Bai, X. Hu, *Angew. Chem., Int. Ed.* **2020**, *59*, 8072.
[68] S. Klaus, Y. Cai, M. W. Louie, L. Trotochaud, A. T. Bell, *J. Phys. Chem. C* **2015**, *119*, 7243.
[69] S. Watzele, P. Hauenstein, Y. Liang, S. Xue, J. Fichtner, B. Garlyyev, D. Scieszka, F. Claudel, F. Maillard, A. S. Bandarenka, *ACS Catal.* **2019**, *9*, 9222.
[70] A. Alobaid, C. Wang, R. A. Adomaitis, *J. Electrochem. Soc.* **2018**, *165*, J3395.
[71] A. C. Garcia, T. Touzalin, C. Nieuwland, N. Perini, M. T. M. Koper, *Angew. Chem., Int. Ed.* **2019**, *58*, 12999.
[72] J. R. Swierk, S. Klaus, L. Trotochaud, A. T. Bell, T. D. Tilley, *J. Phys. Chem. C* **2015**, *119*, 19022.

Bifunctional Catalysts

International Edition: DOI: 10.1002/anie.201916507
German Edition: DOI: 10.1002/ange.201916507

Advanced Bifunctional Oxygen Reduction and Evolution Electrocatalyst Derived from Surface-Mounted Metal–Organic Frameworks

Weijin Li, Song Xue, Sebastian Watzele, Shujin Hou, Johannes Fichtner, A. Lisa Semrau, Liujiang Zhou, Alexander Welle, Aliaksandr S. Bandarenka,* and Roland A. Fischer**

Abstract: *Metal–organic frameworks (MOFs) and their derivatives are considered as promising catalysts for the oxygen reduction reaction (ORR) and oxygen evolution reaction (OER), which are important for many energy provision technologies, such as electrolyzers, fuel cells and some types of advanced batteries. In this work, a "strain modulation" approach has been applied through the use of surface-mounted NiFe-MOFs in order to design an advanced bifunctional ORR/OER electrocatalyst. The material exhibits an excellent OER activity in alkaline media, reaching an industrially relevant current density of 200 mA cm^{-2} at an overpotential of only ≈ 210 mV. It demonstrates operational long-term stability even at a high current density of 500 mA cm^{-2} and exhibits the so far narrowest "overpotential window" $\Delta E_{ORR\text{-}OER}$ of 0.69 V in 0.1 M KOH with a mass loading being two orders of magnitude lower than that of benchmark electrocatalysts.*

Introduction

The oxygen reduction reaction (ORR) and oxygen evolution reaction (OER) play a crucial role in renewable energy provision schemes, which are relevant for e.g., metal-air batteries, fuel cells and electrolyzers.[1] Many efforts have been made to develop efficient bifunctional ORR/OER catalysts, which are typically based on precious metal oxides, [2] perovskites[3] and non-noble metal oxides.[4] Among a large number of state-of-the-art electrode materials capable to efficiently catalyze both reactions, metal–organic frameworks (MOFs) and their derivatives have attracted considerable attention due to their tunable lattice structures, porosity and well-defined compositions, just to name a few aspects.[5]

However, the previously reported MOF-based materials including MOF derived materials typically had a low density of accessible active sites. On the other hand, recent studies have shown that the number of catalytic centers can be increased by exfoliating catalysts into nanosheets,[6] through phosphorylation of materials (leading to various hierarchy), by increasing their wettability[7] or nanostructuring.[8] Such catalysts are typically utilized as microcrystalline powders drop-casted onto electrodes by adding hydrophilic binders. However, the latter multi-component mixtures can permanently shield most active sites of oxide-based materials and therefore are rarely used in industrial applications. Moreover, these catalysts show a large bifunctional ORR/OER overpotential window ($\Delta E_{ORR\text{-}OER}$), defined as the difference between the potential required for an OER current density of 10 mA cm^{-2} and the ORR "half-wave" potential.[9] A small $\Delta E_{ORR\text{-}OER}$ is a key requirement for a high efficiency of the above-mentioned energy provision devices.

According to the well-known Sabatier principle, a catalyst should bind reaction intermediates neither too strong nor too weak.[10] For multi-electron transfer reactions such as the ORR and OER, the $\Delta E_{ORR\text{-}OER}$ value is limited by the so-called scaling relations related to the binding energies of the reaction intermediates such as *O, *OH and *OOH (*designates the adsorbed state).[10b] The scaling relations account for the fact that changing the binding energy of one intermediate influences also the binding strength of other adsorbed intermediates at the catalytic center. Thus, designing an

[*] Dr. W. J. Li, A. L. Semrau, Prof. R. A. Fischer
Department of Chemistry, Technical University of Munich
Lichtenbergstraße 4, 85748 Garching b. München (Germany)
E-mail: roland.fischer@tum.de

Dr. W. J. Li, S. Xue, S. Watzele, S. J. Hou, J. Fichtner, A. L. Semrau, Prof. A. S. Bandarenka, Prof. R. A. Fischer
Catalysis Research Center, Technical University of Munich
Ernst-Otto-Fischer-Straße 1, 85748 Garching b. München (Germany)

S. Xue, S. Watzele, S. J. Hou, J. Fichtner, Prof. A. S. Bandarenka
Department of Physics, Technical University of Munich
James-Franck-Straße 1, 85748 Garching b. München (Germany)
E-mail: bandarenka@ph.tum.de

Prof. L. Zhou
Institute of Fundamental and Frontier Sciences, University of Electronic Science and Technology of China
Chengdu 610054 (P. R. China)
E-mail: liujiang86@gmail.com

Dr. A. Welle
Institute of Functional Interfaces, and Karlsruhe Nano Micro Facility, Karlsruhe Institute of Technology
Hermann-von-Helmholtz-Platz 1, 76344 Eggenstein-Leopoldshafen (Germany)

Supporting information and the ORCID identification number(s) for the author(s) of this article can be found under: https://doi.org/10.1002/anie.201916507.

effective bifunctional catalyst with a small overpotential for both the ORR and the OER is a big challenge.

Recently, we have demonstrated that a binder-free NiCo-based hydroxide film derived from surface-mounted metal–organic frameworks (SURMOFs) can exhibit superior OER performance compared to the existing NiCo- and NiFe- based electrocatalysts. To be specific, an anodic current density $>200\,mA\,cm^{-2}$ was achieved at an overpotential of $\approx 250\,mV$.[11] Recent findings show that adjusting the lattice-strain in catalysts can enhance their catalytic activity.[12] The intercalation of ions into electrode materials such as graphite or transition-metal dichalcogenides has proven to be an accessible way to introduce a controllable level of strain and therefore tune the catalytic activity of certain catalysts.[13] The positive impact of the strain on the catalytic activity of certain materials can be traced back to a shift of the binding energy of adsorbates towards the optimum.[14]

Inspired by these findings, we developed an electrocatalyst strain modulation approach to design highly active bifunctional ORR/OER electrocatalysts based on surface mounted metal–organic frameworks (SURMOFs).

In this work, a NiFe-BDC SURMOF (BDC = 1,4-benzenedicarboxylic acid) was synthesized and transformed into a NiFe-based oxy-hydroxide thin film, which retains the BDC component (NiFe-BDC SURMOFD, denoted as **1**–H), via a facile one-step alkaline treatment (Figure 1). The electrocatalytic activity towards the OER of **1**–H was optimized. Various functional groups such as –Br, $-OCH_3$, and $-NH_2$ were introduced to BDC in order to stimulate defect strain and to tailor the binding energies of the SURMOFDs for an enhanced OER activity.[15,16] Among the prepared electrocatalysts, NiFe-BDC(NH_2) SURMOFD (denoted as **1**–NH_2) shows particularly high OER activity, with an anodic current density of $200\,mA\,cm^{-2}$ at an overpotential of just $\approx 210\,mV$. Moreover, **1**–NH_2 remains stable for more than 120 h at a current density of $500\,mA\,cm^{-2}$. The $\Delta E_{ORR\text{-}OER}$ was found to be ≈ 0.69 V, outperforming the state-of-the-art catalysts.

Results and Discussion

Adjustment of the Ni/Fe Feeding Ratio and Deposition Cycles of 1–H for the Optimization of the OER Performance

The OER activity of NiFe-based oxo-hydroxo compounds typically correlates with the Ni to Fe ratios and deposition cycles.[17] Thus, we studied the electrocatalytic activity of **1**–H with different Ni/Fe feeding ratios and a different number of deposition cycles. The corresponding NiFe-BDC SURMOFs were prepared on self-assembled monolayer modified electrodes by a liquid phase layer-by-layer deposition technique (Figure 1 a,b, Table S6 and Figure S1 in the Supporting Information). Afterwards, they were transformed into NiFe-based oxy-hydroxides (SURMOFDs) in alkaline electrolytes (Figure 1 c,d and [Eq. (1)]).

$$[x\,Ni^{2+},\,(1-x)Fe^{2+}][BDC] + 2\,KOH = Ni_xFe_{(1-x)}(OH)_2 + K_2BDC \quad (1)$$

Where $[xNi^{2+}, (1-x)Fe^{2+}][BDC]$ is the chemical formula of the defined NiFe-BDC SURMOF. The one-step post-

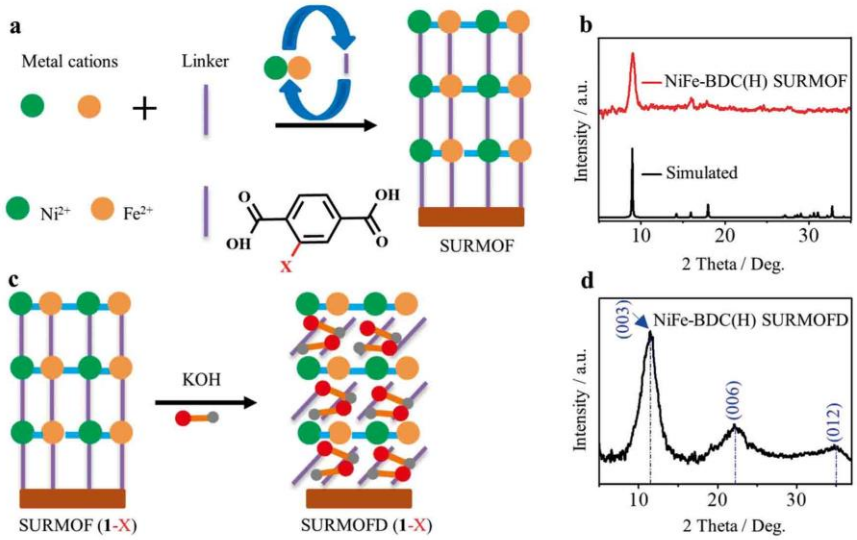

Figure 1. a) Preparation of NiFe-BDC (X) SURMOFs (X = NH_2, H, OCH_3 and Br) by layer-by-layer deposition; b) Grazing incidence X-ray diffraction (GIXRD) of NiFe-BDC(H) SURMOF; c) Transformation of NiFe-BDC (X) SURMOFs to NiFe-BDC (X) SURMOFDs (denoted as **1**–X); d) GIXRD of NiFe-BDC (H) SURMOFD (denoted as **1**–H). Surface-mounted metal–organic frameworks: SURMOFs; surface-mounted metal–organic frameworks derivatives: SURMOFDs; NiFe-BDC (NH_2) SURMOFD: **1**–NH_2; NiFe-BDC(OCH_3) SURMOFD: **1**–OCH_3; NiFe-BDC(Br) SURMOFD: **1**–Br.

treatment of NiFe-BDC with KOH leads to the formation of bimetallic NiFe-hybrid hydroxide thin films with some retention of BDC and intercalation of potassium cations and water.

In order to minimize effects of electrolyte resistances, to suppress the formation of macro oxygen bubbles, and to study the intrinsic activity of our catalysts, microelectrodes have been utilized as substrates for the SURMOFDs. As shown in Figure S2, **1**–H with a Ni/Fe feeding ratio of 6:1 shows the highest electrocatalytic activity towards OER. X-ray photoelectron spectroscopy (XPS) analysis reveals an actual Ni/Fe ratio of 3:1, which is in agreement with the optimum Ni/Fe ratio reported in the literature (Figure S3, Table S1).[18] It is also well-known that the activity of a catalyst is associated with the mass loading.[19] However, the determination of the mass loading would be inaccurate due to the small geometric size of the microelectrode and the low loading of **1**–H (nanograms level). Therefore, we focused on optimizing the number of deposition cycles of **1**–H to achieve the highest catalytic OER activity normalized to the electrode geometric surface area. Although the exact quantitative determination of the mass at the level of nanograms on the microelectrode is not possible, the number of deposition cycles can be correlated to the mass loading on the electrode (Figure S1). Upon increasing the number of deposition cycles of **1**–H from 10 to 30, the anodic current density at the overpotential of 300 mV ($j_{\eta=300\,mV}$) rises from 0.09 to 1.43 A cm^{-2} (Figure S4a). This enhancement of activity with the number of deposition cycles is attributed to a higher catalyst mass loading. However, further increasing the number of deposition cycles of **1**–H from 30 to 60 leads to a decrease of $j_{\eta=300\,mV}$ to 1.16 A cm^{-2}. The reduced activity can probably be explained by an increasing electric resistance of the electrocatalyst film, hindering efficient charge transfer and further impeding the OER process at a certain amount of deposition cycles. Herein, a film with an optimum electrocatalytic activity is reached after 30 deposition cycles. In a word, we found that preparation of a NiFe-BDC SURMOF with a Ni/Fe feeding ratio of 6:1 and 30 deposition cycles leads to a SURMOFD with an optimum OER activity. Thus, this deposition protocol served as a starting point for the following modifications.

Structural, Morphological and Compositional Studies of 1–H

Before further probing the electrochemical properties of **1**–H, the structure, morphology and composition of NiFe-BDC SURMOF and **1**–H were investigated. As shown in Figure 1b, the grazing incidence X-ray diffraction (GIXRD) patterns of NiFe-BDC SURMOF match well with the ones of 2D nanosheet NiCo-BDC MOF.[6b] The only significant peak at 8.95° reflects the preferred [200]-orientation growth. After immersing the SURMOF into 0.1 M aqueous KOH, it selectively transforms into SURMOFD **1**–H. Figure 1d displays the XRD patterns of **1**–H, which we assign to a NiFe-LDH (LDH, layer double hydroxide) with intercalated BDC according to equation 1. X-ray photoelectron spectroscopy (XPS) data further confirm this assignment; the O 1s binding energy is shifted from 531.4 eV to 531.0 eV, the Ni 2p3/2 binding energy from 855.9 eV to 855.5 eV and the Fe 2p3/2 peak is shifted from 712.2 eV to 711.5 eV (Figure S3, Table S1). Attenuated total reflectance IR (ATR-IR) spectra show the typical peaks at 1541 cm^{-1} and 1362 cm^{-1}, which are assigned to the symmetric and asymmetric carboxylate signals of BDC, suggesting that BDC is still present in the **1**–H interlayer after KOH treatment (Figure S5).

Scanning electron microscopy (SEM) and atomic force microscopy (AFM) images show that the **1**–H exhibits the same homogenous and dense morphology as the NiFe-BDC SURMOF (Figures 2a,b and Figures S6a, S6b). Energy-dispersive X-ray spectroscopy (EDS) mapping images indicate a homogenous distribution of Ni and Fe in the SURMOF and the corresponding **1**–H (Figure S6c–f).[9a] ToF-SIMS analysis further confirms that all the elements are homogeneously distributed on the surface (Figure 2c,d and Figure S7).

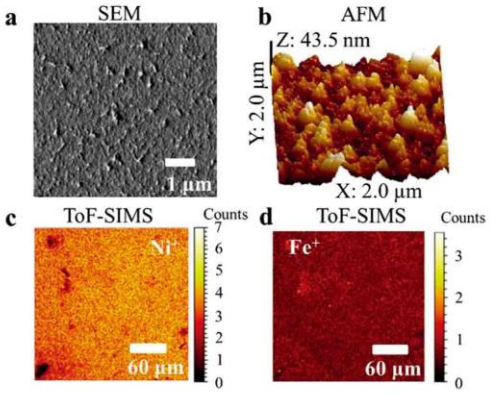

Figure 2. a) SEM and b) AFM image of **1**–H. c, d) High-resolution time of flight secondary ion mass spectrometry (ToF-SIMS) ion images of **1**–H: c) Ni^+ signals; d) Fe^+ signals. The ToF-SIMS ion images suggest the homogenous distributions of Ni and Fe.

Electrocatalytic Activity of 1–H Towards the Oxygen Evolution Reaction

To assess the electrocatalytic activity, polarization curves of **1**–H were recorded in O_2 saturated 0.1 M KOH standard conditions. It can be seen that, at an overpotential of 300 mV, **1**–H exhibits a current density of 0.70 A cm^{-2}, which is ≈3 times higher than the one recently reported for NiCo-BDC SURMOFD (0.26 A cm^{-2}; Figure S8).[9a] This result suggests that replacing Co with Fe in the respective SURMOFD system can further enhance the electrochemical activity towards OER. This can at least partially be ascribed to the fact that Fe can not only generate more vacancies for Ni due to the Ni–Fe electronic coupling but also enhances the electronic conductivity of the SURMOFD.[20] When heating the system, the current density of **1**–H increases with temperature, which is beneficial for the application of this

material in electrolyzers typically operating at elevated temperatures (Figure S9).

The products of the OER were analyzed by rotating-ring disk electrode (RRDE) measurements.[9a] To determine the onset potential of the OER, a constant potential of 0.70 V vs. the reversible hydrogen electrode (RHE) was applied to the Pt ring electrode while the potential of the disc was cycled. As shown in Figure S10a, at a working electrode (WE) potential of 1.45 V vs. RHE, a current at the ring can be observed, indicating the onset of the OER.

To investigate possible side reactions, such as the partial oxidation of H_2O to H_2O_2 (Figure S10b), the potential of the ring was changed to 0.20 V vs. RHE. No current at the ring was observed for WE potentials below 1.45 V vs. RHE, implying a four-electron process takes place, where no H_2O_2 is produced at the **1**–H surface. At a ring potential of 1.50 V vs. RHE, no ring current was detected in a WE potential range of 0.90 to 1.65 V vs. RHE (Figure S11). These results further confirm the four-electron transfer process for the OER.[21]

Durability of a catalyst is a crucial parameter for the practical application of electrocatalysts. A long-term stability test of **1**–H was performed by chronopotentiometry response experiments. As shown in Figure S12, while the current density was kept at 500 mA cm^{-2}, the potential remained stable at ≈1.54 V vs. RHE for more than 120 h, endorsing good long-term robustness of the **1**–H catalyst. The PXRD pattern shows that **1**–H changed to amorphous NiFe-LDH after the long term OER test (Figure S13a). The decrease of the crystallinity can be ascribed to some leaching of BDC and the intercalation of potassium ions during the long-term stability test (Figure S13b and Figure S7). However, crystallinity is not a significant factor in OER activity.[22] The morphology of **1**–H did not show a significant change after the long-term stability test (Figure S14).

SURMOFDs Based on Functionalized BDC and their Electrocatalytic Activity

BDC(X) modified with various functional groups (X) was used to grow different NiFe-SURMOFs. These precursors were transformed into SURMOFDs (**1**–X) (Figure S15) and their catalytic activity towards the OER and ORR was studied. The functional groups are expected to modulate the defect strain of the SURMOFDs. This should allow to tailor the binding strength between the active sites of the SURMOFDs and the OER reaction intermediates, and thus to further improve OER activity.[23a] To prove this hypothesis, GIXRD, Raman spectroscopy and XPS were used to investigate the degree of lattice distortion and strain of SURMOFDs interlayered with BDC–X (X = NH_2, H, OCH_3 and Br) (Figure 3).

As shown in Figure 3a, the GIXRD peaks at ≈11.30° and ≈22.15° are shifted from **1**–Br over **1**–H, **1**–OCH_3 and **1**–NH_2. The shift of the peaks is probably ascribed to the introduction of different functional groups in BDC and strain effects (Table S2). To confirm the existence of the strain effect, the Williamson–Hall (W–H) equation was used to estimate the degree of strain in SURMOFDs.[23a] According to the W–H equation, a change of defect strain from **1**–Br over **1**–OCH_3 and **1**–H to **1**–NH_2 can be assumed (Figure S16, Table S3).[23] The change of strain could also induce material phonon softening and thus further result in a red shift of Raman spectra.[24] The tensile strain (phonon softening) of the materials is supposed to improve the electrocatalytic activities of **1**–X.[23c,24c] As shown in Figure 3b and Table S4, Raman spectra of **1**–X indeed show a slight red shift of the Ni–O bonds (Ni–O, Ni–OH) from **1**–Br (peaks at 455 cm^{-1} and 533 cm^{-1}) to **1**–NH_2 (corresponding peaks at 449 cm^{-1} and 527 cm^{-1}). XPS analysis was used to further

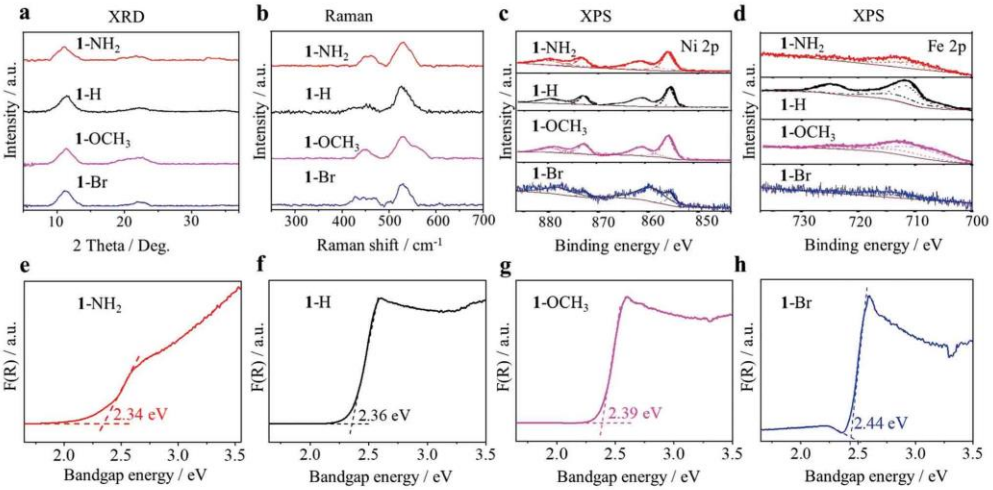

Figure 3. Evidences of defect strain in **1**–X: a) XRD patterns; b) the corresponding Raman spectra (error bar ±0.5 cm^{-1}); XPS spectra of c) Ni 2p; and d) Fe 2p (error bar: ±0.2 eV); band gap energy of the **1**–X calculated from the UV/Vis diffuse reflectance spectra: e) **1**–NH_2; f) **1**–H; g) **1**–OCH_3; h) **1**–Br (error bar: ±0.01 eV). The films were prepared by 30 deposition cycles, using a precursor Ni/Fe feeding ratio of 6:1.

confirm the different degree of strain among **1**–Br, **1**–OCH_3, **1**–H and **1**–NH_2. As shown in Figure S17, the O 1s peak energies increase in the following order: **1**–OCH_3 (530.8 eV), **1**–H (531.0 eV) and **1**–NH_2 (531.5 eV), which can be assigned to the adsorbed O–O species.[25] This result indicates an increase of the binding strength between the SURMOFD's surface and reaction intermediates upon functionalization from $-OCH_3$ to –H and $-NH_2$.[26] The Ni 2p3/2 binding energies of **1**–Br are negatively shifted by 0.1 eV and 0.9 eV compared to the corresponding Ni 2p3/2 peaks of **1**–OCH_3 and **1**–NH_2, respectively. Conversely, the Fe 2p3/2 peaks of **1**–Br are positively shifted by 1.6 eV and 2.4 eV, compared to the corresponding Fe peaks of **1**–OCH_3 and **1**–NH_2, respectively (Figure 3c–d and Table S5). To sum up, the binding energies of Ni 2p3/2 and Fe 2p3/2 are shifted, which suggests a change of bond lengths of Ni–O or Fe–O caused by defect strain.[27]

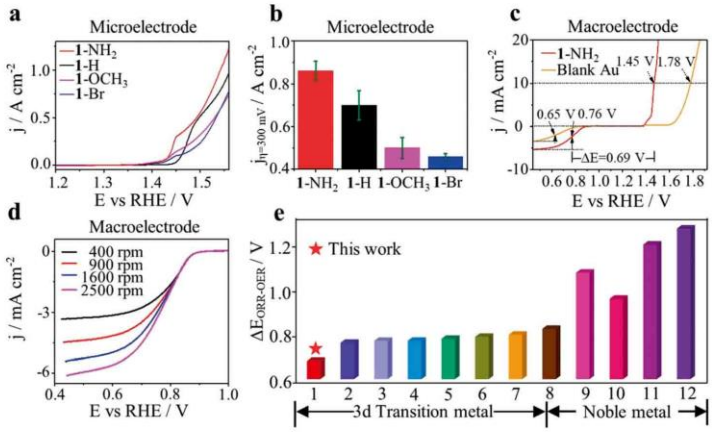

Figure 4. a) Anodic polarization curves of **1**–X (supported on a Pt microelectrode, diameter = 25 μm), recorded in O_2-saturated 0.1 M KOH at a scan rate of 5 $mV s^{-1}$. Temperature: 25 °C. All polarization curves are shown without iR drop compensation; b) Comparison of the current density of **1**–NH_2, **1**–H, **1**–OCH_3 and **1**–Br for the OER at 1.53 V vs. RHE ($\eta = 300$ mV); c) Anodic polarization curves from ORR to OER regime on **1**–NH_2 (supported on an Au disc electrode, diameter = 5 mm) and blank Au electrodes in O_2-saturated 0.1 M KOH at a scan rate of 10 $mV s^{-1}$ after 85% iR-compensation. Temperature: 25 °C. Rotation speed: 1600 rpm; ΔE refer to the difference between the potential required for an OER current density of 10 $mA cm^{-2}$ and the ORR half-wave potential; d) polarization curve of **1**–NH_2 (supported on an Au disc electrode) at various rotational speeds; e) Comparison of bifunctional activities of ORR and OER with literature data: 2: CoZn-NC-700,[31] 3:Co-N-CNTs,[32] 4: Co_3O_4-N-Carbon,[33] 5: $NiCo_2S_4$@g-C_3N_4-CNT,[34] 6: N-GCNT/FeCo,[35] 7: NC@Co-NGC,[36] 8: Co@Co_3O_4/NC,[9a] 9: Au, 10: Pt/C,[9a] 11: RuO_2,[9a] 12: IrO_2.[9a]

UV/Vis diffuse reflection spectroscopy shows that the band gap energy of **1**–X exhibits a slight but significant red-shift of 2.44 eV, 2.39 eV, 2.36 eV and 2.34 eV, for **1**–Br, **1**–OCH_3, **1**–H and **1**–NH_2, respectively (Figure 3e–h and Figure S18). The red-shift of the band gap energy of **1**–X is assigned to the defect strain increasing from **1**–Br to **1**–OCH_3, to **1**–H and to **1**–NH_2. This shifts the d-band center towards the Fermi level and leads to a less filled anti-bonding state according to the d-band theory.[28] The partially filled anti-bonding state is expected to offer more active sites for the adsorption of oxygen species, which are essential for OER.[23a,28]

To study the effect of defect strain in SURMOFDs on the OER, the activity of the **1**–X samples grown on Pt microelectrode substrates were measured in O_2-saturated 0.1 M aqueous KOH electrolytes. As shown in Figure 4a and b, **1**–NH_2 shows the highest anodic current density of ≈ 0.86 A cm^{-2} among all tested OER catalysts at an overpotential of 300 mV, followed by **1**–H (0.70 A cm^{-2}), **1**–OCH_3 (0.50 A cm^{-2}) and **1**–Br (0.46 A cm^{-2}). The observations correlate with the degree of defect strain, which increases from **1**–Br to **1**–OCH_3 or **1**–H and **1**–NH_2.The OER activities of SURMOFDs are not exactly consistent with the XRD, Raman and XPS of Ni and Fe. The reason is probably ascribed to the synergetic effects of the size and electron affinity of the substitutes.[29]

Moreover, the Tafel slopes were investigated to examine the OER reaction kinetics of **1**–X. As shown in Figure S19, the Tafel slopes at $\eta \approx 0.20$ V were determined: to be ≈ 26 mV dec^{-1} for **1**–NH_2, ≈ 28 mV dec^{-1} for **1**–H, ≈ 50 mV dec^{-1} for **1**–OCH_3, and ≈ 51 mV dec^{-1} for **1**–Br. The Tafel slope trends of **1**–X from $-NH_2$ to –H, $-OCH_3$ and –Br are consistent with the trends observed by XRD, XPS, Raman spectroscopy and UV/Vis. A comparison of the calculated electron affinities of **1**–X further supports the importance of the strain approach for enhanced the OER activity. Low electron affinities of intercalated linkers BDC-(X) can increase the density of the unoccupied state of transition metals, boost the binding strength between the active sites of the SURMOFDs and the OER reaction intermediates and further enhancing their OER activity.[30] As shown in Figure S20, NH_2–BDC shows the lowest electron affinity (0.18 eV) and Br–BDC (0.66 eV) shows the largest electron affinity. The results match well with the observed trend; **1**–NH_2 shows the highest OER activity, while **1**–Br shows the lowest OER activity in the whole potential range above 1.45 V vs. RHE.

Besides, due to the high OER activity of **1**–NH_2, its potential application as a bifunctional ORR/OER catalysts was explored. Remarkably, **1**–NH_2 shows a ΔE of ≈ 0.69 V, outperforming typical benchmark catalysts (Figure 4c, Figure 4e and Table S7). In case of the ORR, the number of electrons transferred by **1**–NH_2 was calculated using the Koutecký–Levich (KL) equation. According to the slopes of the KL plots (Figure 4d and Figure S21), the number of electrons transferred per O_2 molecule in the ORR was

calculated to be 3.88, suggesting a predominantly four-electron reduction pathway. These results conclusively verify the capability of **1**–NH_2 to be a good bifunctional ORR/OER catalyst.

Conclusion

In summary, we developed a highly active NiFe-based bifunctional ORR/OER electrocatalyst using a simple layer-by-layer deposition approach based on the strain modulation concept. The electrode material was derived from well-defined surface-mounted metal–organic frameworks and exhibits a high density of electroactive surface sites. We assume that the binding strength between the reaction intermediates and the catalytically active centers can be experimentally tuned by introducing precursor functional group such as −Br, $-OCH_3$, and $-NH_2$ into the organic linker. These functional groups induce strain, which allows to optimize the interaction of reaction intermediates with the surface of the catalyst and further improves the OER activity. Despite partial leaching of the BDC linker during the OER process, the catalyst still shows remarkable activity after more than 120 h of operation. The prepared SURMOFD catalyst shows a unique bifunctional ORR/OER performance, while the mass loading of the catalyst thin film is about two orders of magnitude lower than the loading of other state-of-the-art bifunctional catalysts reported in the literature. Our discoveries show a simple and effective way to tailor the binding strength between reaction intermediates and active sites. This advancement complements the benefits of the well-controlled deposition of MOF films with the properties of mixed metal oxides/hydroxides and functionalized organic linkers, which altogether act as a versatile platform for the synthesis of active electrocatalyst structures.

Acknowledgements

W.J.L. is grateful for the support of an Alexander von Humboldt Fellowship for Postdoctoral Researchers. W.J.L. is particularly grateful to Prof. Dr. Hubert Gasteiger for offering the facilities in his laboratories (TUM-TEC). S.X., S.W., S.H., J.F. and A.S.B. are grateful for the financial support from Deutsche Forschungsgemeinschaft (DFG, German Research Foundation) under Germany's excellence cluster "e-conversion" (BA 5795/4-1 and BA 5795/3-1) and financial support from TUM IGSSE (project 11.01). S.X. and S.H. thank the China Scholarship Council (CSC) for the financial support (201606180040 and 201806140125, respectively). A.L.S. is grateful for a PhD scholarship donated by the German Chemical Industry Fund (FCI). W.J.L. is grateful to Dr. Katia Rodewald, Prof. Bernhard Rieger for the SEM micrographs and Xinyu Jiang, Prof. Müller Buschbaum for providing the UV/Vis diffuse reflection spectroscopic data.

Conflict of interest

The authors declare no conflict of interest.

Keywords: derivatives · Metal–organic frameworks · oxygen evolution reaction · oxygen reduction reaction · thin films

How to cite: *Angew. Chem. Int. Ed.* **2020**, *59*, 5837–5843
Angew. Chem. **2020**, *132*, 5886–5892

[1] a) J. Park, T. Kwon, J. Kim, H. Jin, H. Y. Kim, B. Kim, S. H. Joo, K. Lee, *Chem. Soc. Rev.* **2018**, *47*, 8173–8202; b) N. T. Suen, S. F. Huang, Q. Quan, N. Zhang, Y. J. Xu, H. M. Chen, *Chem. Soc. Rev.* **2017**, *46*, 337–365; c) G. Liu, J. Li, J. Fu, G. Jiang, G. Lui, D. Luo, Y.-P. Deng, J. Zhang, Z. P. Cano, A. P. Yu, D. Su, Z. Bai, L. Yang, Z. Chen, *Adv. Mater.* **2019**, *31*, 1806761; d) M. Zhang, M. de Respinis, H. Frei, *Nat. Chem.* **2014**, *6*, 362–367.

[2] H. N. Nong, T. Reier, H.-S. Oh, M. Gliech, P. Paciok, T. H. T. Vu, D. Teschner, M. Heggen, V. Petkov, R. Schlögl, T. Jones, P. Strasser, *Nat. Catal.* **2018**, *1*, 841–851.

[3] E. Fabbri, M. Nachtegaal, T. Binninger, X. Cheng, B. J. Kim, J. Durst, F. Bozza, T. Graule, R. Schäublin, L. Wiles, M. Pertoso, N. Danilovic, K. E. Ayers, T. J. Schmidt, *Nat. Mater.* **2017**, *16*, 925–934.

[4] a) L. Han, S. J. Dong, E. Wang, *Adv. Mater.* **2016**, *28*, 9266–9291; b) J. S. Kim, B. Kim, H. Kim, K. Kang, *Adv. Energy Mater.* **2018**, *8*, 1702774; c) E. M. Miner, T. Fukushima, D. Sheberla, L. Sun, Y. Surendranath, M. Dincă, *Nat. Commun.* **2016**, *7*, 1092.

[5] a) S. Dang, Q.-L. Zhu, Q. Xu, *Nat. Rev. Mater.* **2017**, *2*, 17075–17088; b) Q. R. Shi, S. F. Fu, C. Z. Zhu, J. H. Song, D. Du, Y. H. Lin, *Mater. Horiz.* **2019**, *6*, 684–702; c) H. B. Aiyappa, J. Masa, C. Andronescu, M. Muhler, R. A. Fischer, W. Schuhmann, *Small Methods* **2019**, *3*, 1800415.

[6] a) K. Jayaramulu, J. Masa, D. M. Morales, O. Tomanec, V. Ranc, M. Petr, P. Wilde, Y.-T. Chen, R. Zboril, W. Schuhmann, R. A. Fischer, *Adv. Sci.* **2018**, *5*, 1801029; b) S. Zhao, Y. Wang, J. Dong, C.-T. He, H. Yin, P. An, K. Zhao, X. Zhang, C. Gao, L. Zhang, J. Lv, J. Wang, J. Zhang, A. M. Khattak, N. A. Khan, Z. Wei, J. Zhang, S. Liu, H. Zhao, Z. Tang, *Nat. Energy* **2016**, *1*, 16184–16193.

[7] a) Y. B. Li, C. Zhao, *ACS Catal.* **2017**, *7*, 2535–2541; b) W. B. Jung, G. T. Yun, Y. Kim, M. Kim, H. T. Jung, *ACS Appl. Mater. Interfaces* **2019**, *11*, 7546–7552.

[8] a) T. N. Huan, G. Rousse, S. Zanna, I. T. Lucas, X. Xu, N. Menguy, V. Mougel, M. Fontecave, *Angew. Chem. Int. Ed.* **2017**, *56*, 4792–4796; *Angew. Chem.* **2017**, *129*, 4870–4874; b) S. Ghosh, R. N. Basu, *Nanoscale* **2018**, *10*, 11241–11280.

[9] a) A. Aijaz, J. Masa, C. Rösler, W. Xia, P. Weide, A. J. Botz, R. A. Fischer, W. Schuhmann, M. Muhler, *Angew. Chem. Int. Ed.* **2016**, *55*, 4087–4091; *Angew. Chem.* **2016**, *128*, 4155–4160; b) S. Dresp, F. Luo, R. Schmack, S. Kühl, M. Gliech, P. Strasser, *Energy Environ. Sci.* **2016**, *9*, 2020–2024.

[10] a) G. L. Chai, K. Qiu, M. Qiao, M. Titirici, C. Shang, Z. Guo, *Energy Environ. Sci.* **2017**, *10*, 1186–1195; b) G. Rothenberg, *Catalysis: concepts and green applications*, Wiley-VCH, Weinheim, **2008**, p. 65.

[11] W. J. Li, S. Watzele, H. A. El-Sayed, Y. C. Liang, G. Kieslich, A. S. Bandarenka, K. Rodewald, B. Rieger, R. A. Fischer, *J. Am. Chem. Soc.* **2019**, *141*, 5926–5933.

[12] a) Y. Yao, S. Hu, W. Chen, Z. Huang, W. Wei, T. Yao, R. Liu, K. Zang, X. Wang, G. Wu, W. Yuan, T. Yuan, B. Zhu, W. Liu, Z. Li, D. He, Z. Xue, Y. Wang, X. Zheng, J. Dong, C. Chang, Y. Chen, X. Hong, J. Luo, S. Wei, W. Li, P. Strasser, Y. Wu, Y. Li, *Nat.*

Catal. **2019**, *2*, 304 – 312; b) P. Strasser, S. Koh, T. Anniyev, J. Greeley, K. More, C. Yu, Z. Liu, S. Kaya, D. Nordlund, H. Ogasawara, M. F. Toney, A. Nilsson, *Nat. Chem.* **2010**, *2*, 454 – 460.

[13] H. Wang, S. Xu, C. Tsai, Y. Li, C. Liu, J. Zhao, Y. Liu, H. Yuan, F. Abild-Pedersen, F. B. Prinz, J. K. Nørskov, Y. Cui, *Science* **2016**, *354*, 1031 – 1036.

[14] B. You, M. T. Tang, C. Tsai, F. Abild-Pedersen, X. L. Zheng, H. Li, *Adv. Mater.* **2019**, *31*, 1807001.

[15] a) M. Gong, H. J. Dai, *Nano Res.* **2015**, *8*, 23 – 39; b) Z. K. Goldsmith, A. K. Harshan, J. B. Gerken, M. Vörös, G. Galli, S. S. Stahl, S. Hammes-Schiffer, *Nat. Chem.* **2017**, *114*, 3050 – 3055; c) Z. Qiu, C. W. Tai, G. A. Niklasson, T. Edvinsson, *Energy Environ. Sci.* **2019**, *12*, 572 – 581; d) J. Y. C. Chen, L. Dang, H. F. Liang, W. Bi, J. B. Gerken, S. Jin, E. E. Alp, S. S. Stahl, *J. Am. Chem. Soc.* **2015**, *137*, 15090 – 15093; e) D. Friebel, M. W. Louie, M. Bajdich, K. E. Sanwald, Y. Cai, A. M. Wise, M. J. Cheng, D. Sokaras, T. C. Weng, R. Alonso-Mori, R. C. Davis, J. R. Bargar, J. K. Nørskov, A. Nilsson, A. T. Bell, *J. Am. Chem. Soc.* **2015**, *137*, 1305 – 1313.

[16] a) L. Wang, K. A. Stoerzinger, L. Chang, X. Yin, Y. Li, C. S. Tang, E. Jia, M. E. Bowden, Z. Yang, A. Abdelsamie, L. You, R. Guo, J. Chen, A. Rusydi, J. Wang, S. A. Chambers, Y. Du, *ACS Appl. Mater. Interfaces* **2019**, *11*, 12941 – 12947; b) J. R. Petrie, C. Mitra, H. Jeen, W. S. Choi, T. L. Meyer, F. A. Reboredo, J. W. Freeland, G. Eres, H. N. Lee, *Adv. Funct. Mater.* **2016**, *26*, 1564 – 1570.

[17] a) B. M. Hunter, J. R. Winkler, H. B. Gray, *Molecules* **2018**, *23*, 903 – 909; b) S. Piontek, C. Andronescu, A. Zaichenko, B. Konkena, K. J. Puring, B. Marler, H. Antoni, I. Sinev, M. Muhler, D. Mollenhauer, B. Roldan-Cuenya, W. Schuhmann, U. P. Apfel, *ACS Catal.* **2018**, *8*, 987 – 996; c) R. Fayad, J. Dhainy, H. Ghandour, L. Halaoui, *Catal. Sci. Technol.* **2017**, *7*, 3876 – 3891.

[18] a) B. M. Hunter, J. D. Blakemore, M. Deimund, H. B. Gray, J. R. Winkler, A. M. Müller, *J. Am. Chem. Soc.* **2014**, *136*, 13118 – 13121; b) C. Zhang, M. Shao, L. Zhou, Z. H. Li, K. M. Xiao, M. Wei, *ACS Appl. Mater. Interfaces* **2016**, *8*, 33697 – 33703.

[19] a) T. T. H. Hoang, A. A. Gewirth, *ACS Catal.* **2016**, *6*, 1159 – 1164; b) J. H. Huang, J. T. Chen, T. Yao, J. F. He, S. Jiang, Z. H. Sun, Q. H. Liu, W. R. Cheng, F. C. Hu, Y. Jiang, Z. Y. Pan, S. Q. Wei, *Angew. Chem. Int. Ed.* **2015**, *54*, 8722 – 8727; *Angew. Chem.* **2015**, *127*, 8846 – 8851.

[20] a) Y. Wang, M. Qiao, Y. Li, S. Wang, *Small* **2018**, *14*, 18001361; b) S. H. Zou, M. S. Burke, M. G. Kast, J. Fan, N. Danilovic, S. W. Boettcher, *Chem. Mater.* **2015**, *27*, 8011 – 8020.

[21] a) W. T. Hong, K. A. Stoerzinger, Y. L. Lee, L. Giordano, A. Grimaud, A. M. Johnson, J. Hwang, E. J. Crumlin, W. Yang, Y. Shao-Horn, *Energy Environ. Sci.* **2017**, *10*, 2190 – 2200; b) R. Zhou, Y. Zheng, M. Jaroniec, S. Z. Qiao, *ACS Catal.* **2016**, *6*, 4720 – 4728.

[22] a) Y. Ye, N. Zhang, X. Liu, *J. Mater. Chem. A* **2017**, *5*, 24208 – 24216; b) W. D. Chemelewski, H. C. Lee, J. F. Lin, A. J. Bard, C. B. Mullins, *J. Am. Chem. Soc.* **2014**, *136*, 2843 – 2850; c) L. Liardet, X. L. Hu, *ACS Catal.* **2018**, *8*, 644 – 650.

[23] a) V. D. Mote, Y. Purushotham, B. N. Dole, *J. Theor. Appl. Phys.* **2012**, *6*, 6 – 13; b) P. M. Kibasomba, S. Dhlamini, M. Maaza, C. Liu, M. M. Rashad, D. A. Rayan, B. W. Mwakikunga, *Results Phys.* **2018**, *9*, 628 – 635; c) D. Zhou, S. Wang, Y. Jia, X. Xiong, H. Yang, S. Liu, J. Tang, J. Zhang, D. Liu, L. Zheng, Y. Kuang, X. Sun, B. Liu, *Angew. Chem. Int. Ed.* **2019**, *58*, 736 – 740; *Angew. Chem.* **2019**, *131*, 746 – 750; d) S. E. Temmel, E. Fabbri, D. Pergolesi, T. Lippert, T. J. Schmidt, *ACS Catal.* **2016**, *6*, 7566 – 7576; e) R. Chattot, O. L. Bacq, V. Beermann, S. Kühn, T. Asset, L. Guétaz, G. Renou, J. Drnec, P. Bordet, A. Pasturel, A. Eychmüller, T. J. Schmidt, P. Strasser, L. Dubau, F. Maillard, *Nat. Mater.* **2018**, *17*, 827 – 833.

[24] a) Z. M. Chan, D. A. Kitchaev, J. N. Weker, C. Schnedermann, K. Lim, W. Tumas, M. F. Toney, D. G. Nocera, *Proc. Natl. Acad. Sci. USA* **2018**, *115*, E5261 – E5268; b) Y. Sun, H. Cheng, S. Gao, Z. Sun, Q. Liu, Q. Liu, F. Lei, T. Yao, J. He, S. Wei, Y. Xie, *Angew. Chem. Int. Ed.* **2012**, *51*, 8727 – 8731; *Angew. Chem.* **2012**, *124*, 8857 – 8861; c) G. Tsoukleri, J. Parthenios, K. Papagelis, R. Jalil, A. C. Ferrari, A. K. Geim, K. S. Novoselov, C. Galiotis, *Small* **2009**, *5*, 2397 – 2402.

[25] Y. Wang, Y. Zhang, Z. Liu, C. Xie, S. Feng, D. Liu, M. Shao, S. Wang, *Angew. Chem. Int. Ed.* **2017**, *56*, 5867 – 5871; *Angew. Chem.* **2017**, *129*, 5961 – 5965.

[26] H. B. Tao, L. Fang, J. Chen, H. B. Yang, J. Gao, J. Miao, S. Chen, B. Liu, *J. Am. Chem. Soc.* **2016**, *138*, 9978 – 9985.

[27] a) W. Cheng, X. Zhao, H. Su, F. Tang, W. Che, H. Zhang, Q. Liu, *Nat. Energy* **2019**, *4*, 115 – 122; b) Q. Wang, L. Shang, X. Zhang, Y. Zhao, G. I. N. Waterhouse, L. Z. Wu, C. H. Tung, T. Zhang, *Adv. Energy Mater.* **2017**, *7*, 1700467; c) P. S. Bagus, A. Wieckowski, H. Freund, *Comput. Theor. Chem.* **2012**, *987*, 22 – 24; d) C. Huang, Y. Zou, Y. Ye, T. Ouyang, K. Xiao, Z. Q. Liu, *Chem. Commun.* **2019**, *55*, 7687 – 7690.

[28] a) K. A. Stoerzinger, W. S. Choi, H. Jeen, H. N. Lee, Y. Shao-Horn, *J. Phys. Chem. Lett.* **2015**, *6*, 487 – 492; b) J. R. Kitchin, J. K. Nørskov, M. A. Barteau, J. G. Chen, *J. Phys. Rev. Lett.* **2004**, *93*, 156801 – 156803; c) M. Mavrikakis, B. Hammer, J. K. Nørskov, *Phys. Rev. Lett.* **1998**, *81*, 2819 – 2822.

[29] a) D. Zhou, Z. Cai, Y. Bi, W. Tian, M. Luo, Q. Zhang, Q. Xie, J. Wang, Y. Li, Y. Kuang, X. Duan, M. Bajdich, S. Siahrostami, X. Sun, *Nano Res.* **2018**, *11*, 1358 – 1368; b) Y. Xu, Y. Hao, G. Zhang, Z. Lu, S. Han, Y. Li, X. Sun, *RSC Adv.* **2015**, *5*, 55131 – 55135; c) Y. Wang, D. Yan, S. E. Hankari, Y. Zou, S. Wang, *Adv. Sci.* **2018**, *5*, 1800064; d) Y. Y. Dong, D. D. Ma, X. T. Wu, Q. L. Zhu, *Inorg. Chem. Front.* **2020**, *7*, 270-276. https://doi.org/10.1039/C9QI01367A.

[30] C. Yang, A. Grimaud, *Catalysts* **2017**, *7*, 149 – 175.

[31] B. Chen, X. He, F. Yin, H. Wang, D. Liu, R. Shi, J. Chen, H. Yin, *Adv. Funct. Mater.* **2017**, *27*, 1700795.

[32] T. Wang, Z. Kou, S. Mu, J. Liu, D. He, I. S. Amiinu, W. Meng, K. Zhou, Z. Luo, S. Chaemchuen, F. Verpoort, *Adv. Funct. Mater.* **2018**, *28*, 1705048.

[33] L. Zhu, D. Zheng, Z. Wang, X. Zheng, P. Fang, J. Zhu, M. Yu, Y. Tong, X. Lu, *Adv. Mater.* **2018**, *30*, 1805268.

[34] X. Han, W. Zhang, X. Ma, C. Zhong, N. Zhao, W. Hu, Y. Deng, *Adv. Mater.* **2019**, *31*, 1808281.

[35] C. Su, H. Cheng, W. Li, Z. Liu, N. Li, Z. Hou, F. Bai, H. Zhang, T. Ma, *Adv. Energy Mater.* **2017**, *7*, 1602420.

[36] S. Liu, Z. Wang, S. Zhou, F. Yu, M. Yu, C. Chiang, W. Zhou, J. Zhao, J. Qiu, *Adv. Mater.* **2017**, *29*, 1700874.

Manuscript received: December 24, 2019
Accepted manuscript online: January 8, 2020
Version of record online: January 29, 2020

7 References

[1] Z. W. Seh, J. Kibsgaard, C. F. Dickens, I. Chorkendorff, J. K. Nørskov, T. F. Jaramillo, Combining theory and experiment in electrocatalysis: Insights into materials design, *Science* 355 (2017) eaad4998.

[2] Net zero by 2050 – Analysis – IEA. https://www.iea.org/reports/net-zero-by-2050 (accessed February 2022)

[3] M. Höök, X. Tang, Depletion of fossil fuels and anthropogenic climate change—A review, *Energy Policy* 52 (2013) 797-809.

[4] A. Grubler, C. Wilson, N. Bento, B. Boza-Kiss, V. Krey, D. L. McCollum, N. D. Rao, K. Riahi, J. Rogelj, S. De Stercke, J. Cullen, S. Frank, O. Fricko, F. Guo, M. Gidden, P. Havlík, D. Huppmann, G. Kiesewetter, P. Rafaj, W. Schoepp, H. Valin, A low energy demand scenario for meeting the 1.5 °C target and sustainable development goals without negative emission technologies, *Nature Energy* 3 (2018) 515-527.

[5] Renewable energy: The clean facts. https://www.nrdc.org/stories/renewable-energy-clean-facts (accessed February 2022)

[6] A. Hussain, S. M. Arif, M. Aslam, Emerging renewable and sustainable energy technologies: State of the art, *Renewable and Sustainable Energy Reviews* 71 (2017) 12-28.

[7] P. Moriarty, D. Honnery, Global renewable energy resources and use in 2050, in: T.M. Letcher, (Ed.), *Managing global warming: An interface of technology and human issues*, Academic Press (2019), pp. 221-235.

[8] Renewables global status report. https://www.ren21.net/wp-content/uploads/2019/05/GSR2021_Full_Report.pdf (accessed February 2022)

[9] S. Agrawal, R. Soni, Renewable energy, *Energy* (2021) 131-150.

[10] P. Bezerra Leite Neto, O. R. Saavedra, D. Q. Oliveira, Renewable Sources Complementarity, in: A.C. Zambroni de Souza, B. Venkatesh, (Eds.), *Planning and operation of active distribution networks: Technical, social and environmental aspects*, Springer International Publishing, Cham (2022), pp. 353-376.

[11] F. Stöckl, W.-P. Schill, A. Zerrahn, Optimal supply chains and power sector benefits of green hydrogen, *Scientific Reports* 11 (2021) 14191.

[12] M. Fasihi, C. Breyer, Baseload electricity and hydrogen supply based on hybrid PV-wind power plants, *Journal of Cleaner Production* 243 (2020) 118466.

[13] The national hydrogen strategy. https://www.energypartnership.cn/fileadmin/user_upload/china/media_elements/Documents/German_National_Hydrogen_Strategy.pdf (accessed February 2022)

[14] UNFCCC. Adoption of the Paris agreement. Report No. FCCC/CP/2015/L.9/Rev.1, http://unfccc.int/resource/docs/2015/cop21/eng/l09r01.pdf (accessed February 2022)

[15] Office of energy efficiency & renewable energy, US. https://www.energy.gov/eere/fuelcells/hydrogen-production (accessed February 2022)

[16] Office of energy efficiency & renewable energy, US. https://www.energy.gov/eere/fuelcells/hydrogen-shot (accessed February 2022)

[17] The future of hydrogen, IEA. https://www.iea.org/reports/the-future-of-hydrogen (accessed February 2022)

[18] M. Yu, K. Wang, H. Vredenburg, Insights into low-carbon hydrogen production methods: Green, blue and aqua hydrogen, *International Journal of Hydrogen Energy* 46 (2021) 21261-21273.

[19] Office of energy efficiency & renewable energy, US. https://www.energy.gov/eere/fuelcells/h2scale (accessed February 2022)

[20] C. Hu, L. Zhang, J. Gong, Recent progress made in the mechanism comprehension and design of electrocatalysts for alkaline water splitting, *Energy & Environmental Science* 12 (2019) 2620-2645.

[21] K. Zeng, D. Zhang, Recent progress in alkaline water electrolysis for hydrogen production and applications, *Progress in Energy and Combustion Science* 36 (2010) 307-326.

[22] F. Safari, I. Dincer, A review and comparative evaluation of thermochemical water splitting cycles for hydrogen production, *Energy Conversion and Management* 205 (2020) 112182.

[23] R. Kothari, D. Buddhi, R. L. Sawhney, Comparison of environmental and economic aspects of various hydrogen production methods, *Renewable and Sustainable Energy Reviews* 12 (2008) 553-563.

[24] J. Brauns, T. Turek, Alkaline water electrolysis powered by renewable energy: A review, *Processes* 8 (2020) 248.

[25] P. Denholm, E. Ela, B. Kirby, M. Milligan. *Role of energy storage with renewable electricity generation*. No. NREL/TP-6A2-47187. National renewable energy lab.(NREL), Golden, CO (United States) (2010).

[26] K. G. dos Santos, C. T. Eckert, E. De Rossi, R. A. Bariccatti, E. P. Frigo, C. A. Lindino, H. J. Alves, Hydrogen production in the electrolysis of water in Brazil, a review, *Renewable and Sustainable Energy Reviews* 68 (2017) 563-571.

[27] O. Schmidt, A. Gambhir, I. Staffell, A. Hawkes, J. Nelson, S. Few, Future cost and performance of water electrolysis: An expert elicitation study, *International Journal of Hydrogen Energy* 42 (2017) 30470-30492.

[28] J. K. Nørskov, B. Weckhuysen, G. Centi, I. Chorkendorff, G. Marin, A. Grimaud, J. Rossmeisl, P. Strasser, M. Koper, B. Roldan, M. Behrens. Research needs towards sustainable production of fuels and chemicals. *Energy X*. (2019).

[29] T. D. Bennett, S. Horike, Liquid, glass and amorphous solid states of coordination polymers and metal–organic frameworks, *Nature Reviews Materials* 3 (2018) 431-440.

[30] Q.-L. Zhu, Q. Xu, Metal–organic framework composites, *Chemical Society Reviews* 43 (2014) 5468-5512.

[31] M. J. Van Vleet, T. Weng, X. Li, J. R. Schmidt, In situ, time-resolved, and mechanistic studies of metal–organic framework nucleation and growth, *Chemical Reviews* 118 (2018) 3681-3721.

[32] J. Zhou, B. Wang, Emerging crystalline porous materials as a multifunctional platform for electrochemical energy storage, *Chemical Society Reviews* 46 (2017) 6927-6945.

[33] J.-R. Li, J. Sculley, H.-C. Zhou, Metal–organic frameworks for separations, *Chemical Reviews* 112 (2012) 869-932.

[34] S. T. Meek, J. A. Greathouse, M. D. Allendorf, Metal-organic frameworks: A rapidly growing class of versatile nanoporous materials, *Advanced Materials* 23 (2011) 249-267.

[35] H. J. Buser, D. Schwarzenbach, W. Petter, A. Ludi, The crystal structure of Prussian Blue: $Fe_4[Fe(CN)_6]_3.xH_2O$, *Inorganic Chemistry* 16 (1977) 2704-2710.

[36] A. Werner, Beitrag zur Konstitution anorganischer Verbindungen, *Zeitschrift für Anorganische Chemie* 3 (1893) 267-330.

[37] A. Werner. On the constitution and configuration of higher-order compounds. Nobel Lecture, 11 December 1913. *The Nobel Prize* https://www.nobelprize.org/prizes/chemistry/1913/werner/lecture (accessed February 2022).

[38] K. A. Hofmann, F. Küspert, Verbindungen von kohlenwasserstoffen mit metallsalzen, *Zeitschrift für Anorganische Chemie* 15 (1897) 204-207.

[39] B. F. Hoskins, R. Robson, Design and construction of a new class of scaffolding-like materials comprising infinite polymeric frameworks of 3D-linked molecular rods. A reappraisal of the zinc cyanide and cadmium cyanide structures and the synthesis and structure of the diamond-related frameworks $[N(CH_3)_4][Cu^{I}Zn^{II}(CN)_4]$ and Cu^{I}[4,4',4",4'"-tetracyanotetraphenylmethane]$BF_4.xC_6H_5NO_2$, *The Journal of the American Chemical Society* 112 (1990) 1546-1554.

[40] O. M. Yaghi, H. Li, Hydrothermal synthesis of a metal-organic framework containing large rectangular channels, *The Journal of the American Chemical Society* 117 (1995) 10401-10402.

[41] M. Munakata, T. Kuroda-Sowa, M. Maekawa, A. Hirota, S. Kitagawa, Building of 2D sheet of tetrakis(methylthio)tetrathiafulvalenes coordinating to copper(I) halides with zigzag and helical frames and the 3D network through the S.cntdot. .cntdot. .cntdot.S contacts, *Inorganic Chemistry* 34 (1995) 2705-2710.

[42] D. Riou, O. Roubeau, G. Férey, Composite microporous compounds. Part I: Synthesis and structure determination of two new vanadium alkyldiphosphonates (MIL-2 and MIL-3) with three-dimensional open frameworks, *Microporous and Mesoporous Materials* 23 (1998) 23-31.

[43] H. Li, M. Eddaoudi, M. O'Keeffe, O. M. Yaghi, Design and synthesis of an exceptionally stable and highly porous metal-organic framework, *Nature* 402 (1999) 276-279.

[44] S. Y. Chui Stephen, M. F. Lo Samuel, P. H. Charmant Jonathan, A.G. Orpen, D. Williams Ian, A chemically functionalizable nanoporous material $[Cu_3(TMA)_2(H_2O)_3]_n$, *Science* 283 (1999) 1148-1150.

[45] M. J. Kalmutzki, N. Hanikel, O. M. Yaghi, Secondary building units as the turning point in the development of the reticular chemistry of MOFs, *Science Advances* 4 (2018) eaat9180.

[46] M. Eddaoudi, D. B. Moler, H. Li, B. Chen, T. M. Reineke, M. O'Keeffe, O. M. Yaghi, Modular chemistry: Secondary building units as a basis for the design of highly porous and robust metal−organic carboxylate frameworks, *Accounts of Chemical Research* 34 (2001) 319-330.

[47] O. M. Yaghi, M. J. Kalmutzki, C. S. Diercks. *Introduction to reticular chemistry: Metal-organic frameworks and covalent organic frameworks*. John Wiley & Sons, (2019).

[48] HKUST-1: Cage-like structure surrounded by benzene. https://www.chem-station.com/chemglossary/2021/01/hkust-1.html (accessed February 2022)

[49] A. Schneemann, V. Bon, I. Schwedler, I. Senkovska, S. Kaskel, R. A. Fischer, Flexible metal–organic frameworks, *Chemical Society Reviews* 43 (2014) 6062-6096.

[50] D. Bousquet, F.-X. Coudert, A. G. J. Fossati, A. V. Neimark, A. H. Fuchs, A. Boutin, Adsorption induced transitions in soft porous crystals: An osmotic potential approach to multistability and intermediate structures, *The Journal of Chemical Physics* 138 (2013) 174706.

[51] F.-X. Coudert, A. Boutin, A. H. Fuchs, A. V. Neimark, Adsorption deformation and structural transitions in metal–organic frameworks: From the unit cell to the crystal, *The Journal of Physical Chemistry Letters* 4 (2013) 3198-3205.

[52] S. M. Moosavi, A. Nandy, K. M. Jablonka, D. Ongari, J. P. Janet, P. G. Boyd, Y. Lee, B. Smit, H. J. Kulik, Understanding the diversity of the metal-organic framework ecosystem, *Nature Communications* 11 (2020) 4068.

[53] S. Mukherjee, S. Hou, S. A. Watzele, B. Garlyyev, W. Li, A. S. Bandarenka, R. A. Fischer, Avoiding pyrolysis and calcination: Advances in the benign routes leading to MOF-derived electrocatalysts, *ChemElectroChem* 9 (2021) e202101476.

[54] A. L. Semrau, Z. Zhou, S. Mukherjee, M. Tu, W. Li, R. A. Fischer, Surface-mounted metal–organic frameworks: Past, present, and future perspectives, *Langmuir* 37 (2021) 6847-6863.

[55] L. Heinke, C. Wöll, Surface-mounted metal–organic frameworks: Crystalline and porous molecular assemblies for fundamental insights and advanced applications, *Advanced Materials* 31 (2019) 1806324.

[56] D. Zacher, O. Shekhah, C. Wöll, R. A. Fischer, Thin films of metal–organic frameworks, *Chemical Society Reviews* 38 (2009) 1418-1429.

[57] K. B. Lausund, O. Nilsen, All-gas-phase synthesis of UiO-66 through modulated atomic layer deposition, *Nature Communications* 7 (2016) 13578.

[58] X. Zhang, K. Wan, P. Subramanian, M. Xu, J. Luo, J. Fransaer, Electrochemical deposition of metal–organic framework films and their applications, *Journal of Materials Chemistry A* 8 (2020) 7569-7587.

[59] O. Shekhah, H. Wang, S. Kowarik, F. Schreiber, M. Paulus, M. Tolan, C. Sternemann, F. Evers, D. Zacher, R. A. Fischer, C. Wöll, Step-by-step route for the synthesis of

metal−organic frameworks, *The Journal of the American Chemical Society* 129 (2007) 15118-15119.

[60] M. Usman, Q.-L. Zhu, *Metal–organic frameworks for electrocatalysis*, in: Inamuddin, R. Boddula, A.M. Asiri, (Eds.), *Methods for electrocatalysis: Advanced materials and allied applications*, Springer International Publishing, Cham (2020) pp. 29-66.

[61] W. Zheng, L. Y. S. Lee, Metal–organic frameworks for electrocatalysis: catalyst or precatalyst? *ACS Energy Letters* 6 (2021) 2838-2843.

[62] S. Zhao, Y. Yang, Z. Tang, Insight into structural evolution, active sites, and stability of heterogeneous electrocatalysts, *Angewandte Chemie International Edition* (2022) e202110186.

[63] R. Dong, M. Pfeffermann, H. Liang, Z. Zheng, X. Zhu, J. Zhang, X. Feng, Large-area, free-standing, two-dimensional supramolecular polymer single-layer sheets for highly efficient electrocatalytic hydrogen evolution, *Angewandte Chemie International Edition* 54 (2015) 12058-12063.

[64] R. Dong, Z. Zheng, D. C. Tranca, J. Zhang, N. Chandrasekhar, S. Liu, X. Zhuang, G. Seifert, X. Feng, Immobilizing molecular metal dithiolene-diamine complexes on 2D metal-organic frameworks for electrocatalytic H_2 production, *Chemistry - A European Journal* 23 (2017) 2255-2260.

[65] Y. K. Hwang, D.-Y. Hong, J.-S. Chang, S. H. Jhung, Y.-K. Seo, J. Kim, A. Vimont, M. Daturi, C. Serre, G. Férey, Amine grafting on coordinatively unsaturated metal centers of MOFs: Consequences for catalysis and metal encapsulation, *Angewandte Chemie* 120 (2008) 4212-4216.

[66] L. Tao, C.-Y. Lin, S. Dou, S. Feng, D. Chen, D. Liu, J. Huo, Z. Xia, S. Wang, Creating coordinatively unsaturated metal sites in metal-organic-frameworks as efficient electrocatalysts for the oxygen evolution reaction: Insights into the active centers, *Nano Energy* 41 (2017) 417-425.

[67] D. Li, H.-Q. Xu, L. Jiao, H.-L. Jiang, Metal-organic frameworks for catalysis: State of the art, challenges, and opportunities, *EnergyChem* 1 (2019) 100005.

[68] S. Dou, C.-L. Dong, Z. Hu, Y.-C. Huang, J.-l. Chen, L. Tao, D. Yan, D. Chen, S. Shen, S. Chou, S. Wang, Atomic-scale CoO_x species in metal–organic frameworks for oxygen evolution reaction, *Advanced Functional Materials* 27 (2017) 1702546.

[69] S. Zhao, Y. Wang, J. Dong, C.-T. He, H. Yin, P. An, K. Zhao, X. Zhang, C. Gao, L. Zhang, J. Lv, J. Wang, J. Zhang, A.M. Khattak, N.A. Khan, Z. Wei, J. Zhang, S. Liu, H. Zhao, Z. Tang, Ultrathin metal–organic framework nanosheets for electrocatalytic oxygen evolution, *Nature Energy* 1 (2016) 16184.

[70] X. Yang, Y. Wang, X. Tong, N. Yang, Strain engineering in electrocatalysts: Fundamentals, progress, and perspectives, *Advanced Energy Materials* 12 (2022) 2102261.

[71] W. Cheng, X. Zhao, H. Su, F. Tang, W. Che, H. Zhang, Q. Liu, Lattice-strained metal–organic-framework arrays for bifunctional oxygen electrocatalysis, *Nature Energy* 4 (2019) 115-122.

[72] Y. Mousazade, M. R. Mohammadi, P. Chernev, R. Bagheri, Z. Song, H. Dau, M. M. Najafpour, Revisiting metal–organic frameworks for oxygen evolution: A case study,

Inorganic Chemistry 59 (2020) 15335-15342.

[73] J. Tian, F. Jiang, D. Yuan, L. Zhang, Q. Chen, M. Hong, Electric‐field assisted in situ hydrolysis of bulk metal–organic frameworks (MOFs) into ultrathin metal oxyhydroxide nanosheets for efficient oxygen evolution, *Angewandte Chemie International Edition* 59 (2020) 13101-13108.

[74] M. Liu, L. Kong, X. Wang, J. He, J. Zhang, J. Zhu, X.-H. Bu, Deciphering of advantageous electrocatalytic water oxidation behavior of metal-organic framework in alkaline media, *Nano Research* 14 (2021) 4680-4688.

[75] Q. Qian, Y. Li, Y. Liu, L. Yu, G. Zhang, Ambient fast synthesis and active sites deciphering of hierarchical foam-like trimetal–organic framework nanostructures as a platform for highly efficient oxygen evolution electrocatalysis, *Advanced Materials* 31 (2019) 1901139.

[76] K. Rui, G. Zhao, Y. Chen, Y. Lin, Q. Zhou, J. Chen, J. Zhu, W. Sun, W. Huang, S. X. Dou, Hybrid 2D dual-metal–organic frameworks for enhanced water oxidation catalysis, *Advanced Functional Materials* 28 (2018) 1801554.

[77] W. Zheng, M. Liu, L. Y. S. Lee, Electrochemical instability of metal–organic frameworks: In situ spectroelectrochemical investigation of the real active sites, *ACS Catalysis* 10 (2020) 81-92.

[78] X. Cao, Y. Jie, N. Wang, Z. L. Wang, Triboelectric nanogenerators driven self-powered electrochemical processes for energy and environmental science, *Advanced Energy Materials* 6 (2016) 1600665.

[79] C. L. Bentley, M. Kang, P. R. Unwin, Nanoscale surface structure–activity in electrochemistry and electrocatalysis, *Journal of the American Chemical Society* 141 (2019) 2179-2193.

[80] J. Qiao, Y. Liu, F. Hong, J. Zhang, A review of catalysts for the electroreduction of carbon dioxide to produce low-carbon fuels, *Chemical Society Reviews* 43 (2014) 631-675.

[81] X. Zhang, Y. Xia, C. Xia, H. Wang, Insights into practical-scale electrochemical H_2O_2 synthesis, *Trends in Chemistry* 2 (2020) 942-953.

[82] A. U. Pawar, C. W. Kim, M.-T. Nguyen-Le, Y. S. Kang, General review on the components and parameters of photoelectrochemical system for CO_2 reduction with in situ analysis, *ACS Sustainable Chemistry & Engineering* 7 (2019) 7431-7455.

[83] B. Wang, X. Cui, J. Huang, R. Cao, Q. Zhang, Recent advances in energy chemistry of precious-metal-free catalysts for oxygen electrocatalysis, *Chinese Chemical Letters* 29 (2018) 1757-1767.

[84] Y. Zheng, Y. Jiao, Y. Zhu, L. H. Li, Y. Han, Y. Chen, A. Du, M. Jaroniec, S. Z. Qiao, Hydrogen evolution by a metal-free electrocatalyst, *Nature Communications* 5 (2014) 3783.

[85] I. Chorkendorff, J. W. Niemantsverdriet, *Concepts of modern catalysis and kinetics*, Wiley-VCH, Weinheim (2017).

[86] R. A. van Santen, *Modern heterogeneous catalysis: An introduction*, Wiley-VCH Verlag, Weinheim (2017).

[87] P. Sabatier, Hydrogénations et déshydrogénations par catalyse. *Berichte der deutschen chemischen Gesellschaft* 3 (1911) 1984.

[88] P. Quaino, F. Juarez, E. Santos, W. Schmickler, Volcano plots in hydrogen electrocatalysis – uses and abuses, *Beilstein Journal of Nanotechnology* 5 (2014) 846-854.

[89] H. Gerischer, Mechanismus der elektrolytischen wasserstoffabscheidung und adsorptionsenergie von atomarem wasserstoff, *Bulletin des Sociétés Chimiques Belges* 67 (1958) 506-527.

[90] R. Parsons, The rate of electrolytic hydrogen evolution and the heat of adsorption of hydrogen, *Transactions of the Faraday Society* 54 (1958) 1053-1063.

[91] E. Santos, W. Schmickler, eds. *Catalysis in electrochemistry: from fundamental aspects to strategies for fuel cell development*. Vol. 7. John Wiley & Sons (2011).

[92] S. Trasatti, Work function, electronegativity, and electrochemical behaviour of metals: III. Electrolytic hydrogen evolution in acid solutions, *Journal of Electroanalytical Chemistry and Interfacial Electrochemistry* 39 (1972) 163-184.

[93] J. K. Nørskov, J. Rossmeisl, A. Logadottir, L. Lindqvist, J. R. Kitchin, T. Bligaard, H. Jónsson, Origin of the overpotential for oxygen reduction at a fuel-cell cathode, *The Journal of Physical Chemistry B* 108 (2004) 17886-17892.

[94] J. Rossmeisl, A. Logadottir, J. K. Nørskov, Electrolysis of water on (oxidized) metal surfaces, *Chemical Physics* 319 (2005) 178-184.

[95] J. Greeley, T. F. Jaramillo, J. Bonde, I. Chorkendorff, J. K. Nørskov, Computational high-throughput screening of electrocatalytic materials for hydrogen evolution, *Nature Materials* 5 (2006) 909-913.

[96] F. Zaera, Probing liquid/solid interfaces at the molecular level, *Chemical Reviews* 112 (2012) 2920-2986.

[97] B. L. Mojet, S. D. Ebbesen, L. Lefferts, Light at the interface: the potential of attenuated total reflection infrared spectroscopy for understanding heterogeneous catalysis in water, *Chemical Society Reviews* 39 (2010) 4643-4655.

[98] A. S. Bandarenka, M. T. M. Koper, Structural and electronic effects in heterogeneous electrocatalysis: Toward a rational design of electrocatalysts, *Journal of Catalysis* 308 (2013) 11-24.

[99] B. Hammer, Special sites at noble and late transition metal catalysts, *Topics in Catalysis* 37 (2006) 3-16.

[100] A. Nilsson, L. G. M. Pettersson, B. Hammer, T. Bligaard, C. H. Christensen, J. K. Nørskov, The electronic structure effect in heterogeneous catalysis, *Catalysis Letters* 100 (2005) 111-114.

[101] M. T. M. Koper, Structure sensitivity and nanoscale effects in electrocatalysis, *Nanoscale* 3 (2011) 2054-2073.

[102] R. R. Adžić, A. V. Tripković, W. E. O'Grady, Structural effects in electrocatalysis, *Nature* 296 (1982) 137-138.

[103] E. Santos, P. Quaino, W. Schmickler, Theory of electrocatalysis: Hydrogen evolution and more, *Physical Chemistry Chemical Physics* 14 (2012) 11224-11233.

[104] J. Greeley, I. E. L. Stephens, A. S. Bondarenko, T. P. Johansson, H. A. Hansen, T. F. Jaramillo, J. Rossmeisl, I. Chorkendorff, J. K. Nørskov, Alloys of platinum and early transition metals as oxygen reduction electrocatalysts, *Nature Chemistry* 1 (2009) 552-556.

[105] W. Wan, C. A. Triana, J. Lan, J. Li, C. S. Allen, Y. Zhao, M. Iannuzzi, G. R. Patzke, Bifunctional single atom electrocatalysts: coordination–performance correlations and reaction pathways, *ACS Nano* 14 (2020) 13279-13293.

[106] J. Liu, J. Xiao, B. Luo, E. Tian, G. I. N. Waterhouse, Central metal and ligand effects on oxygen electrocatalysis over 3d transition metal single-atom catalysts: A theoretical investigation, *Chemical Engineering Journal* 427 (2022) 132038.

[107] J. Hu, C. Zhang, X. Meng, H. Lin, C. Hu, X. Long, S. Yang, Hydrogen evolution electrocatalysis with binary-nonmetal transition metal compounds, *Journal of Materials Chemistry A* 5 (2017) 5995-6012.

[108] Y. Zheng, Y. Jiao, A. Vasileff, S.-Z. Qiao, The hydrogen evolution reaction in alkaline solution: From theory, single crystal models, to practical electrocatalysts, *Angewandte Chemie International Edition* 57 (2018) 7568-7579.

[109] M. Zhou, C. Li, J. Fang, Noble-metal based random alloy and intermetallic nanocrystals: Syntheses and applications, *Chemical Reviews* 121 (2021) 736-795.

[110] V. Čolić, A. S. Bandarenka, Pt alloy electrocatalysts for the oxygen reduction reaction: From model surfaces to nanostructured systems, *ACS Catalysis* 6 (2016) 5378-5385.

[111] F. Dionigi, P. Strasser, NiFe-based (oxy)hydroxide catalysts for oxygen evolution reaction in non-acidic electrolytes, *Advanced Energy Materials* 6 (2016) 1600621.

[112] M. Görlin, J. Ferreira de Araújo, H. Schmies, D. Bernsmeier, S. Dresp, M. Gliech, Z. Jusys, P. Chernev, R. Kraehnert, H. Dau, P. Strasser, Tracking catalyst redox states and reaction dynamics in Ni–Fe oxyhydroxide oxygen evolution reaction electrocatalysts: The role of catalyst support and electrolyte pH, *Journal of the American Chemical Society* 139 (2017) 2070-2082.

[113] H. Shin, H. Xiao, W. A. Goddard, In silico discovery of new dopants for Fe-doped Ni oxyhydroxide ($Ni_{1-x}Fe_xOOH$) catalysts for oxygen evolution reaction, *Journal of the American Chemical Society* 140 (2018) 6745-6748.

[114] L. Trotochaud, S. L. Young, J. K. Ranney, S. W. Boettcher, Nickel–iron oxyhydroxide oxygen-evolution electrocatalysts: The role of intentional and incidental iron incorporation, *Journal of the American Chemical Society* 136 (2014) 6744-6753.

[115] D. Friebel, M. W. Louie, M. Bajdich, K. E. Sanwald, Y. Cai, A. M. Wise, M.-J. Cheng, D. Sokaras, T.-C. Weng, R. Alonso-Mori, R. C. Davis, J. R. Bargar, J. K. Nørskov, A. Nilsson, A. T. Bell, Identification of highly active Fe sites in (Ni,Fe)OOH for electrocatalytic water splitting, *Journal of the American Chemical Society* 137 (2015) 1305-1313.

[116] Y. Li, Y. Sun, Y. Qin, W. Zhang, L. Wang, M. Luo, H. Yang, S. Guo, Recent advances on water-splitting electrocatalysis mediated by noble-metal-based nanostructured materials, *Advanced Energy Materials* 10 (2020) 1903120.

[117] H. Xu, H. Shang, C. Wang, Y. Du, Low-dimensional metallic nanomaterials for advanced electrocatalysis, *Advanced Functional Materials* 30 (2020) 2006317.

[118] M. D. Pohl, S. Watzele, F. Calle-Vallejo, A. S. Bandarenka, Nature of highly active electrocatalytic sites for the hydrogen evolution reaction at Pt electrodes in acidic media, *ACS Omega* 2 (2017) 8141-8147.

[119] M. Rück, A. Bandarenka, F. Calle-Vallejo, A. Gagliardi, Fast identification of optimal pure platinum nanoparticle shapes and sizes for efficient oxygen electroreduction, *Nanoscale Advances* 1 (2019) 2901-2909.

[120] A. J. Bard, L. R. Faulkner, *Electrochemical methods: Fundamentals and applications*, 2nd edn., Wiley, Hoboken, NJ (2001).

[121] H. Wang, L. Pilon, Accurate simulations of electric double layer capacitance of ultramicroelectrodes, *The Journal of Physical Chemistry C* 115 (2011) 16711-16719.

[122] H. Helmholtz, Studien über electrische grenzschichten, *Annalen der Physik* 243 (1879) 337-382.

[123] R. Burt, G. Birkett, X. S. Zhao, A review of molecular modelling of electric double layer capacitors, *Physical Chemistry Chemical Physics* 16 (2014) 6519-6538.

[124] M. Gouy, Constitution of the electric charge at the surace of an electrolyte. *Journal de Physique Théorique et Appliquée* 9 (1910) 457-468.

[125] D. L. Chapman, LI. *A contribution to the theory of electrocapillarity*, The London, Edinburgh, and Dublin Philosophical Magazine and Journal of Science 25 (1913) 475-481.

[126] O. Stern, Zur theorie der elektrolytischen doppelschicht, *Zeitschrift für Elektrochemie und angewandte physikalische Chemie* 30 (1924) 508-516.

[127] D. C. Grahame, The electrical double layer and the theory of electrocapillarity, *Chemical Reviews* 41 (1947) 441-501.

[128] K. Krischer, E. R. Savinova, *Fundamentals of electrocatalysis*, In Handbook of Heterogeneous Catalysis (eds G. Ertl, H. Knözinger, F. Schüth and J. Weitkamp) (2008).

[129] C. Dong, Y. Li, D. Cheng, M. Zhang, J. Liu, Y.-G. Wang, D. Xiao, D. Ma, Supported metal clusters: Fabrication and application in heterogeneous catalysis, *ACS Catalysis* 10 (2020) 11011-11045.

[130] J.C. Védrine, Heterogeneous catalysis on metal oxides, *Catalysts* 7 (2017) 341.

[131] W. Williams, C. Marks, L. Schmidt, Steps in the reaction $H_2 + O_2 \rightleftharpoons H_2O$ on Pt: OH desorption at high temperatures, *The Journal of Physical Chemistry* 96 (1992) 5922-5931.

[132] B. Garlyyev, K. Kratzl, M. Rück, J. Michalička, J. Fichtner, J. M. Macak, T. Kratky, S. Günther, M. Cokoja, A. S. Bandarenka, A. Gagliardi, R. A. Fischer, Optimizing the size of platinum nanoparticles for enhanced mass activity in the electrochemical oxygen reduction reaction, *Angewandte Chemie International Edition* 58 (2019) 9596-9600.

[133] B. Garlyyev, S. Xue, S. Watzele, D. Scieszka, A. S. Bandarenka, Influence of the nature of the alkali metal cations on the electrical double-layer capacitance of model Pt(111) and Au(111) electrodes, *The Journal of Physical Chemistry Letters* 9 (2018) 1927-1930.

[134] B. Deng, M. Huang, X. Zhao, S. Mou, F. Dong, Interfacial electrolyte effects on electrocatalytic CO_2 reduction, *ACS Catalysis* 12 (2022) 331-362.

[135] L. V. Haynes, D. T. Sawyer, Electrochemistry of carbon dioxide in dimethyl sulfoxide at gold and mercury electrodes, *Analytical Chemistry* 39 (1967) 332-338.

[136] M. C. Figueiredo, I. Ledezma-Yanez, M. T. M. Koper, In situ spectroscopic study of CO_2 electroreduction at copper electrodes in acetonitrile, *ACS Catalysis* 6 (2016) 2382-2392.

[137] John O'M. BockrisAmulya K. N. ReddyMaria Gamboa-Aldeco, *Modern electrochemistry 2A: Fundamentals of electrodics*, Springer Science & Business Media (2000).

[138] M. M. Waegele, C. M. Gunathunge, J. Li, X. Li, How cations affect the electric double layer and the rates and selectivity of electrocatalytic processes, *The Journal of Chemical Physics* 151 (2019) 160902.

[139] S. Xue, B. Garlyyev, S. Watzele, Y. Liang, J. Fichtner, M. D. Pohl, A. S. Bandarenka, Influence of alkali metal cations on the hydrogen evolution reaction activity of Pt, Ir, Au, and Ag electrodes in alkaline electrolytes, *ChemElectroChem* 5 (2018) 2326-2329.

[140] B. Garlyyev, S. Xue, M. D. Pohl, D. Reinisch, A. S. Bandarenka, Oxygen electroreduction at high-index Pt electrodes in alkaline electrolytes: A decisive role of the alkali metal cations, *ACS Omega* 3 (2018) 15325-15331.

[141] D. Zhou, Z. Cai, Y. Bi, W. Tian, M. Luo, Q. Zhang, Q. Zhang, Q. Xie, J. Wang, Y. Li, Y. Kuang, X. Duan, M. Bajdich, S. Siahrostami, X. Sun, Effects of redox-active interlayer anions on the oxygen evolution reactivity of NiFe-layered double hydroxide nanosheets, *Nano Research* 11 (2018) 1358-1368.

[142] B. M. Hunter, W. Hieringer, J. R. Winkler, H. B. Gray, A. M. Müller, Effect of interlayer anions on [NiFe]-LDH nanosheet water oxidation activity, *Energy & Environmental Science* 9 (2016) 1734-1743.

[143] Cornell A. Hydrogen production by electrolysis. In: 1st international conference on electrolysis, Copenhagen, Denmark, June, 12-15; 2017. https:// energiforskmedia.blob.core.windows.net/media/23562/5- hydrogen-production-by-electrolysis-ann-cornell-kth.pdf (accessed February 2022)

[144] A. Le Goff, V. Artero, B. Jousselme, D. Tran Phong, N. Guillet, R. Métayé, A. Fihri, S. Palacin, M. Fontecave, From hydrogenases to noble metal–free catalytic nanomaterials for H_2 production and uptake, *Science* 326 (2009) 1384-1387.

[145] A. Ursua, L. M. Gandia, P. Sanchis, Hydrogen production from water electrolysis: Current status and future trends, *Proceedings of the IEEE* 100 (2012) 410-426.

[146] Y. Jiao, Y. Zheng, M. Jaroniec, S. Z. Qiao, Design of electrocatalysts for oxygen- and hydrogen-involving energy conversion reactions, *Chemical Society Reviews* 44 (2015) 2060-2086.

[147] C. G. Morales-Guio, L.-A. Stern, X. Hu, Nanostructured hydrotreating catalysts for electrochemical hydrogen evolution, *Chemical Society Reviews* 43 (2014) 6555-6569.

[148] J. Liu, S. Hou, W. Li, A. S. Bandarenka, R. A. Fischer, Recent approaches to design electrocatalysts based on metal–organic frameworks and their derivatives, *Chemistry—*

An Asian Journal 14 (2019) 3474-3501.

[149] J. Tymoczko, F. Calle-Vallejo, W. Schuhmann, A. S. Bandarenka, Making the hydrogen evolution reaction in polymer electrolyte membrane electrolysers even faster, *Nature Communications* 7 (2016) 10990.

[150] Q. Shao, J. Yang, X. Huang, The design of water oxidation electrocatalysts from nanoscale metal–organic frameworks, *Chemistry – A European Journal* 24 (2018) 15143-15155.

[151] K. S. Exner, Why the breaking of the OOH versus OH scaling relation might cause decreased electrocatalytic activity, *Chem Catalysis* 1 (2021) 258-271.

[152] N. Zhang, Y. Chai, Lattice oxygen redox chemistry in solid-state electrocatalysts for water oxidation, *Energy & Environmental Science* 14 (2021) 4647-4671.

[153] N.-T. Suen, S.-F. Hung, Q. Quan, N. Zhang, Y.-J. Xu, H. M. Chen, Electrocatalysis for the oxygen evolution reaction: recent development and future perspectives, *Chemical Society Reviews* 46 (2017) 337-365.

[154] J. Song, C. Wei, Z.-F. Huang, C. Liu, L. Zeng, X. Wang, Z. J. Xu, A review on fundamentals for designing oxygen evolution electrocatalysts, *Chemical Society Reviews* 49 (2020) 2196-2214.

[155] H. Jiang, Q. He, Y. Zhang, L. Song, Structural self-reconstruction of catalysts in electrocatalysis, *Accounts of Chemical Research* 51 (2018) 2968-2977.

[156] L. C. Seitz, C. F. Dickens, K. Nishio, Y. Hikita, J. Montoya, A. Doyle, C. Kirk, A. Vojvodic, H. Y. Hwang, J. K. Norskov, T. F. Jaramillo, A highly active and stable IrOx/$SrIrO_3$ catalyst for the oxygen evolution reaction, *Science* 353 (2016) 1011-1014.

[157] E. Fabbri, M. Nachtegaal, T. Binninger, X. Cheng, B.-J. Kim, J. Durst, F. Bozza, T. Graule, R. Schäublin, L. Wiles, M. Pertoso, N. Danilovic, K. E. Ayers, T. J. Schmidt, Dynamic surface self-reconstruction is the key of highly active perovskite nano-electrocatalysts for water splitting, *Nature Materials* 16 (2017) 925-931.

[158] J. T. Mefford, X. Rong, A. M. Abakumov, W. G. Hardin, S. Dai, A. M. Kolpak, K. P. Johnston, K. J. Stevenson, Water electrolysis on $La_{1-x}Sr_xCoO_{3-\delta}$ perovskite electrocatalysts, *Nature Communications* 7 (2016) 11053.

[159] Z.-F. Huang, J. Song, Y. Du, S. Xi, S. Dou, J. M. V. Nsanzimana, C. Wang, Z. J. Xu, X. Wang, Chemical and structural origin of lattice oxygen oxidation in Co–Zn oxyhydroxide oxygen evolution electrocatalysts, *Nature Energy* 4 (2019) 329-338.

[160] A. Grimaud, O. Diaz-Morales, B. Han, W. T. Hong, Y.-L. Lee, L. Giordano, K. A. Stoerzinger, M. T. M. Koper, Y. Shao-Horn, Activating lattice oxygen redox reactions in metal oxides to catalyse oxygen evolution, *Nature Chemistry* 9 (2017) 457-465.

[161] H. N. Nong, T. Reier, H.-S. Oh, M. Gliech, P. Paciok, T. H. T. Vu, D. Teschner, M. Heggen, V. Petkov, R. Schlögl, T. Jones, P. Strasser, A unique oxygen ligand environment facilitates water oxidation in hole-doped IrNiOx core–shell electrocatalysts, *Nature Catalysis* 1 (2018) 841-851.

[162] Y. Tian, S. Wang, E. Velasco, Y. Yang, L. Cao, L. Zhang, X. Li, Y. Lin, Q. Zhang, L. Chen, A Co-doped nanorod-like RuO_2 electrocatalyst with abundant oxygen vacancies for acidic water oxidation, *iScience* 23 (2020) 100756.

[163] D. Scieszka, J. Yun, A. S. Bandarenka, What do laser-induced transient techniques reveal for batteries? Na- and K-intercalation from aqueous electrolytes as an example, *ACS Applied Materials & Interfaces* 9 (2017) 20213-20222.

[164] Rotating ring disk electrode fundamentals, https://pineresearch.com/shop/kb/theory/hydrodynamic-electrochemistry/rotating-electrode-theory/ (accessed February 2022)

[165] L. Alonso, S. Palmero, E. Muñoz, S. Sanllorente, M. A. García-García, Electrochemical behavior of menadione on glassy carbon rotating disk electrode (RDE), *Electroanalysis* 12 (2000) 757-762.

[166] L. S. Rocha, J. P. Pinheiro, H. M. Carapuça, Evaluation of nanometer thick mercury film electrodes for stripping chronopotentiometry, *Journal of Electroanalytical Chemistry* 610 (2007) 37-45.

[167] Hamann, C. H., Hamnet A. & Vielstich, W., *Electrochemistry*, (2007). 2nd edition, Wiley-VCH., Weinheim

[168] M. H. Pournaghi-Azar, H. Razmi-Nerbin, Electrocatalytic characteristics of ascorbic acid oxidation at nickel plated aluminum electrodes modified with nickel pentacyanonitrosylferrate films, *Journal of Electroanalytical Chemistry* 488 (2000) 17-24.

[169] E3PK fixed-disk RDE tips PEEK, https://pineresearch.com/shop/products/electrodes/rde/e3pk-fixed-disk/ (accessed February 2022)

[170] J. Kibsgaard, I. Chorkendorff, Considerations for the scaling-up of water splitting catalysts, *Nature Energy* 4 (2019) 430-433.

[171] K. D. Kwon, H. Green, P. Björn, J. D. Kubicki, Model bacterial extracellular polysaccharide adsorption onto silica and alumina: Quartz crystal microbalance with dissipation monitoring of dextran adsorption, *Environmental Science & Technology* 40 (2006) 7739-7744.

[172] W.-Y. Tsai, P.-L. Taberna, P. Simon, Electrochemical quartz crystal microbalance (EQCM) study of ion dynamics in nanoporous carbons, *Journal of the American Chemical Society* 136 (2014) 8722-8728.

[173] D. Voiry, M. Chhowalla, Y. Gogotsi, N. A. Kotov, Y. Li, R. M. Penner, R. E. Schaak, P. S. Weiss, Best practices for reporting electrocatalytic performance of nanomaterials, *ACS Nano* 12 (2018) 9635-9638.

[174] J. R. Swierk, S. Klaus, L. Trotochaud, A. T. Bell, T. D. Tilley, Electrochemical study of the energetics of the oxygen evolution reaction at nickel iron (oxy)hydroxide catalysts, *The Journal of Physical Chemistry C* 119 (2015) 19022-19029.

[175] Hüfner, Stephan. *Photoelectron spectroscopy: principles and applications*. Springer Science & Business Media (2013).

[176] Photoelectron spectrometer, ESCALAB Mk II by vacuum generators, https://jacobs.physik.uni-saarland.de/home/index.php?page=steinbeiss/home_cms_steinbeissdet3-1&navi=service (accessed February 2022).

[177] Lee, Myeongkyu. *X-Ray diffraction for materials research: From fundamentals to applications*. CRC Press (2017).

[178] J. Perlich, J. Rubeck, S. Botta, R. Gehrke, S. V. Roth, M. A. Ruderer, S. M. Prams, M. Rawolle, Q. Zhong, V. Körstgens, P. Müller-Buschbaum, Grazing incidence wide angle x-ray scattering at the wiggler beamline BW4 of HASYLAB, *Review of Scientific Instruments* 81 (2010) 105105.

[179] S. Mosca, C. Conti, N. Stone, P. Matousek, Spatially offset Raman spectroscopy, *Nature Reviews Methods Primers* 1 (2021) 21.

[180] R. N. S. Sodhi, Time-of-flight secondary ion mass spectrometry (TOF-SIMS):—versatility in chemical and imaging surface analysis, *Analyst* 129 (2004) 483-487.

[181] G. Binnig, C. F. Quate, C. Gerber, Atomic force microscope, *Physical Review Letters* 56 (1986) 930-933.

[182] McClelland, Gary M., Ragnar Erlandsson, and Shirley Chiang. "Atomic force microscopy: General principles and a new implementation." In *review of progress in quantitative nondestructive evaluation*, pp. 1307-1314. Springer, Boston, MA (1987).

[183] I. W. Rangelow, T. Ivanov, A. Ahmad, M. Kaestner, C. Lenk, I. S. Bozchalooi, F. Xia, K. Youcef-Toumi, M. Holz, A. Reum, Active scanning probes: A versatile toolkit for fast imaging and emerging nanofabrication, *Journal of Vacuum Science & Technology B* 35 (2017) 06G101.

[184] S. Hou, W. Li, S. Watzele, R. M. Kluge, S. Xue, S. Yin, X. Jiang, M. Döblinger, A. Welle, B. Garlyyev, M. Koch, P. Müller‐Buschbaum, C. Wöll, A. S. Bandarenka, R. A. Fischer, Metamorphosis of heterostructured surface‐mounted metal–organic frameworks yielding record oxygen evolution mass activities, *Advanced Materials* 33 (2021) 2103218.

[185] M. Liu, L. Kong, X. Wang, J. He, X.-H. Bu, Engineering bimetal synergistic electrocatalysts based on metal–organic frameworks for efficient oxygen evolution, *Small* 15 (2019) 1903410.

[186] S. Zhao, C. Tan, C.-T. He, P. An, F. Xie, S. Jiang, Y. Zhu, K.-H. Wu, B. Zhang, H. Li, J. Zhang, Y. Chen, S. Liu, J. Dong, Z. Tang, Structural transformation of highly active metal–organic framework electrocatalysts during the oxygen evolution reaction, *Nature Energy* 5 (2020) 881-890.

[187] W. Li, S. Watzele, H. A. El-Sayed, Y. Liang, G. Kieslich, A. S. Bandarenka, K. Rodewald, B. Rieger, R. A. Fischer, Unprecedented high oxygen evolution activity of electrocatalysts derived from surface-mounted metal–organic frameworks, *Journal of the American Chemical Society* 141 (2019) 5926-5933.

[188] P. Thangavel, M. Ha, S. Kumaraguru, A. Meena, A. N. Singh, A. M. Harzandi, K. S. Kim, Graphene-nanoplatelets-supported NiFe-MOF: high-efficiency and ultra-stable oxygen electrodes for sustained alkaline anion exchange membrane water electrolysis, *Energy & Environmental Science* 13 (2020) 3447-3458.

[189] Z. Cai, L. Li, Y. Zhang, Z. Yang, J. Yang, Y. Guo, L. Guo, Amorphous nanocages of Cu-Ni-Fe hydr(oxy)oxide prepared by photocorrosion for highly efficient oxygen evolution, *Angewandte Chemie International Edition* 58 (2019) 4189-4194.

[190] Y. Zhou, Z. Wang, Z. Pan, L. Liu, J. Xi, X. Luo, Y. Shen, Exceptional performance of hierarchical Ni–Fe (hydr)oxide@NiCu electrocatalysts for water splitting, *Advanced Materials* 31 (2019) 1806769.

[191] B. Liu, Y. Wang, H.-Q. Peng, R. Yang, Z. Jiang, X. Zhou, C.-S. Lee, H. Zhao, W. Zhang, Iron vacancies induced bifunctionality in ultrathin feroxyhyte nanosheets for overall water splitting, *Advanced Materials* 30 (2018) 1803144.

[192] J. Xie, J. Xin, R. Wang, X. Zhang, F. Lei, H. Qu, P. Hao, G. Cui, B. Tang, Y. Xie, Sub-3 nm pores in two-dimensional nanomesh promoting the generation of electroactive phase for robust water oxidation, *Nano Energy* 53 (2018) 74-82.

[193] F. Song, X. Hu, Ultrathin cobalt–manganese layered double hydroxide is an efficient oxygen evolution catalyst, *Journal of the American Chemical Society* 136 (2014) 16481-16484.

[194] M. B. Stevens, L. J. Enman, A. S. Batchellor, M. R. Cosby, A. E. Vise, C. D. M. Trang, S. W. Boettcher, Measurement techniques for the study of thin film heterogeneous water oxidation electrocatalysts, *Chemistry of Materials* 29 (2017) 120-140.

[195] J. Huang, J. Chen, T. Yao, J. He, S. Jiang, Z. Sun, Q. Liu, W. Cheng, F. Hu, Y. Jiang, Z. Pan, S. Wei, CoOOH nanosheets with high mass activity for water oxidation, *Angewandte Chemie International Edition* 54 (2015) 8722-8727.

[196] H. Guo, Z. Fang, H. Li, D. Fernandez, G. Henkelman, S. M. Humphrey, G. Yu, Rational design of rhodium–iridium alloy nanoparticles as highly active catalysts for acidic oxygen evolution, *ACS Nano* 13 (2019) 13225-13234.

[197] A. W. Jensen, G. W. Sievers, K. D. Jensen, J. Quinson, J. A. Arminio-Ravelo, V. Brüser, M. Arenz, M. Escudero-Escribano, Self-supported nanostructured iridium-based networks as highly active electrocatalysts for oxygen evolution in acidic media, *Journal of Materials Chemistry A* 8 (2020) 1066-1071.

[198] T. Kwon, H. Hwang, Y. J. Sa, J. Park, H. Baik, S. H. Joo, K. Lee, Cobalt assisted synthesis of IrCu hollow octahedral nanocages as highly active electrocatalysts toward oxygen evolution reaction, *Advanced Functional Materials* 27 (2017) 1604688.

[199] Q. Zhang, N. M. Bedford, J. Pan, X. Lu, R. Amal, A fully reversible water electrolyzer cell made up from FeCoNi (oxy)hydroxide atomic layers, *Advanced Energy Materials* 9 (2019) 1901312.

[200] J. Zhou, Z. Han, X. Wang, H. Gai, Z. Chen, T. Guo, X. Hou, L. Xu, X. Hu, M. Huang, S. V. Levchenko, H. Jiang, Discovery of quantitative electronic structure-OER activity relationship in metal-organic framework electrocatalysts using an integrated theoretical-experimental approach, *Advanced Functional Materials* 31 (2021) 2102066.

[201] Y. Huang, L.-W. Jiang, B.-Y. Shi, K. M. Ryan, J.-J. Wang, Highly efficient oxygen evolution reaction enabled by phosphorus doping of the Fe electronic structure in iron–nickel selenide nanosheets, *Advanced Science* 8 (2021) 2101775.

[202] F. Sun, G. Wang, Y. Ding, C. Wang, B. Yuan, Y. Lin, NiFe-based metal–organic framework nanosheets directly supported on nickel foam acting as robust electrodes for electrochemical oxygen evolution reaction, *Advanced Energy Materials* 8 (2018) 1800584.

[203] L. Yang, H. Liu, H. Shen, Y. Huang, S. Wang, L. Zheng, D. Cao, Physically adsorbed metal ions in porous supports as electrocatalysts for oxygen evolution reaction, *Advanced Functional Materials* 30 (2020) 1909889.

[204] T. T. H. Hoang, A. A. Gewirth, High activity oxygen evolution reaction catalysts from additive-controlled electrodeposited Ni and NiFe films, *ACS Catalysis* 6 (2016) 1159-1164.

[205] C. Cai, Y. Mi, S. Han, Q. Wang, W. Liu, X. Wu, Z. Zheng, X. Xia, L. Qiao, W. Zhou, X. Zu, Engineering ordered dendrite-like nickel selenide as electrocatalyst, *Electrochimica Acta* 295 (2019) 92-98.

[206] X. Miao, L. Zhang, L. Wu, Z. Hu, L. Shi, S. Zhou, Quadruple perovskite ruthenate as a highly efficient catalyst for acidic water oxidation, *Nature Communications* 10 (2019) 3809.

[207] Z. L. Zhao, Q. Wang, X. Huang, Q. Feng, S. Gu, Z. Zhang, H. Xu, L. Zeng, M. Gu, H. Li, Boosting the oxygen evolution reaction using defect-rich ultra-thin ruthenium oxide nanosheets in acidic media, *Energy & Environmental Science* 13 (2020) 5143-5151.

[208] E. A. Paoli, F. Masini, R. Frydendal, D. Deiana, C. Schlaup, M. Malizia, T. W. Hansen, S. Horch, I. E. L. Stephens, I. Chorkendorff, Oxygen evolution on well-characterized mass-selected Ru and RuO_2 nanoparticles, *Chemical Science* 6 (2015) 190-196.

[209] R. G. Pearson, Hard and soft acids and bases, *Journal of the American Chemical Society* 85 (1963) 3533-3539.

[210] Z. Qiu, C.-W. Tai, G. A. Niklasson, T. Edvinsson, Direct observation of active catalyst surface phases and the effect of dynamic self-optimization in NiFe-layered double hydroxides for alkaline water splitting, *Energy & Environmental Science* 12 (2019) 572-581.

[211] D. L. A. de Faria, S. Ven âncio Silva, M. T. de Oliveira, Raman microspectroscopy of some iron oxides and oxyhydroxides, *Journal of Raman Spectroscopy* 28 (1997) 873-878.

[212] M. W. Louie, A. T. Bell, An investigation of thin-film Ni–Fe oxide catalysts for the electrochemical evolution of oxygen, *Journal of the American Chemical Society* 135 (2013) 12329-12337.

[213] F. Dionigi, Z. Zeng, I. Sinev, T. Merzdorf, S. Deshpande, M. B. Lopez, S. Kunze, I. Zegkinoglou, H. Sarodnik, D. Fan, A. Bergmann, J. Drnec, J. F. d. Araujo, M. Gliech, D. Teschner, J. Zhu, W.-X. Li, J. Greeley, B. R. Cuenya, P. Strasser, In-situ structure and catalytic mechanism of NiFe and CoFe layered double hydroxides during oxygen evolution, *Nature Communications* 11 (2020) 2522.

[214] A. Z. Chen, M. Shiu, J. H. Ma, M. R. Alpert, D. Zhang, B. J. Foley, D.-M. Smilgies, S.-H. Lee, J. J. Choi, Origin of vertical orientation in two-dimensional metal halide perovskites and its effect on photovoltaic performance, *Nature Communications* 9 (2018) 1336.

[215] W. Li, S. Xue, S. Watzele, S. Hou, J. Fichtner, A. L. Semrau, L. Zhou, A. Welle, A. S. Bandarenka, R. A. Fischer, Advanced bifunctional oxygen reduction and evolution electrocatalyst derived from surface-mounted metal–organic frameworks, *Angewandte Chemie International Edition* 59 (2020) 5837-5843.

[216] W. Li, F. Li, H. Yang, X. Wu, P. Zhang, Y. Shan, L. Sun, A bio-inspired coordination polymer as outstanding water oxidation catalyst via second coordination sphere engineering, *Nature Communications* 10 (2019) 5074.

[217] Y. Shi, Y. Yu, Y. Liang, Y. Du, B. Zhang, In situ electrochemical conversion of an ultrathin tannin nickel iron complex film as an efficient oxygen evolution reaction electrocatalyst, *Angewandte Chemie International Edition* 58 (2019) 3769-3773.

[218] J. Chen, P. Zhuang, Y. Ge, H. Chu, L. Yao, Y. Cao, Z. Wang, M. O. L. Chee, P. Dong, J. Shen, M. Ye, P. M. Ajayan, Sublimation-vapor phase pseudomorphic transformation of template-directed MOFs for efficient oxygen evolution reaction, *Advanced Functional Materials* 29 (2019) 1903875.

[219] Z. Xue, Y. Li, Y. Zhang, W. Geng, B. Jia, J. Tang, S. Bao, H.-P. Wang, Y. Fan, Z.-w. Wei, Z. Zhang, Z. Ke, G. Li, C.-Y. Su, Modulating electronic structure of metal-organic framework for efficient electrocatalytic oxygen evolution, *Advanced Energy Materials* 8 (2018) 1801564.

[220] Z. Cai, D. Zhou, M. Wang, S.-M. Bak, Y. Wu, Z. Wu, Y. Tian, X. Xiong, Y. Li, W. Liu, S. Siahrostami, Y. Kuang, X.-Q. Yang, H. Duan, Z. Feng, H. Wang, X. Sun, Introducing Fe^{2+} into nickel–iron layered double hydroxide: Local structure modulated water oxidation activity, *Angewandte Chemie International Edition* 57 (2018) 9392-9396.

[221] W. He, H.-M. Gao, R. Shimoni, Z.-Y. Lu, I. Hod, Synergistic coupling of anionic ligands to optimize the electronic and catalytic properties of metal–organic framework-converted oxygen-evolving catalysts, *ACS Applied Energy Materials* 2 (2019) 2138-2148.

[222] F. Kong, W. Zhang, L. Sun, L. Huo, H. Zhao, Interface electronic coupling in hierarchical FeLDH(FeCo)/$Co(OH)_2$ arrays for efficient electrocatalytic oxygen evolution, *ChemSusChem* 12 (2019) 3592-3601.

[223] J. Y. C. Chen, L. Dang, H. Liang, W. Bi, J. B. Gerken, S. Jin, E. E. Alp, S. S. Stahl, Operando analysis of NiFe and Fe oxyhydroxide electrocatalysts for water oxidation: Detection of Fe^{4+} by mössbauer spectroscopy, *Journal of the American Chemical Society* 137 (2015) 15090-15093.

[224] D. Zhu, C. Guo, J. Liu, L. Wang, Y. Du, S.-Z. Qiao, Two-dimensional metal–organic frameworks with high oxidation states for efficient electrocatalytic urea oxidation, *Chemical Communications* 53 (2017) 10906-10909.

[225] O. Diaz-Morales, I. Ledezma-Yanez, M. T. M. Koper, F. Calle-Vallejo, Guidelines for the rational design of Ni-based double hydroxide electrocatalysts for the oxygen evolution reaction, *ACS Catalysis* 5 (2015) 5380-5387.

[226] F.-L. Li, P. Wang, X. Huang, D. J. Young, H.-F. Wang, P. Braunstein, J.-P. Lang, Large-scale, bottom-up synthesis of binary metal–organic framework nanosheets for efficient water oxidation, *Angewandte Chemie International Edition* 58 (2019) 7051-7056.

[227] B. S. Yeo, A. T. Bell, In situ raman study of nickel oxide and gold-supported nickel oxide catalysts for the electrochemical evolution of oxygen, *The Journal of Physical Chemistry C* 116 (2012) 8394-8400.

[228] S. Lee, K. Banjac, M. Lingenfelder, X. Hu, Oxygen isotope labeling experiments reveal different reaction sites for the oxygen evolution reaction on nickel and nickel iron oxides, *Angewandte Chemie International Edition* 58 (2019) 10295-10299.

[229] S. Lee, L. Bai, X. Hu, Deciphering iron-dependent activity in oxygen evolution catalyzed by nickel–iron layered double hydroxide, *Angewandte Chemie International Edition* 59 (2020) 8072-8077.

[230] S. Klaus, Y. Cai, M. W. Louie, L. Trotochaud, A. T. Bell, Effects of Fe electrolyte impurities on $Ni(OH)_2$/NiOOH structure and oxygen evolution activity, *The Journal of Physical Chemistry C* 119 (2015) 7243-7254.

[231] S. Watzele, P. Hauenstein, Y. Liang, S. Xue, J. Fichtner, B. Garlyyev, D. Scieszka, F. Claudel, F. Maillard, A. S. Bandarenka, Determination of electroactive surface area of Ni-, Co-, Fe-, and Ir-based oxide electrocatalysts, *ACS Catalysis* 9 (2019) 9222-9230.

[232] A. Alobaid, C. Wang, R. A. Adomaitis, Mechanism and kinetics of HER and OER on NiFe LDH films in an alkaline electrolyte, *Journal of The Electrochemical Society* 165 (2018) J3395-J3404.

[233] A. C. Garcia, T. Touzalin, C. Nieuwland, N. Perini, M. T. M. Koper, Enhancement of oxygen evolution activity of nickel oxyhydroxide by electrolyte alkali cations, *Angewandte Chemie International Edition* 58 (2019) 12999-13003.

[234] I. Roger, M. A. Shipman, M. D. Symes, Earth-abundant catalysts for electrochemical and photoelectrochemical water splitting, *Nature Reviews Chemistry* 1 (2017) 0003.

[235] Q. Zhang, E. Uchaker, S. L. Candelaria, G. Cao, Nanomaterials for energy conversion and storage, *Chemical Society Reviews* 42 (2013) 3127-3171.

[236] T. R. Cook, D. K. Dogutan, S. Y. Reece, Y. Surendranath, T. S. Teets, D. G. Nocera, Solar energy supply and storage for the legacy and nonlegacy worlds, *Chemical Reviews* 110 (2010) 6474-6502.

[237] D. Strmcnik, K. Kodama, D. van der Vliet, J. Greeley, V. R. Stamenkovic, N. M. Marković, The role of non-covalent interactions in electrocatalytic fuel-cell reactions on platinum, *Nature Chemistry* 1 (2009) 466-472.

[238] J. Zaffran, M. B. Stevens, C. D. M. Trang, M. Nagli, M. Shehadeh, S. W. Boettcher, M. Caspary Toroker, Influence of electrolyte cations on Ni(Fe)OOH catalyzed oxygen evolution reaction, *Chemistry of Materials* 29 (2017) 4761-4767.

[239] M. Görlin, J. Halldin Stenlid, S. Koroidov, H.-Y. Wang, M. Börner, M. Shipilin, A. Kalinko, V. Murzin, O. V. Safonova, M. Nachtegaal, A. Uheida, J. Dutta, M. Bauer, A. Nilsson, O. Diaz-Morales, Key activity descriptors of nickel-iron oxygen evolution electrocatalysts in the presence of alkali metal cations, *Nature Communications* 11 (2020) 6181.

[240] K. Li, D. Xue, Estimation of electronegativity values of elements in different valence states, *The Journal of Physical Chemistry A* 110 (2006) 11332-11337.

[241] S. K. Searles, I. Dzidic, P. Kebarle, Proton affinities of the alkali hydroxides, *Journal of the American Chemical Society* 91 (1969) 2810-2811.

[242] J. D. Michael, E. L. Demeter, S. M. Illes, Q. Fan, J. R. Boes, J. R. Kitchin, Alkaline electrolyte and Fe impurity effects on the performance and active-phase structure of

NiOOH thin films for OER catalysis applications, *The Journal of Physical Chemistry C* 119 (2015) 11475-11481.

[243] F. D. Hardcastle, I. E. Wachs, Determination of molybdenum–oxygen bond distances and bond orders by Raman spectroscopy, *Journal of Raman Spectroscopy* 21 (1990) 683-691.

[244] D. Scieszka, C. Sohr, P. Scheibenbogen, P. Marzak, J. Yun, Y. Liang, J. Fichtner, A. S. Bandarenka, Multiple potentials of maximum entropy for a $Na_2Co[Fe(CN)_6]$ battery electrode material: Does the electrolyte composition control the interface? *ACS Applied Materials & Interfaces* 10 (2018) 21688-21695.

[245] T. C. Nagaiah, A. Tiwari, M. Kumar, D. Scieszka, A. S. Bandarenka, In situ probing of Mn_2O_3 activation toward oxygen electroreduction by the laser-induced current transient technique, *ACS Applied Energy Materials* 3 (2020) 9151-9157.

[246] X. Ding, T. K. Sarpey, S. Hou, B. Garlyyev, W. Li, R. A. Fischer, A. S. Bandarenka, Prospects of using the laser-induced temperature jump techniques for characterisation of electrochemical systems, *ChemElectroChem* (2021) e202101175.

[247] X. Ding, D. Scieszka, S. Watzele, S. Xue, B. Garlyyev, R. W. Haid, A. S. Bandarenka, A systematic study of the influence of electrolyte ions on the electrode activity, *ChemElectroChem* 9 (2022) e202101088.

[248] V. Climent, B. A. Coles, R. G. Compton, Coulostatic potential transients induced by laser heating of a Pt(111) single-crystal electrode in aqueous acid solutions. Rate of hydrogen adsorption and potential of maximum entropy, *The Journal of Physical Chemistry B* 106 (2002) 5988-5996.

[249] N. García-Araez, V. Climent, J. M. Feliu, Evidence of water reorientation on model electrocatalytic surfaces from nanosecond-laser-pulsed experiments, *Journal of the American Chemical Society* 130 (2008) 3824-3833.

[250] I. Ledezma-Yanez, W. D. Z. Wallace, P. Sebastián-Pascual, V. Climent, J. M. Feliu, M. T. M. Koper, Interfacial water reorganization as a pH-dependent descriptor of the hydrogen evolution rate on platinum electrodes, *Nature Energy* 2 (2017) 17031.

[251] V. Climent, B. A. Coles, R. G. Compton, Laser induced current transients applied to a Au(111) single crystal electrode. A general method for the measurement of potentials of zero charge of solid electrodes, *The Journal of Physical Chemistry B* 105 (2001) 10669-10673.

[252] Z. Morgan Chan, D. A. Kitchaev, J. Nelson Weker, C. Schnedermann, K. Lim, G. Ceder, W. Tumas, M. F. Toney, D. G. Nocera, Electrochemical trapping of metastable Mn^{3+} ions for activation of MnO_2 oxygen evolution catalysts, *Proceedings of the National Academy of Sciences* 115 (2018) E5261.

[253] Y. Sun, H. Cheng, S. Gao, Z. Sun, Q. Liu, Q. Liu, F. Lei, T. Yao, J. He, S. Wei, Y. Xie, Freestanding tin disulfide single-layers realizing efficient visible-light water splitting, *Angewandte Chemie International Edition* 51 (2012) 8727-8731.

[254] G. Tsoukleri, J. Parthenios, K. Papagelis, R. Jalil, A. C. Ferrari, A. K. Geim, K. S. Novoselov, C. Galiotis, Subjecting a graphene monolayer to tension and compression, *Small* 5 (2009) 2397-2402.

[255] H. B. Tao, L. Fang, J. Chen, H. B. Yang, J. Gao, J. Miao, S. Chen, B. Liu, Identification

of surface reactivity descriptor for transition metal oxides in oxygen evolution reaction, *Journal of the American Chemical Society* 138 (2016) 9978-9985.

[256] Q. Wang, L. Shang, R. Shi, X. Zhang, Y. Zhao, G. I. N. Waterhouse, L.-Z. Wu, C.-H. Tung, T. Zhang, NiFe layered double hydroxide nanoparticles on Co,N-codoped carbon nanoframes as efficient bifunctional catalysts for rechargeable zinc–air batteries, *Advanced Energy Materials* 7 (2017) 1700467.

[257] P. S. Bagus, A. Wieckowski, H. Freund, The contribution of lattice strain to core-level binding energy shifts in metal nanoparticles: Generality and origin of the shifts, *Computational and Theoretical Chemistry* 987 (2012) 22-24.

[258] J. R. Kitchin, J. K. Nørskov, M. A. Barteau, J. G. Chen, Role of strain and ligand effects in the modification of the electronic and chemical properties of bimetallic surfaces, *Physical Review Letters* 93 (2004) 156801.

[259] M. Mavrikakis, B. Hammer, J. K. Nørskov, Effect of strain on the reactivity of metal surfaces, *Physical Review Letters* 81 (1998) 2819-2822.

[260] D. Zhou, S. Wang, Y. Jia, X. Xiong, H. Yang, S. Liu, J. Tang, J. Zhang, D. Liu, L. Zheng, Y. Kuang, X. Sun, B. Liu, NiFe hydroxide lattice tensile strain: Enhancement of adsorption of oxygenated intermediates for efficient water oxidation catalysis, *Angewandte Chemie International Edition* 58 (2019) 736-740.